ZINC OXIDE-BASED THIN FILM ELECTRONICS

WONG LAI MUN
(M. Sc. (Electrical Eng.), NUS, B. Eng. (Hons.), NUS)

A THESIS SUBMITTED

FOR THE DEGREE OF DOCTOR OF PHILOSOPHY

DEPARTMENT OF ELECTRICAL AND COMPUTER ENGINEERING

NATIONAL UNIVERSITY OF SINGAPRE

2012

Declaration

I hereby declare that this thesis is my original work and it has been written by me in its entirety.
I have duly acknowledged all the sources of information which have been used in the thesis.

This thesis has also not been submitted for any degree in any university previously

Wong Lai Mun
21 May 2012

Acknowledgements

First of all, I would like to express my sincere gratitude to my supervisors, Dr Wang Shijie (IMRE) and Associate Professor Chim Wai Kin (Department of Electrical and Computer engineering, NUS). Working with both of my supervisors proved to be successful and productive. I am indebted to Dr Wang for his continuous guidance, constructive comments and technical support during the course of this part-time PhD. study. I am grateful to Professor Chim for providing excellent supervision throughout the whole project. His support and invaluable advice were greatly appreciated. It has been my good fortune to be their student. Thank you so much for everything.

This project would not have been possible without much assistance from scientists as well as excellent research environment in IMRE. I would like to thank a few more special persons here: Dr Chiam Sing Yang for all the help in performing the experiments and who taught me lots of things which I never know, and Dr Huang Jinquan for his guidance in characterization. I would also like to thank the other research staffs and students from IMRE, NUS and NTU, Dr Chai Jian Wei, Dr Pan Ji Sheng, Dr Chen Qian, Ms Christina Tan Yuen Ling, Ms June Ong, Ms Tan Hui Ru, Ms Hui Hui Kim, Dr Liu Hong, Ms Chew Ah Bian, Mr Liu Zhi Qiang, Mr Ren Yi and Mr Tang Jiao Huang, for their patient and generous technical assistance. It has been a pleasure and privilege for me to work with them.

Completing this PhD study has been the most challenging time in my life. I am very grateful to my husband, Kai Yon, who have accompanied me throughout my studies and helped me tide over the difficult times. I also would like to thank my mum

and dad for their consistent encouragement, support, understanding and prepared lots of nice cooking for me during my study. Without them, I will not be what I am today.

My post-graduate study was supported by A*STAR (Agency for Science, Technology and Research) scientific staff development awards.

Table of Content

Summary

In this dissertation, the growth and characterization of Group III-doped zinc oxide as well as its applications are presented. The first part focused on optimizing the room temperature growth of gallium-doped zinc oxide (GZO) and aluminum-doped zinc oxide (AZO) on low-cost substrates, such as glass and polyethylene terephthalate (PET), using the pulsed laser deposition (PLD) technique. It was found that a desirable amount of oxygen can reduce defect related scattering which enhances carrier mobility of the GZO and AZO films. The second part focused on application of these films.

The structural, surface morphology, optical and electrical property of the room temperature and high temperature deposited GZO films were examined. A figure-of-merit was introduced to correlate the optical and electrical property of transparent conducting oxides (TCOs) based on a normalized transparency index (TI_N), thereby giving a standardized method of evaluating the transparency and electrical property simultaneously. The TI_N clearly showed the dependence on oxygen pressure, carrier concentration and band gap changes which can affect the quality of TCOs. For the room temperature GZO films, an excellent resistivity of ~3.9×10^{-4} Ω-cm and an electron mobility of ~19.2 cm^2/V-s with a TI_N of 0.84 (84% of total solar spectrum transmitted) was achieved.

For AZO thin films, the study was focused on deposition onto glass and PET substrates by varying the oxygen pressure and thicknesses of the films. An appropriate thickness of good quality films is important as it is directly related to the cost of material needed. For a ~115 nm thick AZO on PET, a low resistivity of ~6.6 ×

10^{-4} Ω-cm was achieved with carrier mobility of ~15.4 cm^2/Vs, carrier concentration of ~6.2×10^{20} cm^{-3} and a TI_N of 0.9 in the visible region. This shows that both room temperature GZO and AZO films are suitable electrodes for use in photovoltaic and organic devices.

Next, indium-free multilayer structures, such as silver (Ag)/GZO and GZO/Ag/GZO structures, deposited by electron beam evaporation and PLD, were investigated. The effect of an additional germanium (Ge) buffer layer prior to Ag deposition was also investigated and results show that this can reduce surface roughness of the film, improve electrical properties and also enhance transparency in the ultraviolet and near infrared (NIR) regions. In addition to the single-layer sandwich structure of GZO, the optical and electrical properties of multilayered sandwich structures of AZO/Ag/Ge/AZO were also examined. The latter showed better electrical properties than the single AZO layer and offer control on the NIR transparency.

To demonstrate the potential applications of TCOs for photovoltaic devices, sensors and thin film transistors (TFT), room temperature growth of p-type cuprous oxide (Cu_2O), undoped zinc oxide (ZnO) and indium-tin oxide (ITO) films were also optimized. P-type single phase Cu_2O and undoped ZnO were obtained by the magnetron sputtering technique by precise control of oxygen. For photovoltaic application, the focus of investigation is on the band alignment of Cu_2O with GZO (potential electrode or n-type layer). To demonstrate the effect of using transparent and non-transparent electrodes on a photo-sensing ZnO device, a comparative study on photoconductivity using different electrodes such as gold, AZO and ITO was

performed. For TFT application, the band alignment of hafnium oxide deposited on ZnO substrates was investigated and a TFT using ZnO film as channel material and hafnium oxide gate dielectric was fabricated and examined.

List of Tables

List of Figures

List of Symbols

ρ	Electrical resistivity
n	Carrier concentration
μ	Carrier mobility
q	Electron charge
d	Thickness of film
R_s	Sheet resistance
$\langle\tau\rangle$	Average relaxation time
m^*	Effective mass of the charge carrier
m_v^*	Valence band effective mass
m_c^*	Conduction band effective mass
μ_{tot}	Total carrier mobility
ε_o	Permittivity of free space
ε_r	Relative permittivity of the material
h	Planck's constant
$\hbar$	Reduced Planck's constant ($h/2\pi$)
n_N	Concentration of neutral impurities
μ_{IIS}	Ionized impurity scattering
μ_N	Neutral impurity scattering
μ_g	Grain boundary scattering
Φ_b	Grain boundary potential
L	Grain size
k_B	Boltzmann constant

T	Temperature
TI_N	Normalized transparency index
α	Absorption coefficient
E	Energy of the photon
E_g	Band gap
ΔE_g	Optical band gap shift
$h\upsilon$	Photon energy
n_{op}	Refractive index
k	Extinction coefficient
λ	Wavelength
ε	Permittivity of material
τ	Relaxation time
ω_p	Plasma resonance frequency
n_i	Refractive index of the medium at the incidence side
n_r	Refractive index of the medium at the refracted side
θ_i	Incident angle at the interface
θ_r	Refracted angle at the interface
Γ	Reflection coefficient
F	Correction factor
Q	Symmetry factor
E	Electric field
B	Magnetic field
F	electrostatic forces
ν	Carrier velocity
V_H	Hall voltage

N	Carrier density
W	Separation between the two contacts
N_b	Bulk carrier density
ρ_{op}	Ratio of Fresnel reflection coefficients
$\widetilde{R}_p$	P-polarized light
$\widetilde{R}_s$	S-polarized light
Ψ	Measured values of VASE (psi)
Δ	Measured values of VASE (delta)
t_{cg}	Average dimension of the crystallites normal to the reflecting planes
λ_x	Wavelength of the X-ray
B_w	Width at the full-width at half-maximum (FWHM) of the observed peak
Γ_n	Measured transmittance at the wavelength n (nm)
I_n	Intensity of the spectrum with a unit of $Wm^{-2}nm^{-1}$
TI_N	Normalized transparency index
α_n	Absorption coefficient at the particular wavelength
ε_∞	Dielectric constant at very high frequency (value = 3.85)
φ_{TC}	Haacke's figure of merit
E_i^S	Binding energy of the core level "*i*" for the sample "*s*"
E_{VBM}^S	Valence band maximum (VBM)for the sample "*s*"
W	Channel width
L	Channel length
I_D	Drain current
V_D	Drain voltage

V_G	Gate voltage
C_{ox}	Oxide capacitance per area
V_{TH}	Threshold voltage
S	Subthreshold swing
μ_{sat}	Saturation mobility

Chapter 1 Introduction

Transparent conducting oxides (TCOs) have gained increasing importance as key components in the daily lives of individuals, especially for applications such as flat panel display technology, optoelectronic devices, photovoltaic devices and electrochromic devices.[1-5] Most of these films are fabricated with polycrystalline or amorphous microstructures. For the above-mentioned applications, the TCO thin films generally have to exhibit a resistivity of the order of at least ~10^{-3} Ω-cm, for efficient carrier transport, and have an average transmittance that is larger than 80 % in the visible region for suitable use as a transparent electrode.[6]

1.1 Background

Generally, transparent materials are insulators (absorbing little light), while metallic or semiconducting materials normally appear black or reflective (absorbing most frequencies of visible light). The coexistence of high transparency with excellent conductivity is uncommon. However, there are two classes of materials which possess such a combination of transparency and conductivity. The first group is formed by extremely thin metal films (~10 nm) such as gold, silver, chromium and copper with transmittance of up to 50 %.[7] However, as these films are metallic in nature, they are not very stable in air and there is also an adhesion problem onto substrates, especially on low-cost substrates such as glass.[8] These materials, such as silver and gold, are widely used in-between other film layers to reflect heat and provide thermal insulation.[9] The second group of materials consist of wide band gap oxide semiconductors. As early as 1907, cadmium oxide was formed using thermal oxidation; it was reported that both good electrical conductivity and optical

transmittance were obtained.[10] Over the years, TCOs have gained great interest for their potential industrial applications. Over the last thirty to forty years, other than indium oxide, tin oxide, indium tin oxide (ITO) and zinc oxide (ZnO) were also recognized as materials with high conductivity, comparable to metallic materials, while possessing very large optical band gaps of greater than 3 eV. This opened a new era of transparent conducting oxides with ITO currently dominating the present industry standard for use as electrical electrodes in solar cells, flat panel displays and other optoelectronic applications.

Zinc oxide is one of the compound semiconducting materials that has been investigated as early as 1930-40s for electrical conductivity at different temperatures.[11,12] Having a wide band gap of ~3.4 eV and high transparency, ZnO has wide usage in terms of applications in transistor devices and as a photovoltaic layer. Throughout the years, many researches have been done on ZnO as evidenced by the various reviews published.[13-17] Intrinsic ZnO is a n-type material; it is transparent and fairly conducting. However, as compared to ITO, undoped ZnO has a much higher resistivity. Therefore, in order to make ZnO attractive as a transparent conducting oxide, doping is necessary as it reduces its resistivity. Controllable n-type doping of ZnO can be readily achieved by substituting the Zn^{2+} ions with group III elements which release excess electrons to reduce its resistivity.

1.2 Motivation

Conventional Si-based and III-V-based electronics are non-transparent and their basic device structure consists of semiconductor junctions and transistors.[18] However, one current trend in the electronics industry is the usage of transparent

substrates in the device structure. The advantage of transparent electronics is that it allows electronic devices to be integrated (stacked) and embedded into large area like windows, shop displays and even wall partitions to small item like items such as refrigerators, ovens, etc. It allows the traditional transparent panels to become functional, thus giving it a more spacious and eye-catching look. To realize transparent electronics, one will first think of using a low cost transparent substrate such as glass. However, glass by itself is non-conducting and hence thin film coatings with circuitries are required to transform glass into useful transparent devices. In addition, the building blocks of the transparent electronics have to be transparent in the visible range, meaning that the semiconductor layers, the electrodes and dielectric/passivation layers now have to be transparent. One big challenge is that not all semiconductors and electrodes have high transparency in the visible region. In terms of conducting electrodes, currently ITO has been the primary transparent conductive oxide for most applications, especially in large-area applications such as displays.[19] However, the supply of indium has become inconsistent during the last 20 years, resulting in great fluctuations in indium prices and thus affecting the manufacturing cost.[20,21] With the rapidly expanding flat panel display market, alternative materials are sought and much research is being conducted on seeking alternative candidates to replace ITO, such as carbon nanotube films, graphene films, metal nanowire gratings, fluorinated tin oxide and doped ZnO.[22-27] Moreover, the toxicity of indium compounds is also a concern in both the manufacturing and usage of the devices.[28] Therefore, there is an urgent need to seek cheaper alternative materials to replace ITO due to cost and toxicity considerations.[29,30] Furthermore, ITO thin films are not the ideal choice for organic devices. One of the reasons is the need for a moderate heat treatment (>300 °C) to obtain the desired transparency and

resistivity for ITO.[31,32] This means that using ITO as a top electrode material, the elevated processing temperature can cause unwanted modifications to the underlying plastic materials, since the latter typically has a lower glass transition temperature.[33] As a bottom electrode material, the heat treatment of ITO can cause roughening of the film surface, which can affect the quality of subsequent film coating or deposition.[34-37] It is therefore necessary to seek alternative TCOs that can achieve the desired characteristics at low growth or processing temperatures for applications in organic electronics as well as flexible displays.[38-42]

In terms of thin film deposition, ZnO is a potential candidate with a wide direct band gap and high transparency. In addition, it is also non-toxic, abundant and most importantly inexpensive. Doping different materials into ZnO can give many interesting results. Doped zinc oxide can be used as contact electrodes for many applications. It can also be used as channel materials for transparent transistors, light-emitting diodes, sensors as well as photovoltaic devices. The electrical and optical performances are, to a large extent, determined by fundamental properties such as structure and composition, which can be tuned and manipulated in the deposition and post-deposition processes.

Other than TCO thin films to realize transparent electronics, this work is also motivated by the increasing need for applications on low-cost, light-weight substrates and even flexible ones.[2,43] Flexible electronics is an emerging and significant market. Due to the advantage of light weight, small size and cost effectiveness of the substrates, it offers a new era for device engineering. However, in terms of process, the manufacturing temperature of TCO materials on polymers is restricted by the low

melting point of polymers, which negatively influences their performance.[44] The process conditions of TCOs on polymeric substrates need to be adjusted to avoid substrate damages. Under these circumstances, it is important to understand the fundamental properties of the materials and optimize their performance in order to meet the technological requirements. The deposition techniques to be used have to allow precise control of the fundamental properties, which assist the research of high-performance TCOs on polymeric substrates.

1.3 Research Objectives

The primary aim of the work reported in this thesis is the fabrication of cost-effective zinc oxide-based TCOs on economical substrates with electrical and optical properties comparable to ITO. Taking into consideration the constraint of thermal budget when polymeric substrates are used, the desired growth condition of these TCOs is targeted to be performed at room temperature while maintaining the high quality of the TCO films. The second objective is to integrate these films for potential applications in photovoltaic structures, sensors and thin film transistors.

In this work, pulsed laser deposition and magnetron sputtering are used to deposit zinc oxide-based TCO films onto low-cost glass substrates and polymeric substrates. Investigations on the electrical, structural, optical and morphology properties of the TCO films are performed. Extensive analysis is conducted using various characterization techniques to study relevant properties in order to optimize the performance of these TCOs films. To demonstrate some applications of the TCOs, other oxide materials such as cuprous oxide, cupric oxide and hafnium oxide are also investigated using magnetron sputtering.

1.4 Organization of Thesis

Following the presentation of the background, motivation and objectives of this work in **Chapter 1**, a brief overview of the fundamental aspects of TCOs was provided in **Chapter 2**. Among the various TCOs, the background and relevant literature survey of doped zinc oxides were presented. The basic concepts and the fundamental properties of doped zinc oxide were discussed. Other oxide materials used in the demonstration of the TCO applications were also discussed.

In **Chapter 3**, the growth techniques employed for the preparation of doped zinc oxide thin films, other oxide materials and metallic films were summarized. The working principle of the various characterization techniques was also briefly discussed.

There are three main chapters which discussed the experimental findings. In **Chapter 4**, the experimental procedures for obtaining gallium-doped zinc oxide (GZO) were discussed. In this work, the GZO films were first deposited at room temperature by varying the oxygen pressure. Next, the growth condition of the optimized GZO film was chosen and then varied with higher substrate temperature. The correlation between the oxygen pressure with the structural, electrical, optical and surface morphology properties of deposited films was discussed. In addition, the growth of GZO films, with a sandwiched thin metallic layer, was also investigated. The variation of the thicknesses of the metallic layers was examined together with investigation on the effect of an additional buffer layer prior to depositing the metallic

layer. In this work, the surface morphology, electrical and optical properties of GZO multilayer films were discussed.

In **Chapter 5**, the experimental procedures of another Group III-doped ZnO, that is aluminum zinc oxide (AZO), on glass and polymeric substrates were presented. In this work, the oxygen pressure was first varied to optimize the AZO thin films. Then, the optimized AZO films were examined at different thicknesses and their electrical and optical properties were discussed. Next, the optical property was further examined by measuring the refractive index of AZO thin film. In this work, electrical and optical properties of single, double and triple multilayered sandwich structures of AZO/Ag/Ge/AZO were also examined.

In **Chapter 6**, some potential applications of these TCOs were demonstrated. Here, the growth of cuprous oxide (Cu_2O) for the photovoltaic applications was studied and the band alignment of GZO/Cu_2O was discussed. Next, the AZO thin film was used as contact electrode for a potential optical sensor. Then, the band alignment of hafnium oxide on zinc oxide for thin film transistor application was discussed. A high-*k* dielectric transistor was also demonstrated using zinc oxide as the channel layer.

Lastly, in **Chapter 7**, the research findings and the important results of this work were summarized and some possible directions for future works were also provided.

Chapter 2 Literature Review

In this chapter, some background information on transparent conducting oxides (TCOs), such as zinc oxide (ZnO) and cuprous oxide (Cu_2O), is presented. Some potential applications of these TCOs, such as in solar cells and in thin film transistors, are also discussed.

2.1 Zinc Oxide and Doped Zinc Oxide

Zinc oxide (ZnO) is a compound semiconductor with a wide band gap of ~3.4 eV at room temperature.[14] Naturally, ZnO has a hexagonal wurtzite structure. There are two other phases which are known to exist, namely the zincblende structure and rock salt structure. Zincblende ZnO is stable only by growing on cubic structures.[45,46] For rock salt ZnO, it is formed under high pressure of about 10 GPa at room temperature or above 6 GPa at 1200 K, and cannot be epitaxially stabilized.[47,48]

Zinc oxide single crystals have been widely grown using pressurized melt growth, seeded sublimation growth and hydrothermal solution growth.[49-52] Good quality ZnO single crystals have been obtained using the hydrothermal growth method with a growth rate about 0.2 mm per day.[51] Zinc oxide epitaxial thin films have been grown using molecular beam epitaxy (MBE) [53,54], pulsed laser deposition (PLD) [55], magnetron sputtering [56], metal-organic chemical vapour deposition (MOCVD) [57] and other methods. Polycrystalline ZnO films can also be

grown on low cost substrates, such as glass and flexible polymeric substrates, at low temperature.

Zinc oxide is naturally a n-type semiconductor due to its deviation from stoichiometry related to the presence of intrinsic defects such as oxygen vacancies and zinc interstitials.[14] In undoped ZnO, the electrical conductivity is not high enough for practical application. The conductivity of ZnO can be increased either by doping with group III elements, such as Boron (B), Aluminum (Al), Gallium (Ga) and Indium (In) to replace zinc (Zn) atoms, or by doping with group VII elements, such as fluorine (F) to substitute oxygen (O) atoms.[58,59] Other metal oxides, with three or more valence electrons, can also be used to increase the conductivity of ZnO. In this work, the focus is on doping with Group III elements as these elements can be doped into intrinsic ZnO to enhance its electrical property. Table 2.1 shows the atomic radius, ionic radius, covalent radius and the abundance of various Group III elements and the elements comprising ZnO. Aluminum-, Ga- and In-doped ZnO (i.e., AZO, GZO and IZO) semiconductors are some promising alternatives to ITO for thin film transparent electrode applications, whereas B has a much smaller ionic diameter than Zn and Thallium is highly toxic.[60-63] Although IZO still uses Indium which is scarce, the weighted percentage of indium needed in the target is greatly reduced from a commonly used 90% (in ITO) to 1-2% (in IZO). Among the group III elements, Al and Ga are the two of the most abundant elements. Figure 2.1 shows the comparison between the variation in resistivity with film thickness from other independent reports of GZO and AZO film are shown.[30,43,64-89] These values are categorized by room temperature growth and non-room temperature growth. In terms of room temperature growth, the AZO and GZO films give similar resistivity at smaller film thicknesses. It

was observed that for non-room-temperature grown GZO films, the resistivity of the film is lower for most thicknesses. For non-room-temperature AZO films, there is no obvious trend that the AZO film has better resistivity due to higher substrate temperature growth or post annealing.

Table 2.1 Atomic radius, ionic radius and covalent radius of Group III and ZnO elements and their abundance in the Earth's crust [90,91]

Elements	Atom radius (Å)	Ionic radius (Å)	Covalent radius (Å)	Abundance in Earth's Crust of the element (%)*
Boron	0.85	0.41	0.82	0.00086
Aluminum	1.25	0.68	1.18	8.1
Gallium	1.30	0.76	1.26	0.0019
Indium	1.55	0.94	1.44	0.000016
Thallium	1.90	1.03	1.48	0.000053
Zinc	1.35	0.88	1.31	0.0078
Oxygen	0.60	1.24	0.73	46

*Data are provided by Mathematica's Element Data function from Wolfram Research, Inc.

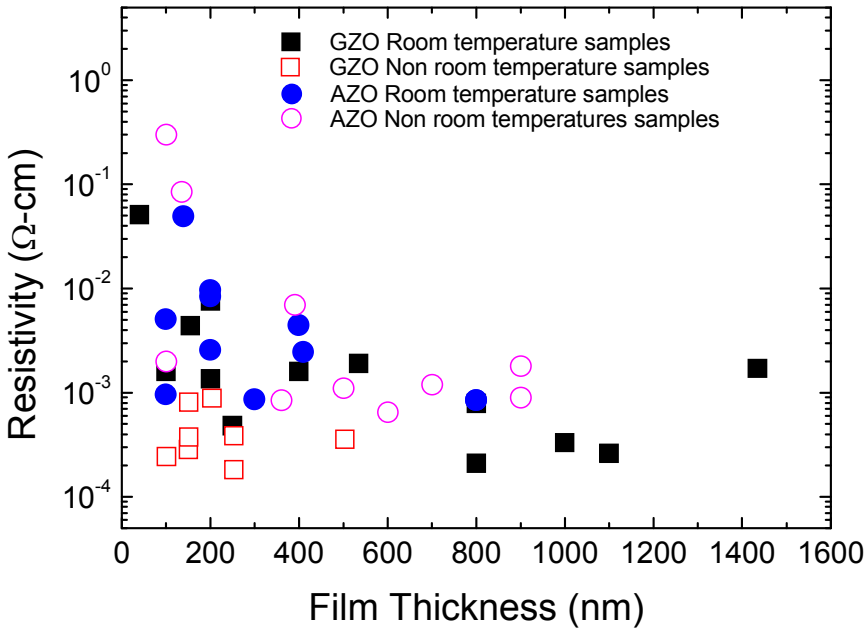

Figure 2.1 Comparison between the variation in resistivity with film thickness from other independent reports of GZO and AZO film are shown.[30,43,64-89] These values are categorized by room temperature growth and non-room temperature growth.

2.1.1 Crystallographic Structure of ZnO

At room temperature and atmospheric pressure, ZnO has a wurtzite (B4 type) structure as shown in Figure 2.2. Zinc oxide has a hexagonal lattice, belonging to the space group of $P6_3mc$.[92] In this structure, each zinc cation (Zn^{2+}) is surrounded by four oxygen anions (O^{2-}) at the corners of a tetrahedron, and vice versa. In other words, the ZnO crystal structure is composed of alternating planes of Zn^{2+} and O^{2-} ions stacking along the c-axis.[93] The lattice constants are a = 3.2498Å and c = 5.2066Å.[94]

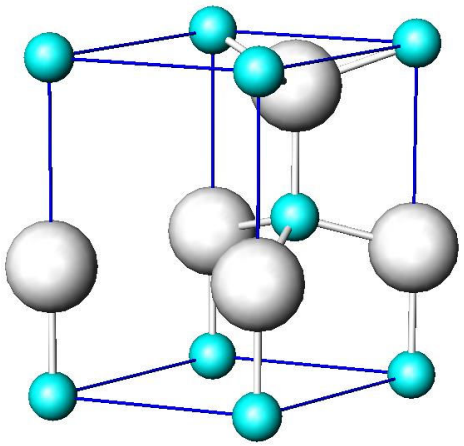

Figure 2.2 Wurtzite structure of ZnO. The smaller cyan coloured balls represent zinc cations while the larger white coloured balls represent oxygen anions.

2.1.2 Band Structure of ZnO

Zinc oxide (a II-VI material) has a direct wide band gap of ~3.4 eV and is an optoelectronic semiconductor in competition with GaN.[14] The schematic energy band diagram of ZnO is shown in Figure 2.3.[95] By doping with group III elements (for example, Ga, Al or In), the Group III element will act as a shallow donor when substituted on the Zn site. The shallow donors will release electrons to make doped ZnO a n-type semiconductor. If ZnO is doped with group VII elements such as

fluorine (F), the F atom will act as a shallow donor when it occupies the oxygen site and release one electron.[96] By alloying with cadmium oxide (with band gap, Eg = 2.2 eV), the band gap of ZnO can be narrowed while by alloying with magnesium oxide (Eg = 7.8 eV), the band gap of ZnO can be widened.[97,98]

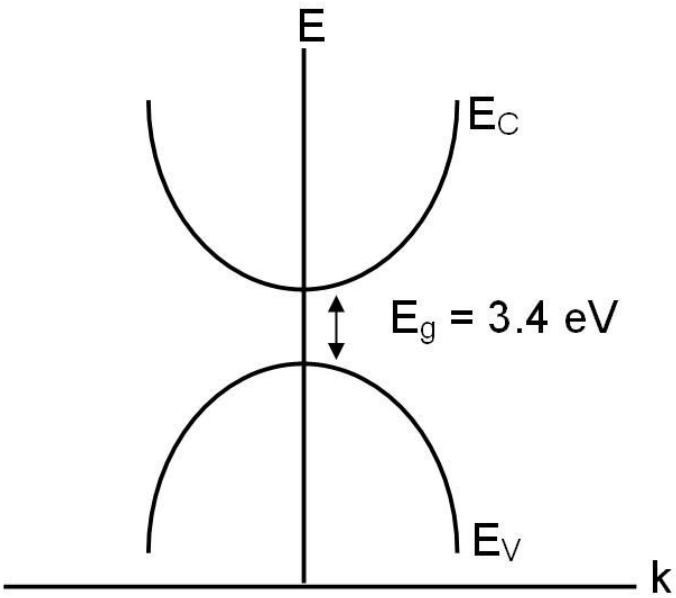

Figure 2.3 Schematic band diagram of ZnO

2.1.3 Electrical Properties of ZnO

Electrical resistivity (ρ) depends on the carrier concentration (n) and carrier mobility (μ) and their relationship is given by

$$\rho = \frac{1}{qn\mu} \tag{2.1}$$

where q is the electron charge.[99] For a thin film of uniform thickness d, the resistivity of the film can be expressed in terms of the sheet resistance R_s as follows:

$$R_s = \frac{\rho}{d} \tag{2.2}$$

Other than the thickness, the sheet resistance is independent of the film dimensions. From equation (2.1), to decrease the resistivity, one can increase the carrier concentration by doping, whereby these dopants can occupy the substitutional sites, fill the interstitials sites or create vacancies. The type of dopants will determine whether the film material will be p-type or n-type. If the dopants are donors and donate electrons, the material will become n-type. If the dopants are acceptors and accept electrons, the material will become p-type.

Another way to reduce resistivity is to increase the carrier mobility. However, carrier mobility is dependent on scattering and cannot be controlled directly. To further examine mobility, the expression of the mobility of charge carrier, as seen below, was examined:

$$\mu = \frac{q\langle\tau\rangle}{m^*} \tag{2.3}$$

where $\langle\tau\rangle$ is the average relaxation time and m^* is the effective mass of the charge carrier. The average relaxation time depends on the drift velocity and the mean free path of the charge carriers, which in turn depends on various scattering events such as lattice scattering, electron-electron scattering, electron-impurity scattering, ionized impurity scattering, neutral impurity scattering, and grain boundary scattering.[100] Therefore, the total carrier mobility (μ_{tot}) can be expressed as the summation of the mobilities which are in turn influenced by various scattering mechanisms as follows:

$$\frac{1}{\mu_{tot}} = \sum_i \frac{1}{\mu_i} \tag{2.4}$$

where the mobility μ_i is related with the i scattering mechanism.

Lattice scattering is the scattering of conducting electrons by the thermal vibration of atoms in a lattice. This effect can be qualitatively understood as phonons colliding with charge carriers.[101] As lattice scattering, electron-electron scattering and electron-impurity scattering exist in most materials, there is difficulty in influencing these individual scattering events to increase mobility directly.[102-104] In the following part, neutral impurity scattering, ionized impurity scattering and grain boundary scattering are discussed.

Neutral impurity scattering can be expressed as

$$\mu_N = \frac{m^* q^3}{20\varepsilon_o \varepsilon_r n_N \hbar^3} \tag{2.5}$$

where m^* is the effective mass of the carriers, ε_o is the permittivity of free space, ε_r is the relative permittivity of the material, $\hbar$ is the reduced Planck's constant ($h/2\pi$) and n_N is the concentration of neutral impurities.[105] Yang *et al*. has reported that for an undoped material, the neutral-impurity scattering is more significant compared to a doped material.[106] For doped materials, ionized impurity scattering is one of the major factors affecting the carrier mobility.

Ionized impurity scattering is the scattering of charge carriers by impurity ions in the lattice. This scattering is significant in highly degenerate semiconductors because the electrostatic field due to such impurities (present in a high concentration) remains effective even at a great distance. Ionized impurity scattering can be expressed as [96]

$$\mu_{IIS} = \frac{4q}{h}\left(\frac{\pi}{3}\right)^{1/3} n^{-2/3} \tag{2.6}$$

From equations (2.1) and (2.6), it can be observed that there is a trade-off between low resistivity, carrier concentration and mobility because the relationship between the carrier concentration and mobility is governed by $\mu_{IIS} \propto n^{-2/3}$.

Grain boundary scattering is an important scattering mechanism in polycrystalline films, especially those with small grain size. At the grain boundaries, there are many defect states, such as foreign impurities, self-interstitial-type atoms, voids, vacancies and dangling bonds, which can trap free carriers from the bulk material.[107] Petritz's model (equation (2.7) below) has been commonly used to explain the transport phenomenon in polycrystalline films:

$$\mu_g = \mu_o \exp\left(-\frac{\Phi_b}{k_B T}\right) \tag{2.7}$$

where $\mu_o = \left(\frac{L^2 q^2}{2\pi m^* k_B T}\right)^{1/2}$, Φ_b is the grain boundary potential, L is the grain size, k_B is the Boltzmann constant and T is temperature. The grain boundary scattering will have a significant effect on the carrier mobility if the grain size is of similar order as the mean free path of the charge carrier.

2.1.4 Optical Property of ZnO

ZnO is a well-known transparent conducting oxide (TCO). It has controllable electrical property by doping with different materials. ZnO also has selective transmitting behaviour in terms of optical property. In the visible and near-infrared region, ZnO is transparent while in the thermal infrared region, it is reflective.[108] A typical transmission spectrum of a TCO is shown in Figure 2.4.

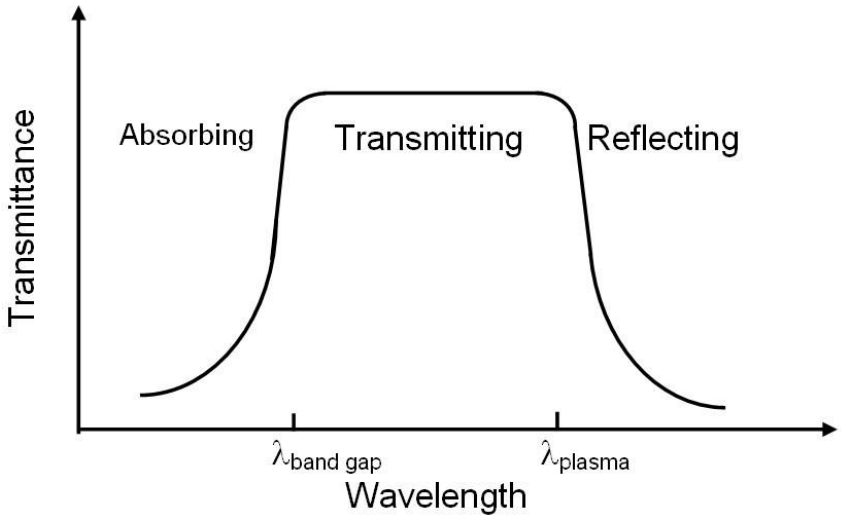

Figure 2.4 Spectral dependence of a transparent conducting oxide (diagram adapted from [108])

At short wavelengths (below the band gap absorption wavelength, $\lambda_{bandgap}$), the absorption is due to the fundamental band gap. One can estimate the value of the band gap (E_g) of the direct band gap material by using the relationship between the absorption coefficient (α) and photon energy ($h\upsilon$) as expressed in equation (2.8):

$$\alpha E = A(E - E_g)^z \tag{2.8}$$

where α is the absorption coefficient, E is the energy of the photon, E_g is the band gap and z = 2 for a direct band gap material while z = 1/2 for an indirect band gap material. By plotting $(\alpha h\upsilon)^2$ against the photon energy ($h\upsilon$), the optical E_g can be obtained by extrapolating the linear portion of the curve to intersect the horizontal axis whereby $(\alpha h\upsilon)^2 = 0$. For direct wide band gap materials like ZnO, the absorbing edge of the energy band was found to be ~3.2 to 3.5 eV. At larger wavelengths (above the free electron plasma absorption wavelength, λ_{plasma}), little light is transmitted due to free electron absorption. This will be discussed further in the next section.

The refractive index of the thin film is also an importance optical factor as it determines the direction of the light path after it passes through from one medium to another medium. The angle of the refracted path is governed by Snell's law as expressed in Eq. (2.9).[109] As the light passes from a denser medium to a less dense medium, the light will be refracted. If the incidence angle is greater to the critical angle, total internal reflection will occur. For light refraction, it can be shown that

$$n_i \sin\theta_i = n_r \sin\theta_r \tag{2.9}$$

where n_i and n_r are the refractive indices of the two different media while θ_i and θ_r are the incident angle and refracted angle respectively at the interface of the two media.

In additional, the extinction coefficient (k) is also related to the absorption coefficient by Eq. (2.10).[110]

$$\alpha = \frac{4\pi k}{\lambda} \tag{2.10}$$

where α is the absorption coefficient and λ is the wavelength. For example, to use a TCO in a light-emitting diode (LED), there is a need to consider the refractive index of the material. The photons generated in a semiconductor may encounter three different kinds of losses namely, photon absorption within the semiconductor, Fresnel loss and critical angle loss. Fresnel loss occurs when photons pass from one medium to another medium while critical angle loss is caused by the overall internal reflection of photons incident to the surface at angles greater than the critical angle defined by Snell's law. The effect of Fresnel loss can be represented by the reflection coefficient (Γ): [111]

$$\Gamma = \left(\frac{n_2 - n_1}{n_2 + n_1} \right)^2 \tag{2.11}$$

where Γ is the reflection coefficient which is the fraction of incident photons that are reflected back into the semiconductor and n_1 and n_2 are the refractive index of the two media respectively. Therefore, there is a need to take these optical properties when applying the TCO as a contact electrode in a device. Jeong *et al.* have reported that using ITO as a channel layer increased the output power of their GaN-based LEDs by ~20 % at 100 mA, compared to LEDs using silicon dioxide layers, due to the higher refractive index of ITO.[112] Kuo *et al.* also reported that higher refractive indices of AZO and ITO films do provide higher output powers to their GaN-based LEDs.[113]

2.1.5 Correlation between Optical and Electrical Properties

The free carrier absorption phenomenon can be described by the classical Drude free electron theory for free electrons in metals, where the permittivity (ε) can be expressed as [114]

$$\varepsilon = (n_{op} - ik)^2 \tag{2.12}$$

where n_{op} is the refractive index and k is the extinction coefficient.

The permittivity can be expressed as the real part and complex part as follows:

$$\varepsilon' = n_{op}^2 - k^2 = \varepsilon_r \left(1 - \frac{\omega_p^2}{\omega^2 + (1/\tau^2)} \right) \tag{2.13}$$

and

$$\varepsilon'' = 2n_{op}k = \frac{\omega_p^2 (1/\tau)\varepsilon_r}{\omega\left(\omega^2 + \left(1/\tau^2\right)\right)} \tag{2.14}$$

where τ is the relaxation time, which is assumed to be independent of frequency and related to the carrier mobility (see equation (2.3)) that in turn influences the electrical property of the material.

The plasma resonance frequency ω_p is given by

$$\omega_p = \left(\frac{4\pi n q^2}{\varepsilon_o \varepsilon_r m_e^*} \right)^{1/2} \tag{2.15}$$

where n is the carrier concentration, ε_o is the permittivity of free space, ε_r is the dielectric constant of the material and m_e^* is the effective mass of the charge carriers. The values of both the refractive index (n_{op}) and extinction coefficient (k) determine whether the material reflect or absorb at the surface.

In the infrared region, the absorption coefficient falls rapidly and $\omega^2\tau^2 > 1$, resulting in the real part of the permittivity to be negative. This will result in the refractive index and extinction coefficient in this region as follows:

$$n_{op} = \frac{\omega_p \varepsilon_r^{1/2}}{2\omega^2 \tau} \tag{2.16}$$

and

$$k = \sqrt{\left(\frac{\omega_p}{\omega} \right)^2 - 1} \tag{2.17}$$

where ω_p is the plasma resonance frequency, ε_r is the dielectric constant of the material and τ is the relaxation time.

For degenerate semiconductors, as the carrier concentration increases, there is a shift of the band gap and absorption edge towards higher energy, which is known as Burstein-Moss effect.[115] In such highly doped semiconductors, most of the lowest states in the conduction band are filled.[116] Hence, an electron transition from the valence band to the conduction band cannot take place into these filled states. Therefore, the filling of states occurs near (but not at) the bottom of the conduction

band, leading to an apparent band gap with an increased energy value.[117] The shift in band gap is related to the carrier concentration as follows:[118]

$$\Delta E_g = \frac{\hbar^2}{2m^*}\left(3\pi^2 n\right)^{2/3} \tag{2.18}$$

where ΔE_g denotes the optical band gap shift, $\hbar$ (= h/2π) is the reduced Planck's constant, m^* is the reduced effective mass ($\frac{1}{m^*} = \frac{1}{m_v^*} + \frac{1}{m_c^*}$), m_v^* is valence band effective mass, m_c^* is the conduction band effective mass and n is the carrier concentration.[119]

2.2 Other Transparent Conducting Oxides

Zinc oxide and doped ZnO have many potential applications. By integrating them with other materials, their area of applications can increase greatly. One other material investigated in this work (as an integrated structure with ZnO) is cuprous oxide (Cu_2O). The optical, structural and electrical properties of Cu_2O were also examined. Currently, the most widely used TCO is ITO; therefore, ITO film is also deposited for property comparison between doped ZnO and ITO.

2.2.1 Cuprous Oxide (Cu_2O)

Cuprous oxide (Cu_2O), also known as copper (I) oxide, has a cuprite structure, of space group Pn-3 with unit cell parameter a = 4.27Å.[120] Copper has two oxygen neighbours while the oxygen has four copper neighbours as shown in Figure 2.5.

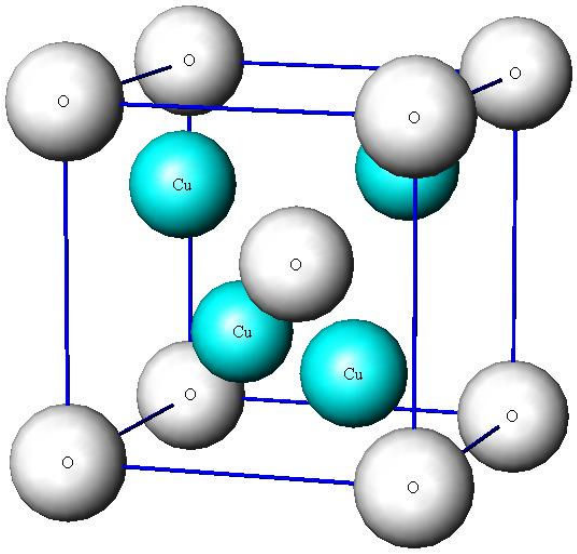

Figure 2.5 Cuprite structure of cuprous oxide. The cyan coloured balls represent copper cations while the white coloured balls represent oxygen anions.

Cu_2O is a direct-gap semiconductor with a band gap of 2.1 eV, a high absorption coefficient in the visible region and is one of the promising materials for photovoltaic applications.[121,122] It is also non-toxic, inexpensive and abundant. Cu_2O is a p-type semiconductor due to copper vacancies and probably interstitial oxygen.[123,124] It can be formed by high temperature thermal oxidation, low temperature thermal oxidation, electrodeposition, anodic oxidation, chemical oxidation, reactive sputtering, or pulsed laser deposition.[125]

In 2000, Ishizuka *et al*. reported p-type Cu_2O deposited on glass, using reactive radio-frequency magnetron sputtering at a substrate temperature of 500 °C, with a hole concentration of ~10^{15} cm^{-3} and a Hall mobility of 60 cm^2/V-s.[126] However, in 2006, Chu *et al*. reported that the p-type cuprous oxide thin films can only be deposited by DC reactive magnetron sputtering within a narrow oxygen partial pressure.[127] They observed that copper oxide initially change from n-type to p-type and then back to n-type with respect to different oxygen partial pressures,

which correspond to variations in Cu, Cu^{+} and Cu^{2+} concentrations. Ogwu *et al*. reported that reactive sputtering power and oxygen partial pressure have an influence on the dominant phase of whether the films deposited are CuO-rich or Cu_2O-rich.[128] They demonstrated that at lower sputtering power, Cu_2O-rich films dominate but the effect of oxygen flow rate has a less significant effect on the optical transmittance compared to the sputtering power. In order to tune the band gap to the desired energy, Ishizuka *et al*. investigated nitrogen doping into cuprous oxide as nitrogen is widely accepted as a non-toxic, inexpensive and abundant material. They observed that with an increase in nitrogen flow during deposition, the resistivity decreases and there is a blue shift in the absorption edge.[129] In 2009, Nakano *et al*. demonstrated p-type Cu_2O film, prepared using nitrogen doping and reactive magnetron sputtering at 400 °C, which caused a blue shift in the optical band gap from 2.1 eV to 2.5 eV.[130]

2.2.2 Indium Tin Oxide (ITO)

Indium tin oxide (ITO) has been widely used as a contact electrode for transparent devices due to its high conductivity and high transparency.[131-133] ITO is indium oxide doped with 10 % tin by weight which is a widely accepted combination.[44] ITO films formed under different processing conditions can exhibit a wide range of electrical properties.[134-141]These processing conditions include the deposition technique, oxygen partial pressure, film thickness, doping and substrate temperature. Generally, a heat treatment at ~300 °C is required to achieve high quality ITO films. An example is the commercially available ITO film on glass which undergo heat treatment of ~300 °C with a measured resistivity (Hall effect) of ~1.7×10^{-4} Ω.cm.[142] However, the heat treatment is not desired for polymeric substrate. In

addition, using heat-treated ITO as the top electrode might degrade the preceding layers of the device. In this work, for a better comparison between ITO films and doped ZnO films, the ITO thin films are fabricated by varying the oxygen partial pressure at room temperature, similar to the doped ZnO process. The fabricated ITO films have a resistivity of the order of ~10^{-4} Ω-cm which is similar to the commercial ones.

2.3 Potential Applications

In this section, some potential applications of TCOs will be introduced, with emphasis on photovoltaic, sensing and thin film transistor applications. Some recent TCOs reported for these applications are also presented.

2.3.1 Photovoltaic Applications

Photovoltaic means converting solar energy into electricity. This process consists of three steps. The absorption of light first causes a transition in the absorbing material from the ground state to an excited state. Then, the excited state generates electron-hole pairs. Next, the generated electrons and holes are then separated by the structure of the solar device, which means that negative-charge carriers will move to cathode and the resulting free positive-charge carriers to move to anode, hence producing electricity.[143]

A conventional photovoltaic device makes use of p-type and n-type silicon (Si) semiconductor junction in the first generation solar cells device. Recently, considerations of cost have made thin film solar cells an important alternative and Si-

based devices have shown remarkable promise.[144,145] However, Si-based solar cells still suffer from a relatively high cost and poor absorption efficiencies and thus it is important to investigate new materials for thin film solar cells.[146] The ideal material will have to be a compromise among low cost, non-toxicity, relative abundance and high efficiency. One such material is semiconductor oxide materials which can be doped with other materials to become p-type or n-type and they are stable. However, there are limited p-type materials such as $CuAlO_2$, $SrCu_2O_2$, Cu_2O and CdS which are used for photovoltaic applications.[147] Cu_2O thin film is a promising material as it is low cost, non-toxic and has high absorption coefficient. ZnO thin films are n-type material with good conductivity.[148,149] Although zinc oxide (ZnO) and cuprous oxide (Cu_2O) are increasingly popular materials due to their favourable properties, homojunctions are hard to form for both ZnO and Cu_2O type materials. A stable p-type ZnO with a sufficient density of holes remains elusive while there is difficulty in forming stable n-type Cu_2O due to its copper vacancies.[150-152] Therefore, combining ZnO and Cu_2O into a p-n heterojunction is currently being investigated.[153-156]

2.3.2 Sensing Applications

ZnO has broad applications in terms of sensing. It is an important piezoelectric material which is used in micro- and nano-electromechanical systems (MEMS and NEMS) due to its large piezoelectric constants.[158] This is due to its low symmetry of the wurtzite crystal structure combined with a large electromechanical coupling.[15] ZnO is also used in biological sensing as Zn is an essential element for enzyme functioning.[159] In addition, ZnO is also used in gas and chemical sensing due to its strong sensitivity of surface conductivity to the presence of the adsorbed

species.[15] It has been demonstrated that ZnO has good gas and chemical sensing properties such as for hydrogen sensing, CO sensing, ozone sensing and even pH sensing.[160-164] In addition, ZnO is also a good ultraviolet (UV) sensor due to its wide band gap of ~3.4 eV and large exciton energy of ~60 meV.[165] Here, the focus of discussion is on UV sensors.

In the past, UV detection is performed using photomultiplier tubes which are fragile, bulky, heavy and costly. Subsequently, silicon-based UV photodiodes were used as they are lightweight, low cost, have good sensitivity and show high speed operation.[166] However, these detectors require band filters to block the visible solar radiation as they have low tolerance of high temperature and has lower efficiency.[16,167] In the past few years, GaN-based UV detectors are developed but they are fabricated using epitaxial growth on lattice-match substrates and hence high cost is incurred.[168] ZnO is a low cost material with strong radiation hardness, high chemical stability and a large band gap of ~3.4 eV at room temperature.[169] In addition, ZnO can be doped with Mg element which can adjust the band gap and the UV sensing at different cut-off wavelengths.[170] Moreover, ZnO also can fabricated as thin films or nanostructures depending on the usage of the devices.[171] ZnO-based sensors can be categorized into mainly nanostructures and thin films. ZnO nanostructures such as nano-rods, crossed nano-rods and nanowires have been fabricated as UV sensors with good sensing property.[163,172,173] Basak *et al.* has reported on a ZnO thin film UV detector fabricated by sol-gel deposition and using gold electrode. They demonstrated a photoresponsivity as high as 0.0040 A/W at a wavelength of 350 nm.[167] Liang *et al.* have demonstrated a ZnO Schottky UV sensor using epitaxial ZnO films on R-sapphire with aluminum and silver electrodes

to form ohmic and Schottky contacts. Their sensor has a photoresponsivity of 1.5A/W, leakage current of ~1 nA at 5V bias and a fast photoresponse component with rise time of 12 ns and a fall time of 50 ns.[174] Recently, ZnO-based UV sensor has been achieved on paper substrates using water-ZnO powder suspension with pencil-drawn graphite lines as electrodes.[175]

2.3.3 Thin Film Transistors

Thin film transistors (TFTs) are used as switching components in many electronics applications, especially in the display industry. At present, amorphous silicon (Si) is used as the channel material in TFTs. However, due to the low carrier mobility (< 1 cm^2/V-s) and high process temperature (350 °C), amorphous Si-TFTs are not suitable for flexible substrates. Organic TFTs have very low carrier mobility (< 1 cm^2/V-s) and may have reliability concerns.[176] Therefore, compared to amorphous Si-TFTs and organic TFTs, oxide-based TFTs may have advantages as metal oxides can be deposited at room temperature and oxide-based TFTs have at least one order higher carrier mobility (>10 cm^2/V-s) than Si-TFTs and organic TFTs.[129] The oxide-based TFTs have a great potential to replace the current amorphous Si-TFTs for more compact electronics. Due to the low process deposition temperature, amorphous oxide films are more suitable than crystalline films for flexible electronics, in addition to the low compressive stress and ability to obtain large area uniform deposition by sputtering.[177,178] Many research groups have reported oxide-based TFTs using ZnO, tin-doped ZnO, indium-doped ZnO, indium-gallium doped ZnO (IGZO), tin oxide and indium oxide as channel layers fabricated on glass substrates.[132,133,135,169,179,180] Some research group have even

demonstrated functional transistors with surprisingly high carrier mobilities of ~10 cm^2 /V-s, even for amorphous films at room temperature.[181,182]

To work towards the transparent electronics trend, full transparent TFTs are necessary. By using TCOs, transparent substrates, oxide channels and dielectrics, full transparent transistors can be achieved.[133,183] Recently, an enhancement-mode transparent TFT using IGZO as the channel layer and Y_2O_3 as the gate dielectric fabricated on a polyethylene terephthalate (PET) substrate was reported.[128] This TFT has a field effect mobility of ~10 cm^2/Vs, threshold voltage of 1.4 V, on-off ratio of $>10^8$, sub-threshold voltage swing of ~0.2 V/decade and which has better performance than amorphous-Si TFTs in terms of electrical properties, optical properties, ease of processing, and even cost. Therefore, oxide-based TFTs can find new applications such as in wind shields, advertising panels on glass panels of buildings, light weight electronic books, flexible roll-type computers for consumers, light-weight rollable military electronics and can eventually revolutionize the whole display industry. In addition, to fulfill such vast applications, the oxide layer and channel layer of the oxide-based TFTs need to be thin to increase flexibility. As thin films are more likely to experience electrical leakage problems, there is a need to study the leakage problem.

Chapter 3 Experimental Techniques

All the thin films are obtained by physical vapour deposition using material targets such as ceramic targets, single crystal targets and metallic targets. Thermal evaporation and electron-beam evaporation are also used to deposit metallic thin films. These thin films are then characterized to optimize their growth parameters.

3.1 Thin Film Deposition Techniques

The growth techniques used in this work are classified as physical vapour deposition techniques namely, pulsed laser deposition (PLD), magnetron sputtering, thermal evaporation and election beam (e-beam) evaporation. More is elaborated in the following sections.

3.1.1 Pulsed Laser Deposition (PLD)

Pulsed laser deposition (PLD) has been used for epitaxial growth of thin films and deposition of multilayers/superlattices of complex materials. In 1987, T. Venketesan used PLD to successfully deposit high-temperature superconducting thin films.[184] In a typical PLD system, a high energy pulsed laser is used to ablate the target and evaporate the target material without changing the target composition. The generated highly energetic particles then interact with the background gas and emit photons, resulting in the characteristic luminous plasma plume. The surrounding gas pressure influences the mean free path of the species in the plume, and determines their energy. By adjusting the background gas pressure, the kinetic energy of the ablated species can be controlled. These ablated species will then arrive at the

unheated/heated substrate and result in film growth. As a result, films with the desired stoichiometry, similar to the target, can be obtained using PLD. The PLD technique has many advantages for depositing oxide films with high melting points and complicated stoichiometries, some of which cannot be achieved by using other growth techniques such as molecular beam epitaxy (MBE) or metalorganic chemical vapour deposition (MOCVD). PLD also has a high deposition rate of up to 1Å/pulse. The actual growth rate of the film can be determined by varying the laser frequency.[185]

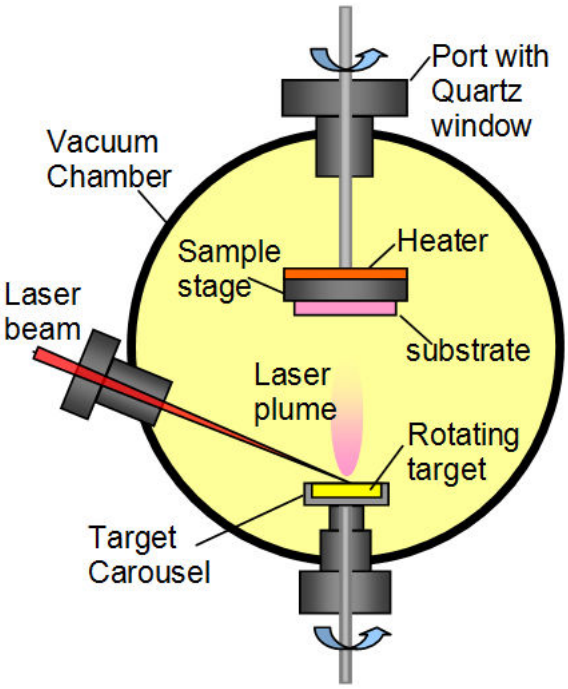

Figure 3.1 Schematic of the pulsed laser deposition system

The schematic of the pulsed laser deposition system used in this work is shown in Figure 3.1. The laser used here is a KrF (wavelength λ = 248 nm) excimer laser (Lambda Physic, Compex 205) which is capable of delivering a maximum pulse energy of up to 700 mJ, measured at low pulse repetition rate with a pulse duration of

25 ns. The pulse repetition rate ranges from 1 to 50 Hz and the average power is 30 W. Using a series of optical lenses, the laser beam is focused to a spot size of ~1 mm^2. This laser beam will then raster along a horizontal distance on the target while the target is in constant rotation at 10 rpm. The substrate is loaded with the sample surface facing down. The substrate holder is equipped with a silicon carbide heater which can heat up from room temperature up to 950 °C and cooled at a constant rate. The heater stage is able to move together with the substrate holder, allowing an adjustable target-to-substrate distance. A maximum of three targets can be mounted together in the system. Multi-layer film deposition can be performed without breaking the vacuum. Prior to deposition, the vacuum chamber is pumped down to a base pressure of the order of 10^{-8} Torr. Oxygen is used as a deposition gas with a flow rate of up to 20 sccm. The operating pressure during deposition is controlled by the combination of oxygen flow rate and the pumping speed using a control valve. This allows the deposition pressure to be adjusted between 0.01 - 100 mTorr with an accuracy of 0.1 mTorr.

A PLD system also has the advantage of deposition in oxygen and other reactive gas ambience, room temperature deposition and ease of thickness control. In terms of large area deposition, current PLD systems are able to support up to 200 mm size wafer.[186] However, like any other deposition techniques, PLD does have some drawbacks such as splashing, uniformity and particulates problem. These could be minimized using target surface improvement (polishing target), rastering of the laser and off-axis deposition.[187] In addition, high start-up cost of the laser system may deter its commercialization process depending on the requirement of the high quality film in the industry. Therefore, to maximise the benefits of the PLD and other

techniques, several other deposition methods such as sputtering and evaporation are also employed in this work.

3.1.2 Magnetron Sputtering

Sputtering is an extensively employed thin film deposition technique which uses highly energetic particles (typically argon ions) to bombard a sputter target. The ion bombardment causes inelastic collisions on the target surface that can dislodge target atoms which are then accelerated to the substrate. As more and more target atoms reach the substrate, they nucleate and form a thin film. Sputtering is performed in vacuum with pressure typically ranging from 1 mTorr to 50 mTorr. At a lower pressure, the mean free path of the ions increases which allows them to accelerate to a higher energy, resulting in dislodged target atoms having more energy to diffuse along the substrate surface to find the lowest energy state.[188] The schematic of the sputtering system used in this work consists of a radio frequency (RF) sputtering cathode and a direct current (DC) sputtering cathode as shown in Figure 3.2. Prior to deposition, the base pressure of the chamber is pumped down to less than 3×10^{-6} Torr. The substrate is loaded with the sample surface facing downwards and the substrate holder is rotated at a constant speed of 4 rpm. The target-to-substrate distance is set to be 14 cm. The sputtering gas used is argon with gas flow rate of up to 50 sccm. Oxygen and nitrogen can be used as the operating gas with a gas flow rate of up to 20 sccm.

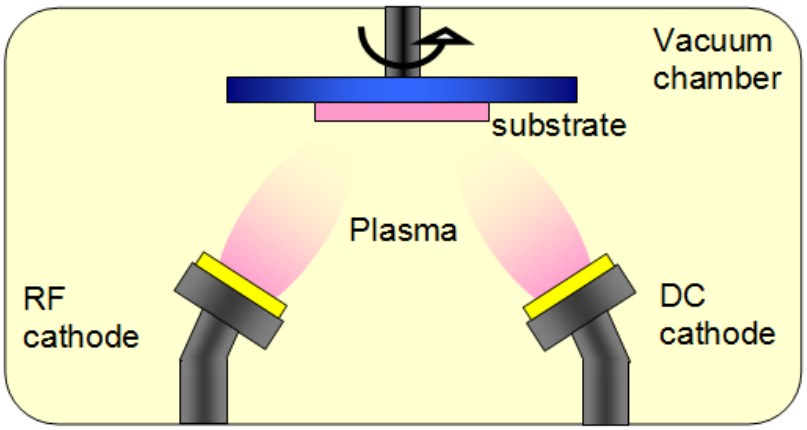

Figure 3.2 Schematic of the sputter system

3.1.3 Thermal Evaporation

Deposition using thermal evaporation is achieved by heating up the desired material to be deposited to a high enough temperature in a vacuum chamber until the material vaporizes. The material vapours finally condense onto the cold surface of the substrate and also onto the vacuum chamber walls. This process is usually performed at a low pressure of $<10^{-5}$ Torr to avoid reaction between the vapours and the atmosphere. The dimension of the vacuum chamber is usually designed according to the same order of the mean free path of the vapour atoms, so that these particles will travel in straight lines from the evaporation source towards the substrate. After many cycles of evaporation and condensation, a thin layer of the desired material is formed on the substrate.[189]

The thermal evaporator used in this work is the Edwards Auto 306 Thermal Evaporator which consists of two thermal evaporation sources. This technique is used to deposit Ti/Au, Cr/Au or aluminum onto the deposited film sample through a shadow mask to form the metallic electrode of the devices being tested.

3.1.4 Electron-Beam Evaporation

In this work, the Denton Explorer Thin Film electron-beam deposition system, as shown in Figure 3.3 and consisting of 6 crucible sources, is used for various metal depositions. The material sources currently used are chromium, silver, gold, nickel, titanium and germanium.

Figure 3.3 Electron beam thin film deposition system

For evaporation to occur, the substrate and source material (pellet form) are first brought to a very low pressure in the range of at least 5 x 10^{-5} Torr. At this low pressure, an electron beam is focused onto the crucible containing the source material until the material begins to evaporate. As the material in the crucible evaporates, its vapours will begin to coat the substrate. The substrate is cooled by a chiller and the temperature of the substrate is maintained at about 30 °C throughout the process. The base pressure of this chamber can be pumped down to 2 x 10^{-7} Torr. There are also two shutters in the system: one shutter is at the source material side and functions to

block the electron beam from hitting the deposition material until the system is ready for the deposition; the other shutter is at the substrate side to block the unwanted vaporized materials until a steady evaporation rate is achieved. This system is equipped with a quartz crystal monitor to accurately display the thickness and rate of the deposition. The thickness of material deposited has been calibrated using atomic force microscopy and the error is less than 10 %.

3.2 Thin Film Characterization

Various measurement techniques were utilized for the characterization of the thin films and devices fabricated. In this section, the techniques used for electrical, optical, structural, compositional and surface characterization are elaborated.

3.2.1 Electrical Characterization

For electrical characterization, the Hall effect, current-voltage (IV) and capacitance–voltage (CV) measurements of the films, as well as devices, were carried out. In the following sections, these techniques are briefly elaborated.

3.2.1.1 **Hall Effect**

Resistivity (ρ), Hall mobility (μ) and carrier concentration (n) of the thin films were characterized with room temperature Hall effect measurements using a standard van der Pauw method, which is a four-point probe technique.[190] Figure 3.4 shows the setup of the resistivity measurement. The current source (I_{12}) is applied to contacts 1 and 2 and the voltage (V_{43}) across contacts 3 and 4 is measured. Then, the current source (I_{14}) is applied to contacts 1 and 4 and the voltage (V_{23}) across contacts 2 and 3 is measured. The resistivity (ρ) is obtained using equation (3.1) as follows:

$$\rho = \frac{\pi.d}{2.\ln(2)}.\left[\frac{V_{43}}{I_{12}} + \frac{V_{23}}{I_{14}}\right].F.Q \qquad (\Omega.\text{cm}) \tag{3.1}$$

where d is the thickness of the active layer, F is the correction factor and Q is the symmetry factor. If the thickness of the active layer is unknown, the sheet resistivity (R_s) can defined as $R_s = \rho/d$ (see equation (2.2)) with units of $\Omega.\square^{-1}$.

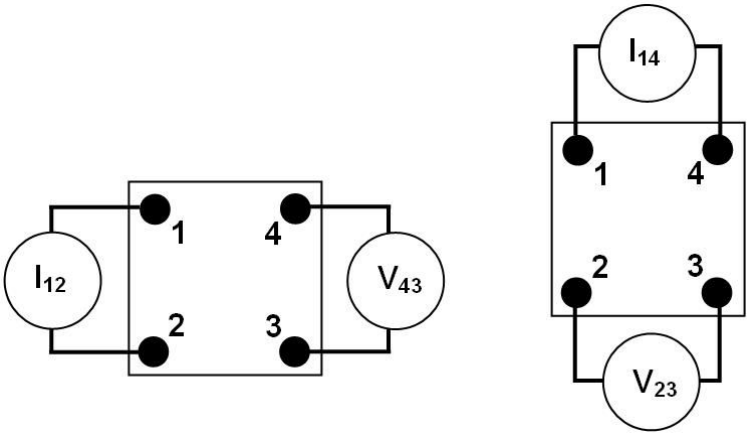

Figure 3.4 Resistivity measurement in Hall effect setup

To measure the carrier concentration and mobility, the Hall effect setup used is shown in Figure 3.5. A constant current I is applied across the two non-adjacent contacts with a magnetic field applied perpendicular to the sample surface. The difference between the potential is measured at the remaining two contacts.

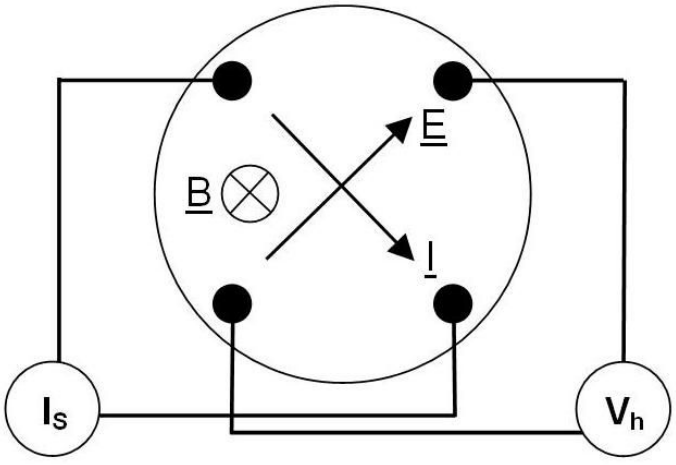

Figure 3.5 Carrier concentration and mobility measurements in Hall effect setup

By balancing the magnetic and electrostatic forces acting on a mobile charge as follows [191]

$$F = q\left[E + \upsilon \times B\right] = 0 \tag{3.2}$$

Equation (3.2) can be rewritten as

$$q.E = q.\upsilon.B \tag{3.3}$$

where E is the electric field along the plane, B is the magnetic field perpendicular to the sample, ν is the carrier velocity and q is the electron charge The induced electrical field along the plane is called the Hall field. The Hall field produces a voltage across the sample which is called the Hall voltage (V_H).

After obtaining ν from equation (3.3), the current I can be expressed as

$$I = q.N.d.W.\nu \tag{3.4}$$

where N is the carrier density, d is the thickness of the film, W is the separation between the two contacts. Equation (3.4) assumes a constant carrier distribution and velocity through the film layer which is assumed to be isotropic. In a real sample, the contacts arrangement is chosen such that the current I is perpendicular to the electric field E and magnetic field B. Having measured the current I and ν, the sheet Hall coefficient (R_H) can be expressed as

$$\frac{1}{q.N.d} = \frac{V_H}{I.B} = R_H \ (\mathrm{m^3/C}) \tag{3.5}$$

where V_H is the Hall voltage and d is the thickness of the film.

When the thickness of the film is unknown, the sheet Hall coefficient can be defined as:

$$R_{Hs} = \frac{R_H}{d} = \frac{V_H}{I.B} \ (\mathrm{m^2/C}) \tag{3.6}$$

The bulk carrier density N_b is then obtained using equation (3.7) as follows:

$$N_b = \frac{1}{q.d.R_{Hs}} \tag{3.7}$$

The hall mobility is calculated using the sheet Hall coefficient divided by the sheet resistivity. The Hall effect can be used to determine whether the sample is p-type or n-type according to the polarity of the Hall voltage. The contact points on the thin films were patterned either by evaporation through a shadow mask, direct soldering of contacts or directly pressed onto the film surface. These contact points were attached to the outermost corner of the square samples to obtain the best results.[192-195] The Hall measurement is performed using a Bio-rad HL5500PC Hall Effect Measurement System ,which is capable of measuring sheet resistivity up to a few $M\Omega.\square^{-1}$. The magnetic field used was 0.32 T and the current bias was 0.1 mA.The resistivity of the film can be calculated by multiplying the known thickness of the film measured by atomic force microscopy.

3.2.1.2 **Current-Voltage Analysis**

Current–voltage (IV) characterizations are performed using the Keithley 236 source measure unit and HP 4140B pA meter/DC voltage source. The solar simulator Air Mass (AM) 1.5 is used in the work and it is installed in a dark enclosure. The lamp is first warmed up for 20 minutes (min) before measurements are performed. During measurements, the samples is placed in an enclosure for the dark measurement while in the light measurement, the samples are illuminated for about 1 min for it to reach saturation.

The electrical characterization performed for the transistor measurement work was performed using the HP 4285A precision LCR meter and HP 4156C parameter analyzer. The contact electrode for the source/drain is Ti (5 nm)/Au (100 nm), which is obtained by evaporation.

3.2.2 Optical Characterization

Optical transparency is a crucial parameter for a transparent conducting oxide. Therefore, it is essential to study the optical properties using various optical equipment.

3.2.2.1 **UV-VIS-NIR Spectrophotometery**

Spectrophotometery involves the quantitative measurement of transmission properties and light absorption by a sample as a function of wavelength. UV-VIS-NIR spectrophotometers are able to measure the absorption of light in the near ultraviolet (UV) region (200 – 400 nm), the visible range (400 – 700 nm) as well as the near infrared (IR) region (700 to 3300 nm).

Optical transmission of the thin films was recorded using the double beam, double monochromators design Perkin-Elmer Lambda 750 UV-VIS-NIR spectrophotometer in the wavelength range of 190 to 3300 nm.[196] The system uses deuterium and tungsten halogen light sources. The scanning operation is chosen to use the auto-sampling mode which will optimize the slit width at different wavelength ranges. In the experiments, a wavelength interval of 1 nm was used. A baseline was first recorded in order to synchronise the two beams. During the measurements, the spectrum was adjusted for baseline absorption in a single measurement, where the film sample was placed in the path of the measuring beam, and a blank reference

substrate in the path of the reference beam. The resulting signal directly records the difference between the sample and the baseline, thus obtaining the spectrum of the film itself.

Optical reflectance was measured using the Craic QDI 2010 UV-Visible-NIR range micro-spectrophotometer in the wavelength range of 200 nm to 1700 nm.[197] The measured area can be selected using different apertures for square area sizes with sides of 1.8 to 31 μm. In the experiments, a reference scan is performed on a reference sample, then the actual sample is scanned. The resulting signal shown is the difference between the sample and the reference sample. For the reflectance measurement, absolute reflectance can be obtained using the built-in gold reference.

3.2.2.2 **Variable Angle Spectroscopic Ellipsometery (VASE)**

VASE is an optical characterization technique which can be used to determine the thickness of thin film and optical constants.[198] It is a non-destructive technique that uses a model-fit method to analyze the measured data and determine the optical properties of the films. The spectral range of the VASE used is 190 to 1700 nm, with absorption band around 1340 – 1450 nm which cannot be used in this spectral region.

The VASE uses a monochromatic light source and measures the change in polarization state of light reflected from (or transmitted through) the surface of a sample. The measured values are expressed as psi (Ψ) and delta (Δ), whereby the values are related to the ratio of Fresnel reflection coefficients (ρ_{op}), $\widetilde{R}_p$ and $\widetilde{R}_s$, for the p-polarized and s-polarized light respectively as shown in equation (3.8) as follows:

$$\rho_{op} = \frac{R_p}{R_s} = \tan(\psi)e^{i\Delta} \tag{3.8}$$

As ellipsometry does not measure the absolute intensity of the light reflected, but rather the ratio of these two values, therefore, it is more accurate than intensity reflectance. For ellipsometry to work best, the thickness of the film should not be too much smaller or larger than the wavelength of the light used in the measurement. Surface roughness of the sample should be less than ~10 % of the probe beam wavelength for ellipsometry to be valid. Variable angle of incidence allows measurements at multiple angles, which can be used to optimize measurement sensitivity to unknown parameters

In this work, the optical constants of AZO and ITO films were measured using VASE. Ellipsometry measurements were carried out at room temperature at three different angles of 65°, 70° and 75° in the wavelength range of 270 to 1700 nm using a computer-controlled Woollam variable angle spectroscopic ellipsometer as shown in Figure 3.6. The experimented data acquired at different angles were fitted using models simultaneously to minimize instrumental errors.

Figure 3.6 Variable angle spectroscopic ellipsometer

3.2.3 Structural and Composition Characterization

Structural characterization of the thin films was performed using a general area detector X-ray-diffraction (XRD) system (GADDS) equipped with Cu $K\alpha$ radiation. The monochromatic X-ray beam generated from the Cu X-ray tube was focused with a flat graphite monochromator to obtain the single Kα beam wavelength of 1.5418Å. A double pin-hole collimator was used to control the beam size and divergence. The D8 goniometer was installed in a horizontal θ-2θ geometry with driving step size of 0.001^{o}. The XRD system uses a HI-STAR area detector which consists of a two-dimensional multi-wire proportional counter.[199]

Microstructure observation was carried out using the JEOL 2100 (LaB_6) transmission electron microscope (TEM) with scanning TEM (STEM) and energy dispersive X-ray (EDX) analysis. The maximum acceleration voltage is 200 kV with

point-to-point resolution of 0.10 nm. Diffraction patterns can be imaged to determine the crystalline nature of the samples.

3.2.4 Electronic Property Characterization

X-ray photoelectron spectroscopy (XPS) was performed using a VG ESCA LAB-220i XL XPS with a monochromatic Al Kα (1486.6 eV) X-ray source. Survey spectra were recorded with a pass energy of 100 eV and a step width of 1 eV. The valence band maximum high-resolution spectra were recorded with a pass energy of 20 eV and step width of 0.1 eV. The XPS instrument is also able to produce elemental mapping with a spatial resolution of 20 to 50 μm, depending on the element to be mapped. The measured results were fitted using Shirley-type background subtraction peak-fitting provided by the Thermo Avantage software.

3.2.5 Surface Morphology Characterization

The morphology and thickness of the thin films were measured using a multi mode scanning probe microscope (Veeco Digital Instruments), capable of performing a full range of atomic force microscopy (AFM) and scanning tunneling microscopy. In this work, the tapping mode AFM is employed using silicon cantilevers at room temperature. All AFM images were taken on a scanned size of 1 μm × 1 μm and the root-mean-square (rms) roughness was calculated using the AFM software.

Scanning Electron Microscopy (SEM) surface analysis was carried out with a JEOL JSM-6700F field emission SEM with 1 nm resolution at an acceleration voltage of 15 kV and 2.2 nm resolution at an acceleration voltage of 1 kV. The magnification of the SEM used can be up to 650,000 times. The images shown in this work are

obtained using the secondary electron image (SEI) mode. The sample is contacted using carbon tape and copper tape. The system is capable of imaging the topography by secondary electrons and backscattered electrons. It is also equipped with an Oxford/LINK EDS (Energy Dispersive X-ray Spectrometer) for elemental composition on a sample surface.

Chapter 4 Gallium-Doped Zinc Oxide (GZO)

One of the reasons that transparent conducting oxides (TCOs) has been heavily researched on is the potential to realise fully transparent electronics using low cost materials. In order to obtain fully transparent electronics, a high quality transparent electrode is essential. In this work, Group III-doped zinc oxide (ZnO) thin films were investigated as an alternative to replace the widely used indium tin oxide (ITO) material. Ga-doped ZnO (GZO) was explored in this chapter as GZO fulfils the high transparency, low resistivity and low cost criteria. Single layers and metal/semiconductor multilayers of GZO thin films were also examined.

4.1 Introduction

Zinc oxide (ZnO) is a promising substitute for ITO since it is non-toxic, abundant, inexpensive and has a wide direct band gap (E_g) of ~3.4 eV with high transparency in the visible region. However, as compared to ITO, undoped ZnO has a higher resistivity. Controllable n-type doping enhancement can be achieved by substituting the Zn^{2+} ions with group III elements (electron doping).[200-202] Among the group III elements investigated, gallium (Ga) is attractive because Ga-O has similar ionic (0.76 Å vs. 0.88 Å) and covalent (1.26 Å vs. 1.31 Å) radii as compared to Zn-O.[67,90,94] This means that gallium-doped ZnO (GZO) can possibly be achieved without substantial ZnO lattice deformation.[200] Indeed, low resistivities of GZO are possible and improvements in the electrical properties of devices employing GZO as a TCO have also been demonstrated.[203-210] However, better transparency and reduced resistivities are shown only for higher temperature processed GZO thin

films.[202,203,211,212] As discussed, a low temperature process is typically required for organic electronics application and in this aspect, this has made the aforementioned higher temperature processed GZO less appealing. More investigations are also required, especially with regards to the transmission property of GZO. At room temperature, the oxygen pressure variation during film deposition can critically affect the electrical properties and influence the transmission property of the thin films.[14] Complications are also possible from structural changes occurring in the films with variations in the oxygen content and thus a detailed correlation with transparency is required.[213,214] It is important to understand the nature of these influences, especially to correlate growth conditions with the optical properties. More details about the influence of oxygen pressure on properties of the thin films are discussed in section 4.2. Since the solid solubility limit allows for the substitution of ~2.7 % of the total Zn atoms by Ga, the key to better electrical properties may lie in a good understanding of the role of oxygen in this material system, especially for room temperature deposition.[215] Therefore, in this work, the effects of room temperature deposition under different oxygen growth pressures were examined carefully and the variations with elevated substrate temperatures were also investigated to discuss the contributing factors in affecting the transmission property of GZO thin films.

Other than single-layer TCO (GZO) films, multilayer TCO film structures have held much interest for investigating both high conductivity and good optical properties in recent years. As mentioned in Section 1.1, single layer metals are not very stable in air and there is adhesion problem onto low cost glass substrates.[8] Hence, single ultra thin layer of thin metal as transparent oxide is not feasible. In addition, single layer TCO (GZO) does not give much control on the transparency in

the UV-VIS-NIR range. Therefore, multilayer TCO film structures are investigated for both high conductivity and good control of optical properties. Homogenous multilayers, such as Aluminum-doped zinc oxide multilayers, have been reported with electrical resistivity of ~7.08 × 10^{-3} Ω-cm and a high transmittance of over 80 % in the visible region.[216] In addition, oxide/metal/oxide multilayers have been investigated for improvement of conductivity, whereby the oxide used can be undoped and doped ZnO. Alford *et al.* have reported an undoped ZnO/Cu/ZnO multilayer structure with optimum resistivity of ~6.9 × 10^{-5} Ω-cm and with average transparency of ~70 % over the 400 to 800 nm wavelength range.[217] Lee *et al*. have reported an indium-doped zinc oxide (IZO)/Al/GZO/ZnO/glass multilayer structure with resistivity of ~2.2 × 10^{-3} Ω-cm and higher than 75 % transmission over the 400 to 800 nm wavelength range.[218] Park *et al.* reported a GZO/silver (Ag)/GZO multilayer and compared the effect with and without 500 °C annealing; the unannealed sample yields a resistivity of ~5.53 × 10^{-5} Ω-cm with transmittance of 87 % at 550 nm.[42] Cheng *et al.* demonstrated a GZO/Pt/GZO multilayer structure which showed that platinum (Pt) does improve the conductivity of the multilayer film. However, there is a drastic drop in transparency and also an increase in surface roughness as thickness of the Pt layer increases.[219] Valkoenen *et. al.* has studied the optical reflection and transmission of thin metal layers (Ag, Au, Cu and Al) at various thicknesses.[220] From their studies, among the various metals, thin Ag film has an advantage in optical property as other metals exhibit unwanted short wavelength absorption at a wavelength of < 500 nm for copper and gold. Although Aluminum does not exhibit unwanted short wavelength absorption in the visible range, it has absorption at ~800 nm. Copper gives a high solar transmittance but its optical property degrades over time when its surface oxidizes. Therefore, Ag has an

advantage among these metals and it is also more cost effective as compared to gold and platinum. Other than metals, semiconductor such as Germanium is also investigated. Saif Islam *et. al.* has reported that ultrasmooth silver thin film can be obtained by prior deposition of a Germanium seeding layer.[221] Hence, in this work, metal/TCO, TCO/metal/TCO, metal/Ge/TCO and TCO/metal/Ge/TCO multilayer structures are fabricated on glass. As most studies focused on the optical property only in the ultraviolet (UV) to visible (VIS) wavelength range, the optical transmission and reflectance in the near infrared (NIR) wavelength range are also investigated in this work.

4.2 Gallium-Doped Zinc Oxide (GZO) Thin Films

GZO thin films grown on borosilicate glass by PLD at various oxygen pressures and various substrate temperatures were investigated here. In the following sections, the growth parameters and results were discussed.

4.2.1 Fabrication of GZO Thin Film

GZO thin films were deposited on borosilicate glass by PLD using a ceramic ZnO/Ga_2O_3 (0.98:0.02) target (99.99% purity). The KrF excimer laser (248 nm wavelength and 25 ns pulse width) was operated at a repetition rate of 20 Hz and with a total energy of 300 mJ. Borosilicate glass substrates were ultrasonically cleaned in both acetone and ethanol before being rinsed in deionized water. The substrates were then blown dry using compressed air before loading into the deposition chamber that was subsequently evacuated to a base pressure of the orders of $\sim 10^{-8}$ Torr. The deposition duration was 30 minutes and the target-to-substrate distance was kept at 6 cm. In the first series of experiments, the deposition was performed at room

temperature with varying oxygen pressure from 2×10^{-5} to 5×10^{-2} Torr. In the following experiments, the optimum oxygen pressure condition of the thin film samples was selected to investigate the effect of deposition temperature. During these tests, the heated samples are cooled down to room temperature in a similar oxygen ambience where they are deposited. This is to prevent annealing in a higher vacuum as it may have a desorption effect.

4.2.2 Electrical Characterization

The effects of varying the oxygen pressure on the electrical properties of the GZO films, achieved through PLD, are shown in Figure 4.1(a). There are three significant regimes that show different reactions to oxygen pressures. In the low oxygen pressure regime (10^{-6} to 10^{-4} Torr), a reduction in the electrical resistivity was observed despite almost similar carrier concentrations from 7.1×10^{20} to 8.2×10^{20} cm^{-3}. The smaller resistivity with increasing pressure above 10^{-6} Torr can be attributed to the increase in carrier mobility as shown in Figure 4.1(a). In this oxygen deficient environment, oxygen vacancies represent the most stable defect formation.[222] Although Zn antisites or Zn interstitials can also be present as donor type defects, their formation energies are higher than those of oxygen vacancies.[223] Therefore, for room temperature deposition, the oxygen vacancies in the grown films are typically deep-level donor defects.[224] This means that their absence or presence should not play a significant role in influencing the free-carrier concentration. However, a charged oxygen defect state can be present, with the 2+ state being more stable than the 1+ state; a consequence of the larger relaxation energy for the former charge state.[225,226] Since there is no significant change in the carrier

concentrations, but an improvement in the carrier mobility, this is consistent with the picture that increasing oxygen pressure removes deep-level oxygen vacancy charged defects (2+ state). The improved carrier mobility can thus be attributed to reduced ionized defect scattering centers in the bulk film although grain boundaries passivation by oxygen can also be a possible reason. A simple conversion of the carrier concentrations into atomic percentage shows that the thin films fabricated in this work consist of 2 ± 0.2% of Ga substituting for Zn in the GZO. This is in excellent agreement with the expected doping of Ga from the 2% doped target giving additional proof that Ga atoms occupy the substitution sites and that oxygen does not play a major role in affecting the free-carrier concentration in this regime.

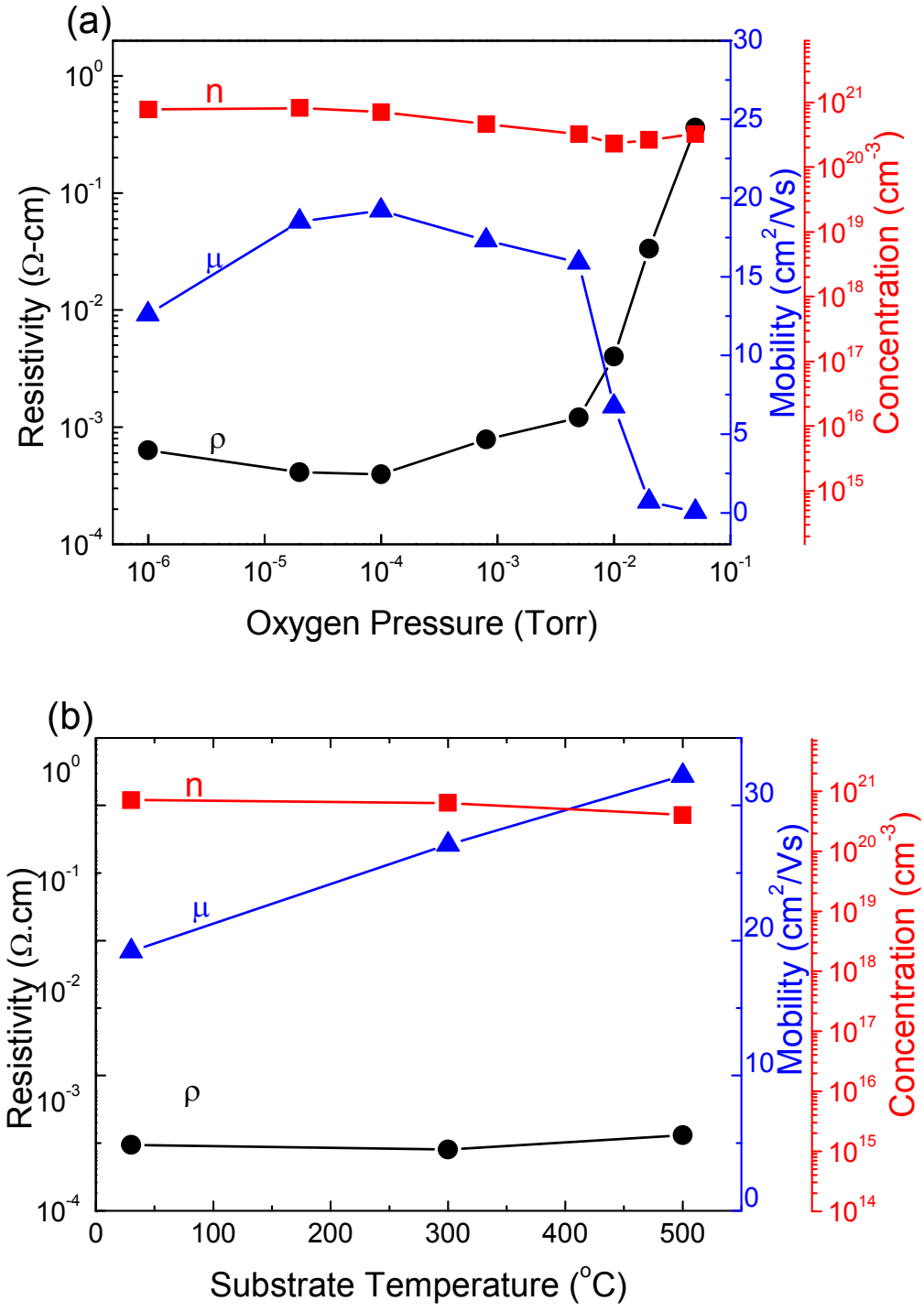

Figure 4.1 Electrical resistivity (ρ), carrier concentration (n), and Hall mobility (μ) of the GZO films plotted as a function of (a) oxygen pressure, during deposition at room temperature, and (b) substrate temperature

In the mid-oxygen pressure regime of 1×10^{-4} to 5×10^{-3} Torr, there is a slight decrease in both the carrier concentration and mobility with increasing oxygen pressure. In this regime, the aforementioned observation can be attributed to the formation of oxygen interstitials as they have low formation energies, especially in a higher oxidizing ambient.[227] Typically, oxygen interstitials can occupy the octahedral, tetrahedral, or the split interstitial sites.[222] When the octahedral sites are occupied, they tend to introduce states in the lower part of the band gap and these states can accept two electrons, therefore acting as compensation centers.[222] This can explain the decrease in the free carrier (electron) concentration with increasing oxygen pressure. As for oxygen interstitials occupying split sites (the tetrahedral site is unstable), the sharing of the lattice site with one of the nearest neighbours can produce a charge state of 1+.[228] The increase in ionized scattering through these defect centers then lowers the mobility of the conduction electrons.

In the high oxygen partial pressure regime above 5×10^{-3} Torr, there is a drastic decrease in carrier mobility even though the overall carrier concentration remains roughly constant. This causes a large increase in the resistivity as observed in the plot in Figure 4.1(a). The decrease in carrier mobility at high oxygen pressure is quite commonly observed.[207,214] Although oxygen interstitials can similarly account for the reduced carrier mobility, such a drastic decrease observed in this work points to the presence of other influencing variations, such as ionized impurity scattering and grain boundary scattering.

Figure 4.1(b) shows the electrical properties of the GZO films as a function of substrate temperature. As the substrate temperature increases from 30 to 500 ^{o}C, the

carrier concentration decreases but the carrier mobility increases as grain boundary scattering decreases, since the grain size is larger as seen later in the AFM plot of Figure 4.6(b). The overall effect is that the resistivity of the GZO remains approximately constant, at the same order of 10^{-4} Ω-cm, despite changes in the substrate temperature.

4.2.3 Structural Characterization

The XRD spectra in Figure 4.2(a) show the diffraction peaks of the GZO films obtained under different oxygen pressures at room temperature. Although only a single peak is obtained, the large area diffraction maps in Figures 4.2(b) to 4.2(d) show that the GZO films are not of single crystal. The films deposited at a low oxygen pressure regime show the hexagonal wurtzite structure as evidenced from the peak at 34.0°. This is close to but slightly smaller than the ZnO (002) diffraction peak at 34.42°.[229] This phenomenon can be attributed to the strong in-plane alignment and the close packing of the crystal grains in the material that gives a highly textured and strongly oriented thin film as can be observed in the large area diffraction map for the low pressure regime (1×10^{-6} Torr) shown. In the low and mid-oxygen pressure regimes, the diffraction peak remains at similar positions. However, at an oxygen pressure of $\geq 5 \times 10^{-3}$ Torr, a shift is observed in the diffraction peak to 34.51° at 5×10^{-2} Torr. The larger 2-θ angle can be associated with a decrease in the out-of-plane (c-axis) lattice constant of the same crystal structure. The diffraction peak is closer to the expected peak position of ZnO, thereby suggesting randomness in the in-plane alignment and thus a loss of the close packing phenomenon observed for lower oxygen pressures. This is also shown in the large area diffraction map by the loss of the preferred orientation diffraction when compared with the lower oxygen pressure

regime. Since no other diffraction peaks are observed with the accompanying peak shift, the film has remained highly oriented in the c-axis with a loss of alignment only in the in-plane configuration. This means that the presence of highly disordered rotation of the crystal grains of the ZnO forms additional grain boundaries with poorer passivation and interfaces. These are sources for significant grain boundary scattering that can explain the drastic decrease in the carrier mobility. The reason for the loss in alignment at higher oxygen pressure during the growth of ZnO can be attributed to a reduction in the diffusion path length for the adatoms. The adatoms, having a smaller diffusion path length at higher oxygen pressures, will have less time to adopt a preferred in-plane orientation. Understandably, this reduction in surface adatom mobility can also lead to rougher surfaces. This agrees with the increase in the root-mean-square (rms) roughness at higher oxygen pressures as measured with the AFM and shown later in Figure 4.5. In addition, although multiple rotated grains are formed at these higher oxygen pressures, surface free energy still governs the c-axis growth and there is no observation of significant variations in the size of the crystal grains normal to the reflecting planes using the Scherrer's formula: [230]

$$t_{cg} = \frac{0.9\lambda_x}{B_w \cos\theta} \tag{4.1}$$

where t_{cg} is the average dimension of the crystallites normal to the reflecting planes, λ_x is wavelength of the X-ray, B_w is the width at the full-width at half-maximum (FWHM) of the observed peak. It should be noted that the calculated grain sizes (out-of plane) range from 16.8 nm to 20.9 nm at the varying oxygen pressure while the AFM micrographs estimates similar lateral grain sizes of ~25 nm. The above structural evolution can then explain the significant loss in carrier mobility through grain boundary scattering even with similar carrier concentrations measured. Columnar polycrystalline grain growth is observed in this work as shown from the

TEM micrograph in Figure 4.3(a) of GZO films deposited at room temperature (oxygen pressure of 1×10^{-4} Torr). However, since the selected area diffraction (SAD) (Figure 4.3(b)) and XRD do not show the presence of other diffraction planes, the columnar grains are highly oriented.

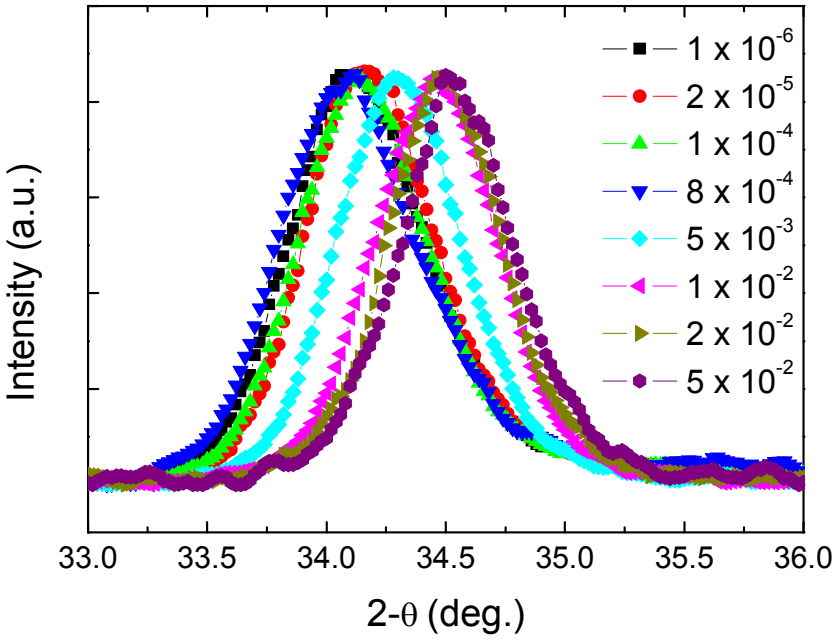

(a) XRD spectra

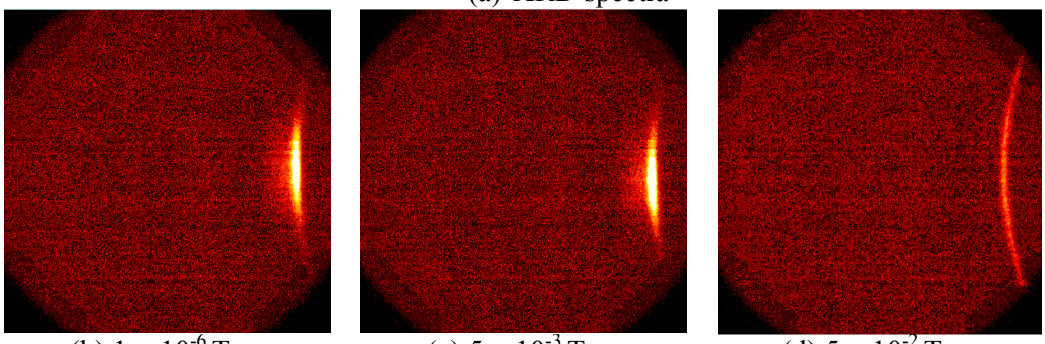

(b) 1×10^{-6} Torr (c) 5×10^{-3} Torr (d) 5×10^{-2} Torr

Figure 4.2 (a) X-ray diffraction spectra of GZO thin films on borosilicate glass deposited at room temperature with various oxygen pressures (unit is in Torr). The images below are the large area diffraction maps for the indicated oxygen pressure at (b) 1×10^{-6} Torr, (c) 5×10^{-3} Torr and (d) 5×10^{-2} Torr

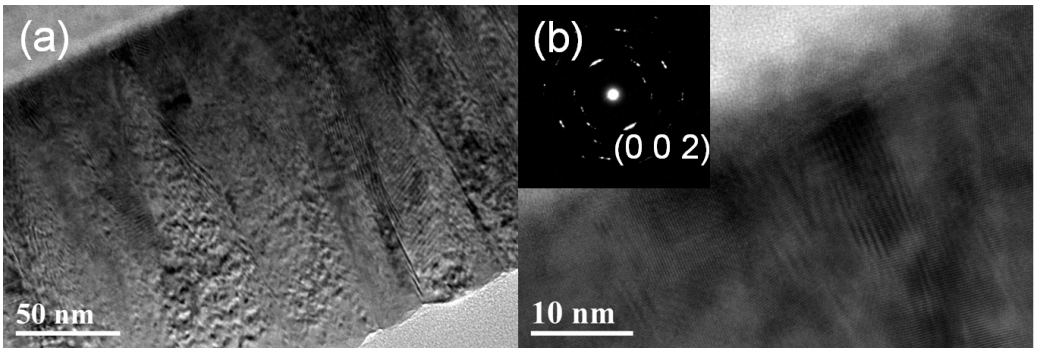

Figure 4.3 (a) Cross-section TEM images of GZO films deposited at room temperature (oxygen pressure of 1×10^{-4} Torr). (b) TEM image at a higher magnification showing the columnar grains. The inset in (b) is the selected area electron diffraction pattern of the sample

Figure 4.4 shows the XRD spectra of GZO deposited at various substrate temperatures of 30 °C, 300 °C and 500 °C. The inset is the large area diffraction map for the GZO sample deposited at 500 °C. In the case of varying substrate temperature, as the growth temperature increased from room temperature to 500 ^{o}C, the FWHM values decreased from 0.53^{o} to 0.38^{o}. This shows that higher growth temperature can improve the crystallinity of GZO as the small crystallites come together to form larger crystallites, thus forming less grain boundaries, as seen later in the AFM result in Figure 4.6(b), and an increase in the carrier mobility as seen in Figure 4.1(b). These results are similar to that reported by Park *et al*. whereby GZO is deposited on quartz and Hirata *et al*. whereby GZO is deposited on glass.[231,232]

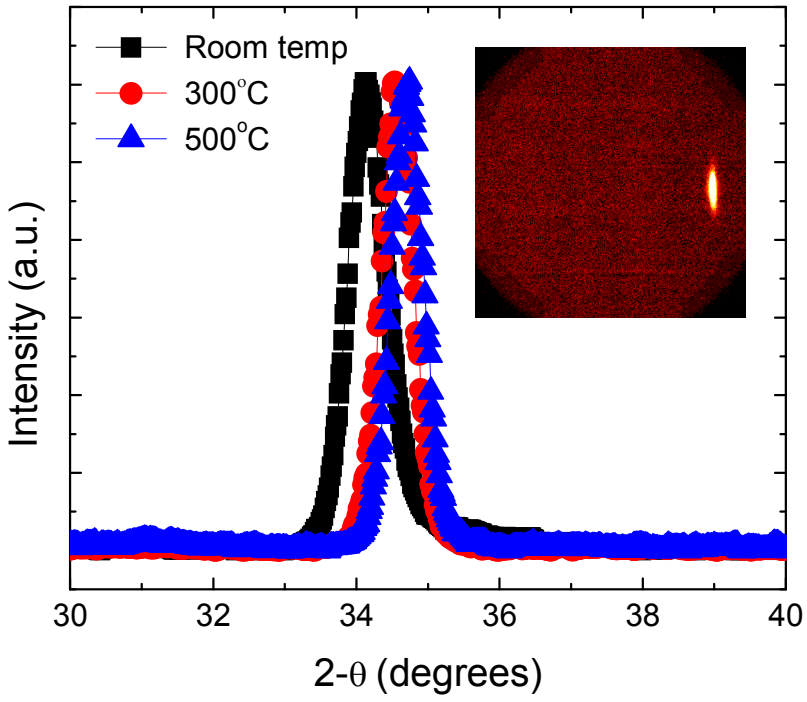

Figure 4.4 X-ray diffraction spectra of GZO thin films on borosilicate glass deposited at 1×10^{-4} Torr and at various substrate temperatures of 30 °C, 300 °C and 500 °C. The inset is the large area diffraction map for the GZO sample deposited at 500 °C

4.2.4 Surface Morphology

The thickness, surface morphology and root mean square (rms) roughness of the various GZO films obtained in this experiment were investigated by AFM, SEM and cross-sectional TEM. The root-mean-square (rms) roughness of the GZO films obtained at various oxygen pressures is shown in Figure 4.5. For GZO deposited at low oxygen pressure, the surface is observed to be relatively flat, with rms roughness of less than 1 nm while at higher oxygen partial pressures above 10 mTorr, the rms roughness is greater than 1 nm. Figure 4.6 shows the AFM image of a GZO film

deposited at 1 x 10^{-4} Torr at (a) room temperature (30 ^{o}C) and (b) 500 ^{o}C. The rms roughness and grain size of GZO deposited at 30 ^{o}C are found to be 0.53 nm and ~20 nm in diameter respectively. The AFM measured grain size is close to the calculated grain size of ~18 nm obtained from the XRD data. The differences in the surface roughness for GZO films grown at different oxygen pressures can be attributed to the change in kinetic energy of atoms in the plasma plume at different oxygen pressures. At low oxygen pressure, the collisions between atoms in the plasma plume may be weak; hence surface adatoms have high kinetic energy, giving a flatter surface. At higher oxygen pressure, the surface mobility of the adatoms is greatly reduced due to excess oxygen, resulting in a film with higher roughness.[233,234] As the substrate temperature increases, an increasing trend in rms roughness is observed. Park *et al*. also reported a similar trend in rms roughness with increasing substrate temperature.[207] Based on the AFM results, the surface roughness of the GZO films depends more on the variation in oxygen pressure than on the substrate temperature whereas the grain size of GZO depends more on the variation in substrate temperature. Figure 4.7 shows the SEM image of a GZO film that was deposited at room temperature and an oxygen pressure of 1×10^{-4} Torr. This shows that the GZO thin film deposited at room temperature has a smooth surface and free of voids.

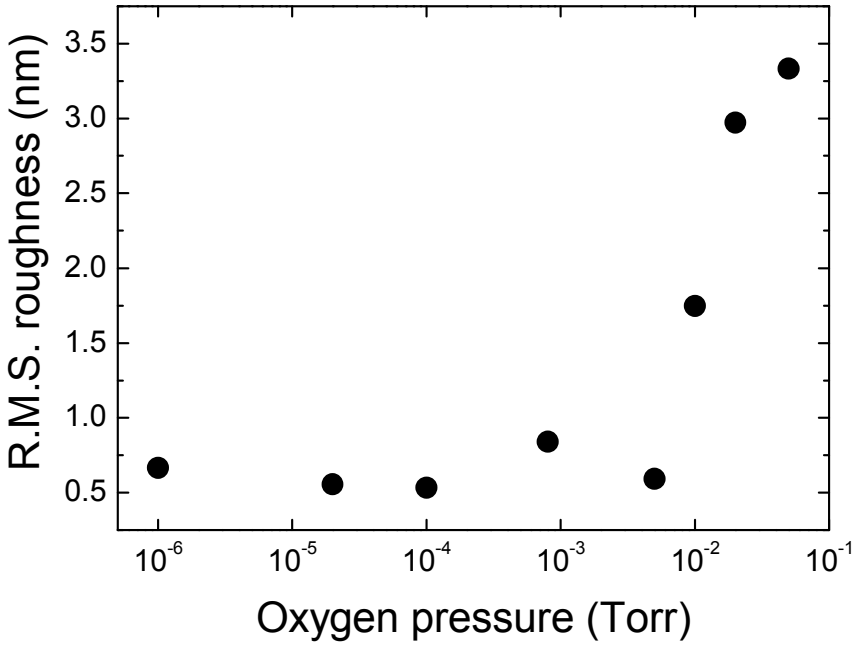

Figure 4.5 AFM rms roughness of the room temperature deposited GZO film plotted as a function of oxygen pressure

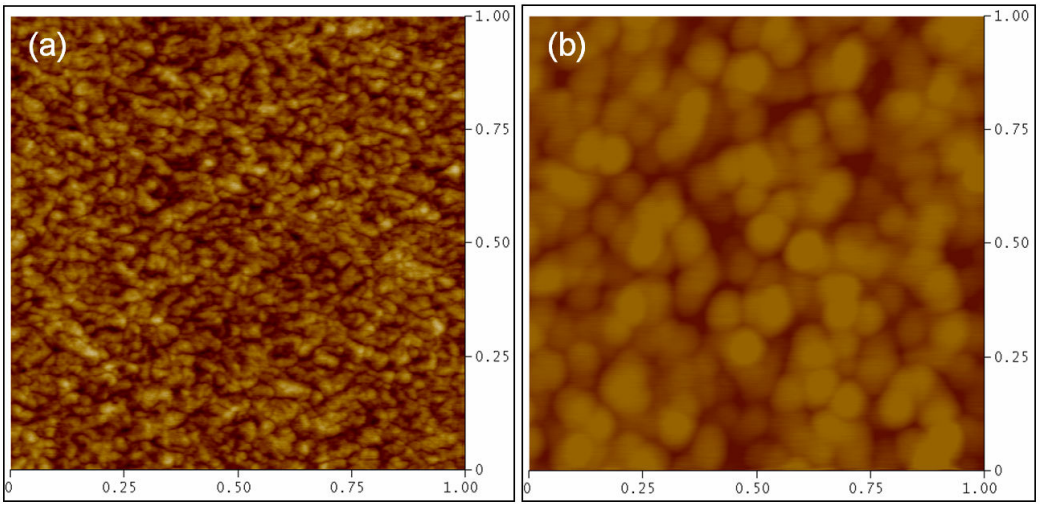

Figure 4.6 AFM image of the GZO film deposited at (a) room temperature and (b) 500 °C; both at an oxygen pressure of 1×10^{-4} Torr . The size of scanned area in both plots is 1 μm × 1 μm respectively

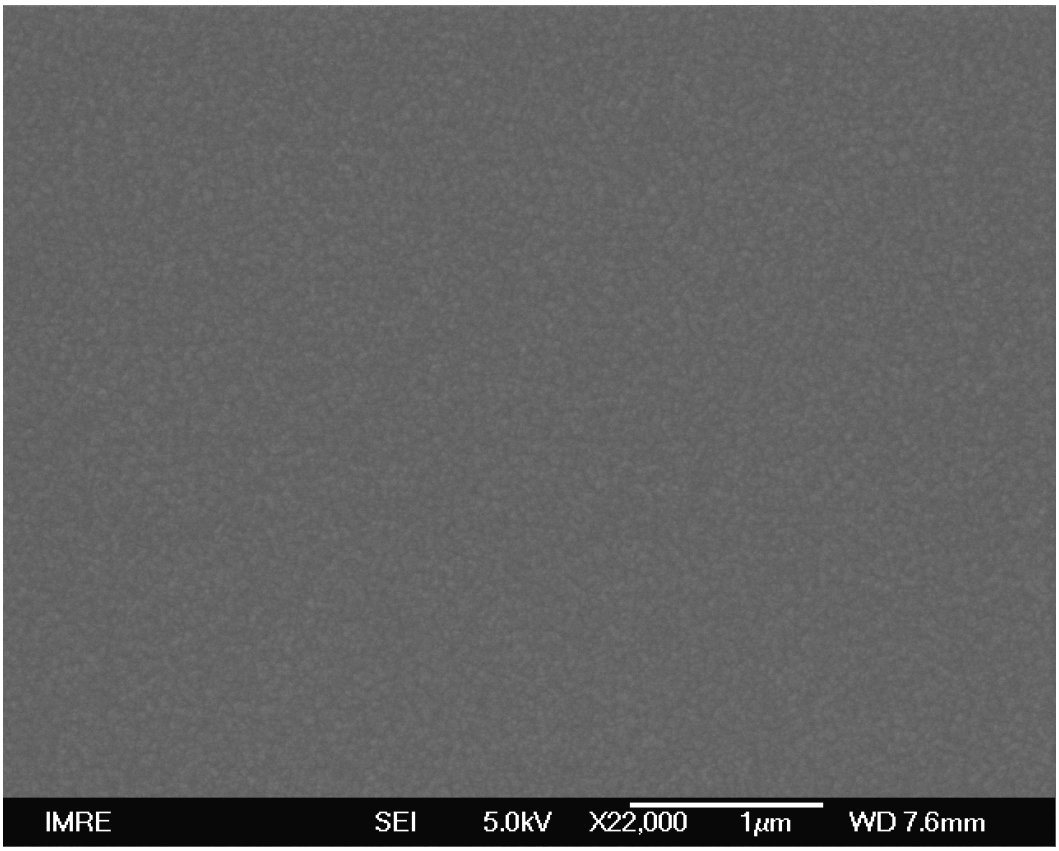

Figure 4.7 SEM image of a GZO film deposited at room temperature and at an oxygen pressure of 1×10^{-4} Torr

4.2.5 Optical Characterization

For TCOs, high transmittance in the desired spectral region is a crucial requirement. In this section, a method to better examine the transparency of the deposited thin films is introduced. In doing so, it provides a better quantification for the transparency of the thin film material. The quantification of transparency varies from different reports and there are no standards in reporting and hence comparing them. The most conventional representation gives an average transmission percentage over the visible region while some reports just use the highest transmission figure.[211,235-237] Recently, an index that can be used as a figure of merit was

proposed by our research group.[238] This index is simply a measure of how transparent the thin film is either relatively (with competing materials such as glass, ITO or even different processing conditions) or absolutely (simply compared against perfect transmission). The index can thus be meaningfully defined for comparisons between different structures. In the straight-forward scenario, for instance the use of transparent conducting electrodes in devices such as light emitting diodes, quantification of transmission is required only in the visible region or at a certain narrow range of wavelengths. In this case, an absolute index against perfect transmission will simply reflect the total measured transmission across the required spectrum and meaningful comparisons can be made across different samples. More considerations are needed if the transparent electrode is to be used for photovoltaic device applications. Not only should the transmission be considered across a larger range of wavelengths, it is also important to factor in the intensity distribution of the solar spectrum. One way to accomplish the above is to examine the total transmitted intensity of an Air Mass (AM) 1.5 spectrum as our group have previously proposed. [239] In this way, the transmitted intensity of the AM 1.5 incident spectrum by the TCO can be computed and meaningful comparison of transparency for use in photovoltaics can then be achieved. The average transparency index for photovoltaic application can be computed as follows:

$$T = \frac{\sum_{n=280}^{1700} \Gamma_n \times I_n}{\sum_{n=280}^{1700} I_n} \tag{4.2}$$

where Γ_n(%) is the measured transmittance at the wavelength n (nm) and I_n is the intensity of the spectrum with a unit of $Wm^{-2}nm^{-1}$(as from ref. [239]). Equation (4.2) is a discretized representation and only wavelengths up to 1700 nm are considered.

Theoretically, continuous integration over the entire spectrum gives the technically precise index but for practical purposes, the above representation is more than sufficient. The computed index will be very useful to show the absolute fraction of the solar spectrum transmitted. This is much better than just an average figure for transmission since performance of the transparency is proportionally represented in different regions of the spectrum according to the power density. Factoring in 'dips', such as water absorption in the solar spectrum, is also useful in giving a more realistic and practical representation of the overall transparency of the electrode. The proposed index is demonstrated to show how it can be useful for comparing different regions of the spectra depending on the choice of summation.

For comparing samples with drastically different thickness, a normalized index TI_N is introduced here that is important for factoring in changes of the absorption due to changes in thicknesses and equation (4.2) can be modified as follows:

$$TI_N = \frac{\sum_{n=280}^{1700} \Gamma_n \times e^{-\alpha_n (x-d)} \times \mathrm{I}_n}{\sum_{n=280}^{1700} \mathrm{I}_n} \tag{4.3}$$

where x is an arbitrary choice of normalization film thickness suitable for the specific application (for example, x = 200 nm), d is the actual thickness of the film in the transmittance measurement and α_n is the absorption coefficient at the particular wavelength. The derivation of equation (4.3) assumes that the reflection of the thin film is identical for samples of different thickness and this condition is usually fulfilled. In this work, although the thicknesses of the films fabricated here do not vary greatly, equation (4.3) has been used to give a more accurate transparency index.

The normalization thickness of 200 nm was used and the absorption coefficient was obtained from the transmittance at different wavelengths.

A summary of the computed normalized transparency index for the thin films measured in this work is shown in Figure 4.8. Correlation was made between the optical data and the resistivity (obtained from section 4.2.2) for the room temperature samples in Figure 4.8. As a reference, the deposited undoped ZnO thin film (resistivity of 1.2×10^{-2} Ω-cm) results in a transparency index of 0.87. As mentioned, the index is a fair figure of merit representing the fraction of the total solar spectrum power intensity, over the wavelength range of 280 to 1700 nm, transmitted through the thin film (normalized for the 200 nm film thickness in this case). It can be seen that the normalized transparency index first increases with increasing oxygen pressure. It peaks at an oxygen pressure of 10^{-2} Torr and decreases at higher oxygen pressures. It is important to note that above an oxygen pressure of 10^{-4} Torr, the increase in transparency comes at the expense of higher film resistivity. Using the values obtained from equation (4.3), the resulting data were carefully analyzed on how the different oxygen pressures affect the transparency.

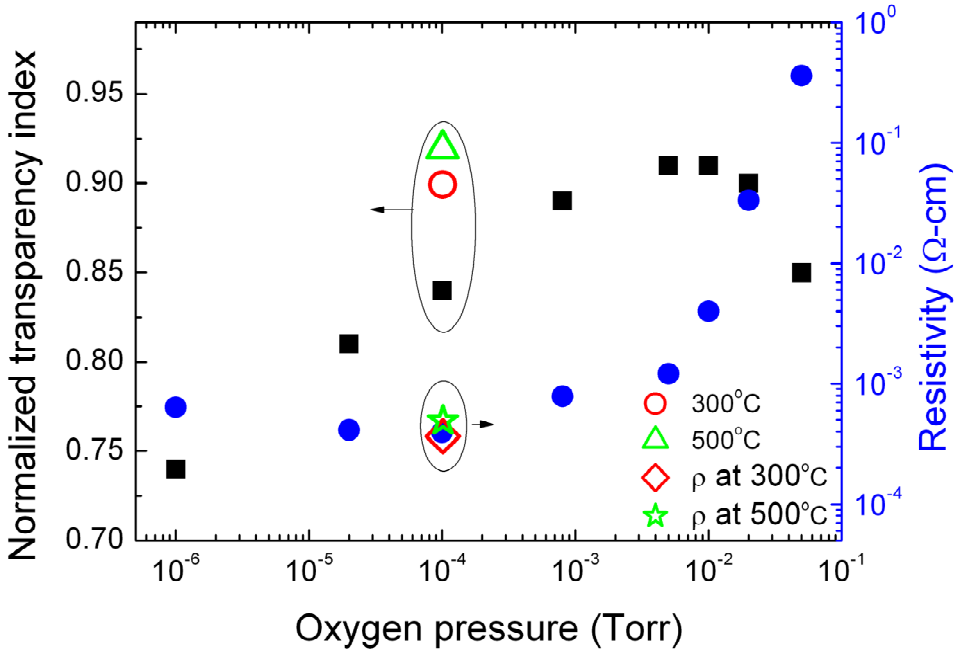

Figure 4.8 Normalized transparency index of GZO (solid square symbol) as a function of oxygen pressure for deposition at room temperature. Also included are the transparency index for GZO films deposited at higher substrate temperatures at an oxygen pressure of 1×10^{-4} Torr. The resistivity (ρ) of the films (solid circle symbol) is also shown for easy comparison

The absolute transmitted intensity spectra for films deposited at different representative oxygen pressures is shown in Figures 4.9(a) and 4.9(b), with three important ranges (A, B and C) of wavelengths indicated. Figures 4.9(a) and 4.9(b) show that with increasing oxygen pressure from low (10^{-6} Torr) to mid pressure (10^{-4} Torr), there is an appreciable increase in transmittance in the visible wavelength range (range B in Figure 4.9(a)). Previously, it was also shown in Figure 4.1(a) that for oxygen pressures from 10^{-6} to 10^{-4} Torr, the carrier concentration of the GZO is not greatly affected even though the carrier mobility is increasing. This shows that the increase in transmittance in the visible region can be attributed to removal of deep

level oxygen defects as mentioned previously in section 4.2.2. This allows for improvements in the carrier mobility without significant variations in the carrier concentration and is consistent with the defect transition levels in the optical range from 490 to 515 nm.[240,241] The higher transparency indices for the higher oxygen pressure regime actually result from improved transmission in the near and far infrared regimes due to a reduction in free-carrier absorption. This agrees with the formation of oxygen interstitials at higher oxygen pressures as discussed previously. This analysis also notes that the measured carrier mobility shows no distinct relationship with the carrier concentration, showing little influence by carrier–carrier scattering, at least in the free-carrier concentration range of 10^{20} to 10^{21} cm^{-3}. This result again shows emphasis on the importance of considering ionized defects and grain boundary scattering in limiting the carrier mobility in TCOs.

Figure 4.8 also shows the transparency of samples deposited at a substrate temperature of 500 °C at an oxygen pressure of 10^{-4} Torr. A better transparency is obtained without any drastic changes in the overall resistivity. The transmittance in Figure 4.9(a) shows even better transmitted intensity and with the increase in the carrier mobility, this suggests the possible role of both bulk and boundary defects. From the AFM results (Figure 4.6(b)) in section 4.2.4, the significant growth in grain sizes can be clearly seen with the increase in deposition substrate temperature. The increase in grain sizes can serve to reduce grain boundary defects and this therefore adds to the improvement in transparency in the optical region.

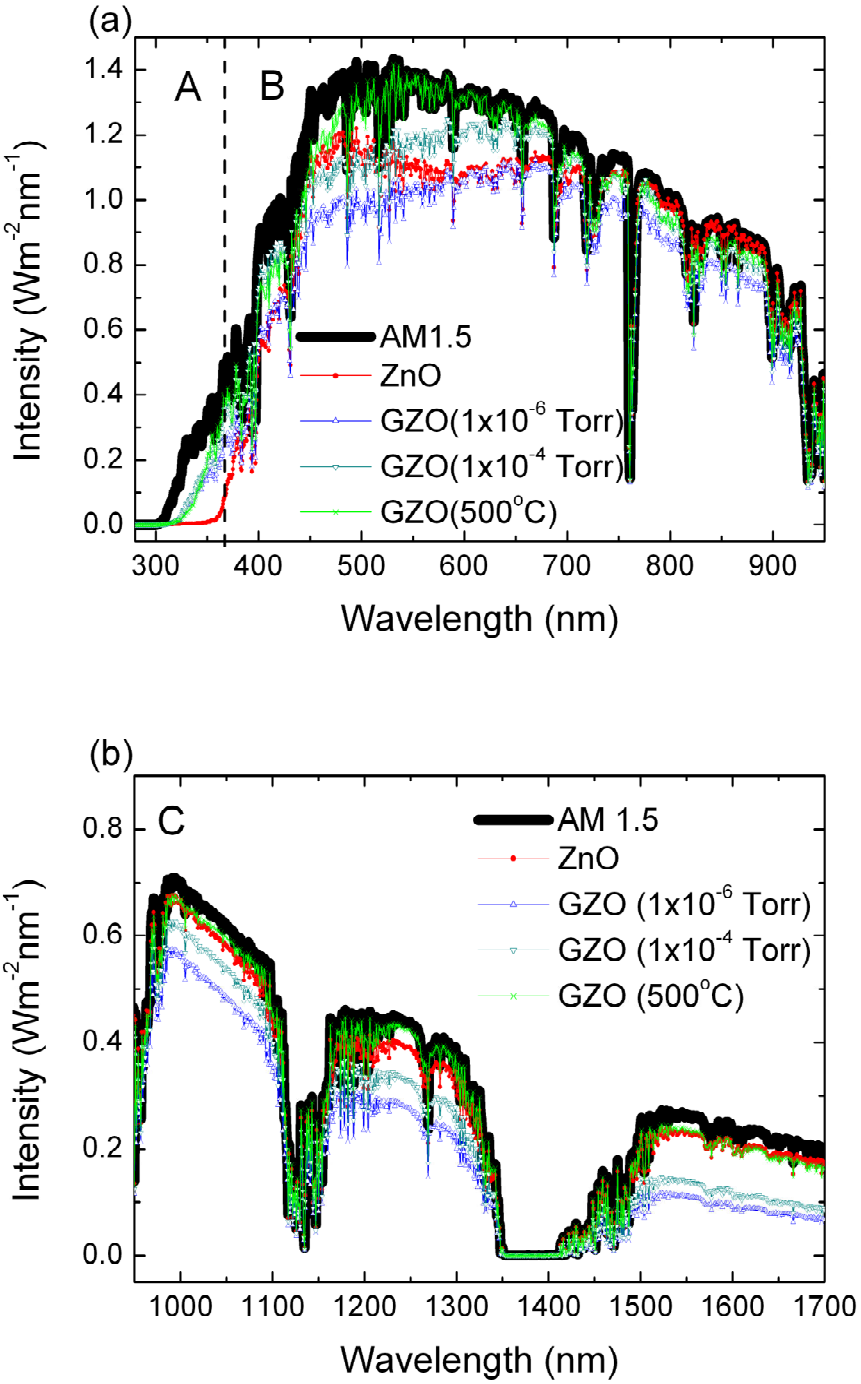

Figure 4.9 Absolute transmitted intensity of the solar spectrum for GZO films deposited at the indicated oxygen pressures and also with the film deposited at 500°C at an oxygen pressure of 1×10^{-4} Torr for the wavelength ranging from (a) 300nm to 950nm and (b) 950nm to 1700nm. The actual AM 1.5 spectrum together with the transmitted intensity of the undoped ZnO is included in the plot for reference. The plot is a representation of the total transmitted intensity through the TCO from solar irradiation. The plots are subdivided into regions A, B and C according to the wavelength range

In the infrared regime shown as range C in Figure 4.9(b), the highly conductive doped ZnO generally has a lower transmittance due to free-carrier absorption. This can explain the increasing trend of higher transparency index for the samples deposited at oxygen pressures above 10^{-4} Torr as they generally have a lower free-carrier concentration due to compensational effects from the oxygen interstitials which was mentioned in section 4.2.2. This explanation agrees well with the increase in resistivity with improvements in the transparency at higher oxygen pressures. Part of the contribution to the increase of the overall transparency index can be seen over range A in Figure 4.9(a). This can be directly related to the variations in the bandgap of the GZO thin films. First, the band gap effect was observed if the variations at different pressures or temperatures are predominantly due to the Burstein-Moss effect. The absorption coefficient was computed from the Beer-Lambert's attenuation equation using film thickness measured from the AFM and cross-sectional TEM.[242] The optical band gap (E_g) are calculated based on the method mentioned in section 2.1.4. The obtained spectrum for the onset of transmission is plotted in Figures 4.10(a) and 4.10(b) while the insets in both figures show the general relationship of E_g with the varying oxygen pressure and substrate temperature. The measured optical E_g ranges from ~3.49 to 3.77 eV over the range of oxygen pressure shown in the inset of Figure 4.10(a) while the measured optical E_g, over different substrate temperatures, ranges from ~3.63 to 3.74 eV (inset in Figure 4.10(b)).

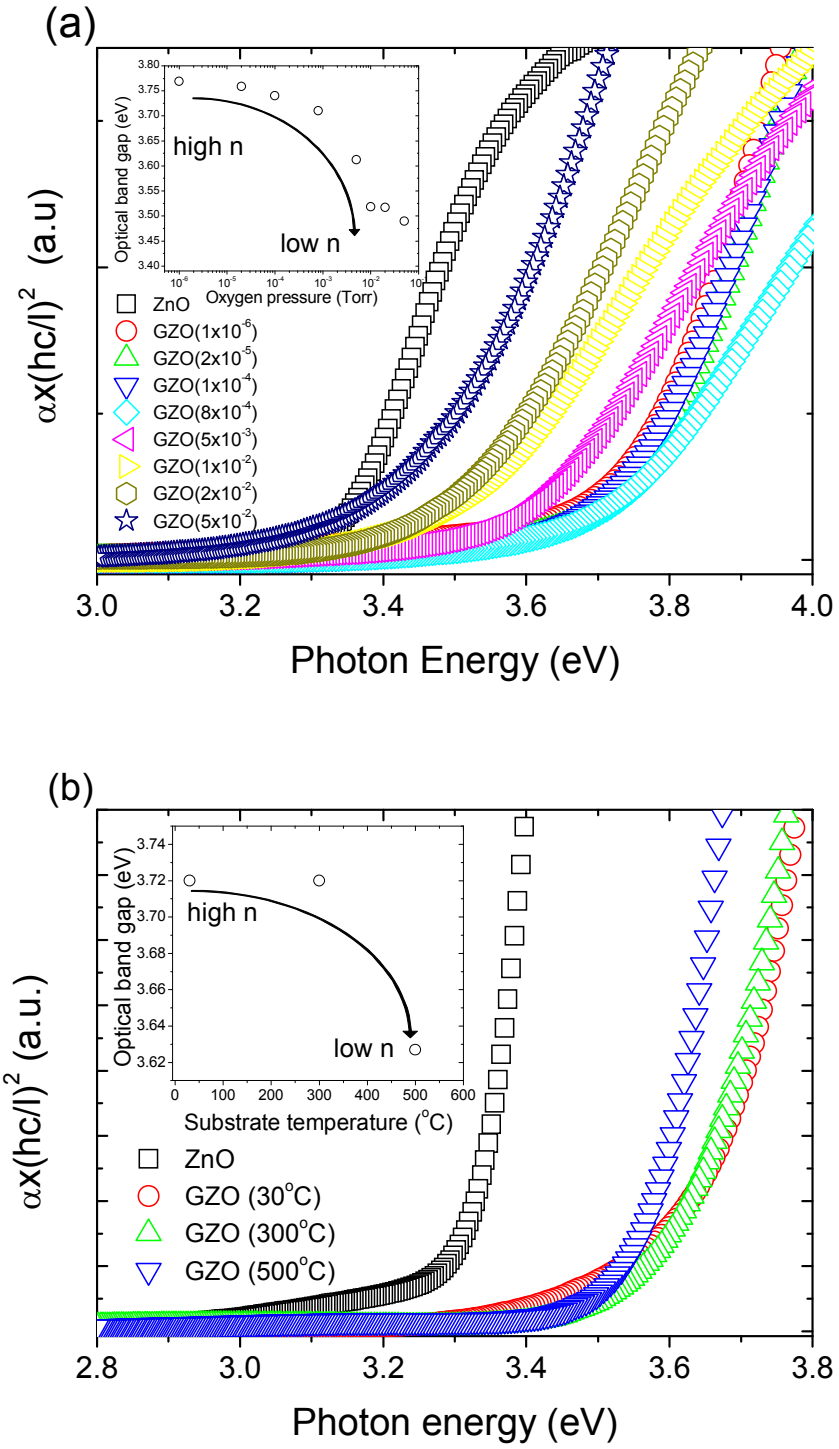

Figure 4.10 Plot of $(\alpha E)^2$ as a function of photon energy for films deposited at different (a) oxygen pressures (room temperature) and (b) substrate temperatures (oxygen pressure of 1×10^{-4} Torr). The insets in (a) and (b) show the trend of the band gap values, measured from the linear extrapolation of the plot, against the oxygen pressure and substrate temperature respectively

If the Burstein-Moss effect is dominant, a plot of the change in E_g as a function of the 2/3 power of carrier concentration should show an approximate linear relationship. This is because according to the Burstein-Moss relationship, red shifts in the absorption edge, and thereby shifts in the band gap are related to the carrier concentration as shown in equation (2.18). Figure 4.11 demonstrates the obtained relationship showing a reasonable correlation of the observed E_g measurements to carrier concentration. However, it should be noted that structural effects such as changes in lattice constant, and hence strain, can affect the resultant band gap and this can be part of the reason for the lack of a better fit. The XRD peak shifts to higher 2-theta values, while retaining the high orientation along the c-axis, is a sign of a change in the in-plane configuration and thus reflects a change in the lattice strain.[233] If this consideration is factored in, by omitting the data with big variations in the structural data (filled or solid circles in Figure 4.11), one can obtain a better straight line fit with reasonable effective mass showing the dominance of the Burstein-Moss effect.

The above discussion shows three dominant effects that influence the transparency of the thin film, namely the band gap, free-carrier absorption and defects. Since the aforementioned effects typically affect absorption at different wavelength regions, one can more clearly observe the role they play if one looks at the transparency index at different wavelength regimes. Figures 4.12(a), 4.12(b) and 4.12(c) show the normalized transparency index in the UV, visible and infrared region plotted individually against E_g, oxygen pressure and carrier concentration respectively. It is useful to look at variations with the selected effect as this will allow one to disregard other changes and target directly at the original cause of the

transmittance changes. For example, different oxygen pressure or varying substrate temperature conditions can result in different carrier concentrations. A plot in the infrared range against the oxygen pressure may not give meaningful relationships since the free-carrier absorption is the dominant parameter that really changes the transparency index in this region. Therefore, by just examining the variations of transparency in the infrared range with carrier concentrations (across deposition conditions) as shown in Figure 4.12(c), a linear relationship was obtained in the log-linear plot. The linearity is expected from the Drude free-carrier model whereby the slope in the plot is proportional to the scattering time of the free carriers.[243]

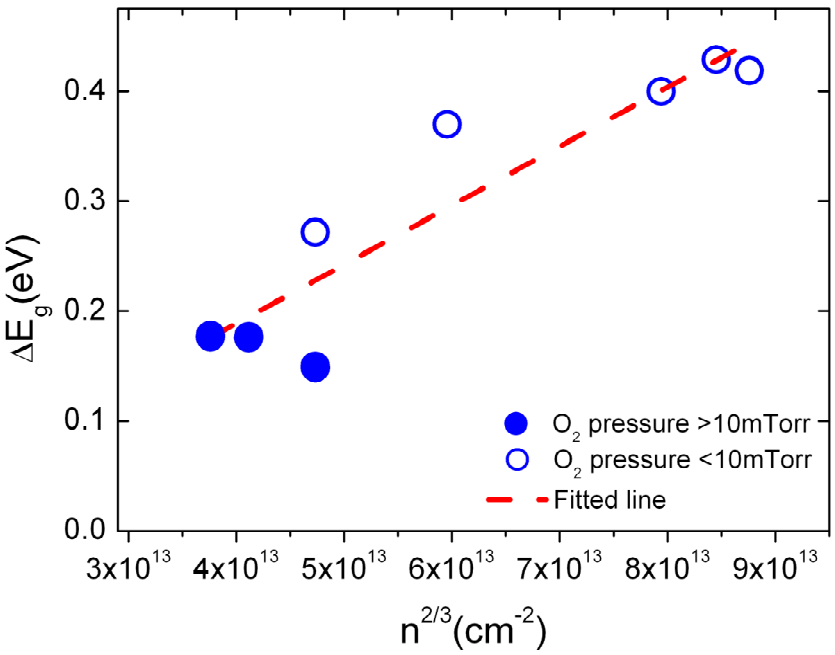

Figure 4.11 Change in the optical band gap plotted against the 2/3 power of carrier concentration ($n^{2/3}$). The solid circles are data from films grown at higher oxygen pressure that resulted in structural changes (relaxation) as observed from the XRD data

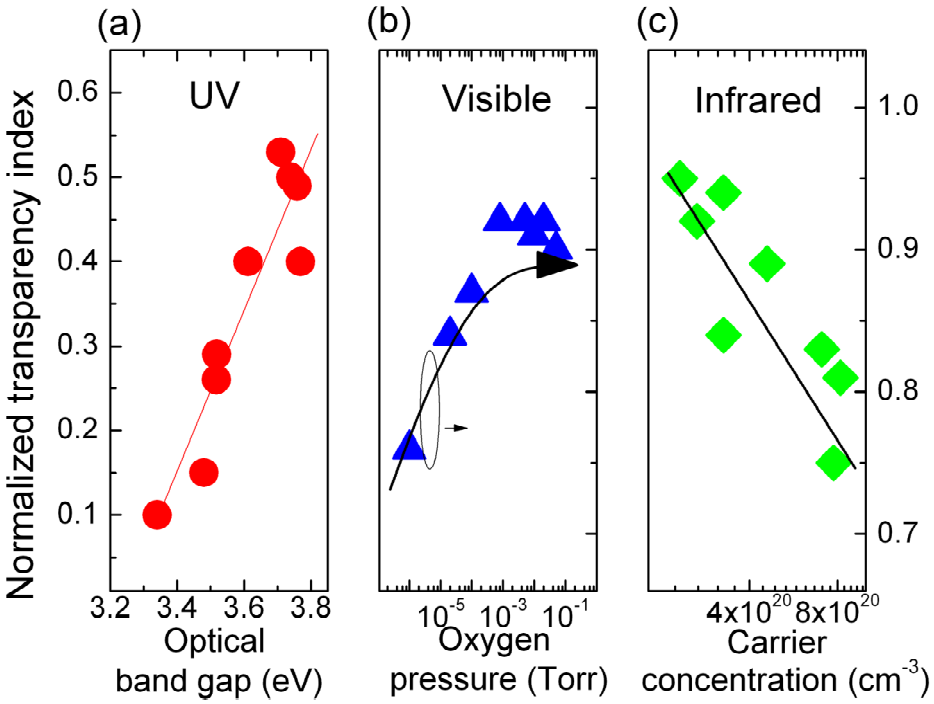

Figure 4.12 Plot of normalized transparency index as a function of (a) optical band gap in the UV range, (b) logarithmic scale of oxygen pressure in the visible range, and (c) logarithmic scale of carrier concentration in the infrared range. The linear relationships in (a) and (c) are from a best-fit function while the big arrow in (b) is included as a guide for the eye. The index values for (b) and (c) are indicated by the axis on the right

Similarly, in Figure 4.12(a), the increase in the transparency index in the UV range is shown to follow well with changes in the optical band gap. The plot also shows that the transparency index in the UV range is generally low and this is expected given the band gap property of ZnO.

In the visible range shown in Figure 4.12(b), the use of the transparency index clearly demonstrates the effects of different oxygen pressure and the role which the defects play. At lower oxygen pressures, the transparency index increases with larger oxygen pressure and this agrees with the analysis of passivation of bulk or boundary

defects. The transparency index, however, saturates to values of ~0.9 at oxygen pressures greater than 10^{-3} Torr as shown in Figure 4.12(b). This can thus be understood that the visible transparency is not improved with higher oxygen pressures and the increase in the overall transparency index as shown in Figure 4.8 is due to variations of the free carrier absorption in the infrared region as discussed. Values of ~0.9 for GZO probably represent the maximum achievable transparency at the selected normalization thickness for the room temperature deposited thin films. Understandably, this figure of merit can be higher with a thinner GZO and vice versa. The normalized index is thus extremely useful to extrapolate any experimentally measured values to different desired thickness (with requirement for different devices) for meaningful comparisons. Conversely, if a known transparency is demanded for a particular application, equation (4.3) can also be a good estimation of the thickness required at the selected deposition conditions. The use of the normalized transparency index is therefore a versatile standard and the above demonstrates how examination of different wavelength regions of the transparency index gives a much clearer picture of the influence of different parameters on the transmission.

4.2.6 Concluding Remarks

In summary, the optical and electrical properties of GZO thin films deposited by pulsed laser ablation at various oxygen pressures are discussed. The influence of oxygen pressure on the oxygen vacancy and interstitial is found to be dominant in the lower and mid-oxygen pressure regimes. At higher oxygen pressure, the effects on the in-plane orientation of the grains can explain for the variations in the carrier concentration and mobility. In understanding this, there is a balance between too much (oxygen interstitials) and too little (oxygen vacancies) oxygen during deposition

at room temperature. The important role of grain boundary scattering is demonstrated by samples deposited at higher oxygen pressures and this is affirmed by samples deposited at higher temperatures. A transparency index was also introduced in this work that takes into account the different intensity of the practical Air Mass (AM) 1.5 solar spectrum. In doing so, an absolute value of the total transmitted solar spectrum that is normalized against film thickness can be accurately reflected in the index, making the normalized transparency index a versatile and useful standard for comparison. The normalized index was used in this work to examine the transparency at different wavelength regimes, which can clearly demonstrate the influence of oxygen pressure, carrier concentration and band gap changes. This allows for a clear understanding of factors that affect the transmittance of the thin film, which will be important for obtaining good quality transparent electrodes. In this work, for room temperature deposition, an excellent resistivity of ~3.9 × 10^{-4} Ω-cm in GZO was obtained with a transparency index of ~0.84 at an oxygen pressure of 1 × 10^{-4} Torr. This makes it a potential candidate for use as a transparent electrode material in plastic electronics or photovoltaic applications.

4.3 Metal/GZO Single and Multilayers

In the following sections, metal/GZO layers and GZO/metal/GZO layers were investigated. The effect of Ag thickness variation on the surface morphology, electrical and optical properties of indium-free Ag/GZO and GZO/Ag/GZO multilayers, under room temperature deposition condition, were compared. In addition, the effect of an additional germanium (Ge) buffer layer prior to the Ag layer deposition was also investigated in terms of surface morphology, electrical and optical properties. Transparent conductors are generally thin metal films or oxide films.[244]

However, single layer metals are highly conducting but they are neither highly transparent nor durable.[245] TCOs are more durable and more transparent but their conductivity is slightly lower than thin metal films. TCOs generally exhibit resistivity of less than 10^{-3} Ω-cm and have an average transmittance exceeding 80% in the visible region, with ITO currently being the most commonly used TCO. [6,246,247] Due to the various issues affecting ITO as mentioned in section 1.2, there is an urgent need to seek alternative TCOs to replace ITO, with doped ZnO being a potential substitute. In addition to the previous section which concentrated on examining a single layer GZO thin film, the focus in this section is on metal/GZO single and multilayers and its optical transmission and reflectance in the near infrared (NIR) wavelength range.

4.3.1 Fabrication of Metal/GZO Single and Multilayers

GZO thin films were deposited on borosilicate glass by pulsed laser deposition (PLD) using a ceramic ZnO/Ga_2O_3 (0.98:0.02) target (99.99% purity). The optimized GZO of thickness ~77.4 nm is used as a base layer on the substrate. Details on the growth of optimized GZO layers are reported in section 4.2.1. In the first series of experiments, the Ag layer is deposited at a rate of 0.1 nm/s using electron beam (e-beam) evaporation technique at room temperature. Prior to deposition, the e-beam evaporation chamber is pumped down to at least 5×10^{-6} Torr. The thickness of the Ag layers is varied from 1 nm to 10 nm using a quartz crystal controller to monitor the thickness during the deposition process. The thickness of Ag has been calibrated previously and the error is less than 10%. For the multilayered samples, a subsequent GZO layer (~38.6 nm) is then deposited using PLD. In the second series of

experiments, a 0.5 nm Ge buffer layer is introduced prior to the Ag deposition in the same evaporation chamber using a deposition rate of ~0.1 nm/s. During all the evaporation process, the substrate holder is water-cooled to around 30°C to prevent possible annealing in a reducing atmosphere. In summary, there are four groups of samples in this work, namely Ag/GZO/bg, Ag/Ge/GZO/bg, GZO/Ag/GZO/bg and GZO/Ag/Ge/GZO/bg, where "bg" denotes borosilicate glass.

4.3.2 Surface Morphology

To investigate the surface morphology of the Ag layer deposited on GZO layer, AFM was performed on each sample. Figure 4.13 shows the AFM image of Ag/GZO and Ag/Ge/GZO multilayer, an uncoated GZO/glass is included for comparison. All the scanned images have a scanned area of 1 μm × 1 μm and a vertical height scale of 20 nm per division. It can be seen that for the case of Ag (1 nm) in Figure 4.13(b), the surface is very hilly as the metallic layer might have aggregated, forming Ag islands.[236] As the thickness of the Ag layer increases (see Figures 4.13(d) and 4.13(f)), the film surface becomes smoother as a continuous Ag film forms; the root mean square roughness (r.m.s.) is also evidence of a smoother surface as shown in Figure 4.14 which is explained further below.

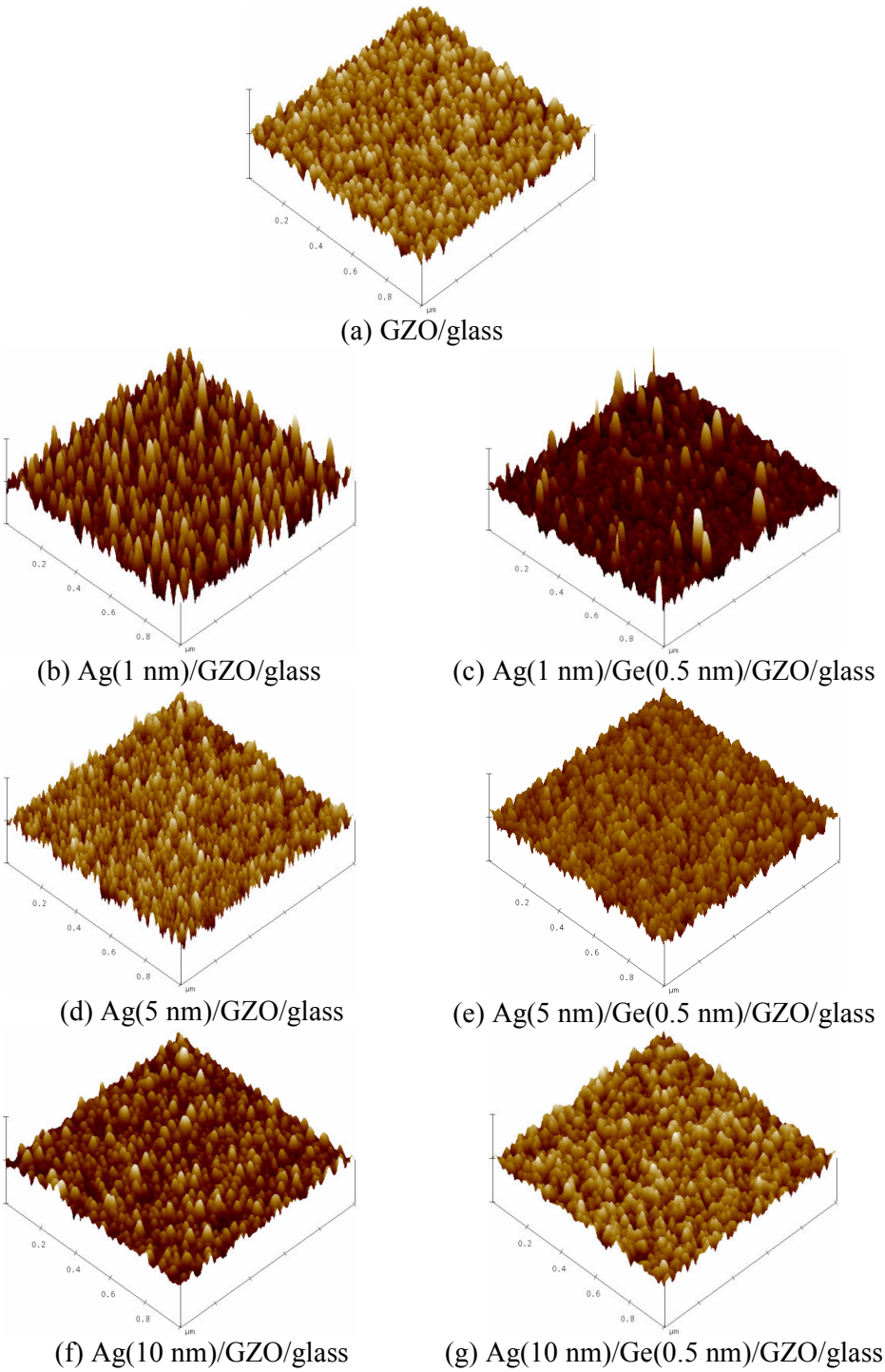

(a) GZO/glass

(b) Ag(1 nm)/GZO/glass

(c) Ag(1 nm)/Ge(0.5 nm)/GZO/glass

(d) Ag(5 nm)/GZO/glass

(e) Ag(5 nm)/Ge(0.5 nm)/GZO/glass

(f) Ag(10 nm)/GZO/glass

(g) Ag(10 nm)/Ge(0.5 nm)/GZO/glass

Figure 4.13 AFM images of the metal/GZO multilayer film. (a) as-deposited GZO/glass, (b) Ag(1 nm)/ GZO/ glass, (c) Ag(1 nm)/ Ge(0.5 nm)/ GZO/ glass, (d) Ag(5 nm)/ GZO/ glass, (e) Ag(5 nm)/ Ge(0.5 nm)/ GZO/ glass , (f) Ag(10 nm)/ GZO/ glass and (g) Ag(10 nm)/ Ge(0.5 nm)/ GZO/ glass. The scanned area and vertical height scale in all images are 1 μm × 1 μm and 20 nm per division respectively

Figure 4.14 shows the plot of r.m.s roughness for Ag/GZO samples, with and without a Ge buffer layer (0.5 nm thickness), as a function of the thickness of the Ag layer. The blue line indicates the r.m.s. roughness of the uncoated reference GZO/glass at ~1.79 nm. With the addition of a Ge buffer layer, it is observed that the overall roughness for all thicknesses of silver decreases; the results agree with the findings in another study which reported that a Ge seed layer decreases the surface roughness of a subsequent metal layer.[248] It is to be noted that as the Ag thickness increases, the r.m.s roughness decreases as a continuous metallic Ag layer is usually smoother. Figure 4.15 shows the surface morphology of GZO/Ag/GZO and GZO/Ag/Ge/GZO multilayers. Similar to the metal/oxide samples, as the thickness of the Ag increases, the surface is smoother due to formation of a continuous Ag film.

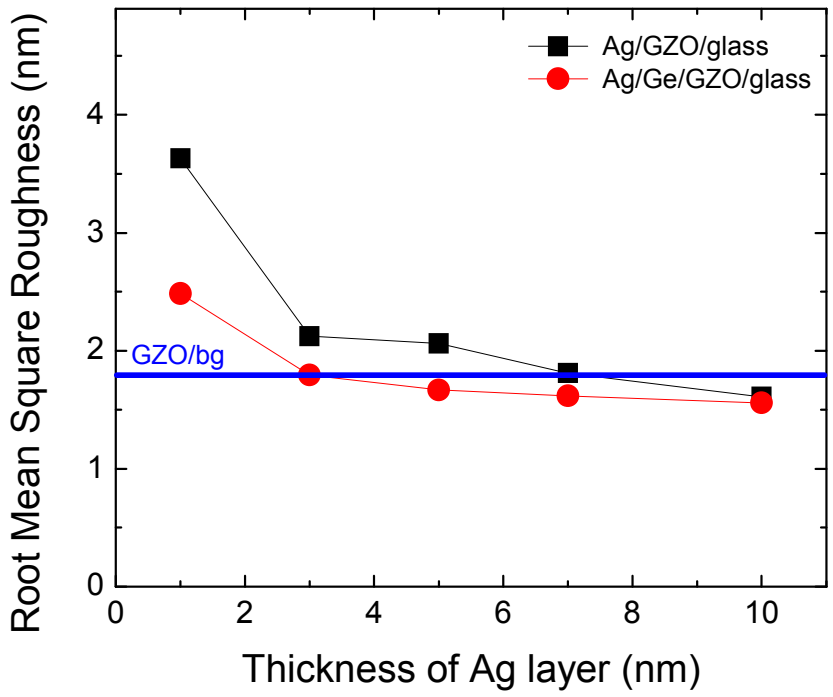

Figure 4.14 Plot of root mean square roughness of Ag/GZO and Ag/Ge/GZO as a function of thickness of the Ag thin film. The root mean square of GZO/glass (i.e., GZO/bg) is shown for reference

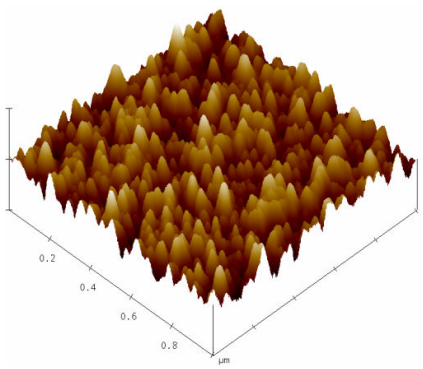

(a) GZO/Ag(1nm)/GZO/glass

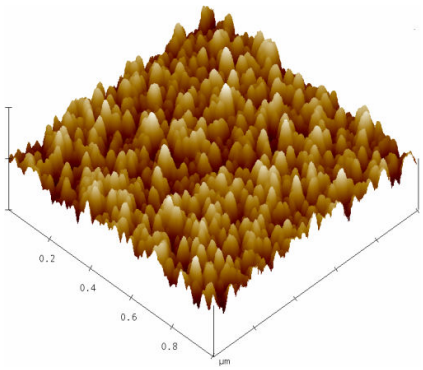

(b) GZO/Ag(1nm)/Ge(0.5nm)GZO /glass

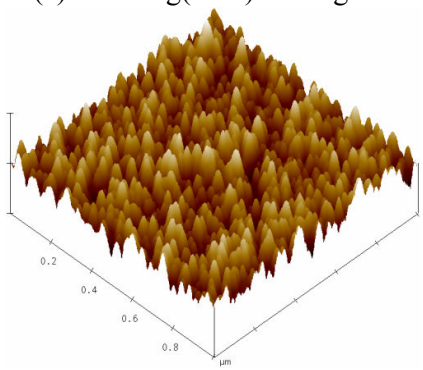

(c) GZO/Ag(5nm)/GZO /glass

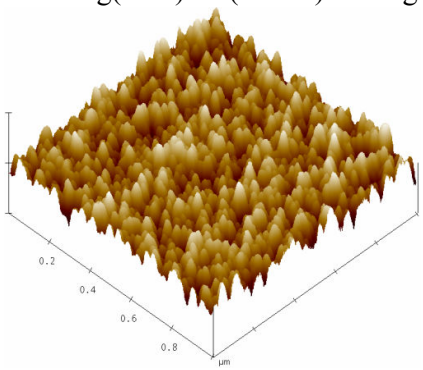

(d) GZO/Ag(5nm)/Ge(0.5nm)GZO /glass

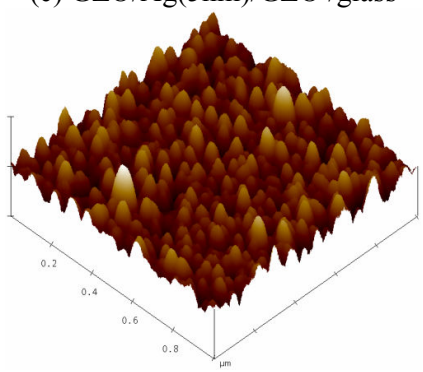

(e) GZO/Ag(10nm)/GZO/glass

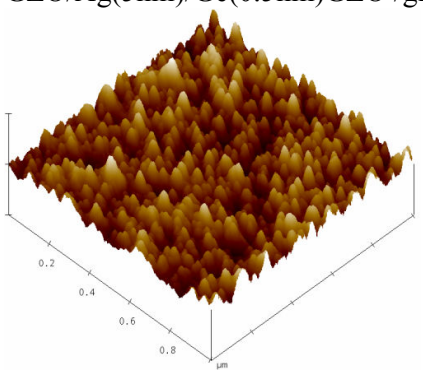

(f) GZO/Ag(10nm)/Ge(0.5nm)GZO/glass

Figure 4.15 AFM images of the GZO/metal/GZO multilayer film. (a) GZO/ Ag(1 nm)/ GZO/ glass, (b) GZO/ Ag(1 nm)/ Ge(0.5 nm)/ GZO/ glass, (c) GZO/ Ag(5 nm)/ GZO/ glass, (d) GZO/ Ag(5 nm)/ Ge(0.5 nm)/ GZO/ glass, (e) GZO/ Ag(10 nm)/ GZO/ glass, (f) GZO/ Ag(10 nm)/Ge (0.5 nm)/ GZO/ glass. The scanned area and vertical height scale in all images are 1 μm × 1 μm and 20 nm per division respectively

The r.m.s roughness also decreases for all samples with the inclusion of a Ge buffer layer (0.5 nm thickness) as seen in Figure 4.16. On the whole, the GZO/Ag/GZO/glass and GZO/Ag/Ge/GZO/glass multilayers have slightly higher r.m.s. roughness compared to the single layer uncoated GZO/glass.

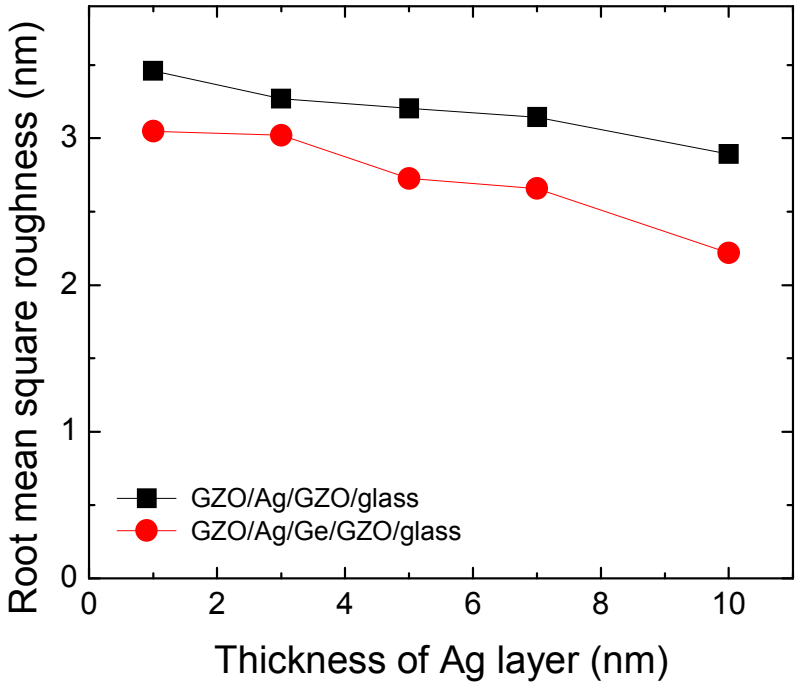

Figure 4.16 Plot of root mean square roughness of GZO/Ag/GZO and GZO/Ag/Ge/GZO as a function of thickness of the Ag thin film

4.3.3 Electrical Characterization

For the Ag/GZO films, as the thickness of the Ag layer increases, there is no significant improvement in the electrical resistivity, which is still of the order of 10^{-4} Ω-cm that is similar to the as-deposited GZO/glass (i.e., the sample with zero thickness of Ag layer) as seen in Figure 4.17(a). The erratic change in carrier mobility and carrier concentration in the Ag/GZO films with increase in Ag layer thickness is likely attributed to the discontinuous Ag islands aggregated on the GZO. Figure 4.17(b) shows the effect of the addition of a Ge buffer layer (0.5 nm thickness) on the electrical properties of the Ag/Ge/GZO films. The work function for Ag, Ge, ZnO and GZO are ~4.35 eV, ~4.75 eV, ~5.4 eV and ~4.23 eV respectively.[249-252] Hence, there is an ohmic contact at the metal oxide interface which accumulates majority carrier electrons in the GZO layer. At low Ag thickness (< 5 nm), the carrier mobility decreases as compared to an uncoated GZO film, implying that the Ag islands are acting as discontinuous scattering centers, thus reducing the carrier mobility. As the thickness of Ag increases, the layer becomes more and more continuous as evidenced by an increase in carrier concentration and mobility. Hence, when the thickness of Ag is greater than 5 nm, the resistivity starts to decrease, indicating that the thin Ge buffer layer indeed enhances the formation of a continuous Ag layer. For the Ag(10 nm)/Ge/GZO/glass sample, there is one order improvement in the resistivity to ~8.1×10^{-5} Ω-cm. This is in agreement as a thicker Ag layer will give a lower resistivity.[42]

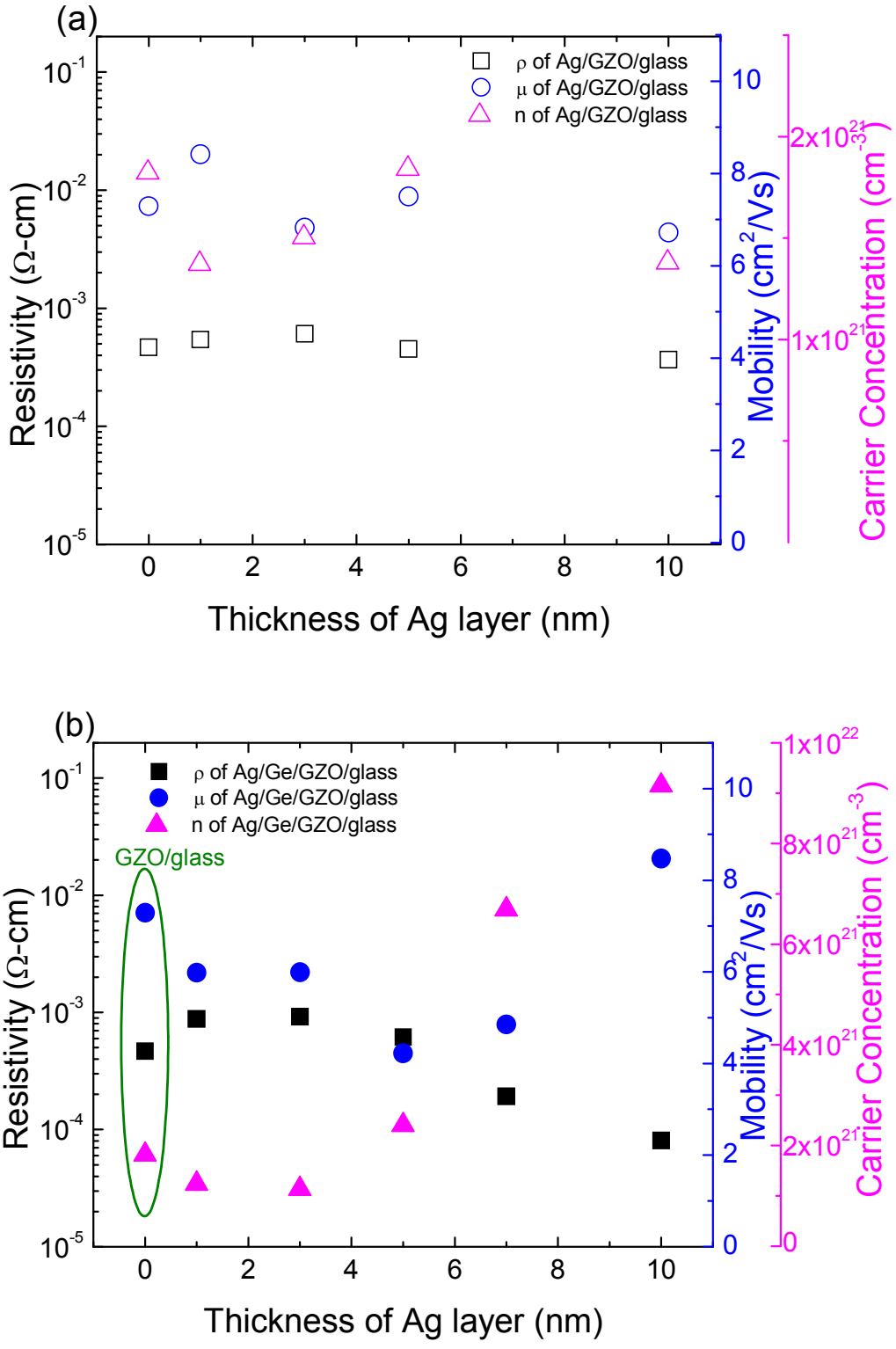

Figure 4.17 Electrical resistivity (ρ), carrier concentration (n) and Hall mobility (μ) of the Ag/GZO films plotted as a function of Ag thickness layer for samples (a) without Ge buffer layer and (b) with Ge buffer layer

Figure 4.18(a) shows the electrical properties of the GZO/Ag/GZO films. As mentioned in Figure 4.17(a), there is no significant change in resistivity even for a thicker Ag layer as the Ag layer has yet to form a continuous film. However, due to the GZO top layer enveloping the Ag islands, a mixture layer of GZO and Ag is formed. Therefore, even at low Ag thickness, the carrier concentration is high. As the thickness of Ag increases, the roughness of this Ag layer also decreases. The GZO top layer is likely to cover the Ag layer more completely, leading to a decrease in carrier concentration. Comparing between the GZO/Ag/GZO and GZO/Ag/Ge/GZO films in Figure 4.18, there is also a half order improvement in the electrical resistivity.

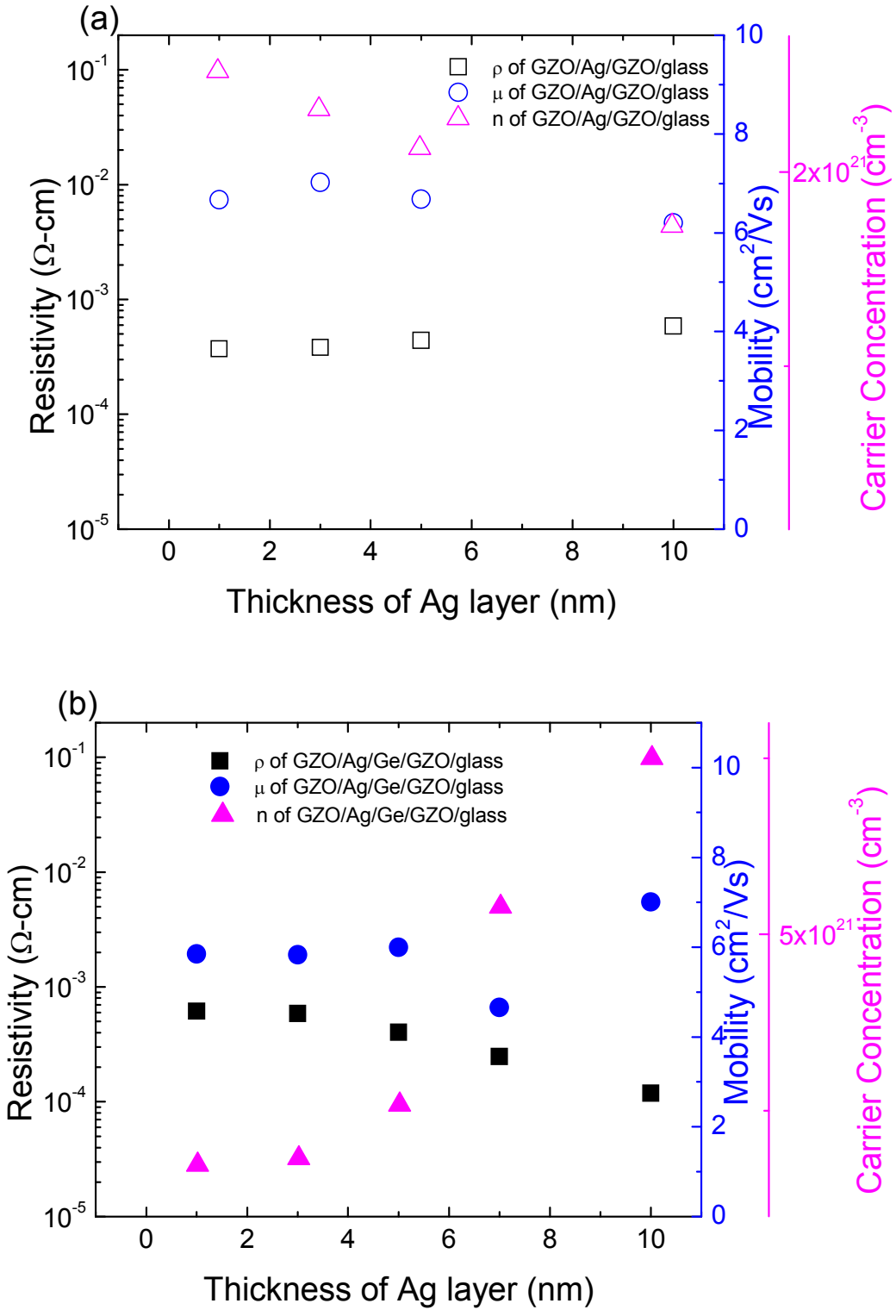

Figure 4.18 Electrical resistivity (ρ), carrier concentration (n) and Hall mobility (μ) of the GZO/Ag/GZO films plotted as a function of the Ag layer thickness for samples (a) without Ge buffer layer and (b) with Ge buffer layer

4.3.4 Optical Characterization

For TCOs, low resistivity usually is a tradeoff for high transparency. Therefore, it is necessary to examine the optical properties of the films. In this section, the optical properties of the films are examined in the ultraviolet-visible (UV-Vis) and near infrared (NIR) ranges. Figure 4.19(a) shows the transmission spectra in the UV-Vis wavelength range for Ag/GZO and Ag/Ge/GZO multilayers. It is observed that with the addition of a thin (0.5 nm) Ge buffer layer, the transmission is generally higher at ~70 % compared to the Ag/GZO samples in the visible region using plain borosilicate glass substrate as a reference. At lower wavelengths close to UV, the transmission of the Ag/GZO films is mainly affected by light absorption due to the interband electronic transition.[244] Silver (Ag) is a metallic layer, so it will have a higher carrier concentration compared to Ge which is a semiconductor. Therefore, Ag/GZO has a much lower transmission in the visible region compared to Ag/Ge/GZO. For the Ag/Ge/GZO, as the thickness of Ag increases, the carrier concentration increases, leading to a slight decrease in transmission in the Ag(10 nm)/Ge/GZO sample as compared to the Ag(1 nm)/Ge/GZO sample. This is similar for the case for GZO/Ag/GZO and GZO/Ag/Ge/GZO multilayers as shown in Figure 4.19(b). Figure 4.20(a) shows the transmission spectra in the NIR region of Ag/GZO and Ag/Ge/GZO. The drastic drop in transmission in Ag/Ge/GZO as compared to Ag/GZO is associated with free carrier absorption, which corresponds to the increase in carrier concentration as seen in Figure 4.17(b), especially as the thickness of Ag layer increases. GZO/Ag/GZO films and GZO/Ag/Ge/GZO films also show a similar trend as shown in Figure 4.20(b).

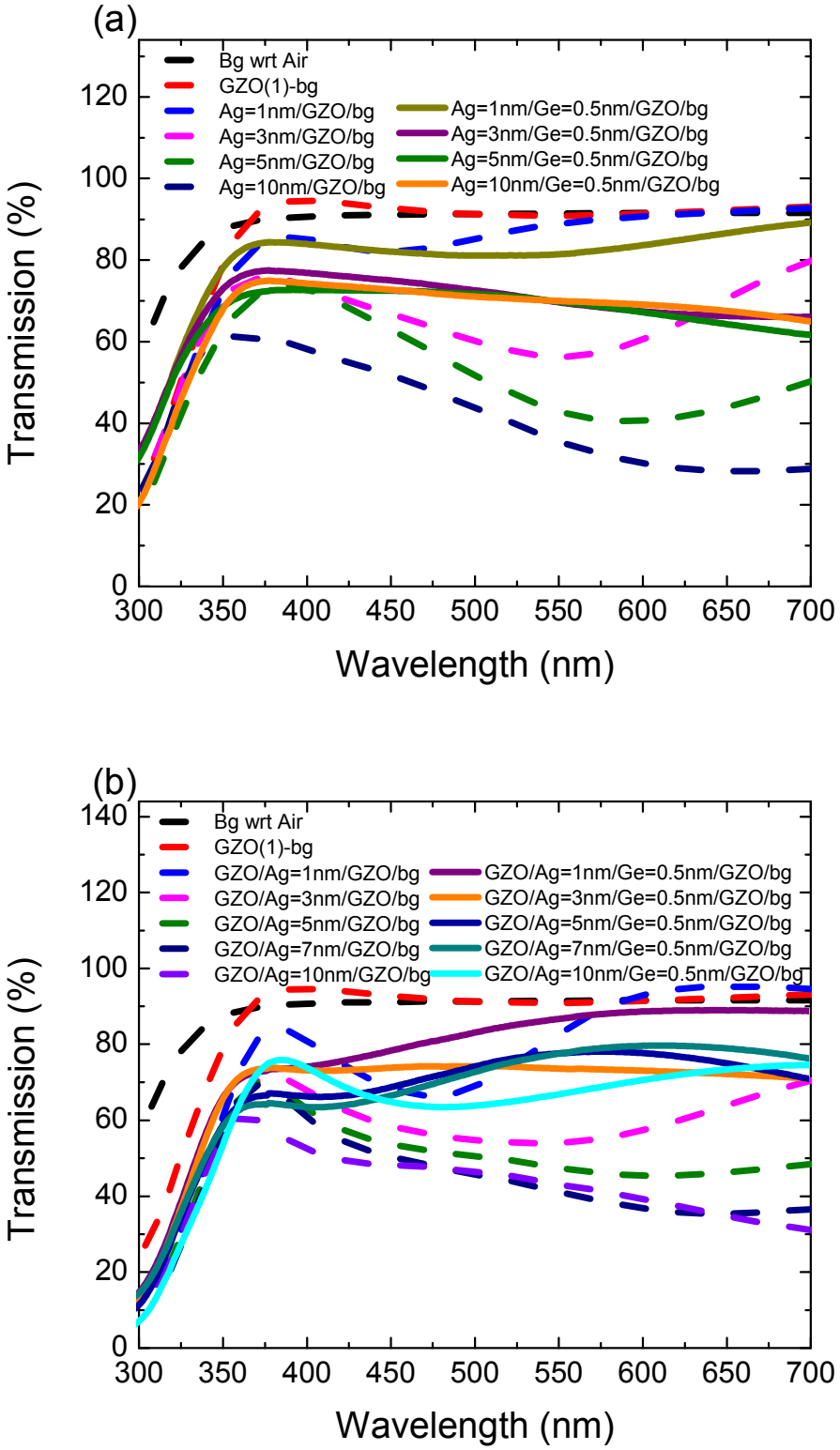

Figure 4.19 Plot of transmission in the UV-Vis region as a function of wavelength for (a) various thicknesses of Ag in Ag/GZO/glass and Ag/Ge/GZO/glass and (b) various thickness of Ag in GZO/Ag/GZO/glass and GZO/Ag/Ge/GZO/glass

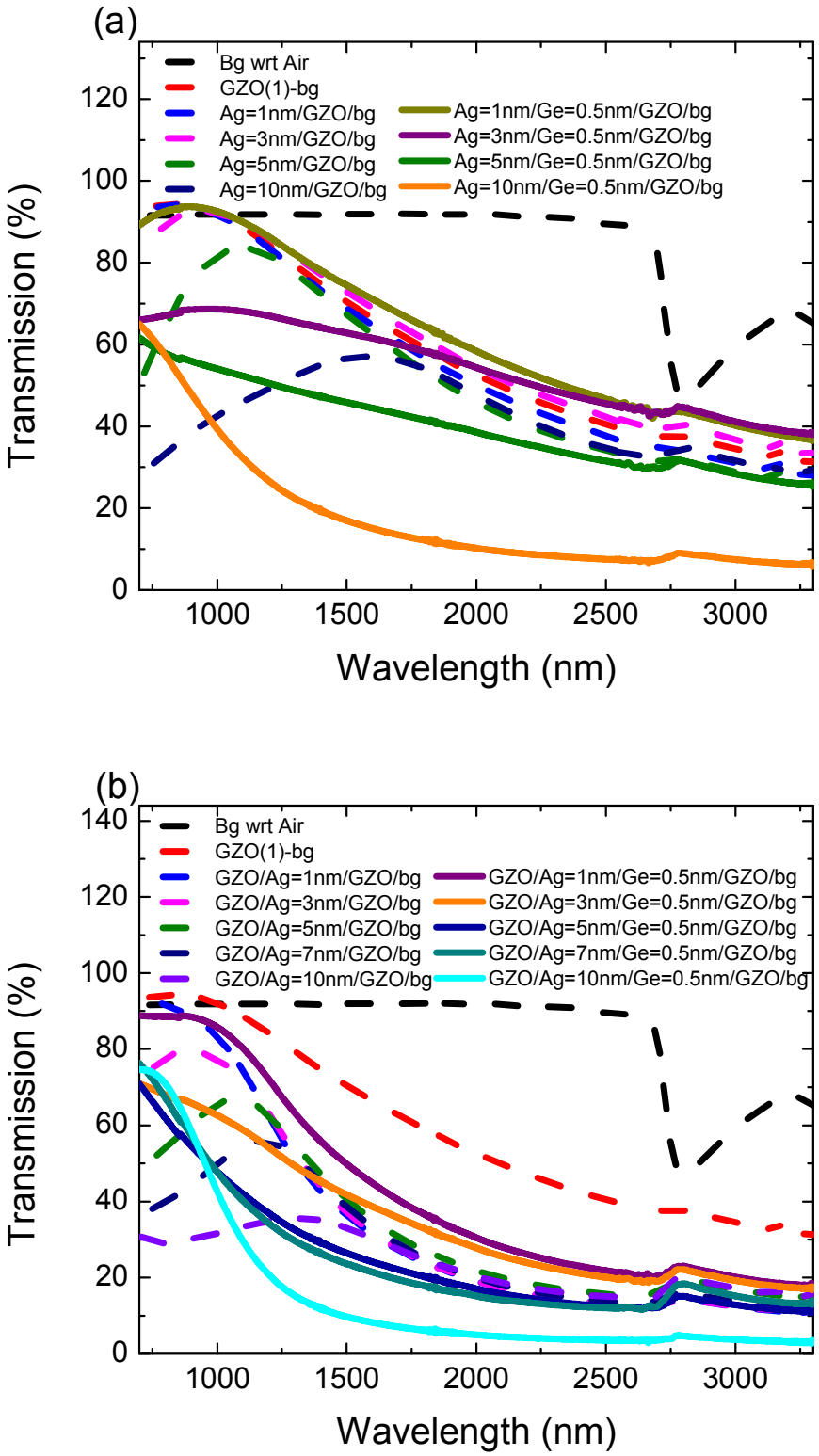

Figure 4.20 Plot of transmission in the NIR region as a function of wavelength for (a) various thicknesses of Ag in Ag/GZO/glass and Ag/Ge/GZO/glass and (b) various thicknesses of Ag in GZO/Ag/GZO/glass and GZO/Ag/Ge/GZO/glass

Figure 4.21 shows the relative reflectance of Ag/GZO and Ag/Ge/GZO films with respect to gold/glass. The artifact peak at around 1350-1450 nm is due to the OH absorbance from the measurement system. For the Ag/GZO film, when the r.m.s. roughness is higher, meaning it has more scattering, the relative reflectance of the film is lower as shown in the Figure 4.21. In addition, lower r.m.s roughness for a thicker Ag layer gives a higher reflectance in the visible and NIR range. The infrared (IR) reflective property of the film is related to the plasma frequency ω_p^2 which has a relation as follows:[253]

$$\omega_p^2 = \frac{nq^2}{\varepsilon_o m_e^*(\varepsilon_\infty - 1) - \left(q / m_e^* \mu\right)^2} \tag{4.4}$$

where n is the carrier concentration, q is the electronic charge, ε_o is the permittivity of free space, $\varepsilon_\infty = 3.85$ is the dielectric constant at very high frequency, $m_e^* = 0.38 m_e$, and μ is carrier mobility. As the thickness of Ag increases in the Ag/Ge/GZO films and GZO/Ag/Ge/GZO films, the carrier mobility and carrier concentration increases, leading to an improvement in the NIR reflectance, according to equation (4.4), of the thin films as shown in Figures 4.21 and 4.22. This finding is in agreement with the results reported by Gong *et al*. [253]

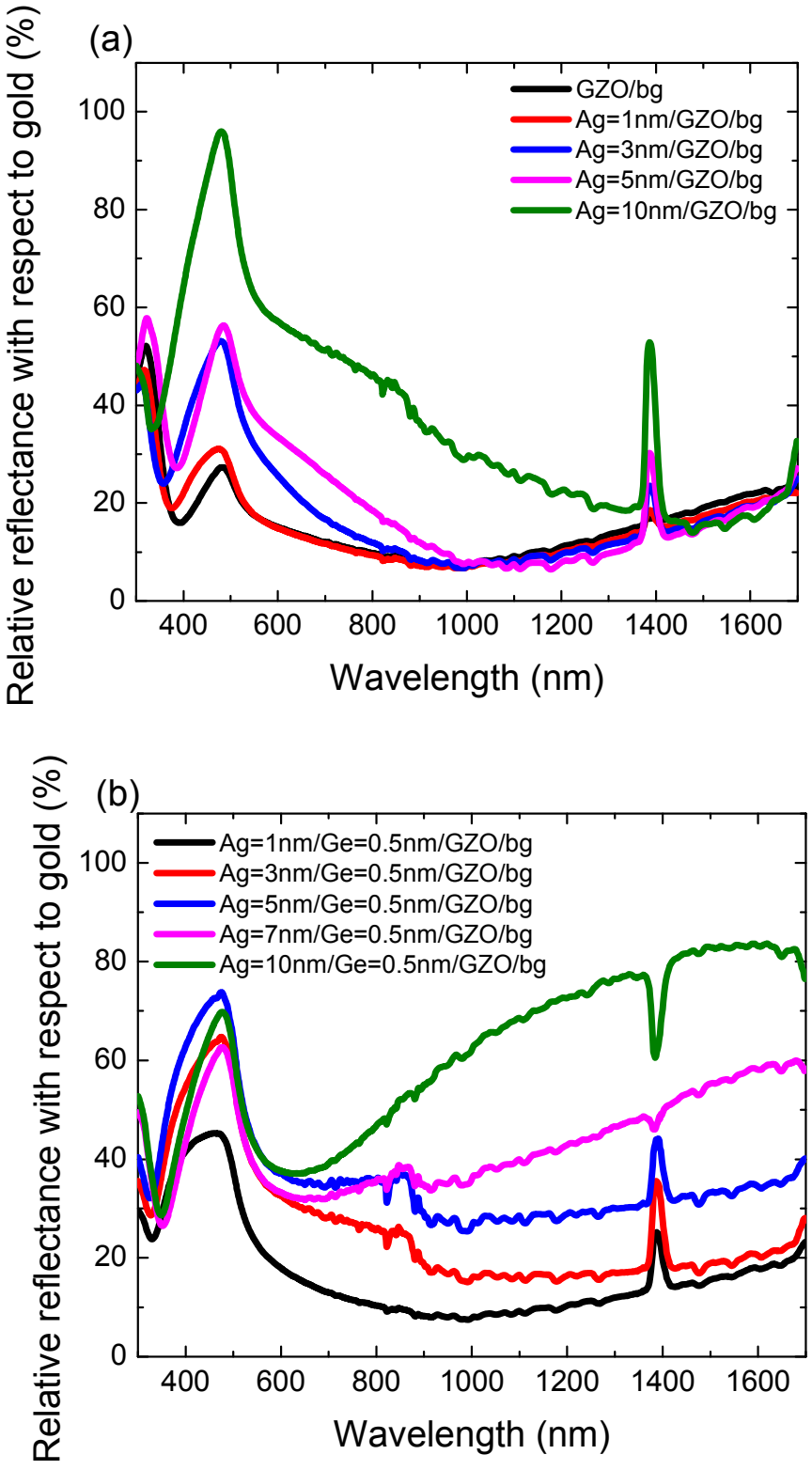

Figure 4.21 Plot of reflectance in the UV-Vis-NIR region as a function of wavelength for various thicknesses of Ag in (a) Ag/GZO/glass and (b) Ag/Ge/GZO/glass

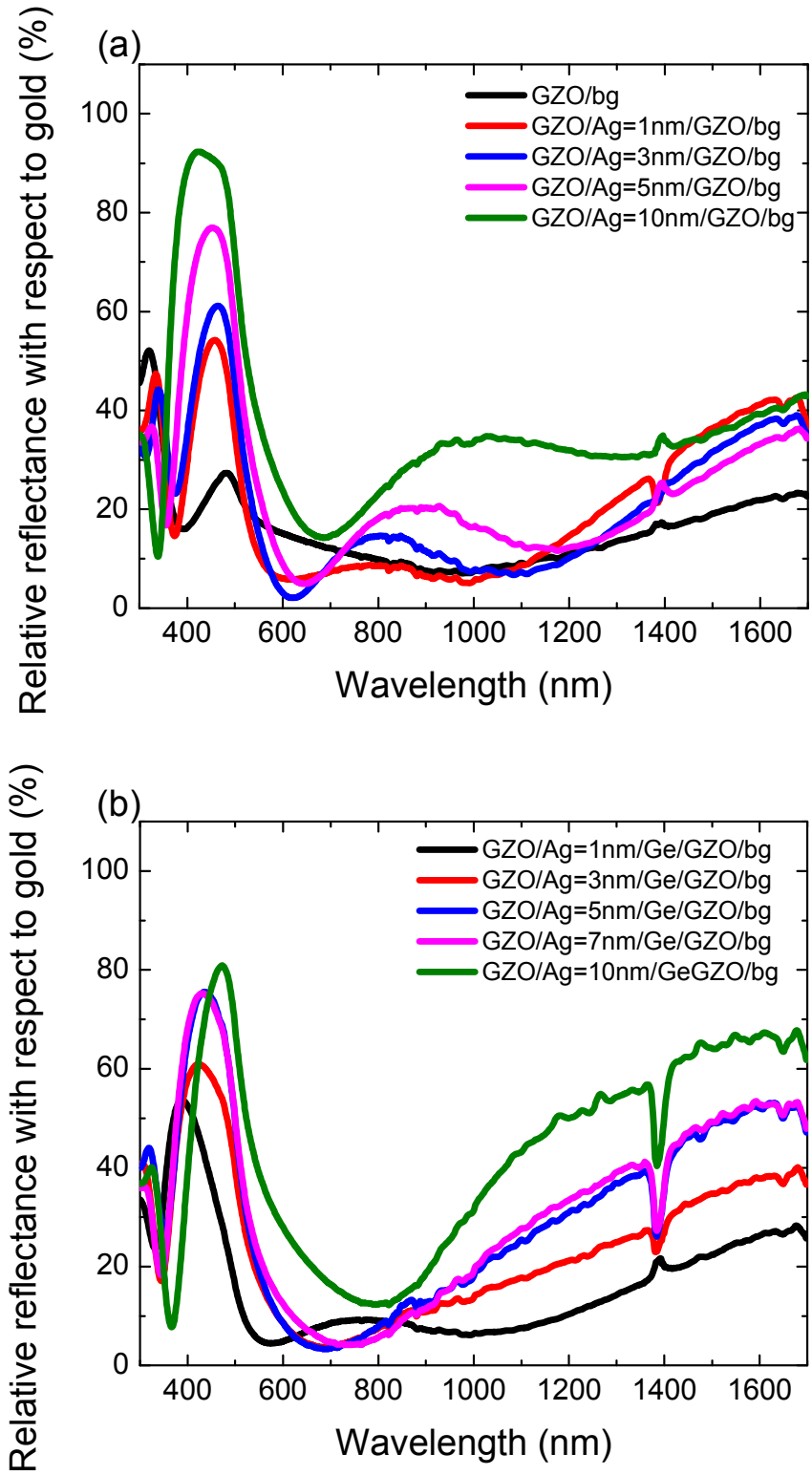

Figure 4.22 Plot of reflectance in the UV-Vis-NIR region as a function of wavelength for various thicknesses of Ag in (a) GZO/Ag/GZO/glass and (b) GZO/Ag/Ge/GZO/glass

4.3.5 Concluding Remarks

High quality transparent conductive Ag/GZO, Ag/Ge/GZO, GZO/Ag/GZO and GZO/Ag/Ge/GZO thin films grown by pulsed laser deposition and e-beam evaporation on low cost borosilicate glass substrate were investigated as a function of thickness of Ag and the addition of a Ge buffer layer. With the addition of a thin (0.5 nm) Ge buffer layer, the surface morphology of Ag/GZO and Ag/Ge/GZO films were improved with lower r.m.s. roughness value for all thicknesses of Ag. In addition, the electrical resistivity has also improved by one order for the Ag/Ge/GZO films and half an order for the GZO/Ag/Ge/GZO films. As the thickness of Ag increases in the Ag/Ge/GZO films and GZO/Ag/Ge/GZO films, the carrier mobility and carrier concentration increase, leading to an improvement in the NIR reflectance. Furthermore, with the addition of Ge buffer layer, there is an increase in transmission to ~70 % in the visible region and there is a drastic decrease in transmission in the NIR region due to free carrier absorption.

Chapter 5 Aluminum-doped zinc oxide (AZO)

Among group III doped zinc oxides, besides GZO, aluminum-doped zinc oxide (AZO) is also another potential candidate for replacing ITO as mentioned in section 2.1. In this chapter, AZO deposited on low-cost borosilicate glass and flexible polyethylene terephthalate (PET) substrates were examined. Multilayers of AZO thin films were also investigated in terms of their electrical and optical properties.

5.1 Introduction

Transparent conducting oxides (TCOs) deposited on polymeric substrates are subjects of extensive research efforts to enable the development of electronic devices for applications in photovoltaics, displays, transistors and electrochromics on flexible substrates.[1,133,254-256] Indium tin oxide (ITO) is currently the most commonly used TCO in many applications of electronic and optical devices.[204,245,246,257,258] However, ITO films need a heat treatment of over 300 °C to achieve the desired high transparency and low resistivity, making it difficult for applications using polymeric-based materials.[31,32] Therefore, there is an urgent need to seek alternative materials that can effectively substitute the use of ITO at lower process temperature to advance the development of electronic or optical devices on plastic substrates which is the future trend of electronics.[29,30,39-42] A lower process temperature also allows for potential usage of TCOs as the top electrode and even the middle electrode of the device, which greatly adds flexibility in the usage of TCOs in polymeric-based devices without possible device degradation due to heat treatment.[1,259]

The development of applications on polymer substrates has many advantages. A typical glass substrate suffers from being brittle, difficulty in deforming and being excessively heavy, especially for large area displays. Hence, glass is unsuitable for applications where flexibility, weight, and safety issues are important such as in touch screens, PDAs (personal digital assistants) and mobile phones. Development of transparent electrodes on flexible plastic substrates provides realistic solutions for a flexible, lightweight, robust and cost-effective starting substrate that can be of great importance to portable, large area or niche devices.[99] Moreover, TCO films on polymer substrates can inherit the numerous merits of the flexible substrates and be used in flexible electronic devices.[92,108]

In the design of a transparent electrode on polymeric substrates using thin film technology, the film thickness of the TCO is of great importance since it is directly related to the strain that it can withstand. Hence, a thinner TCO results in greater flexibility since the critical radius of a thin film is proportional to the film thickness. [260] Unfortunately, it is generally reported that thinner TCOs results in films of lower conductivity.[107] Thus far, it is a challenge to produce thin oxide layers with suitably low resistivity. For example, the lowest resistivity reported for gallium-doped zinc oxide deposited on polyethylene terephthalate (PET) substrates at room temperature is ~7.8×10^{-4} Ω-cm but this is for a relatively thick 800 nm film.[40] However, in order to target smaller critical thicknesses, TCO of less than 100 nm thickness will be beneficial. At such a thickness range, the lowest resistivity is reported by Gadre *et al*. with a value of ~ 4×10^{-3} Ω-cm for a 85 nm thick indium gallium zinc oxide film on polyethylene naphthalate substrates, and this is only achievable after a 150°C post-deposition anneal.[261] The nature of the dependence

of resistivity, or even transparency, on film thickness is not widely reported and it is therefore important to conduct more investigations to understand the dependency. In this study, aluminum doped zinc oxide (AZO) thin films were deposited on polyethylene terephthalate (PET) and borosilicate glass substrates at room temperature using pulsed laser deposition (PLD) without any post high temperature process. The first part of the experiment was to examine the structural, optical and electrical properties of these films as a function of oxygen pressure to optimize the deposited film properties. At the optimized growth condition, the film thicknesses of the deposited AZO film on PET substrates were varied and the effects on resistivity and transparency were discussed.

After examining the single AZO layers, multilayered sandwich structure of AZO were also examined. Unlike the multilayered structures mentioned in section 4.3, the work in this section was focused on the repeated stack of multilayered sandwich with semiconductor/metal/semiconductor structure. Few works have been carried out on investigating the multilayer structure of similar semiconductor/metal/semiconductor sandwich structure.[42,217-219] Therefore, after examining the effect of TCO multilayers, with and without the Ag metal layer, and also the effect of the additional Ge layer in section 4.3, further examination on the electrical and optical properties of these repeated stack of AZO multilayer sandwich structures were carried out.

5.2 Aluminum-Doped Zinc Oxide (AZO) Thin Films

Room temperature deposited AZO thin films grown on PET and borosilicate glass by PLD at various oxygen pressures and various films thicknesses were

investigated here. In the following sections, the growth parameters and results were discussed.

5.2.1 Fabrication of AZO Thin Films

AZO thin were deposited on borosilicate glass and 125 μm thick polymeric PET substrates by the PLD technique using a ZnO:Al (1.5 wt.% Al_2O_3) ceramic target of purity 99.999%. The PLD uses a KrF excimer laser (wavelength λ = 248 nm and 25 ns pulse width) operating at a repetition rate of 20 Hz with a total energy of 300 mJ. The deposition chamber was subsequently evacuated to a base pressure of 1 x 10^{-8} Torr. The target-substrate distance was maintained at 6 cm during the deposition while the oxygen pressure was varied from 2 x 10^{-5} to 1 x 10^{-2} Torr. The entire deposition process was performed at room temperature and typical thickness of the films was about 110 ± 10 nm. In the second part of the experiments, at a chosen oxygen pressure (which gives optimum results), the deposition processes was repeated for different duration to achieve different film thicknesses and investigation on its property dependence with respect to film thickness was performed.

5.2.2 Structural Characterization

Figure 5.1 shows the XRD spectrum of the AZO film on PET substrates obtained under various oxygen pressures and varying film thickness. The most prominent peak of these films is at 34.4° which corresponds to the ZnO (002) diffraction peak (ICDD ZnO pattern 00-036-1451), implying that the films are polycrystalline with a hexagonal wurtzite structure and highly oriented along the c-axis.[103,229] The absence of the crystal phases, such as metallic Zn and Al_2O_3 phase and their compounds in the XRD spectra suggests Al atoms have substituted Zn

in the hexagonal lattice or Al ions may occupy the interstitial sites of ZnO. Using the Scherrer's formula, the calculated grain sizes obtained ranges from 14.6 to 17.6 nm for the various oxygen pressures. A plot of the mobility and overall resistivity for the different calculated grain sizes in Figure 5.2 showed no clear trends. This shows that such small changes in grain sizes may not be significant in affecting the transport properties, and other scattering mechanism (besides grain size) is probably affecting the carrier mobility.

As the thickness increases, the intensity of the peak is higher but there is no obvious peak shift (The peaks shown in the XRD spectrum for various thicknesses are not normalized). These results are similar to those reported by Hao *et al.* for AZO on propylene adipate (PPA) and polyisocyanate (PI) organic substrates.[262] For the small thickness of ~29 nm, there is a small peak of Al_2O_3 at 43.5° which corresponds to the Al_2O_3 (113) peak at 43.4°, perhaps this is reason of higher resistivity for the films as seen in the later section. The XRD peaks show the dominant ZnO (002) peak for all thicknesses, with a difference in intensity due to the differences in thickness. The full width at half maximum (FWHM) of the AZO films decreases as the film thickness increases, implying there is an improvement in the crystallinity. The grain size, as computed from the full width at half maximum (FWHM) of the observed peak, increases slightly from 12.2 nm to 16.8 nm with film thicknesses. A plot of the variation in mobility with grain size is shown in Figure 5.3. Unlike our previous observation at different oxygen pressures (shown again in Figure 5.3 for clarity), the trend of higher mobility for larger grain sizes can be observed for the case of different film thicknesses. Part of the reason may be that once the film growth is optimized in reducing defect related scattering, the effect of grain size can be more easily observed.

On closer examination, it is noted that the larger improvements in mobility is observed when the film thickness is increased from <50 nm to 100 nm. When film thicknesses are comparable to grain sizes, film thickness may perhaps affect the growth of the grains which is shown in this finding that the thinnest sample has a much smaller grain size compared to the thicker samples. From the XRD results on grain size, the grain size of the >100 nm thick films saturate to about 16 nm as the film thickness increases. The increase in film thickness showed substantial increase in carrier concentration and mobility (Figure 5.12(b)). If such variation of grain sizes is not responsible as was discussed, additional mechanisms are needed to account for the observations.

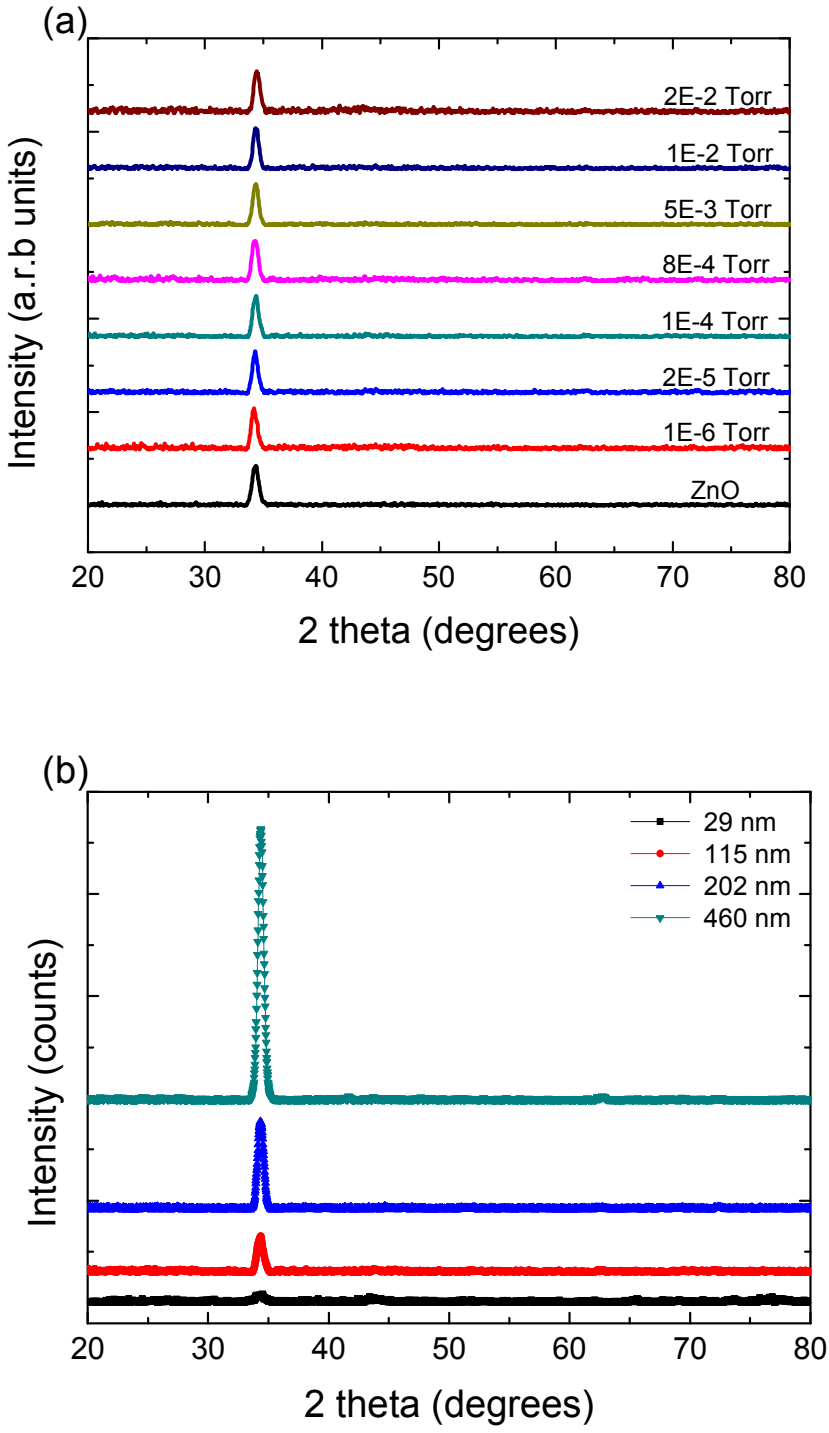

Figure 5.1 X-ray diffraction spectra of AZO thin films deposited on PET substrates at room temperature for various (a) oxygen pressures and (b) film thicknesses

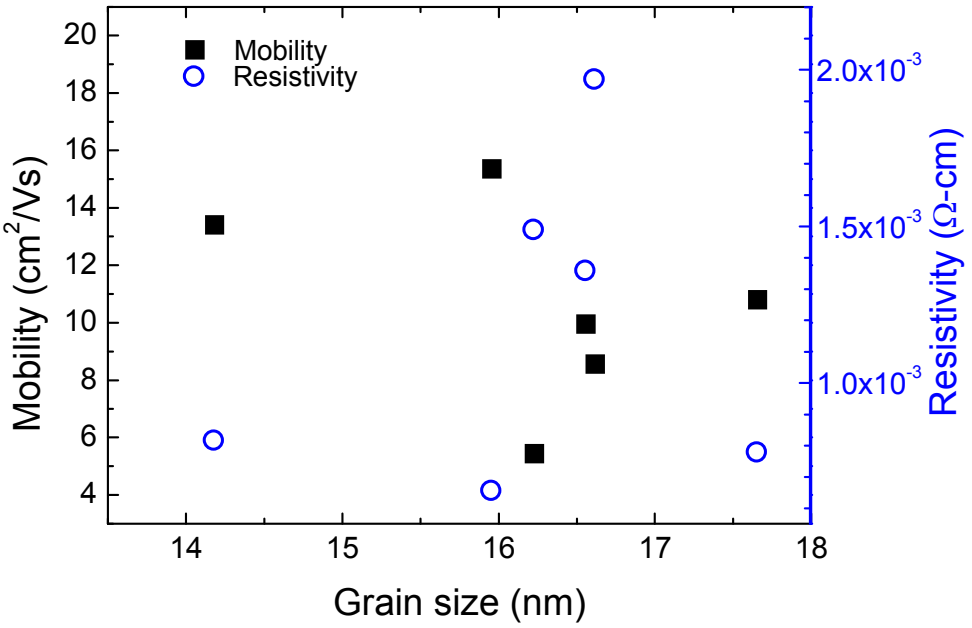

Figure 5.2 Plot of spread in mobility and resistivity for different grain sizes for the AZO/PET substrates. The thin films were deposited at various oxygen pressures at room temperature

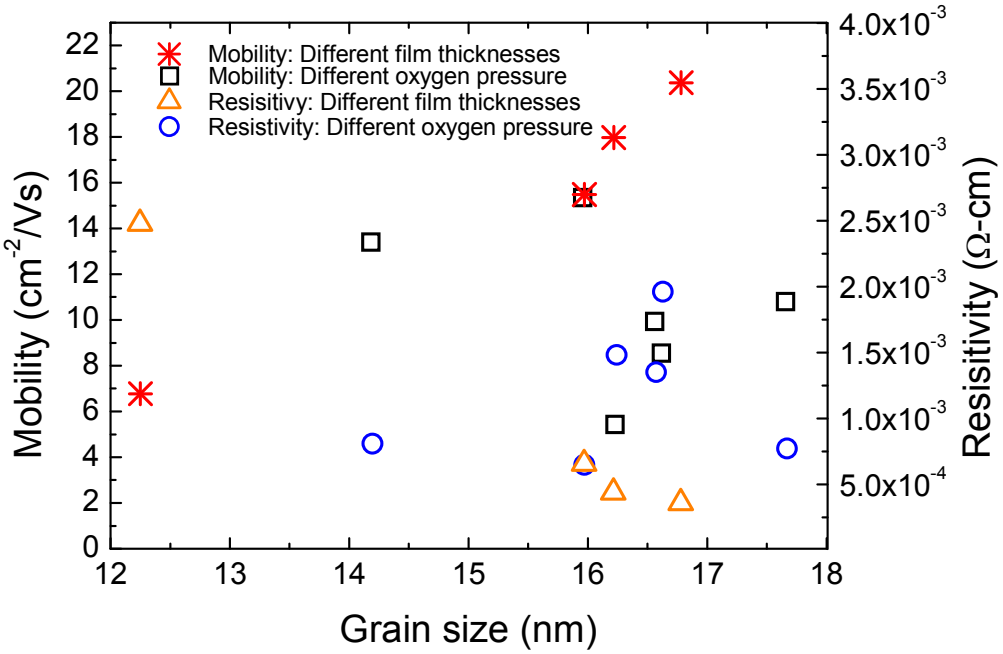

Figure 5.3 Plot of spread in mobility and resistivity for different film thicknesses deposited at an optimized oxygen pressure. Included in the plot are values of mobilities and resistivities at various grain sizes for thin films deposited under non-optimized conditions

5.2.3 Optical Properties

For TCOs, high transmittance in the desired spectral region is a crucial requirement. For example, as a contact electrode in LEDS, high transmittance is needed at least in the visible region while for photovoltaics application, the desired high transmittance is preferred across the entire solar spectrum. Therefore, there is a need to examine the optical properties of the TCO (AZO in this case) thin films. Figure 5.4 shows the transmission plots of the AZO film on PET substrate as a function of (a) varying oxygen pressure and (b) varying film thicknesses. The transmission plots of uncoated PET substrate and undoped ZnO film were also included for comparison. For the undoped ZnO, in the near infrared region, the transmission is much higher than the doped AZO as there is less free carrier absorption (carrier concentration of ZnO is 3.9×10^{19} cm^{-3}) compared to $\sim 10^{20}$ cm^{-3} for all doped AZO films. It was also observed that as the oxygen pressure decreases to 1×10^{-4} Torr, there is an increasing trend in the carrier concentration due to free carrier absorption, which is shown in Figure 5.4(a).[263] Due to this inverse relationship between resistivity and transparency, there is a strong need to optimize both these properties of AZO. In Figure 5.4(b), thicker films do have a lower transmission in the visible range and near infra-red range which is expected. In the short wavelength infra-red range (1.4 - 3 μm), the transmission of the film drastically decreases to less than 20 %, especially for the 463 nm case which has a trend which looks similar to that the GZO multilayer structure as mentioned in section 4.3.3. However, it is noted that the GZO multilayer structure has a better tuneable control on the transparency in the NIR and short wavelength infra-red ranges compared to the single thick doped ZnO film. Moreover, thick doped ZnO films not only use more

material and require longer deposition time, they also have a lower critical strain tolerance.[260]

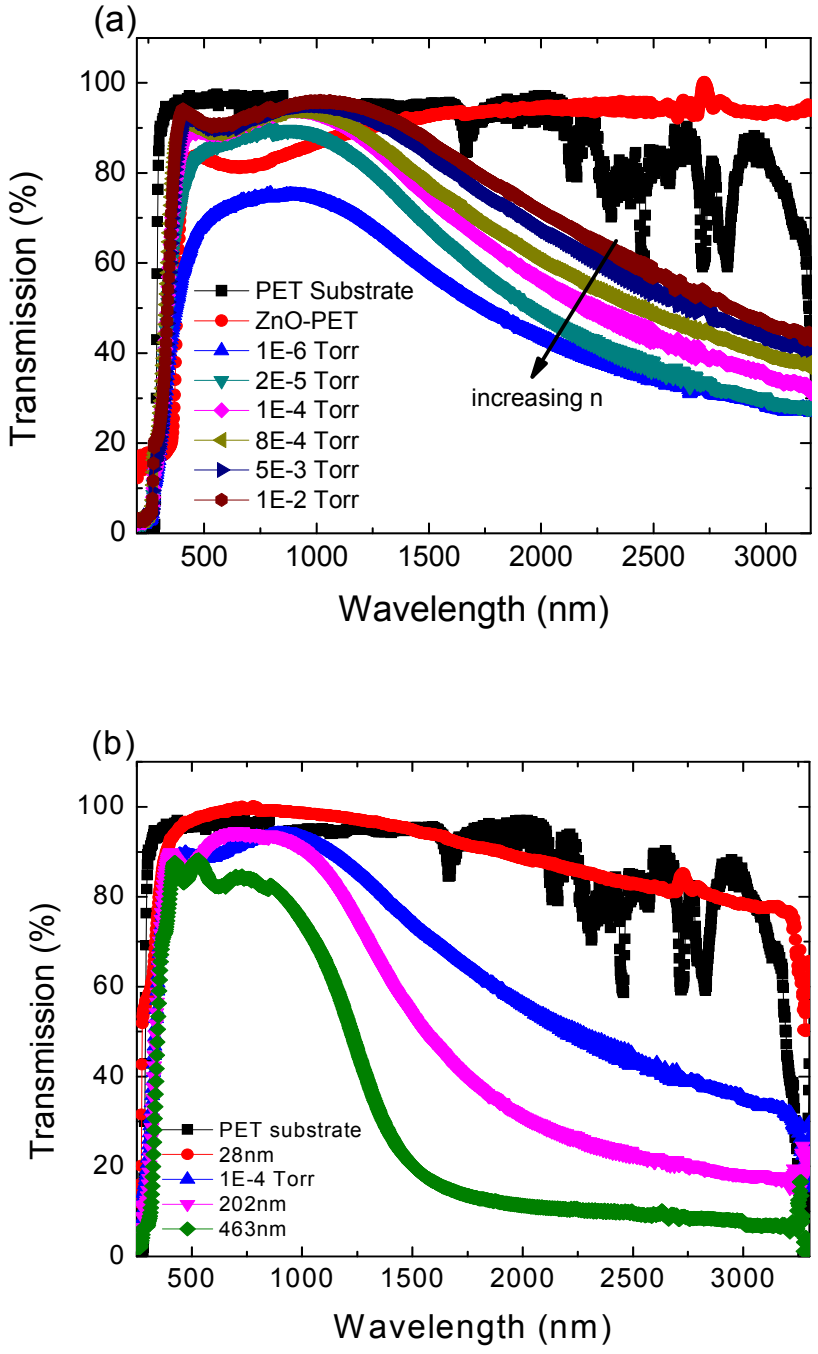

Figure 5.4 Transmission plots of AZO thin films as a function of (a) varying oxygen pressure and (b) varying film thicknesses

A summary of the optical properties, together with the measured resistivity of AZO films deposited at room temperature, is shown in Figure 5.5. The plot shows the measured resistivities and normalized transparency indices at different oxygen pressures. The normalized transparency indices represent the fraction of transmission at various indicated spectral ranges after accounting for variations in film thickness. An arbitrary normalization thickness of 100 nm was selected and the absorption coefficient was obtained from the transmittance at different wavelengths. Details of the calculation are reported in section 4.2.5. Thickness normalization in this aspect is critical to understand the optical properties of the film itself. Different thicknesses give variations in transmittance and this should be corrected in order to understand the film properties at each deposition condition. The use of the normalized index can also be useful for applications in different devices and separation into different wavelength regions can help the understanding of film properties.[238] Figure 5.5 shows that for the visible wavelength range, an oxygen pressure of above 10^{-5} Torr will be sufficient to result in a film with transmittance of greater than 80 %, with the transmittance saturating at higher oxygen pressure. The overall normalized transparency appears to gradually increase with oxygen pressure, with a high transmittance of ~90 % at oxygen pressures of 10^{-4} Torr or larger. The corresponding resistivity, however, shows optimum values in the mid-oxygen pressure regime, with higher resistivities measured at both lower and higher oxygen pressures. The large decrease in carrier concentration should increase the infrared transmittance and our transparency index in the infrared range, shown in Figure 5.5, agrees with this interpretation. The smaller increase, or similar overall transparency, can be explained by the accompanying reduction of transmittance in the ultra-violet region by variation of the band gap through the Burstein Moss effect. This competing factor can be shown by

examination of the measured band gap variations. The band gap (E_g) of the AZO film on PET substrate is found using the method mentioned in section 2.1.4. Figure 5.6 shows the plot of $(\alpha h\upsilon)^2$ and photon energy ($h\upsilon$), which yields an optical E_g ranging from ~3.49 to 3.7 eV. Since there is no observation of any significant structural variations from the XRD (see Figure 5.1(a)), the effective change in band gap is likely related to the attenuation in electron density. As band gap is related to the optical absorption in the electronic band structure, when the carrier concentration increases and with the filling of electrons at the lower band region (Burstein Moss effect), the electrons have to move to a higher band region, leading to an effective change in band gap. Figure 5.7 shows the plot of 2/3 power of carrier concentration as a function of a change in the optical band gap according to equation (2.18), where the optical band gap of 3.29 eV used was measured from our undoped ZnO film as the reference. The good linear relationship through the origin observed from the plot shows that the variation in the band gap can indeed be attributed to the Burstein effect.[116] There is therefore a decrease in transparency in the UV region when the oxygen pressure is increased as the carrier concentration is lowered.

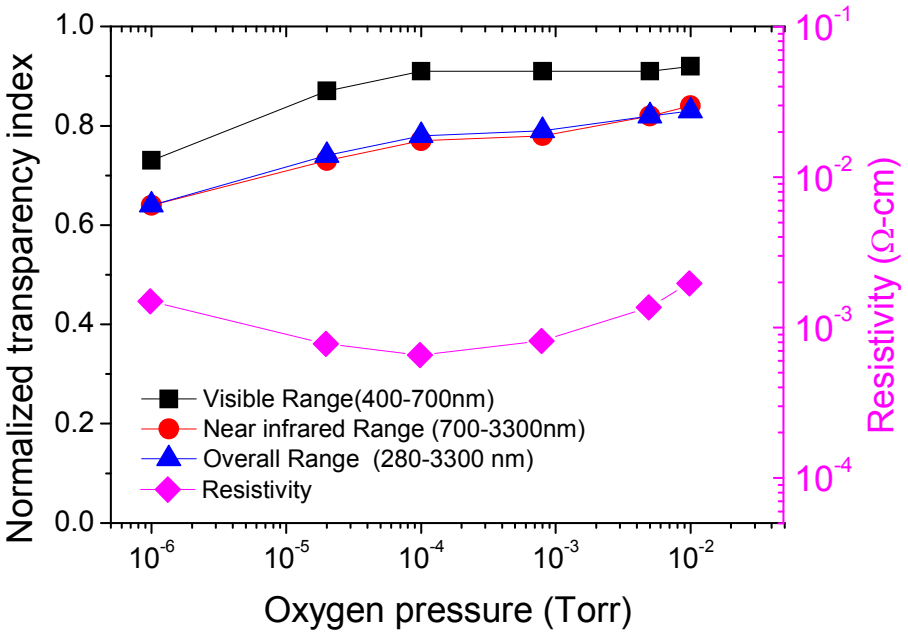

Figure 5.5 Normalized transparency index of AZO films at different indicated wavelength ranges as a function of oxygen pressure during deposition at room temperature. The corresponding measured resistivities of the films are also included

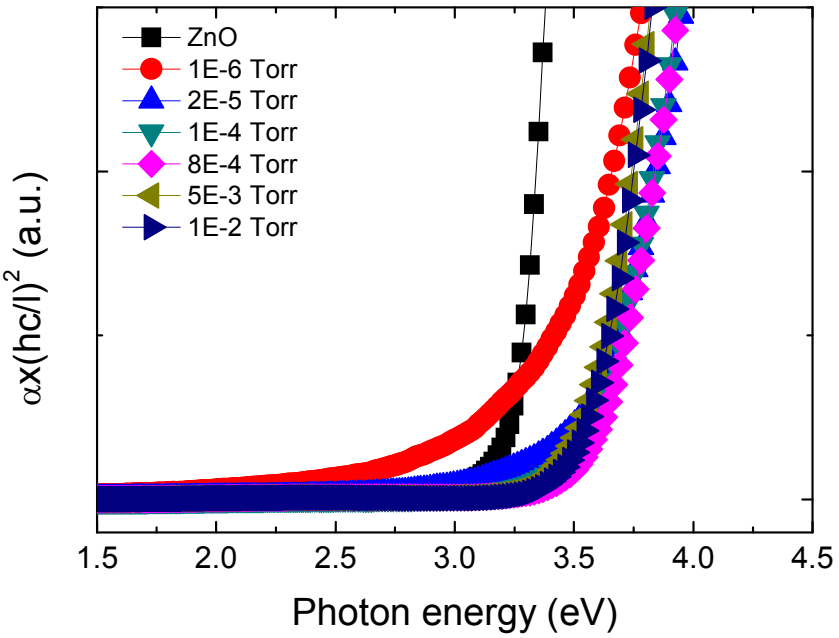

Figure 5.6 Plot of $(\alpha E)^2$ as a function of photon energy for AZO films deposited at different oxygen pressures (room temperature)

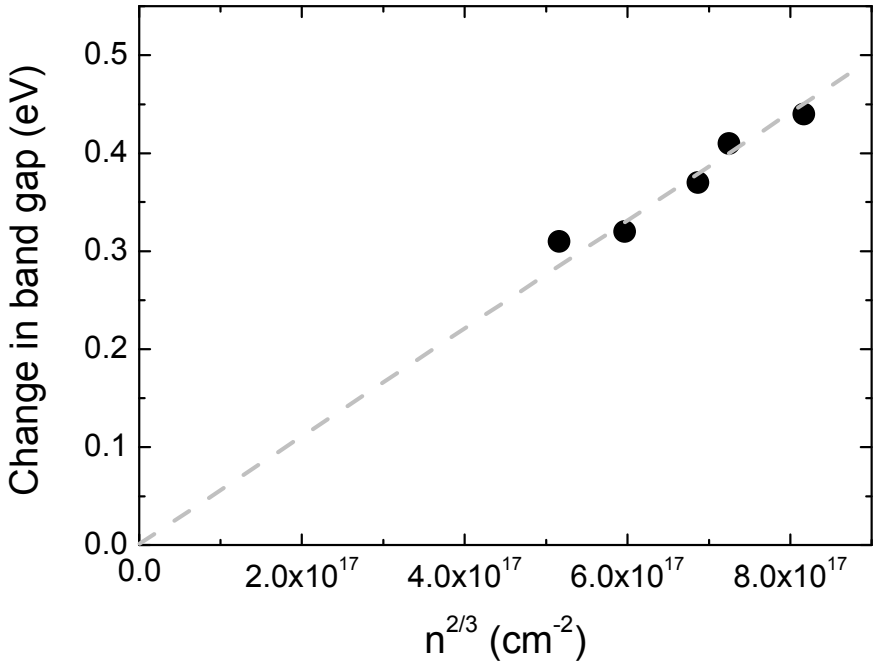

Figure 5.7 Variation of the optical band gap plotted against the 2/3 power of carrier concentration ($n^{2/3}$). Dotted line shows the best fit data through the origin

Since refractive index and extinction coefficient are important optical parameters as mentioned in section 2.1.4, these properties of the AZO thin films were also examined using VASE. The refractive index and extinction coefficient of AZO thin films were measured and shown in Figures 5.8(a) and 5.8(b). A refractive index of ~1.75 at a wavelength of 600 nm was obtained which is similar to a commercial 733 nm thick AZO coating obtained by magnetron sputtering on glass with refractive index of ~1.86.[264] For comparison, the refractive index and extinction coefficient of ITO films were also provided in Figures 5.9(a) and 5.9(b). At 600 nm wavelength, the ITO film also has a similar refractive index as the AZO film of ~1.76. This means the AZO film can serve as a potential electrode alternative to replace ITO in light emitting as well as light absorbing applications.[265]

Shown in Figure 5.10, as the film thickness increases from 29 nm to 460 nm, the optical band gap increases from ~3.38 to 3.75 eV. As the optical band gap increases with an increase in carrier concentration (Figure 5.12(b)), therefore our AZO films followed the expected prediction of equation (2.18) mentioned in section 2.1.5. The transparency of the films at different thicknesses is also compared after normalization, as similarly shown in Figure 5.11. The normalization ensures that one is primarily comparing film properties. Expectedly, there are not much changes in the transparency indices as observed since the films are grown under the same condition. The visible transparency shows comparable values while the decrease in the infrared transmittance is due to the decrease in mobile carriers as discussed above. From these observations, one can conclude that optical properties of the films in the visible range are not greatly affected by different thicknesses. Decreasing transparency is a direct result of thickness dependent absorption and not a reflection of true optical property changes.

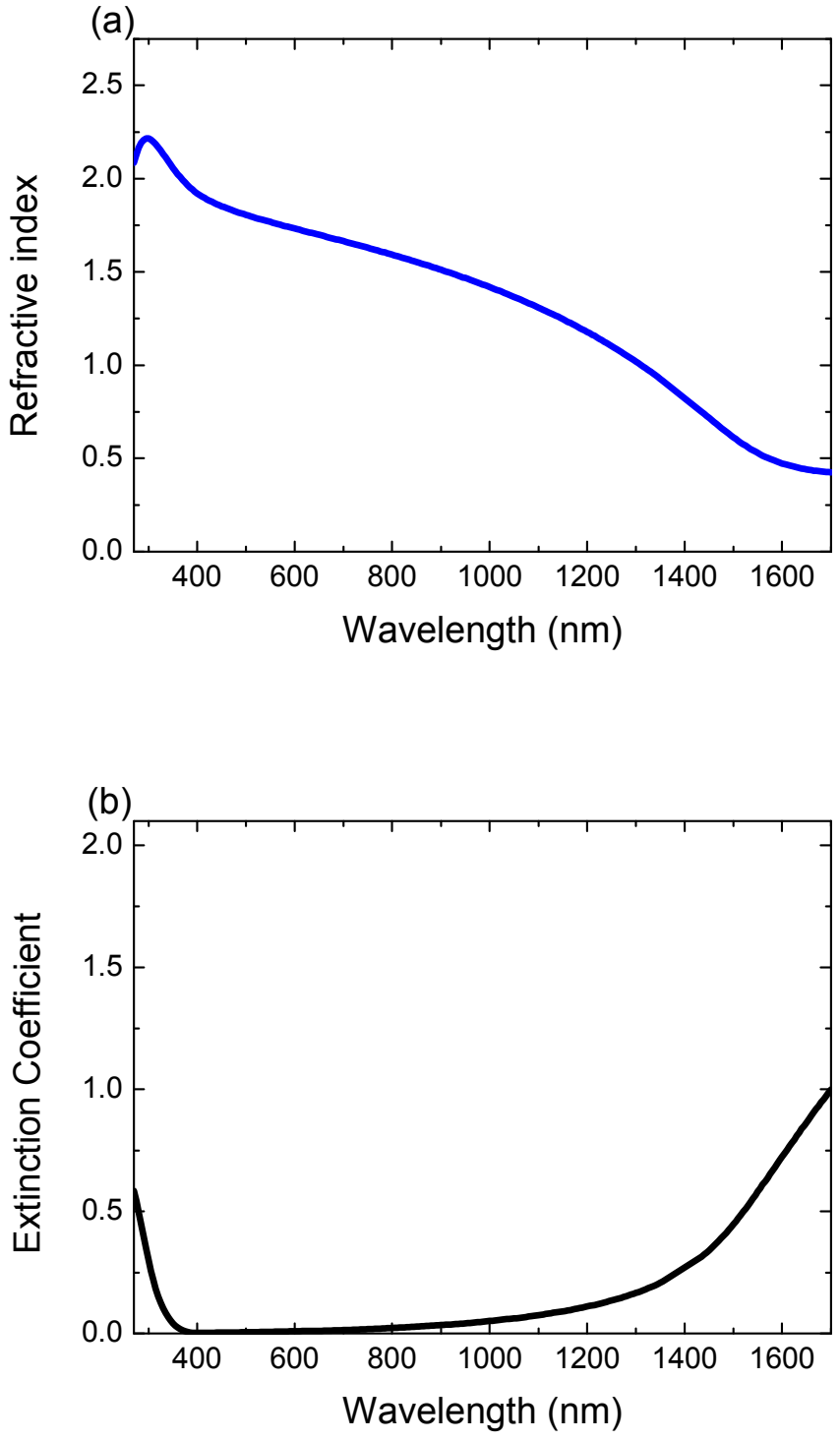

Figure 5.8 (a) Refractive index and (b) extinction coefficient of AZO on glass (115 nm thickness) as a function of wavelength

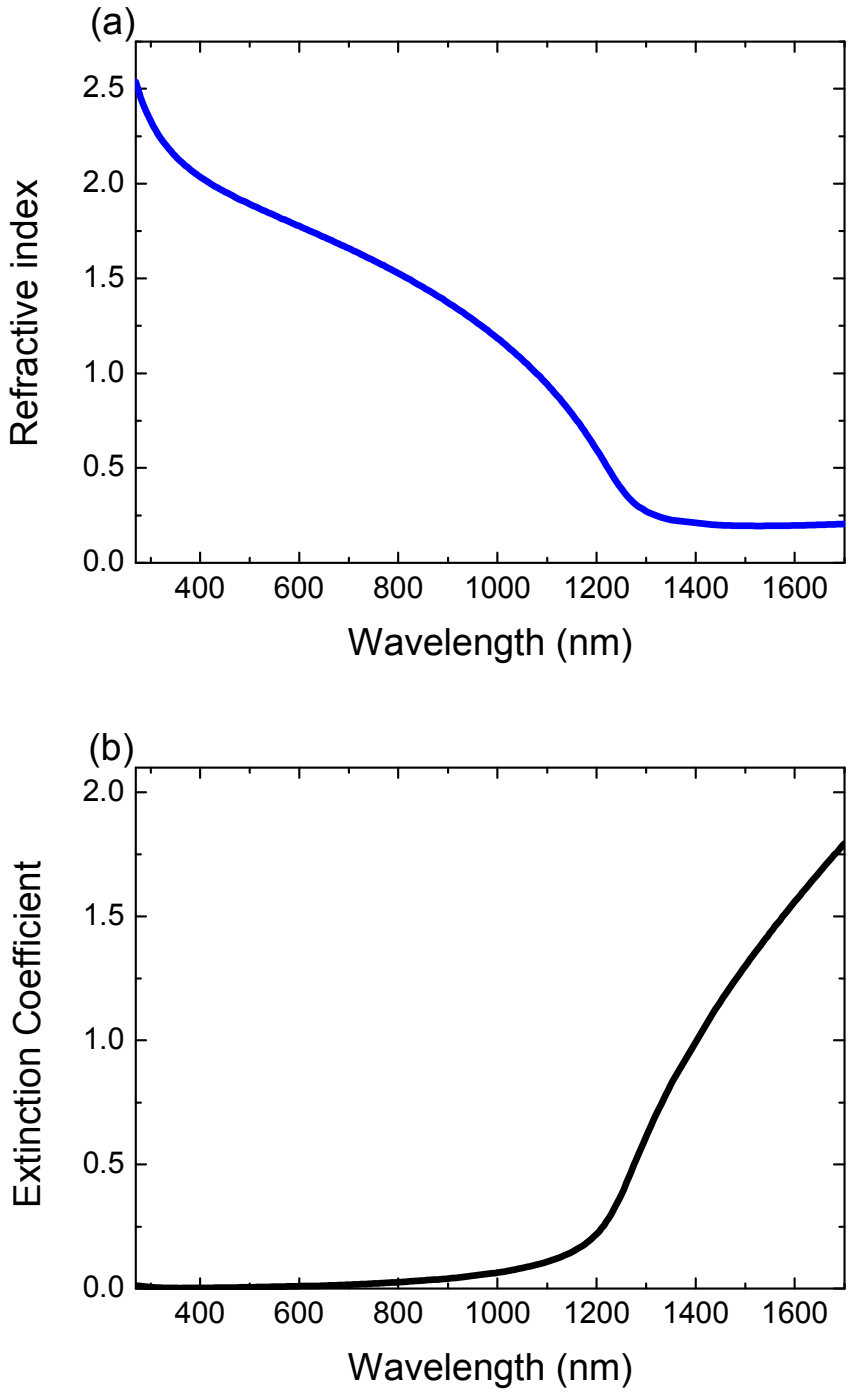

Figure 5.9 (a) Refractive index and (b) extinction coefficient of ITO on glass as a function of wavelength

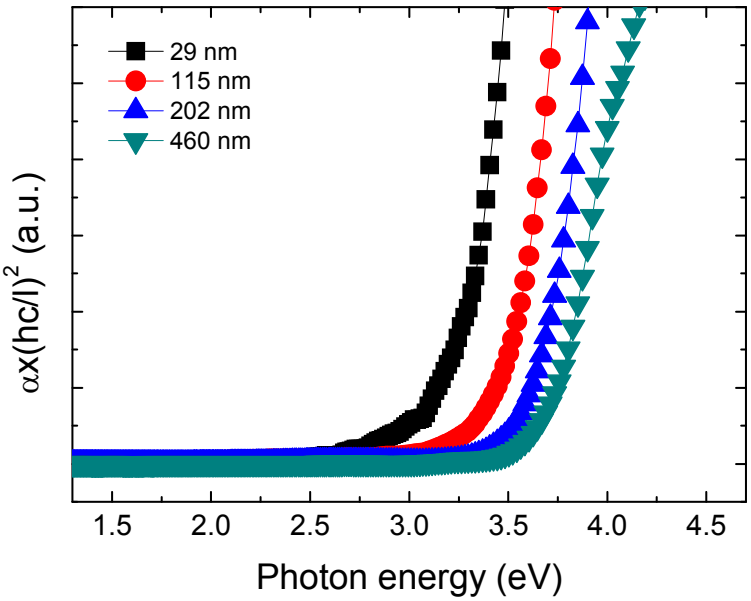

Figure 5.10 Plot of $(\alpha E)^2$ as a function of photon energy for AZO films deposited at different various film thicknesses (oxygen pressure of 1×10^{-4} Torr)

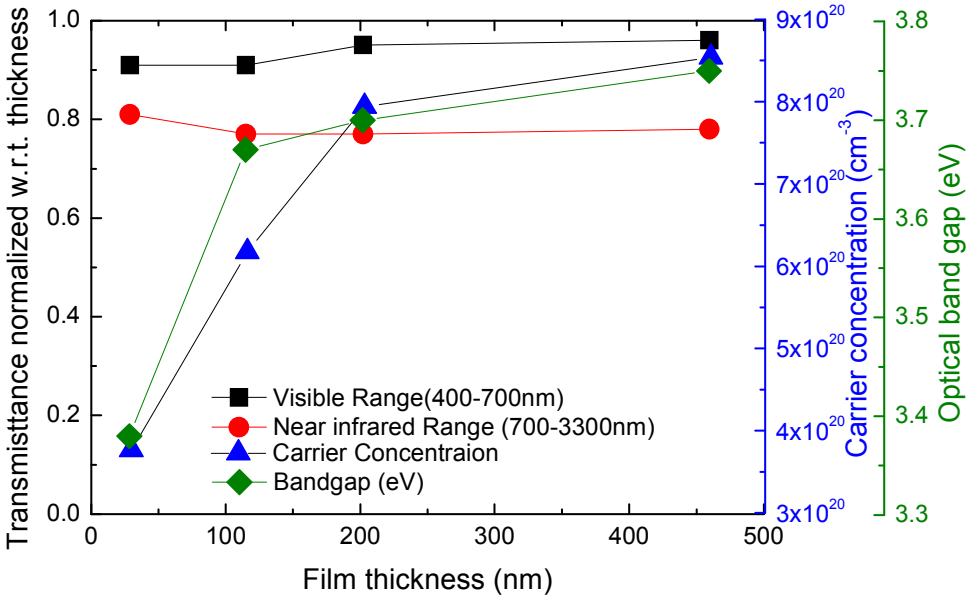

Figure 5.11 Normalized transparency index at different wavelength ranges as a function of film thickness for films deposited at an oxygen pressure of 1×10^{-4} Torr at room temperature. Also included are the corresponding carrier concentration and optical band gap of the AZO films

5.2.4 Electrical Properties

As seen in equation (2.1), to obtain low resistivity, high carrier concentration and high mobility of free carriers have to be achieved.[135] Figures 5.12(a) and 5.12(b) show the variation of resistivity, Hall mobility and carrier density as a function of oxygen pressure and AZO film thickness respectively. As oxygen pressure increases from 1×10^{-6} Torr to 1×10^{-4} Torr, the improvement (decrease) in resistivity for lower oxygen partial pressure can be observed to be due to the significant increase in carrier mobility. This can be due to a reduction in deep-level defects that can improve the carrier mobility by reducing scattering. This agrees with the concomitant improvements in transparency since a reduction of these defects will improve transmittance in the visible range and this is similarly observed in Figure 5.5. This also means that, while defect scattering is dominant, grain boundary scattering may play a less significant role as was discussed before. Kim *et al.* observed a similar trend of a decrease in carrier concentration and increase in mobility with increasing oxygen pressure for AZO film deposited at room temperature. They associated this decrease in resistivity to a reduction in oxygen deficiencies, which consequently reduce the mobility of carriers.[214] The large increase in resistivity at higher oxygen partial pressures (greater than 1×10^{-4} Torr) in Figure 5.12(a) can be attributed to both a decrease in carrier concentration and mobility. This is likely due to the fact that at higher oxygen pressure, there is an increase in oxygen interstitials which acts as electron trapping centres and increases ionized scattering, giving a higher resistivity.[214] However, Lorenz *et. al.* associated this phenomenon to the increase in oxygen corporation and compensation of carriers when the oxygen pressure increases. [266] All these results suggest that the electrical property of AZO is highly related to the oxygen content[238], which is in agreement with the first principles calculations

by Medvedeva *et al.* demonstrating that oxygen vacancies greatly affect the conductivity of GZO films.[202] Therefore, at higher oxygen pressure, which also corresponds to an increase in oxygen content and excessive scattering, it is likely to result in a decrease in oxygen vacancies, hence leading to a high resistivity.

Thicker films give a lower resistivity as seen in Figure 5.12(b), which is in good agreement with the observations by Dong *et al.* who reported on AZO films deposited on glass at different thicknesses.[267] This is likely associated with the better crystallinity for thicker films as seen from the XRD spectra in Figure 5.1(b). The improvements in the electrical properties of the films can be suitably explained by the influence from surface and interface effects. It is noted that the large increase in carrier concentration similarly affects the measured optical band gap as it is reduced from ~3.75 to 3.38 eV as shown in a summary plot in Figure 5.11. This is similar to a Burstein-Moss effect, which is well demonstrated by the same increase of carrier concentration. Since the films are deposited using the same condition, little changes in the bulk film was expected. Therefore, the changes can be attributed to surface and near surface carrier depletion that is much more pronounced for thinner films. This depletion reduces the effective mobile carrier concentration and the resulting space charges that form increases ionized impurity scattering and this can reduce the carrier mobility in the TCO. This hypothesis then describes well the observed saturation of both the increase in carrier concentration and mobility once larger film thicknesses are achieved, since bulk effects are likely to dominate.

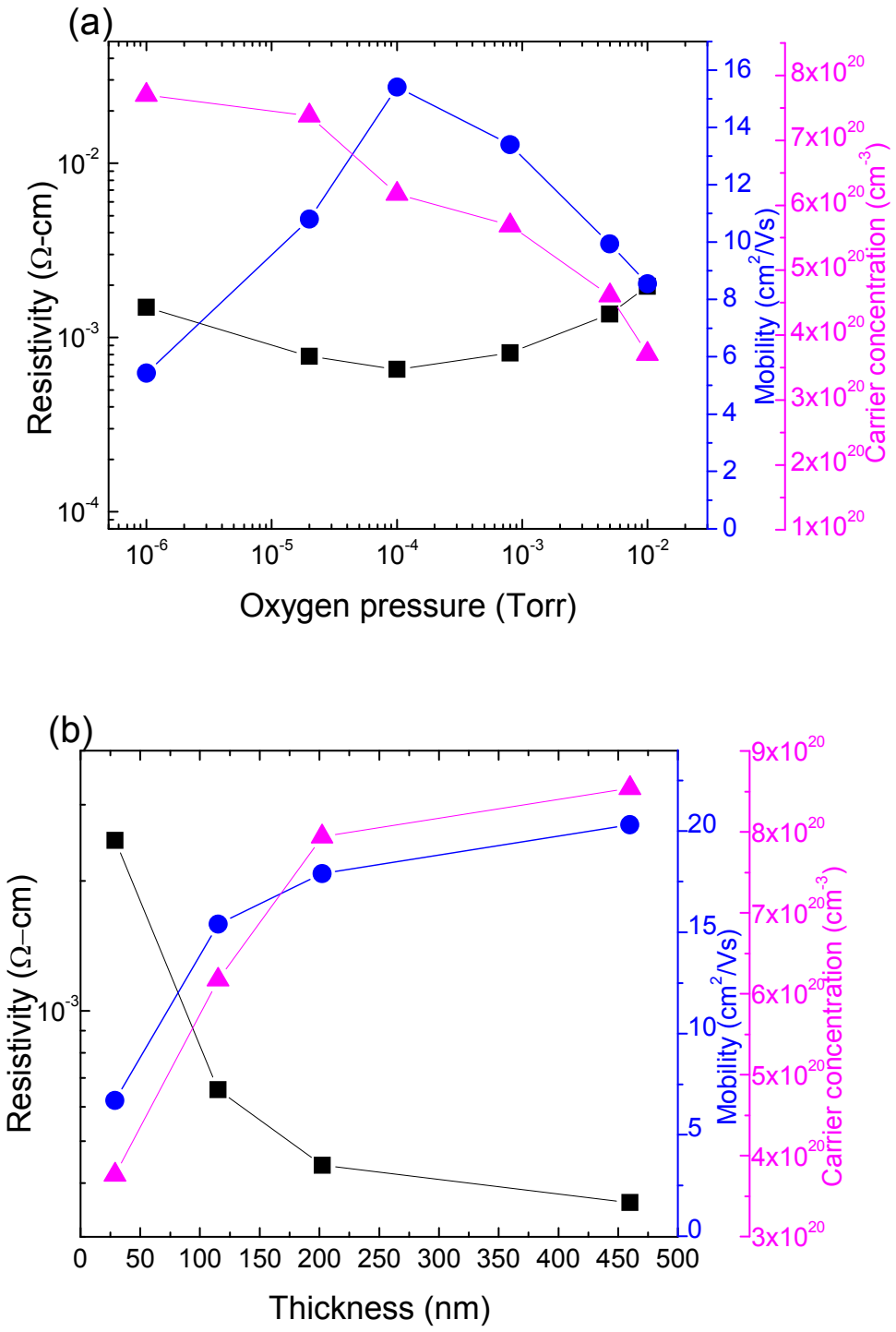

Figure 5.12 Electrical resistivity (ρ), carrier concentration (n), and Hall mobility (μ) of the AZO films plotted as a function of (a) oxygen pressure during deposition at room temperature and (b) film thickness for films deposited at an optimized oxygen pressure of 1×10^{-4} Torr at room temperature

The transparency and resistivity, as discussed in the previous section, show that multiple reasons can simultaneously account for the change in these two properties and, apart from those already mentioned, the effect of film thickness is not well understood. To investigate this effect, deposition of AZO films of different thickness on PET substrates were performed at our optimum oxygen pressure at room temperature. The optimization was selected using a modified figure-of-merit (FOM) to better assess our deposited thin films. Haacke *et. al.* introduced a FOM (φ_{TC}) for transparent conductors defined as [268]

$$\varphi_{TC} = T^{10} / R_{sh} \tag{5.1}$$

where T is the transmittance at peak value and R_{sh} is the sheet resistance. A larger figure-of-merit (FOM) therefore represents a better TCO. Using equation (5.1), the computed figure-of-merit (FOM) of our deposited films used is shown in Table 5-1. However, the Haacke's FOM uses the peak value of transmission that may not be representative of the overall transmission. In this work, the normalized transparency index (TI) was used in a modified figure-of-merit (FOM_{TI}) to give a more complete analysis. Not only does this normalization take into account transparency across a suitable spectral range, this transparency index is free of influence from any thickness variations. Our approach is more suitable if the FOM is to be used to compare across the variations in oxygen pressure since one desires that any changes in transparency to accurately reflect the true changes in film properties. Using the modified FOM as a comparison, it was concluded that an oxygen pressure of 1 x 10^{-4} Torr gives the best overall AZO properties in this setup.

Even though the above discussion highlighted that the inherent transparency does not vary significantly for the TCO, expected thickness dependent absorption still

plays a role even for materials with low absorption coefficients or long attenuation lengths. Optimization of the TCO should therefore involve the optimization of the resistivity for the lowest possible film thickness as cost and deposition time might pose drawback. The obtained resistivity variations in this work were summarized with those that were reported in the literature as shown in Figure 5.13. The general trend of the variation in resistivity with film thickness agrees with the findings from this study. For optimization of AZO thickness, one must consider the grain size restriction at different thicknesses as for thinner thickness, the grain size is smaller compared to thicker samples. This might imply that there is a higher likelihood for grain boundary scattering in thinner samples. Small thicknesses of AZO films with low resistivity are achieved here with room temperature deposition which is highly desired by using AZO as the top electrode. This means that suitable grain sizes can be achieved with thinner films of <100 nm. Compared to a thicker film, surface/interface depletion and scattering effects are likely more dominant in a thinner film when the potential scattering thickness should not change much. At such conditions, surface/interface depletion and scattering effects play an important role, meaning that the optimum thickness for thin films with small grain sizes are restricted by a more general limit. Considering the thickness dependent attenuation, there should be an upper limit in terms of optimization of film thickness. Naturally, if annealing is involved and grain sizes are increased, this general limit will no longer hold. We also highlight that the obtained resistivity in this work show excellent resistivity values for ZnO deposited on PET substrates and this is shown in Figure 5.13. Unlike some of the data shown in the same plot, our highly conducting TCO is notably achieved at room temperature through the optimization of growth conditions, and this finding holds great promise for applications in flexible organic devices.

Table 5.1 Figure of merit and modified figure of merit for AZO samples at various oxygen pressure (indicated in Torr) and thickness (indicated in nm). The transparency indices are also shown for comparison

Sample	Peak Transmission (T^{10})	Normalized Transparency index (TI) at 280 - 3300 nm	Sheet Resistance, R_{sh} (Ω/□)	Haacke's Figure of merit, FOM (Ω^{-1})	Modified figure of merit, FOM_{TI} (Ω^{-1})
Undoped ZnO	1.92	0.85	694.6	2.77×10^{-3}	1.23×10^{-3}
1×10^{-6} Torr	0.06	0.64	128.4	4.63×10^{-4}	4.96×10^{-3}
2×10^{-5} Torr	0.35	0.74	65.8	5.34×10^{-3}	1.12×10^{-2}
1×10^{-4} Torr	0.54	0.78	57.1	9.51×10^{-3}	1.37×10^{-2}
8×10^{-4} Torr	0.54	0.79	76.0	7.09×10^{-3}	1.04×10^{-2}
5×10^{-3} Torr	0.60	0.82	130.3	4.62×10^{-3}	6.27×10^{-3}
1×10^{-2} Torr	0.66	0.83	196.8	3.37×10^{-3}	4.22×10^{-3}
29 nm	1.02	0.80	860.1	1.18×10^{-3}	9.30×10^{-4}
115 nm	0.54	0.78	57.1	9.51×10^{-3}	1.37×10^{-2}
202 nm	0.57	0.79	21.7	2.63×10^{-2}	3.65×10^{-2}
460 nm	0.29	0.81	7.8	3.66×10^{-2}	1.04×10^{-1}

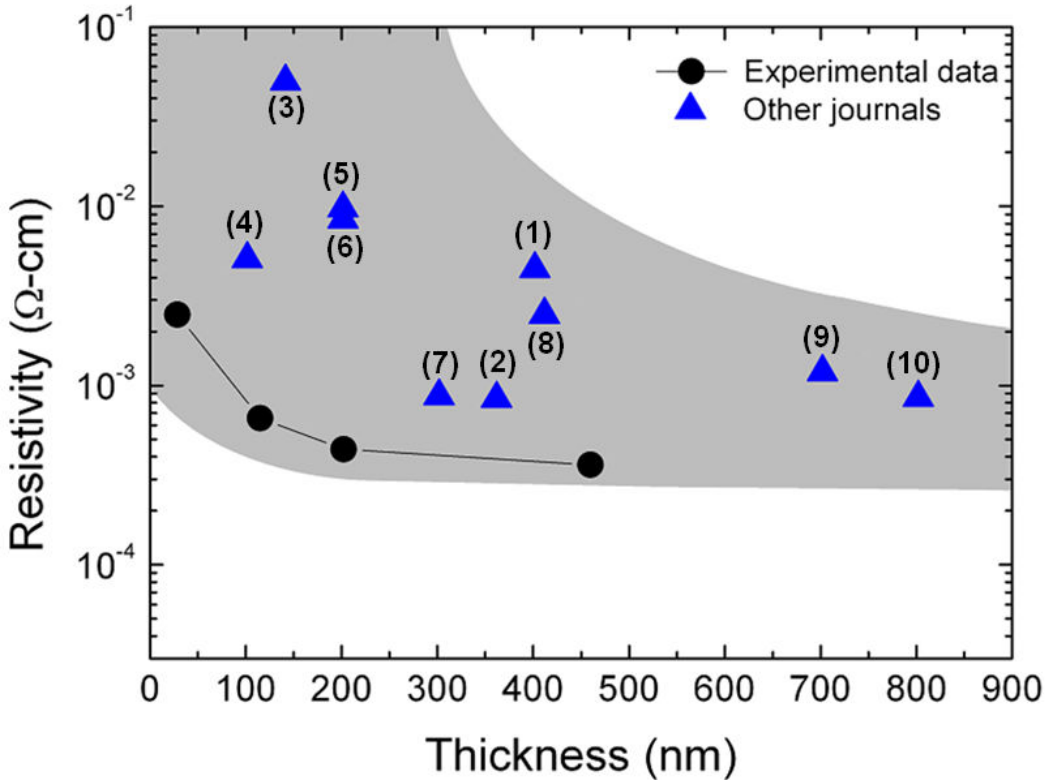

Figure 5.13 Variation in resistivity with film thickness obtained in this work. The values obtained from other independent reports of AZO on polymeric substrates are also shown. These values are obtained from reports as indicated by the reference number for each data point [(1):Ref.[84], (2):Ref.[88], (3):Ref.[80], (4):Ref.[79], (5):Ref.[81], (6):Ref.[82], (7):Ref.[83], (8):Ref.[2626], (9):Ref.[86], (10):Ref.[77]

5.2.5 Concluding Remarks

In summary, high-quality transparent conductive AZO thin films, deposited by pulsed laser deposition on low-cost flexible polyethylene terephthalate substrates and borosilicate glass, were investigated as a function of oxygen pressure and film thickness. Structural, electrical and optical properties of the AZO thin films were examined. All the AZO films grown were observed to have c-axis as-preferred orientation which suggested no degradation of the wurtizite ZnO structure. The refractive index of AZO film on glass, with a value of 1.9 at a wavelength of 600 nm was also obtained. A modified figure-of-merit was proposed to select the optimized deposition condition and investigate the effect of film thickness variation. It was found that grain sizes play only a greater role at smaller film thicknesses in affecting the carrier mobility. With increasing film thickness, near surface/interface depletion and scattering of carriers can affect the mobility and carrier concentration, thereby increasing the resistivity. This serves as a general limit for films with smaller grain sizes and is thus especially relevant for low temperature growth. Although transparency in the UV and infrared regions does change, the overall area under the transmission curve remains unchanged and the visible transparency is not significantly affected. Considering the finite attenuation effect of film thickness, this should serve as an upper limit for the thickness of TCOs in device applications. In this work, a resistivity as low as ~6.6×10^{-4} Ω-cm with a high normalized transparency index of >0.9 in the visible range and >0.78 (78 % of total solar spectrum transmitted) for a 110 ± 10 nm thin film was obtained. This represents one of the best results obtained for such film thicknesses deposited at room temperature.

5.3 AZO Multilayered Sandwich Structure

In this section, details of fabrication of the repeating stacks of TCO/metal/TCO and TCO/metal/Ge/TCO were discussed. The TCO used here is AZO. The electrical and optical properties of these AZO multilayer sandwich structures were examined.

5.3.1 Fabrication of AZO Multilayer Sandwich Structure

AZO films have been deposited on borosilicate glass using PLD at room temperature. Details on the growth parameters have been mentioned in section 5.2.1. The thickness of each AZO layer in a multilayer structure has been carefully calibrated to a thickness of 43 ± 5 nm. In the first series of experiments, the AZO layer is first deposited onto the glass substrate, followed by a 0.5 nm of Ge layer and then a Ag layer by e-beam evaporation, with Ag thickness varying from 1 nm to 20 nm. Subsequently, a second set of samples is covered by another AZO layer, and this is denoted as a single AZO sandwich structure. For double sandwich and triple sandwich structures, a schematic diagram of these AZO sandwich structures is illustrated in Figure 5.14. The thickness of the Ag layer in these AZO sandwich structures is varied to be at 5 nm, 7 nm, 10 nm and 20 nm.

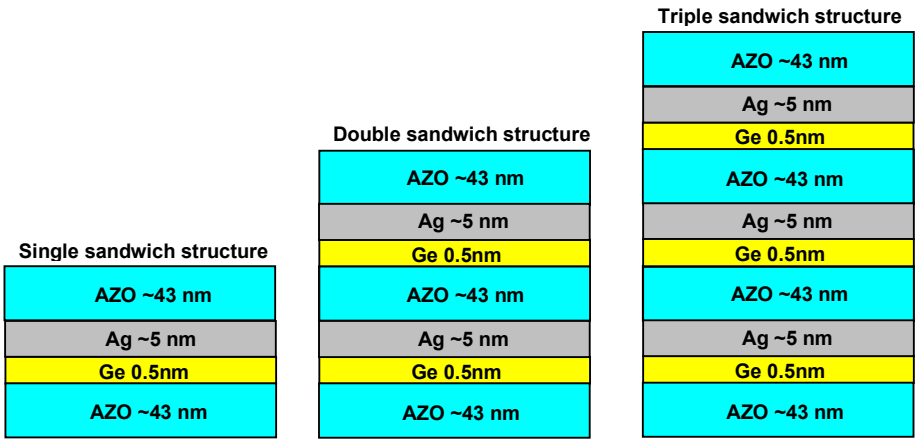

Figure 5.14 Schematic diagram of AZO sandwich structures

5.3.2 Electrical Characterization

Figure 5.15 shows the electrical resistivity, mobility and carrier concentration of the Ag/Ge/AZO film. The electrical properties of the AZO film (zero Ag layer thickness) are also shown for reference. It was observed that as the thickness of Ag layer increases, the resistivity decreases to as low as 3 x 10^{-5} Ω-cm, with carrier concentration increasing by ~1.5 orders as silver is a very conducting metal. It should be noted that the resistivity decreases drastically only at a Ag thickness of 7 nm, which suggests that Ag has formed a continuous layer at this thickness. However, when the Ag/Ge/AZO structure is capped by an additional AZO layer, the mobility of the structure decreases slightly for Ag thickness greater than 7 nm (see Figure 5.16). This implies that there might be an increase in scattering events at the sandwiching interface between AZO to Ag. Despite a decrease in mobility, the resistivity of these single sandwich structures has still improved compared to a single AZO film, which has a resistivity of ~1.3 x 10^{-3} Ω-cm (the single AZO film also has a mobility of ~6.7 cm^2/Vs and a carrier concentration of ~7.1 x 10^{20} cm^{-3}).

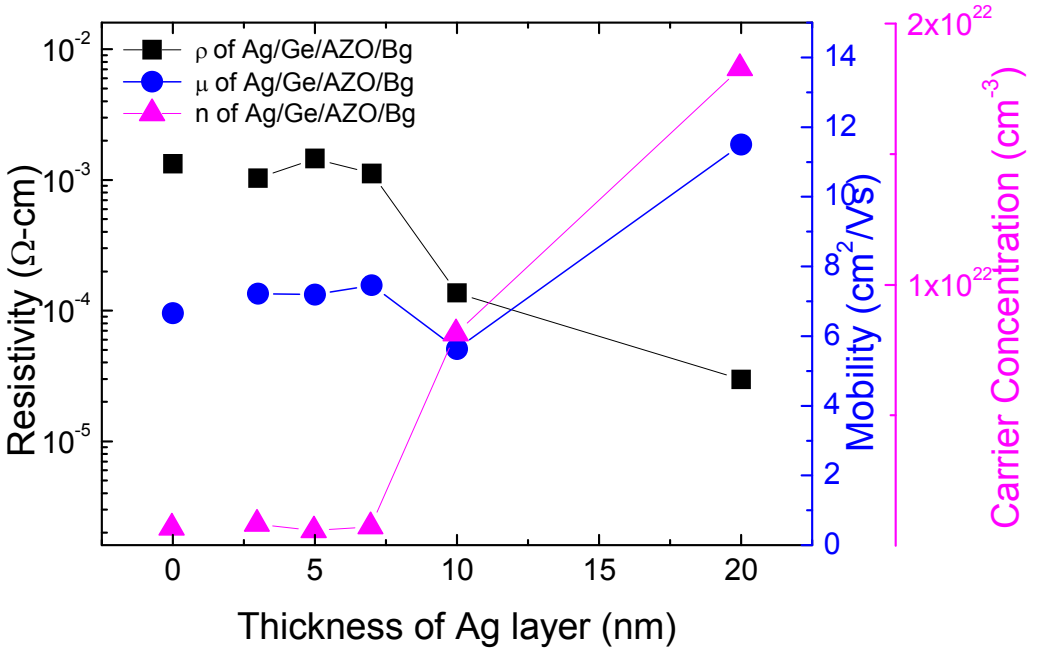

Figure 5.15 Plot of electrical resistivity, mobility and carrier concentration of the Ag/Ge/AZO film as a function of the Ag layer thickness

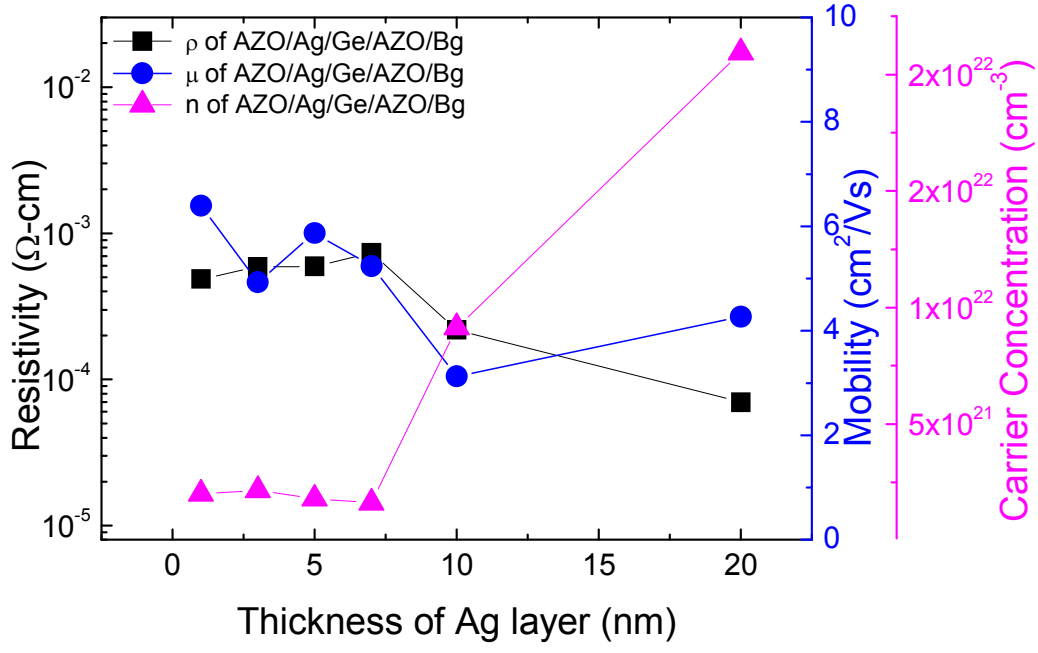

Figure 5.16 Plot of electrical resistivity, mobility and carrier concentration of the AZO/Ag/Ge/AZO single sandwich structure as a function of the Ag layer thickness

The electrical resistivity, mobility and carrier concentration of single sandwich structure, double sandwich and triple sandwich structure with respect to variation in Ag thickness are shown in Figure 5.17. Since the critical thickness of forming a continuous Ag layer is greater than 7 nm, the Ag thickness was varied from 5 nm to 20 nm. From Figure 5.17, the resistivity has improved for a thicker Ag layer, which is expected, as compared to the single AZO film. However, there is only a slight improvement in the resistivity when compared between the single sandwich structure, double sandwich structure and triple sandwich structure. Nonetheless, good electrical property is not the only factor to qualify for an excellent TCO; transparency is also critical and there is a need to examine it. In the next section, the optical property of these AZO sandwich structures is examined.

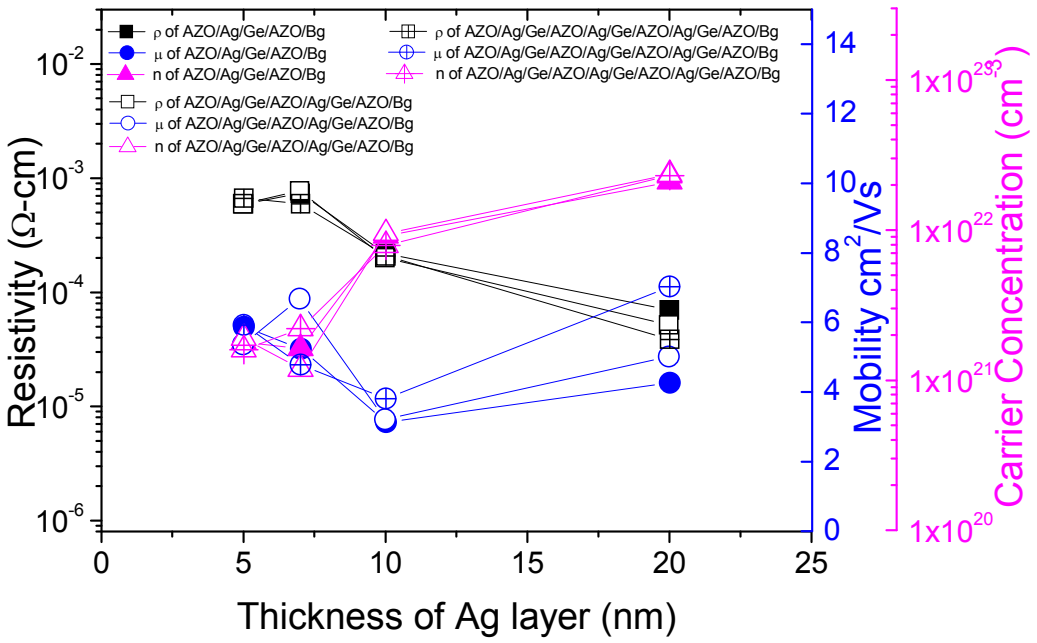

Figure 5.17 Plot of electrical resistivity, mobility and carrier concentration of single sandwich structure, double sandwich and triple sandwich structure with respect to variation in Ag thickness

5.3.3 Optical Analysis

The transmission spectra of each of the AZO film layers used in this work are shown in Figure 5.18. The slight variation at the NIR region is due to the slight differences in the measured carrier concentration. It is to be noted that the transmission in the visible region is ~83 % at a wavelength of 550 nm.

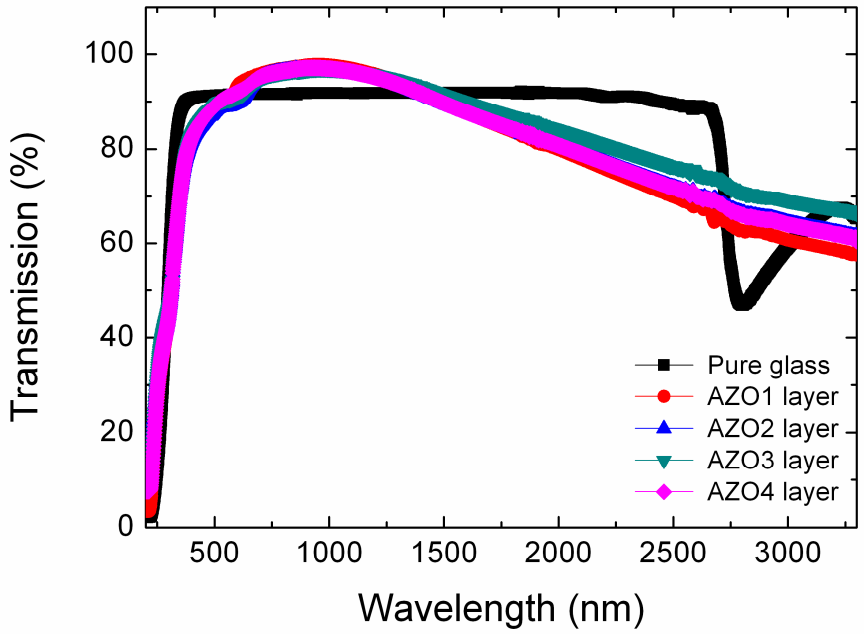

Figure 5.18 Transmission spectra of the AZO film

Figure 5.19 compares the transmission spectra of the Ag/Ge/AZO and AZO/Ag/Ge/AZO single sandwich structure. From the plot, it was observed that as the Ag layer thickness increases, the transmission decreases. For the Ag/Ge/AZO, in the case of 1 nm thick Ag, the increase in transmission in the NIR region is perhaps due to the fact that the Ag layer has not formed a continuous layer and scattered the incident light. The drastic drop in the transmission in the NIR region can be attributed to the free carrier absorption, as evidenced by an increase of up to ~1.5 orders in the carrier concentration as mentioned in the previous section.

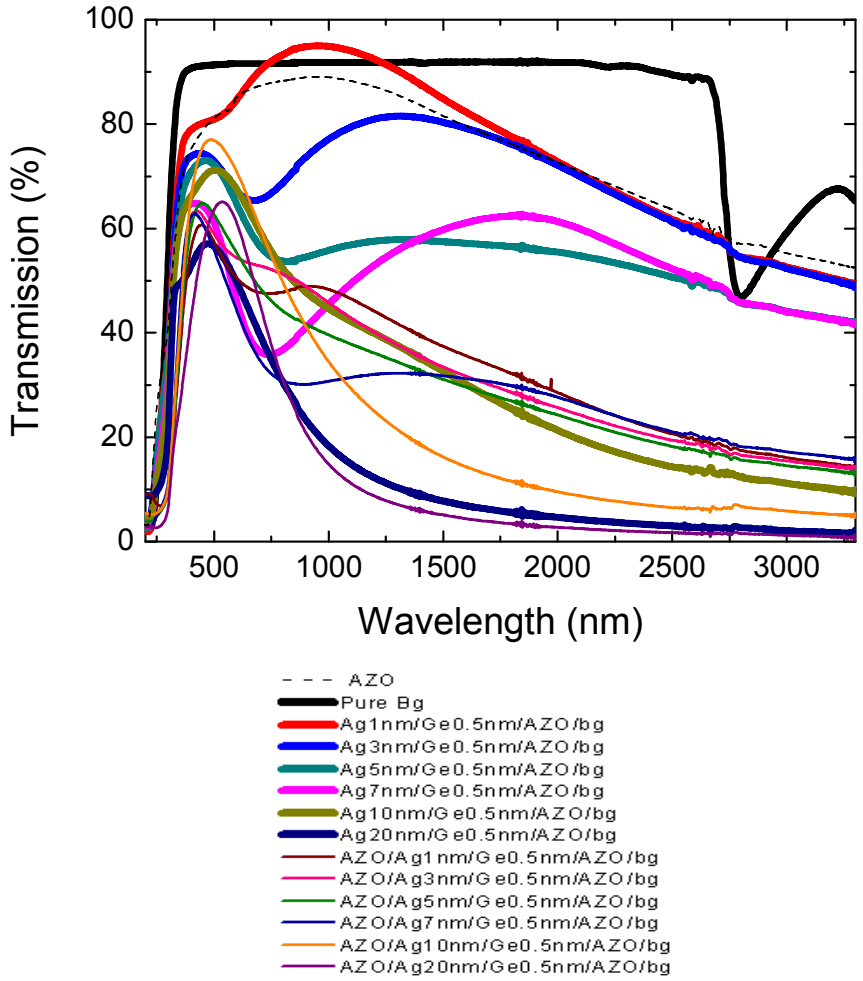

Figure 5.19 Transmission spectra of Ag/Ge/AZO/glass and AZO/Ag/Ge/AZO/glass

Figure 5.20 shows the transmission spectra of the AZO single sandwich structure, double sandwich structure and triple sandwich structure. Using multilayer sandwich structures, one can control the transparency of the film in the NIR region by stacking up semiconductor/metal/semiconductor layers and controlling the thickness of the Ag layer, while having moderate transparency in the visible region. Based on the electrical and optical properties of these sandwich structures, the single sandwich structure with Ag of 10 nm thickness gives an optimized electrical resistivity with high transparency. Therefore, the single sandwich structure seems a much better

structure as compared to the double and triple sandwich structures which also fulfil the aim of seeking low cost TCO on low cost substrate.

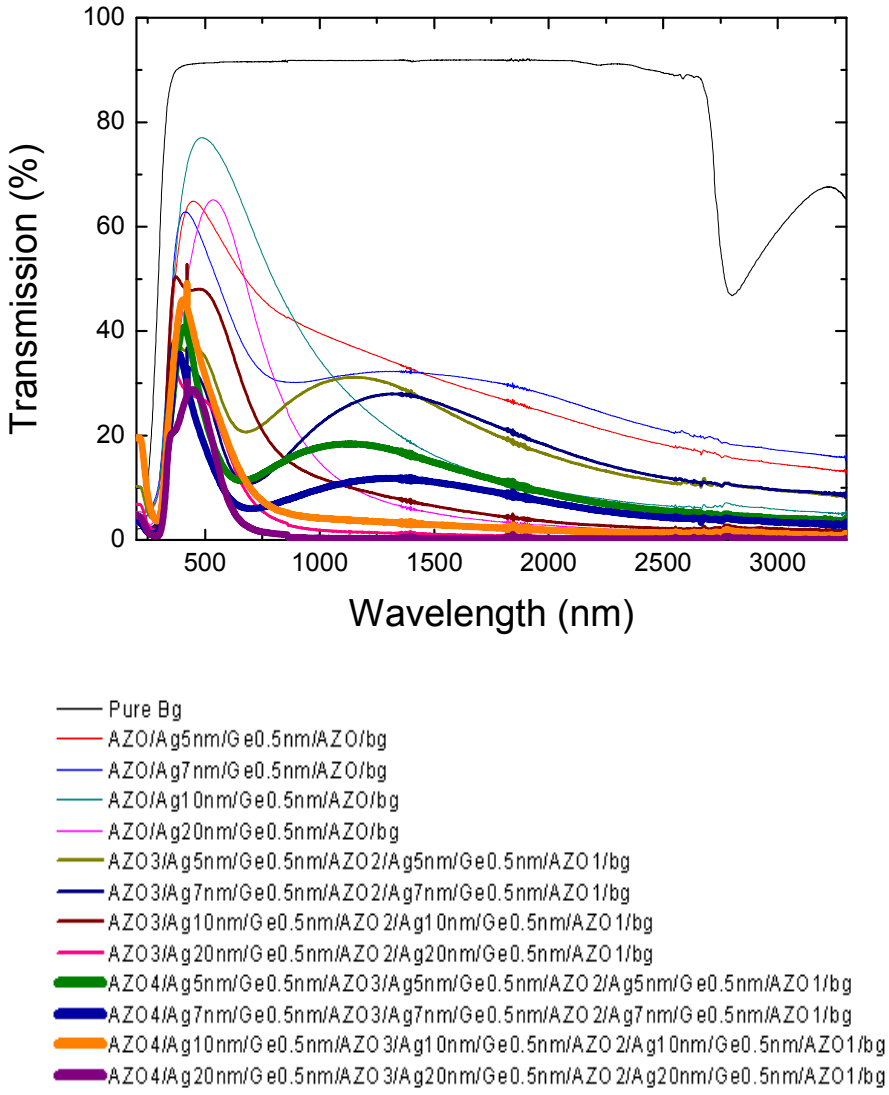

Figure 5.20 Transmission spectra of AZO single sandwich structure, double sandwich structure and triple sandwich structure

5.3.4 Concluding Remarks

AZO multilayer sandwich structures were investigated with varying Ag thickness and various stacking combination. In optimizing the multilayer structures, all the structures do give a lower resistivity, as compared to the single AZO thin film, but at the expense of lower transparency in the visible region. However, by controlling the number of sandwich stacking of semiconductor/metal/semiconductor layers and the thickness of the Ag layer, multilayer sandwich structures do offer a control over the transparency of the film in the NIR region while having moderate transparency in the visible region. A low resistivity of ~2.2 x 10^{-4} Ω-cm, mobility of ~3.1 cm^2/Vs and a carrier concentration of ~9.1 x 10^{21} cm^{-3} and ~75 % transmission at a wavelength of 550 nm are obtained for the case of a single sandwich structure with 10 nm thick Ag, which gives the highest transparency in the visible region and the best electrical property among the AZO multilayer sandwich structures. Therefore, the single sandwich structure seems a much better structure, as compared to the double and triple sandwich structures, as it can provide control of transparency in the NIR region and also fulfil the aim of seeking low cost TCO on low cost substrate.

Chapter 6 Application of Zinc Oxide-Based Structures

Group III-doped zinc oxides have vast applications as highly transparent conducting oxides. Other than serving as transparent electrodes, these thin films are also candidates for the n-type layer in a p-n heterojunction for photovoltaic application or as the channel layer of a transistor. Therefore, in this chapter, some works are investigated on these applications.

In order to form a p-n junction for photovoltaic application, there is a need to have both p-type and n-type materials as mentioned in section 2.3.1. In terms of oxide semiconductors, such as Cu_2O and ZnO, there is difficulty in forming stable homojunctions for both materials. Therefore in this work, the ZnO-Cu_2O heterojunction is studied. As the type of alignment in the heterojunction affects the charge transport of the device and solar cell conversion efficiency, there is a need to examine whether these two materials are matching in terms of the energy band alignment. There are three types of heterostructure band alignment. A type I alignment refers to a heterojunction with band discontinuities whereby electrons and holes are confined in the same material. A type II heterojunction refers to an interface with a staggered gap whereby the conduction and valence bands are both higher in one of the two materials forming the heterojunction. A type III alignment refers to an extended version of the type II alignment whereby the staggered alignment has discontinuity in the conduction and valence bands. Therefore, for efficient charge transport at the interface of these p-n heterojunction, the focus in this work is on the band alignment of these two materials.

Zinc oxide is well-known for having a wide band gap, high melting point, high cohesive energy and high exciton binding energy of 60 meV. These properties are important aspects for UV sensing materials compared to other wide band gap semiconductors such as ZnS, ZnSe and GaN.[165] Due to the large bond strength (high melting point and high cohesive energy) and high stability of the exciton (large exciton binding energy), materials degradation due to defect generation during ZnO device operation is less expected.[165] Zinc oxide devices can also realize exciton gain at room temperature, or even higher temperature as its excitons are stable.[165] Typically, UV sensors are fabricated using a metal-semiconductor-metal (MSM) configuration.[269] However, this configuration is not able to fully utilize the zinc oxide area to the UV illumination due to the contact electrode circuitry. By using TCOs as electrodes, the ZnO sensing area can be fully exposed to the UV and a full transparent ZnO-based UV sensor can be realized. Hence, in this work, a simple device is fabricated to compare the effect on photoconductivity using gold contact, doped zinc oxide contact and ITO contact.

Transparent thin film transistors (TFTs) have potential application in electronic devices such as displays and touch panels. For the new generation of TFTs, ZnO is a promising candidate for the channel layer as it can be grown as a polycrystalline film even at room temperature and it also has extra functions such as for photodetection.[270] It is also chemically stable and thermally stable and can be deposited on various substrates.[271] Most importantly, it has high carrier mobility and can operate at low voltages as desired by many devices (consume less power). Majority of the oxide transistors operate at relatively high voltages, hence has higher power consumption. One way to solve this problem is the development of low-voltage

oxide transistors which includes the use of ultra-thin dielectrics,[272] high-*k* dielectrics,[273] and electrolyte gate dielectrics.[274] Here, in this work, high-*k* dielectric and ZnO TFT are investigated. The gate dielectric, such as high-*k* hafnium oxide (HfO_2), is critical to decrease the operating voltage of the ZnO transistor and improve the on/off current ratio. However, for this HfO_2/ZnO heterostructure, the conduction band offset and valence band offsets are critical as it may lead to large leakage current and, hence, causing device failure. Therefore, the band offsets of the HfO_2/ZnO heterostructure are first examined here. Next, an n-channel enhancement mode ZnO-based TFT, using HfO_2 as a gate dielectric, is fabricated and studied. More details are given in section 6.3.

6.1 Band Alignment Study of GZO/Cu_2O for Photovoltaics Application

As mentioned in chapter 2, Cu_2O is a low-cost and non-toxic material which is currently a potential p-type semiconducting oxide material for photovoltaic device application. ZnO/Cu_2O photovoltaic devices have potentially high energy conversion efficiency, with a theoretical limit of about 18 %. Experimental results have shown a measured conversion efficiency of up to ~2 % using a copper substrate.[157] In order to reduce the cost and improve the device fill factor, a thin film on glass substrate configuration is investigated here.[155] Thin film deposition offers a better control of the stoichiometry of the heterojunctions and is cheaper than the bulk substrate. In addition, doping of the thin films (p-type or n-type) can be controlled during deposition and this will have an impact on the electrical properties. For example,

GZO thin films have high n-carrier concentration which adds flexibility in device fabrication.[75]

To understand the charge transport at the interface of a Cu_2O/GZO heterostructure, the relative band alignment between the two different materials is of critical importance. Obtaining a type II or even type III band alignment is essential for charge separation at the interface which is important for photovoltaic application. In terms of the charge transportation through the thin films, it is important to ensure that the p-type material has a higher conduction band relative to the n-type material. The relative alignment of the valence band of the p-type material with the conduction band of the n-type material will determine the thermodynamic limit of the achievable open circuit voltage (V_{oc}).[275] Therefore in this work, thin film heterojunctions consisting of p-type Cu_2O and n-type GZO on ITO coated glass substrates were fabricated and the relative band offsets were investigated. It is observed that the gallium doping in ZnO has little effect on the resultant band offsets while asymmetry of the Cu_2O/GZO and GZO/Cu_2O interfaces is observed.

6.1.1 Fabrication of Cu_2O/ZnO Heterojunctions

All the thin films structure investigated were deposited on either commercial 100 nm thick ITO coated glass substrates or borosilicate glass at room temperature. Before deposition, the substrates were ultrasonically cleaned in acetone, ethanol and deionized water, for approximately 5 min each, before blowing dry with compressed air. Cu_2O films were deposited using direct current reactive sputtering of a metallic copper target (99.996%), in an argon-oxygen ambience. Prior to deposition, the chamber was pumped down to a base pressure of 6×10^{-7} Torr and the oxygen (O_2)

partial pressure was varied from 0.3 to 0.5 mTorr, with the total pressure maintained at 1 mTorr. The GZO films were deposited by pulsed laser deposition using a 99.99% purity ZnO/Ga_2O_3 (0.98:0.02) target. The laser pulse energy of 300 mJ was focused onto the target at a pulse rate of 10 Hz with a target-to-substrate distance of 8 cm. The O_2 partial pressure was fixed at a calibrated pressure of 1.0 mTorr. In this work, thick ZnO, GZO and Cu_2O (all 15 nm thickness) films and heterostructures of GZO (5 nm)/Cu_2O (15 nm), ZnO (5 nm)/Cu_2O (15 nm) and Cu_2O (5 nm)/GZO (15 nm) were deposited onto the glass substrates.

6.1.2 Results and Discussion

To ascertain the quality of the GZO deposited, the chemical and structural properties of the GZO thin films were examined. The crystal structure of the 15 nm thick GZO deposited on borosilicate glass shows a polycrystalline structure as shown in the XRD spectra in Figure 6.1(a). This is consistent with the commonly observed preferred growth orientation due to its low surface energy plane.[96] A prominent peak of a hexagonal wurtzite ZnO (002) at ~34.5° was measured as shown in Figure 6.1(a). The lack of any prominent crystal structure from the metallic Zn and Ga_2O_3 is a good indication that Ga atoms have substituted Zn in the hexagonal lattice.[75] Therefore, a highly conductive GZO film with a resistivity of $\sim 7.7\times10^{-4}$ Ω-cm, a mobility of ~13 cm^2/Vs and a carrier concentration of ~6.28 x 10^{20} cm^{-3} was obtained. Since GZO is a direct band gap material, the optical band gap can be obtained using the method mentioned in section 2.1.3 From the extrapolation from the plot of $(\alpha E)^2$ against the photon energy, a measured band gap of 3.57 eV is obtained for the GZO film as shown in Figure 6.1(b), which is consistent with other reported values.[242]

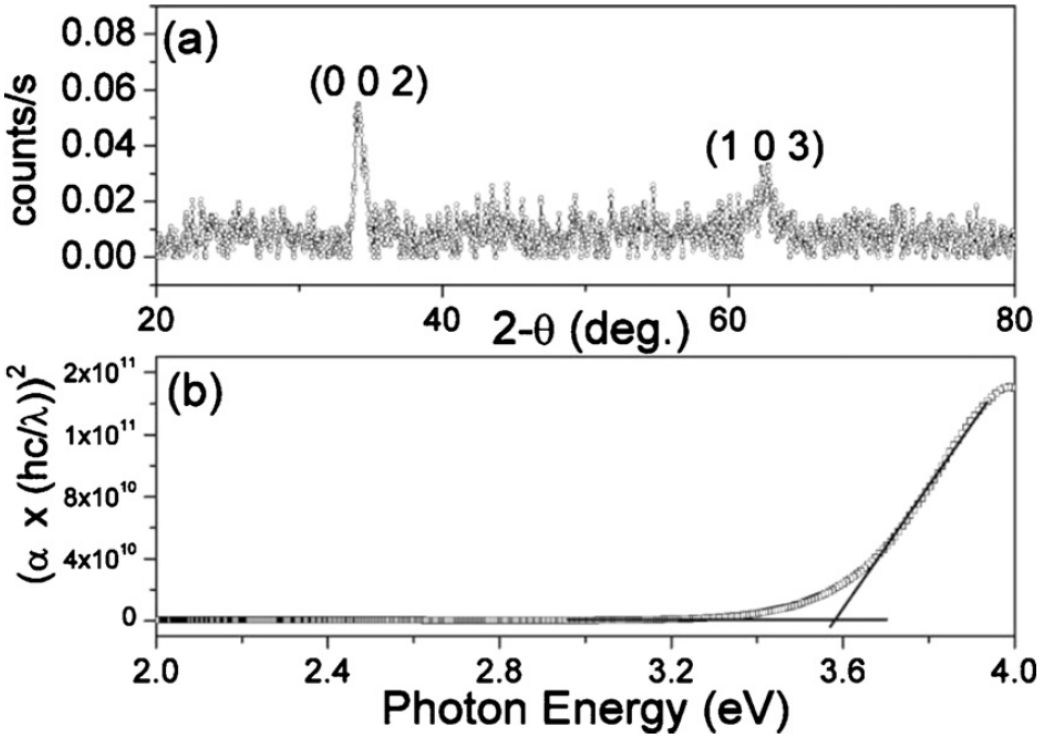

Figure 6.1 (a) XRD spectrum of 15 nm thick GZO on borosilicate glass grown at room temperature using pulsed laser deposition, (b) $(\alpha E)^2$ against photon energy plot for the as-grown GZO. The absorption coefficient is obtained from the attenuation equation using thickness of the grown film that is measured using AFM measurements of the film thickness

The growth of Cu_2O for the Cu_2O/GZO heterostructure has to be carefully calibrated. While Cu_2O is the most stable phase of the copper oxides (>1000 °C), [126] CuO can be formed at low temperatures. Generally, it is found that there can be a phase transition from Cu_2O to CuO at a temperature range of ~300 to 350 °C.[276,277] The underlying reason may however be related to the presence of oxygen during annealing. This is shown by observation of the Cu_2O phase even when the substrate is at an elevated temperature of 400 to 500 °C when a critical pressure of O_2 is not reached.[278] The underlying process for phase transition of Cu_2O to CuO is thus oxidation as a reverse reduction process can similarly take place at higher temperatures since a thin Cu metal layer is preferably formed at the surface of both

Cu_2O or CuO after annealing in a vacuum environment.[279] The importance of the oxygen pressure is demonstrated recently when it is shown that pure phases of both CuO and Cu_2O can be obtained even at room temperature.[280] The authors reported that although a higher O_2 partial pressure is needed for the formation of CuO, a variation in the flow rate at a fixed partial pressure of 0.5 mTorr is needed for the growth of Cu_2O as explained by a variation in the frequency of particle collision. However, changing the flow rate with the same partial pressure amounts to a different total pressure and it has been shown that a high pressure environment (not of O_2) can affect the growth of Cu_2O.[281] Therefore, in this work, the total growth pressure is fixed at 1 mTorr and the partial pressure of O_2 is varied carefully. The Cu_2O films obtained are p-type with an average resistivity of ~380 Ω-cm, a mobility of ~0.62 cm^2/Vs and a carrier concentration of ~2.63×10^{16} cm^{-3}. The low mobility is expected since these Cu_2O thin films are sputtered at room temperature. However, these values still compare favorably with the ones obtained by Reddy *et al.* via sputtering at a substrate temperature of 200 °C.[282]

Figure 6.2 shows the XRD spectrum of the measured films at partial pressure of 0.33, 0.4, and 0.5 mTorr. For samples grown with a lower O_2 partial pressure of 0.2 mTorr, the presence of metallic Cu can still be observed. The XRD diffraction shows that single phase of Cu_2O films are obtained for growth at an O_2 partial pressure of 0.33 mTorr with diffraction peaks at 36.4°, 42.6°, and 61.3° corresponding to the (111), (200), and (220) planes respectively of the cubic-structured Cu_2O.[128] At a higher O_2 partial pressure of 0.4 mTorr, mixed phases of Cu_4O_3 and Cu_2O are obtained, as can be seen by the paramelaconite structure for the (202) plane of Cu_4O_3 at 35.8°. Finally, at higher O_2 partial pressure of 0.5 mTorr, a pure phase of CuO is

observed from the diffraction peaks of 35.2° and 38.5° for the CuO (111) and (200) plane, respectively.

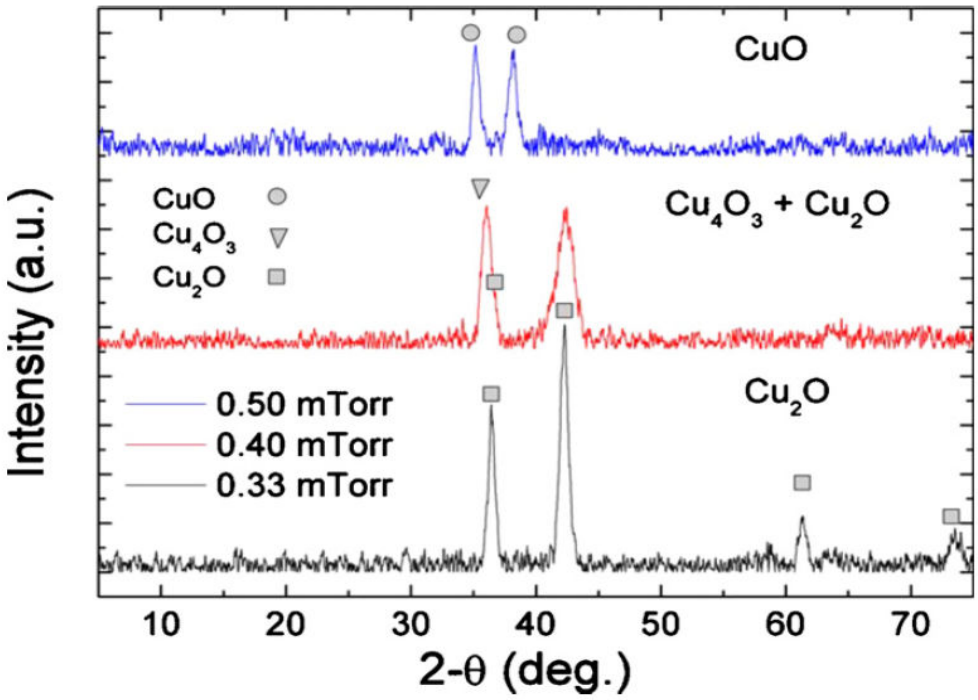

Figure 6.2 XRD spectra of Cu_2O on borosilicate glass grown at room temperature using dc sputtering at the different O_2 partial pressure indicated. At a lower O_2 partial pressure of 0.33 mTorr, a pure phase of Cu_2O is obtained, while at a higher O_2 partial pressure of 0.5 mTorr, a pure phase of CuO is obtained. A mixed phase of Cu_2O and Cu_4O_3 is observed for the intermediate partial pressure of 0.4 mTorr. The total pressure in the growth chamber is kept constant at 1 mTorr for all growth conditions

The band gap of the films grown at different O_2 partial pressure is obtained from the plot of $(\alpha E)^2$ versus photon energy plot as shown in Figure 6.3. The absorption at lower photon energy can be observed for samples grown at a higher O_2 partial pressure of 0.5 mTorr, as can be seen from the shoulder in Figure 6.3 as indicated by the arrow. The inset shows a plot of $(\alpha E)^{1/2}$ versus photon energy for the CuO thin film since it is an indirect band gap material. Therefore, the extrapolation of the plot

yields a CuO band gap of 1.33 eV while the band gap of Cu_2O is measured to be ~2.52 eV. There is a slight increase in the band gap for the sample with a mixed phase of both Cu_2O and Cu_4O_3. For the 0.4 mTorr case, there is a slight increase in the band gap for the sample with a mixed phase of both Cu_2O and Cu_4O_3. From the extrapolation method used in finding the band gap, the presence of Cu_4O_3 resulted in a slight increase in the band gap. This is because Cu_4O_3 is a phase with a smaller band gap of 1.34 eV. This smaller band gap phase at the lower photon energy together with a larger band gap Cu_2O in the $(\alpha \times (hc/l))^2$ against photon energy plot gives this slight increase in the resultant band gap.[283] More importantly, it was shown that at room temperature, both pure phases of CuO and Cu_2O can be obtained by simply controlling the oxygen pressure in reactive sputtering. The formation of Cu_2O can be attributed to the fast oxidation rate of Cu into Cu_2O, as demonstrated in the high temperature oxidation of Cu thin films whereby Cu_2O can be formed at lower O:Cu ratios.[284] Cu_4O_3 may thus be an intermediate or transition state structure when oxidation of Cu is increased before the final phase of CuO forms due to the presence of increasing O_2 partial pressure.

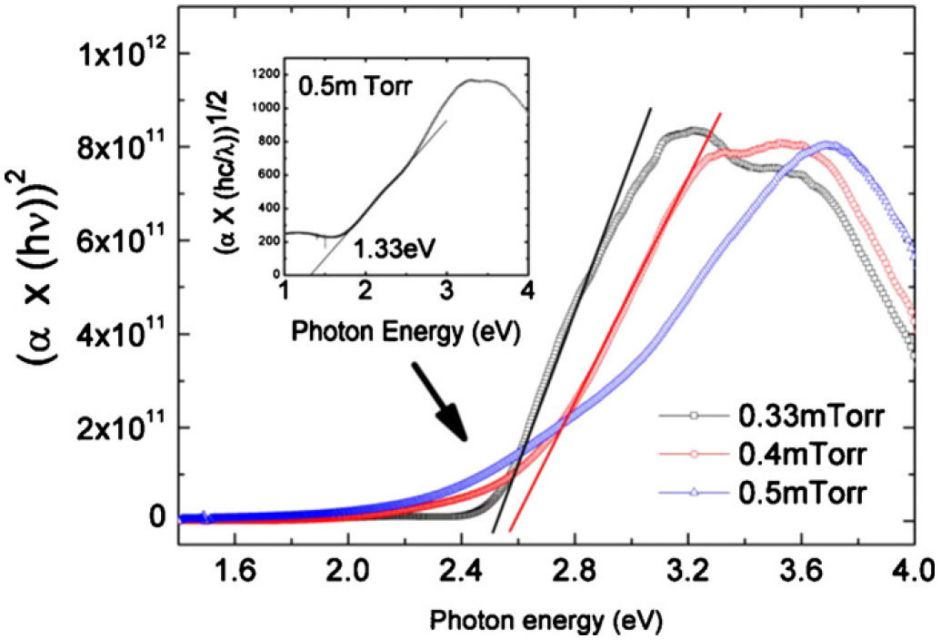

Figure 6.3 Plot of $(\alpha E)^2$ against photon energy for dc reactive sputtering of Cu at different indicated O_2 partial pressures. The extrapolation gives the band gap for a direct gap material (Cu_2O). The inset shows a $(\alpha E)^{1/2}$ against photon energy plot for the film grown at an O_2 partial pressure of 0.5 mTorr that yields the band gap for an indirect gap material (CuO)

The XPS Cu 2*p* profile for CuO is shown in Figure 6.4(a). The fitted Cu 2*p* and O 1*s* XPS spectra for Cu_2O are shown in Figures 6.4(b) and 6.4(c), respectively. It can be seen that the Cu $2p_{3/2}$ core level can be fitted with two separate peaks at a binding energy of 932.46 and 933.61 eV. Although this can possibly represent a mixed phase of Cu_2O and CuO, the XRD spectrum as seen in figure 6.2 does not indicate the formation of CuO type structure. The absence of CuO can also be inferred from the absence of any intense shake-up satellite structures.[285] Satellite peaks due to multiple excitations in copper oxides is known to be absent in Cu_2O structures where there is an oxygen deficiency.[286] The shake-up satellites peaks for CuO are usually intense satellites at a separation of 8.8 and 11 eV from the main Cu 2*p* peak as seen in Figure 6.4(a) from the sample grown in 0.5 mTorr of O_2 partial pressure; these are absent as indicated by the arrows in Figure 6.4(b).[279] Therefore, together with

the correct binding energy of O 1*s* for Cu_2O and CuOH type bonding shown in Figure 6.4(c), the additional peak at a higher binding energy in the Cu 2*p* spectrum is consistent with the presence of hydroxide species adsorbed on the surface of the samples.[279] These hydroxides are most probably surface adsorbants and they will not affect the subsequent analysis.

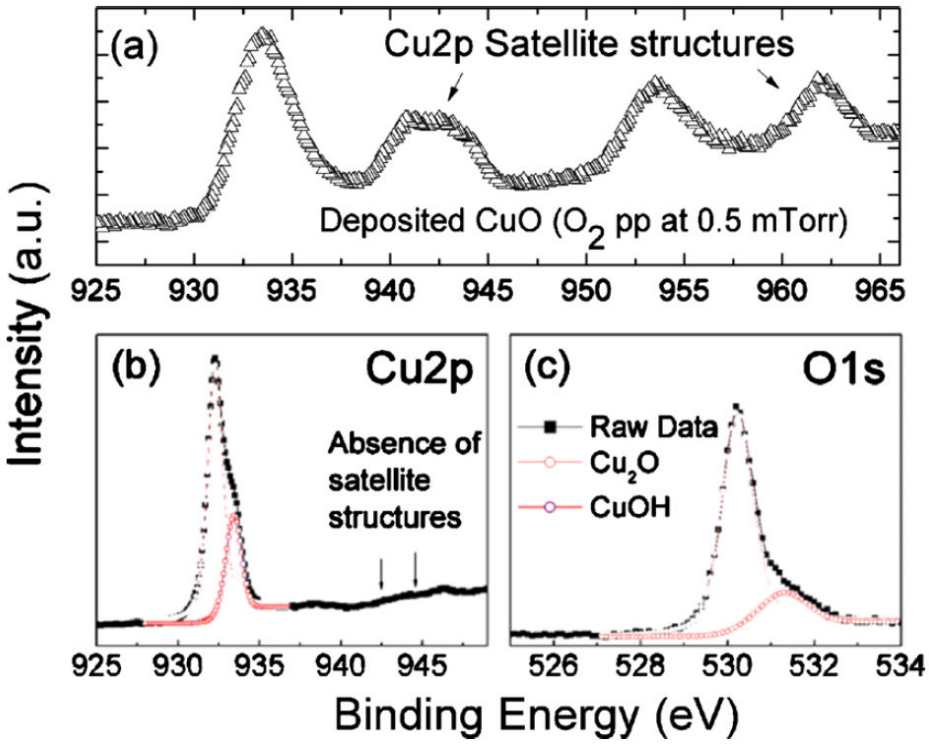

Figure 6.4 (a) XPS profile for Cu 2*p* for the sample deposited at an oxygen partial pressure of 0.5 mTorr, yielding a CuO thin film. This can be clearly seen from the satellite structures indicated by the arrows, (b) XPS profile for Cu 2*p* and (c) XPS profile for O 1*s* of 15 nm thick Cu_2O films. The arrows in the Cu 2*p* plot in (b) indicate the position of the satellite peaks expected for CuO. Both spectra also show best-fit profiles using Lorentzian–Gaussian line shape. The fitted full width at half maximum (FWHM) of the Cu 2*p* is ~1.11 eV for both Cu_2O and CuOH while the fitted FWHM for the O 1*s* is 0.86 eV for Cu_2O and 1.2 eV for CuOH

To investigate the band alignment of GZO and Cu_2O using XPS, the core-level measurement method as proposed by Kraut *et al.* was used here.[287] Core-level

alignment can prevent many measurement errors, giving accurate band offsets measurements.[288] In this method, the VBO of GZO/Cu_2O interface can be obtained using the following equation:

$$\Delta E_V = \left(E_{Cu\,2p}^{GZO/Cu_2O} - E_{Zn\,2p}^{GZO/Cu_2O}\right) + \left(E_{Zn\,2p}^{GZO} - E_{VBM}^{GZO}\right) - \left(E_{Cu\,2p}^{Cu_2O} - E_{VBM}^{Cu_2O}\right) \text{----------(6.1)}$$

where E_i^S denotes the binding energy of the core level "*i*" for the sample "*s*" while E_{VBM}^S denotes the VBM for the sample "*s*". Essentially, the core-level to valence-level separation is measured for the bulk GZO and bulk Cu_2O (second and third terms on the right hand side of equation (6.1)), as shown in Figures 6.5(a) and 6.5(b). The VBM position is determined as the intersection point between the linear extrapolation from the leading edges of the valence band with respect to the background.[289] Thin film core-level separations between the Cu 2*p* and Zn 2*p* are then measured and an example for the GZO/Cu_2O interface is shown in Figure 6.5(c). For these interface core-level separation measurements, it is important that the interface is relatively abrupt and that there is no clustering of the deposited thin films. This is important as any agglomeration or clustering will expose the underlying film that will render the measurements inaccurate since they are not reflective of the core levels at the interface.

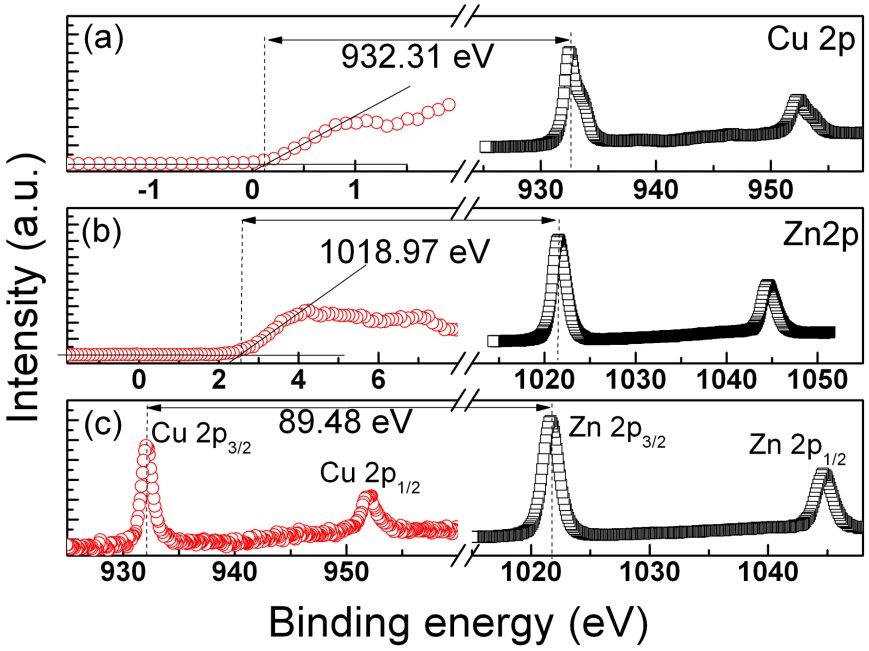

Figure 6.5 XPS spectra showing the measurements needed to determine the valence band offset. (a) Measured separation between Cu 2p core-level and the valence band maximum for bulk Cu_2O (15 nm); (b) Measured separation between Zn 2p and the valence band maximum for bulk GZO (15 nm); (c) Measured core-level separation at the interface between Cu 2p and Zn 2p for a 5 nm GZO film deposited on 15nm Cu_2O

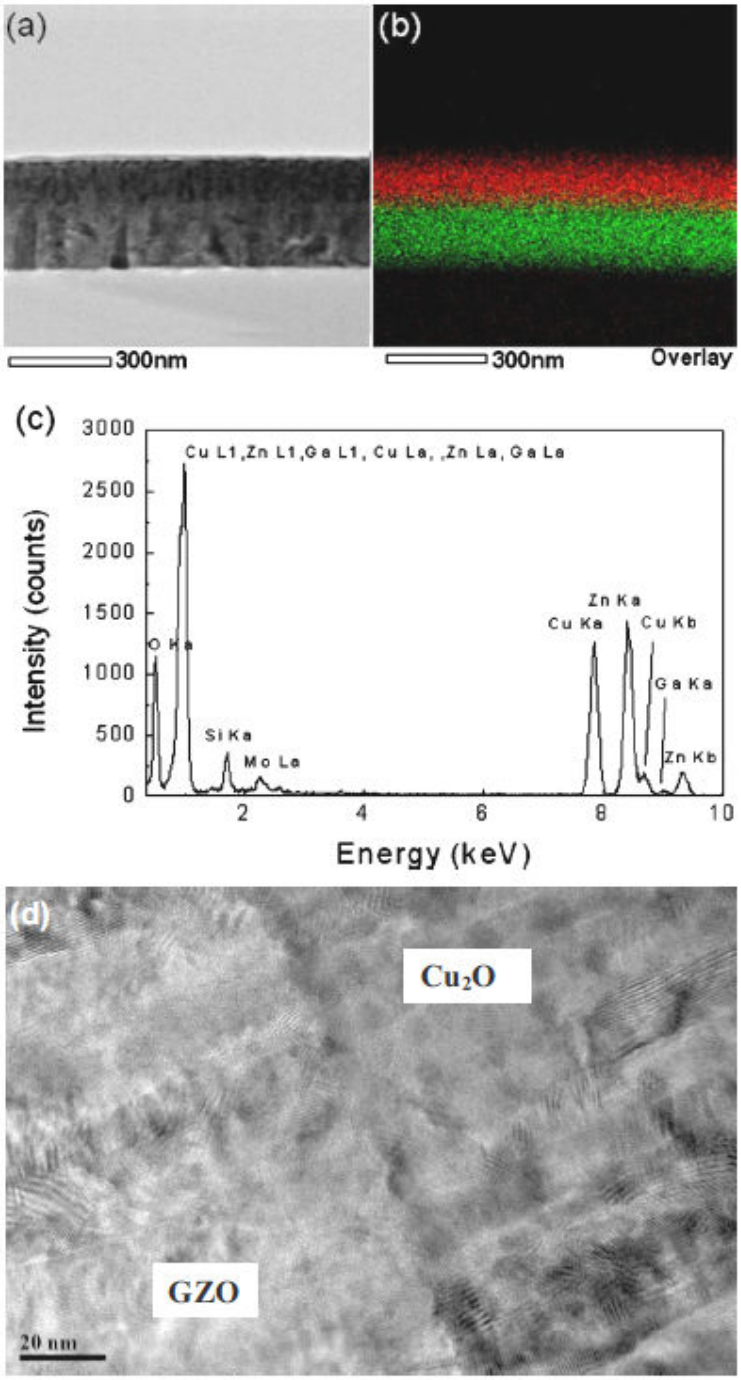

Figure 6.6 (a) TEM image of a Cu_2O/GZO heterojunction. The interface can be distinguished from the contrast shown in the TEM image. (b) Corresponding EDX mapping of the heterojunction is shown as an overlay image whereby the element copper (Cu) and zinc (Zn) is in red (top layer) and green (bottom layer), respectively. Cu signals are obtained from the Cu $K\alpha$ while Zn is obtained from Zn $K\alpha$ as shown in the EDX spectrum in (c). (d) High-resolution TEM image at the interface of the heterojunction showing the polycrystallinity of both GZO and Cu_2O as labeled in the micrograph

Figure 6.6(a) shows the TEM image of the Cu_2O/GZO heterostructure, together with the EDX mapping and the EDX spectrum as shown in Figures 6.6(b) and 6.6(c), respectively. A clear interface between Cu_2O and GZO can be observed from both the TEM contrast in Figure 6.6(a) and the elemental mapping in Figure 6.6(b). A high-resolution TEM image of the Cu_2O/GZO heterostructure is also shown in Figure 6.6(d). The interface is once again clearly defined and lattice fringes showing the polycrystallinity of both GZO and Cu_2O can be observed. The relatively abrupt interface validates the band alignment obtained using the above mentioned method. Therefore, using the measured band gap values of 3.57 eV for GZO and 2.52 eV for Cu_2O, a GZO/Cu_2O heterojunction that forms a type II (staggered) band alignment was obtained with a corresponding VBO of 2.82 eV and CBO of 1.81 eV as shown schematically in Figure 6.7. The higher conduction band of the Cu_2O in the obtained band alignment shows that the materials are suitable for solar cell application based on energy levels consideration. From the conduction band of the GZO and the valence band of the Cu_2O, the corresponding thermodynamic limit for the open-circuit voltage V_{oc} is calculated to be 0.75 V. Similar measurements were made to determine the alignment between ZnO thin film on Cu_2O and also for Cu_2O thin film on GZO. The resultant band offsets are summarized in Table 6.1. It is observed from Table 6.1 that doping variations (from addition of Ga) did not affect the band alignment of the (G)ZnO/Cu_2O heterojunction. If the ZnO is taken as undoped (intrinsic), the measured variation in the Fermi-level will be ~1.73 eV while the measured VBO difference is only ~0.03 eV. It is common for doping to have a significant influence in band alignment changes for metal-organic interfaces.[290,291] It is also expected that doping concentration is important in affecting the built-in potential at a p-n junction, thereby affecting turn-on voltages.[155] However, looking at the flatband barrier

heights, the band offsets are observed to be independent of doping variations, as seen from their Schottky barrier heights.[292] This is similarly observed from the result of this work between two semiconducting materials with band gaps.

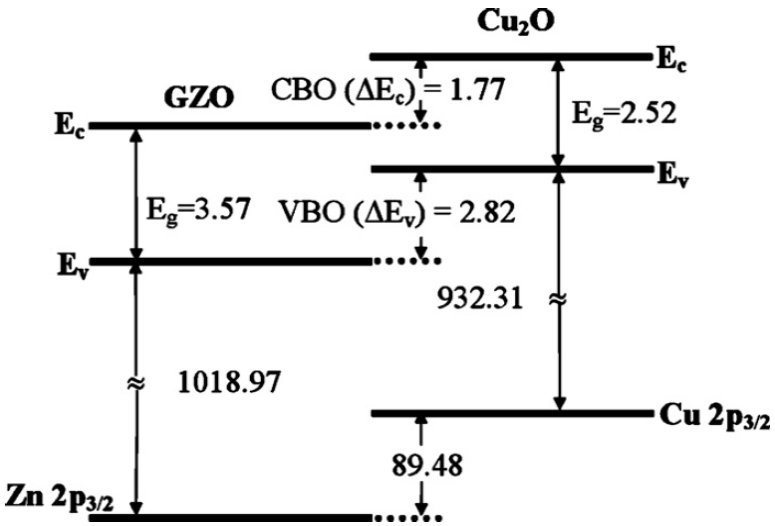

Figure 6.7 Schematic diagram showing the type II band alignment of a GZO/Cu_2O heterojunction. The VBOs can be obtained from the core-level measurements as can be seen from the diagram. The CBOs are obtained with the measured values of the respective band gaps of the films

Table 6.1 Core-valence separation for bulk films and interface core-level differences for thin film heterojunctions measured using XPS. The absolute values of VBO and CBO are also shown, taking into account the type II alignment as shown in Figure 6.7. All values listed are in electron volts (eV).

Sample	Core-valence separation	Core-level differences	VBO	CBO
Bulk Cu_2O (15nm)	932.31			
Bulk GZO (15nm)	1019.0			
Bulk ZnO (15 nm)	1019.1			
GZO (5 nm)/Cu_2O (15 nm)		89.48	2.82	1.47
ZnO (5 nm)/Cu_2O (15 nm)		89.59	2.85	1.50
Cu_2O (5 nm)/GZO (15 nm)		89.37	2.70	1.35

A similar investigation for two materials with band gaps (oxide-semiconductor) also shows little difference in the band offsets for the oxide thin films deposited on n-type and p-type Si, showing perhaps the universal independence of energy alignment with doping variations.[293] One possible reason for the doping insensitivity can be a result of surface Fermi-pinning or surface depletion effects making the Fermi-level at the surface (and hence the interface) essentially intrinsic despite various doping.[294,295] From the standpoint of chemical dipoles, the lack of influence of doping is also reasonable. This is because the density of dopants required to alter the doping of a semiconductor (nondegenerate) is small. This means that the differently doped starting surface constitutes only a small fraction of difference in terms of type of surface atoms. The effective dipole (a result of chemical bonds) at the interface is therefore not greatly affected by the doping process. On the contrary, it was expected that the band offsets measured to be unaffected, but it was observed that there is a slight difference in the alignment of Cu_2O(5 nm)/GZO(15 nm) (henceforth denoted as Cu_2O/GZO) as compared with GZO(5 nm)/Cu_2O(15 nm) (henceforth denoted as GZO/Cu_2O) as shown in Table 6.1. It is reported that Cu_2O tends to be dominated by the (111) oriented crystallographic orientation with ZnO (0001) based on lattice mismatch calculations as shown from XRD measurements.[278] This difference may yield different bonding terminations at the interface, thereby affecting the resultant interface dipoles and the subsequent band offsets.[296] A slight difference in the band offset can thus result from the heterojunction of Cu_2O/GZO and GZO/Cu_2O, despite the similar bulk properties of the GZO and Cu_2O. Interestingly, the asymmetry resulted in a slightly higher thermodynamic V_{oc} limit of 0.87 V, indicating that the (111) phase of Cu_2O may be more suitable as a heterojunction material with ZnO considering only the built-in-potential. From this

work, it is observed that the thermodynamic limit for the V_{oc} may be in a lower range of between ~0.75 to 0.87 V, that is less than the previously assumed values of 0.9 to 1.1 V. This can possibly explain for the lower built-in voltages and V_{oc} (all less than 0.6 V) recorded thus far for a Cu_2O/ZnO heterojunction.

6.1.3 Concluding Remarks

In summary, pure phases in thin films for both CuO and Cu_2O at room temperature have been obtained using DC reactive sputtering. The pure phases are observed from XRD and XPS, and confirmed by band gap measurements. The optical band gap obtained for Cu_2O is ~2.52 eV while that for CuO is ~1.33 eV. The band alignments for Cu_2O/GZO and Cu_2O/ZnO heterostructures on ITO glass were characterized by XPS. A type II heterojunction forms between the doped and undoped ZnO and Cu_2O heterojunctions, yielding a VBO value of ~2.82 to 2.85 eV. The invariant VBO shows that doping (non-degenerate) has no major influence on the band lineup even for heterojunctions of narrow band gap materials. On the contrary, band offsets obtained from the deposition of Cu_2O on GZO may be different from that obtained from the deposition of GZO on Cu_2O, suggesting that the (111) phase of Cu_2O may be a more suitable material based on V_{oc} considerations. All measurements show that the limiting V_{oc} value may lie between ~0.75 to 0.87 V, possibly explaining the low built-in voltages and V_{oc} values obtained in the literature. The higher conduction band of the Cu_2O in the obtained alignments shows that the heterojunctions are suitable for solar cell application based on energy levels consideration.

6.2 Usage of AZO as Electrode for Sensing Applications

Ultraviolet (UV) photosensors has wide applications in medicine, space communications, high-temperature plasma work, chemical and biological sensing. [297-300] UV detectors are also used to determine the thickness of the ozone layer of the Earth.[301] For such a large area detection, solid state UV detector is perhaps a good choice due to its portability and efficiency.[300]

Among solid state UV detectors, GaN-based sensors, fabricated using epitaxial growth technique on lattice-matched substrates, have shown good sensing property.[302] However, such growth techniques are expensive. Recently, high quality ZnO has been grown by various techniques which has similar property as GaN, giving an alternative to GaN-based sensors.[175,303,304]

In this work, an undoped ZnO device on glass was fabricated by magnetron sputtering for the sensing purpose characterized using the Air Mass (AM) 1.5 solar simulator. The effect of using different contact electrodes, such as gold and AZO, in the sensor structure was investigated. In order to compare with the more widely used ITO as an electrode material, ITO electrode was also fabricated on the ZnO sensor device and its property was also examined.

6.2.1 Fabrication of ZnO-Based Sensor

ZnO films were deposited on borosilicate glass and polymeric PET substrates (thickness of 125 μm) by direct current magnetron sputtering using a metallic zinc target of 99.99 % purity at room temperature. The sputtering chamber was pumped down to a base pressure of 1×10^{-6} Torr. Prior to deposition, the targets were cleaned

by pre-sputtering for 20 minutes. The glass substrates were ultrasonically cleaned with acetone, ethanol and rinsed in de-ionised water and subsequently blown dried in compressed air. Operating pressure of 1 mTorr and DC power of 80 W were used in the sputtering. The substrate-to-target distance was kept at 14 cm and the deposition time was kept at 30 min. In this experiment, the argon gas and oxygen gas flow was kept at 20 sccm. Next, an AZO electrode layer was deposited by PLD using a shadow mask. Details of the AZO film fabrication are reported in section 5.2.1. For the next experiment, ITO and AZO were deposited as electrodes on ZnO at room temperature. For the ITO film deposition, the operating pressure was set at 10 mTorr with oxygen flow at 12 sccm. The deposition was performed at a repetition rate of 20 Hz and laser energy of 300 mJ. For comparison, Ti/Au contact electrode was deposited by e-beam evaporation through a shadow mask as shown in Figure 6.8. All the thicknesses of the electrodes are careful calibrated using AFM.

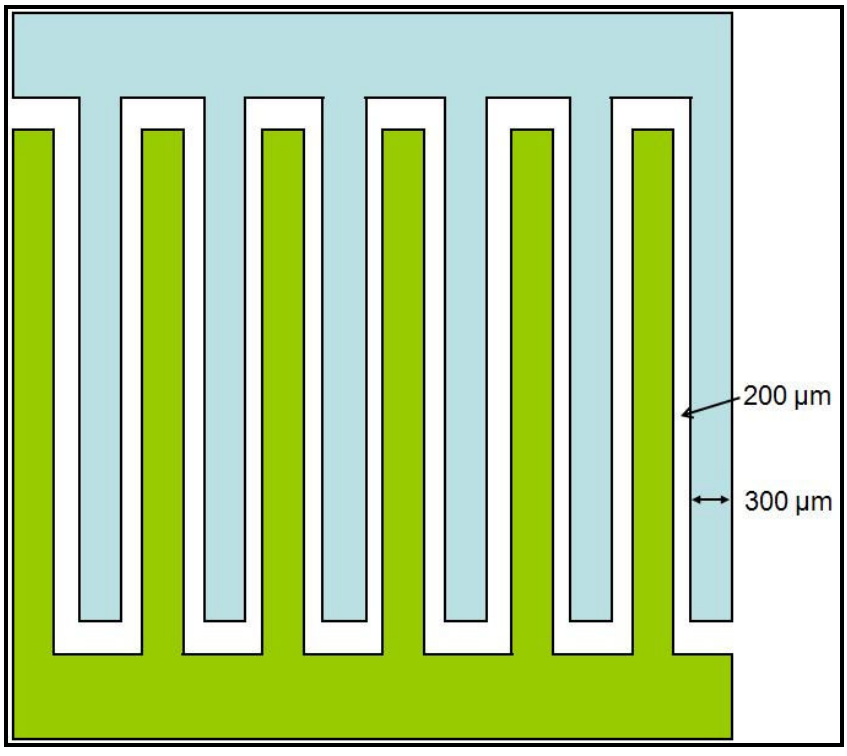

Figure 6.8 Shadow mask design of contact electrode for ZnO on PET and glass

6.2.2 Results and Discussion

Using the shadow mask, the ZnO, with a thickness of ~207.1 nm, covered an area of ~72.3 mm^2 on the 1 cm × 1 cm substrate. The total area covered by the electrode is ~23.08 mm^2. The light intensity from the AM 1.5 simulator is 100 mW/cm^2. Photocurrents were estimated as the difference in the currents measured between two electrodes when the sample was irradiated with and without a light source under a bias voltage of 3 V.

Figure 6.9 shows the I-V plot of the ZnO/PET structure with gold or AZO electrode under dark and light conditions. Care was taken to calibrate the thickness of these two electrodes to ensure that they are almost similar to a value of 100 ± 10 nm. It was observed that there is an increase in photocurrents measured under light irradiation for the structure with AZO electrode. This is likely due to the fact that AZO is a transparent electrode and light can travel to ZnO underneath the electrode, adding an additional irradiation area of ~23.08 mm^2. At an arbitrary +2.5 V bias, there is a ~3.7 times increase in the photocurrent as a result of using the transparent AZO electrode as compared to the gold electrode. It is to be noted that the electrodes have covered about one third of the ZnO film area.

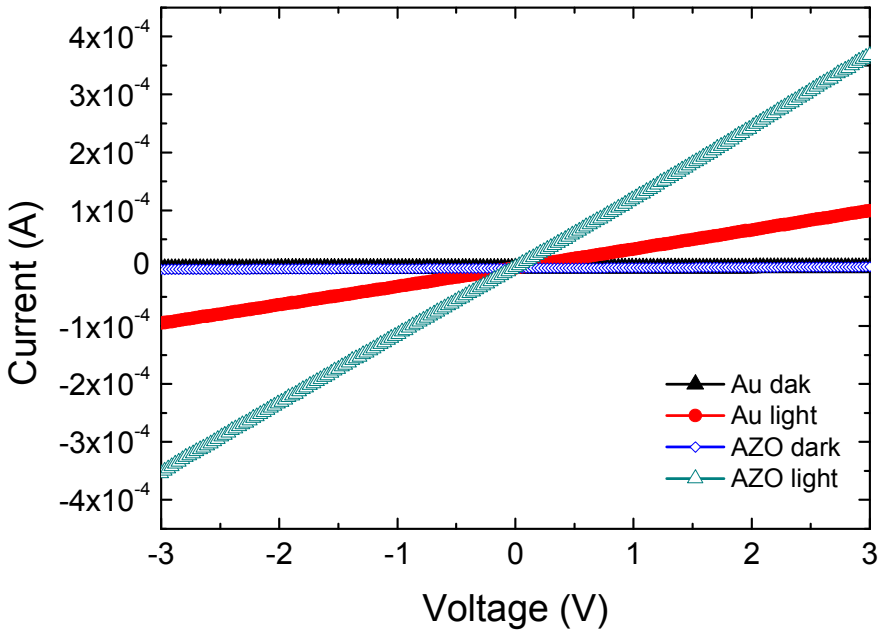

Figure 6.9 Current–voltage characteristics of ZnO/PET using gold electrode or AZO electrode under dark and light conditions. In this sample, using the gold electrode under dark ambience has similar current values as the AZO electrode under dark ambience

After confirming that using a transparent electrode material does increase the area of illumination, the performance of the AZO electrode structure was examined and compared with the ITO electrode structure as shown in Figure 6.10. Care was taken to calibrate the thickness of these two electrodes to ensure that they are almost similar to a value of 150 ± 10 nm. The photocurrents in Figure 6.10 are lower than in Figure 6.9 due to the use of a thinner ZnO film. As seen from Figure 6-10, due to the differences in electrode material used, the photocurrent is different even in the dark. Hence, the order of difference in the photocurrents between the dark and light conditions was compared instead. At an arbitrary +2.5 V bias, the photocurrent was increased by ~3 orders for the structure with ITO electrode as compared to that using

the AZO electrode. Measurements are not performed beyond ± 3V so as to prevent over-stressing the device.

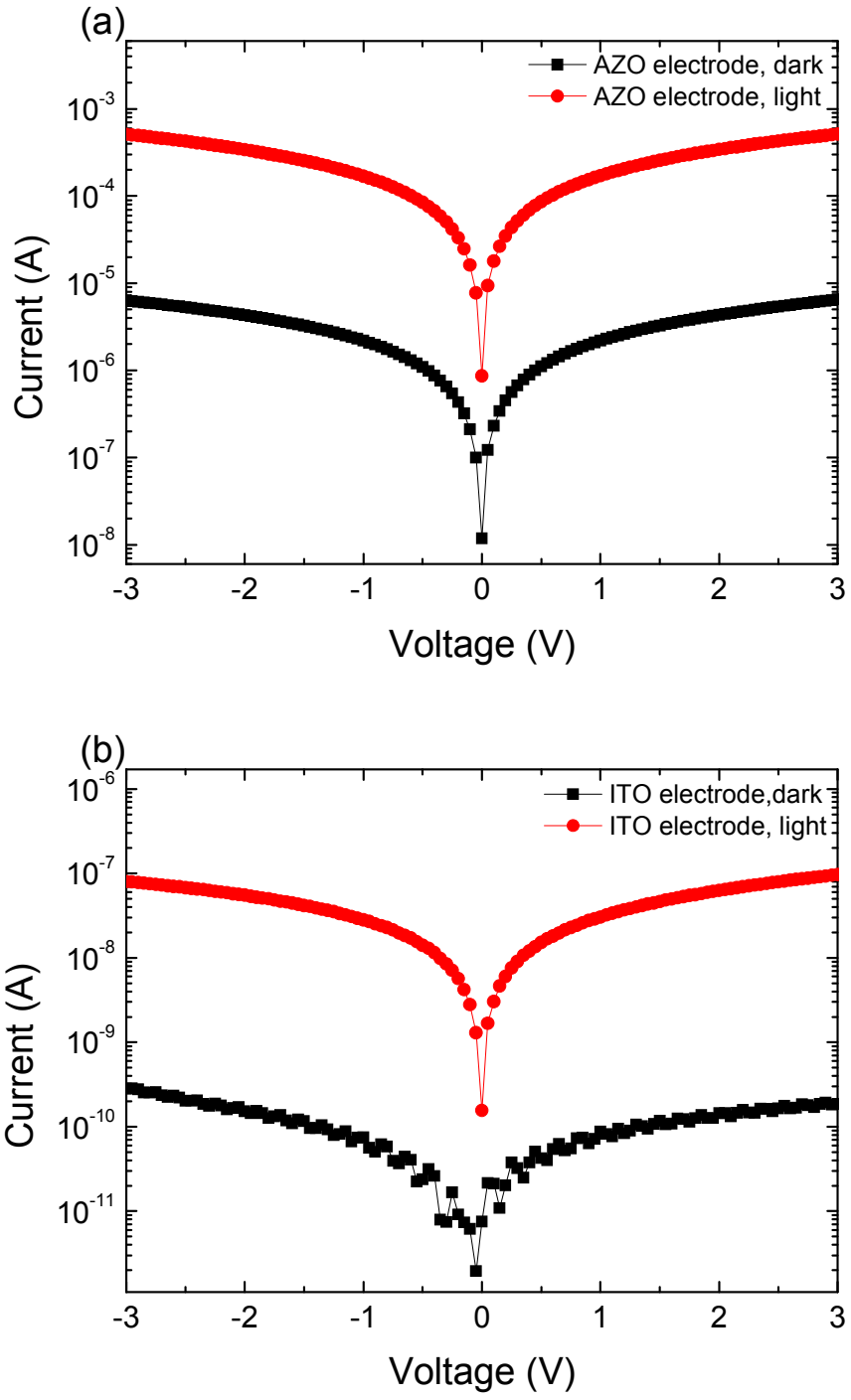

Figure 6.10 Current–voltage characteristics of ZnO on PET substrate using (a) AZO electrode and (b) ITO electrode

6.2.3 Concluding Remarks

A simple ZnO device for potential UV sensing application using AZO electrode compared to gold electrode was demonstrated. There is a ~3.7 time increase in the photocurrent due to the use of a transparent AZO electrode as compared to a gold electrode. In comparing the performance of ITO and AZO electrodes on UV sensing, AZO is still slightly inferior and more research is needed in this area to improve on its performance.

6.3 Thin Film Transistors

Thin film transistors are the building block of many other electronics devices; therefore it has attracted much research interest in this field. In this work, hafnium oxide (HfO_2) is used as the high dielectric constant (high-k) gate oxide while ZnO is used as a channel layer. A band alignment study was carried out to examine the interfaces of the HfO_2/ZnO heterostructure. Other than band alignment of the HfO_2/ZnO heterostructure, a bottom-gate ZnO-based thin film transistor (TFT) using high-*k* hafnium oxide was also fabricated. After high temperature stress, this TFT still showed good device performance using thin ZnO layers. However, leakage current, especially in the linear region, must be corrected to obtain accurate transfer characteristics, which is often ignored in many reported works. A simple and accurate method was introduced to correct for the drain current. Overall, a corrected threshold voltage of +3.7 V, a subthreshold slope of ~300 mV/decade, on-off current ratio of 10^6 with a saturation mobility of 4.6 cm^2/Vs were obtained for the TFT device. All these findings serve as an initial study on these potential combinations for future integration in fully transparent electronics.

6.3.1 Band Alignment of HfO_2/ZnO Film for TFT Application

Silicon dioxide (SiO_2) has been a good dielectric for complementary metal-oxide semiconductor field effect transistors for many years.[305,306] However, due to downscaling of transistors, SiO_2 as a gate dielectric is approaching its fundamental thickness limit, which is estimated as 7 Å.[307] At this critical thickness, the SiO_2 gate dielectric tends to be non-insulating due to significant quantum tunnelling of charge carriers, leading to large gate leakage currents.[308] Therefore, there is a need to replace SiO_2 with a suitable high-*k* gate dielectric material. It is critical that any replacement oxide must have sufficient band offsets of over 1 eV to act as a barrier for both electrons and holes.[309] One of these high-*k* candidates is hafnium oxide (HfO_2).[310,311] Hafnium oxide has a high dielectric constant ($k \sim 25$), good thermal stability on silicon, low leakage current and a good capacitive coupling between the gate and the channel layer that is important to achieve a good subthreshold swing.[312-314]

Aligning with the trend of transparent electronics, fully transparent transistors require both transparent channel layers and TCOs. ZnO is one potential transparent channel layer with carrier mobility greater than 1 cm^2/Vs. Intuitively; integrating HfO_2 gate dielectric with ZnO films is a potential candidate for a new generation of TFTs. Band offsets of the high-*k* oxide/ZnO system have been studied by Robertson *et al.* using a theoretical method based on the charge neutrality level (CNL). The CNL model takes into account only the bulk property of the materials, but does not include the effect of the interface structure.[305,306] Understanding the atomic and electronic structure at the interface is very important for controlling the band alignment at the interface of the HfO_2/ZnO heterostructure. Therefore, in this work, HfO_2 thin films

were deposited on ZnO substrates using DC sputtering at 400°C and the band alignment of the HfO_2 and ZnO (0001) interface was studied using x-ray photoemission spectroscopy (XPS). The result is of importance to investigate if this combination of materials has sufficient band offsets to act as a barrier for both electrons and holes.

6.3.1.1 **Experimental Details**

HfO_2 films (thin film of ~4 nm and thick film of ~15 nm) were deposited on single-crystalline ZnO (0001) substrates by using a ultrahigh-vacuum DC sputtering system at 400 °C in oxygen plasma with a partial pressure of 1.7×10^{-3} Torr. The ZnO substrates were ultrasonically cleaned in acetone, ethanol, rinsed in deionized water and then blown dry using compressed air before loading into the deposition chamber that was subsequently evacuated to a base pressure of 1×10^{-7} Torr. The deposition duration was 1 hour. After plasma oxidation, the samples were *in situ* transferred into the XPS analysis chamber with a background pressure of 1×10^{-10} Torr without breaking the vacuum. All the spectra were obtained in the constant pass energy mode with pass energy of 10 eV using a monochromatic Al (1486.6 eV) source. The binding energy scale was calibrated with pure Au, Ag, and Cu by setting the Au $4f_{7/2}$, Ag $3d_{5/2}$, and Cu $2p_{3/2}$ at binding energies of 83.98, 368.26, and 932.67 eV, respectively.

6.3.1.2 **Results and Discussion**

To investigate the band alignment of HfO_2 and ZnO using XPS, the core-level measurement method as proposed by Kraut *et al*. was used [287] The method is based on the assumption that the energy difference between the core level and valence band edge of the substrate remains constant with/without the deposition of the dielectric

film. In this method, the VBO of the HfO_2/ZnO interface can be calculated using the following equation:

$$\Delta E_V = \left(E_{Hf\,4f}^{HfO_2/ZnO} - E_{Zn\,3d}^{HfO_2/ZnO}\right) + \left(E_{Zn\,3d}^{ZnO} - E_{VBM}^{ZnO}\right) - \left(E_{Hf\,4f}^{HfO_2} - E_{VBM}^{HfO_2}\right) \qquad (6.2)$$

where E_i^S denotes the binding energy of the core level '*i*' for the sample '*s*' while E_{VBM}^S denotes the valence band maximum (VBM) for the sample '*s*'. The VBM position is determined as the intersection point between the linear extrapolation from the leading edge of the valence band spectrum with respect to the background.[305]

As shown in Figure 6.11(a), the valence band edge of ZnO (0001) substrate is located at 2.49 eV. In Figure 6.11(c), for the thick (15 nm) HfO_2, the VBM is at a value of 2.78 eV and the energy distance between the Hf $4f_{7/2}$ core level and the VBM, that is $(E_{Hf4f} - E_v)_{Hf}$, is obtained as 14.02 ± 0.05 eV. Figure 6.11(b) shows the VBM of bulk ZnO (0.5 mm substrate) is located at 2.63 eV, and the energy difference between the Zn $3d_{5/2}$ core level and the VBM, that is $(E_{Zn3d} - E_v)_{Zn}$, is 7.51 ± 0.05 eV. The measured core-level energy separation between Zn $3d_{5/2}$ and Hf $4f_{7/2}$ is 6.8 ± 0.05 eV, as shown in Figure 6.11(b), thus giving a valence band offset of 0.29 eV according to equation (6.2). However, this value of 0.29 eV is much higher than the value of 0.14 eV (2.63 - 2.49 = 0.14 eV) which is obtained by directly subtracting the two aligned valence band edges from the substrate and thin film. From these two values obtained from XPS, the 0.14 eV is believed to be more accurate as the calculation using equation (6.2) is based on averaging the photoelectron signal over many atomic layers from the thick HfO_2 which might inundate the contribution of the interfacial chemical dipoles to the valence band maximum.[288]

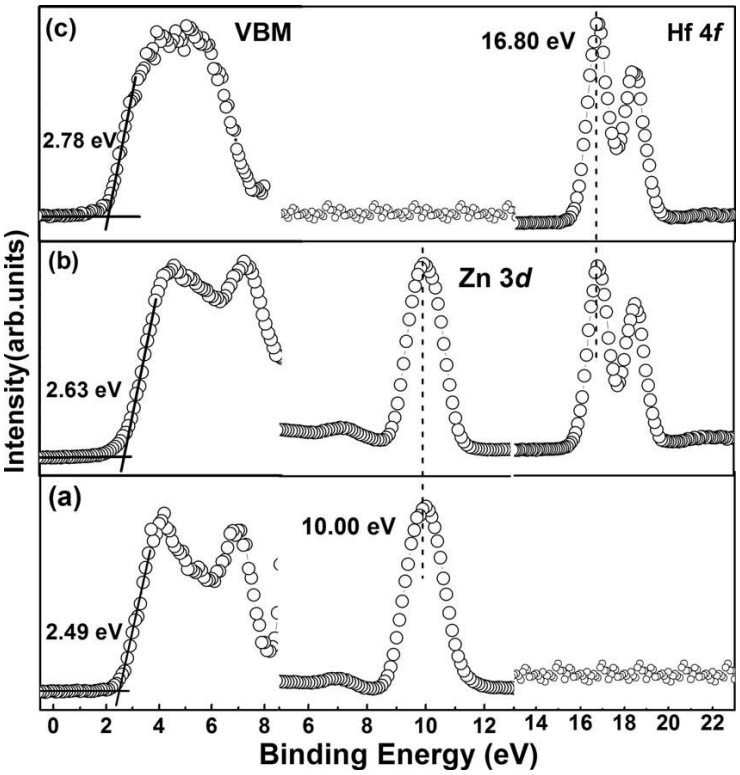

Figure 6.11 XPS spectra showing the measurements needed to determine the valence band offset. (a) Measured core-level separation at the interface between Hf 4f and Zn 3d of ZnO substrate , (b) Measured separation between Zn 3d and the valence band maximum for bulk ZnO, (c) Measured separation between Hf 4f core-level and the valence band maximum for 4 nm thick HfO_2

Using the valence band offset of 0.14 eV, the band gap of HfO_2 as 5.8 eV and the band gap of ZnO as 3.37 eV, the conduction band offset (CBO) is calculated by subtracting the valence-band offset from the energy gap of the substrate; this gives a CBO value of ~2.29 ± 0.05 eV. This value is in agreement with the theoretical calculation obtained by Robertson *et al.* [277] The small valence band offset (VBO) of 0.14 eV might not be sufficient to minimize the possible leakage current in the p-channel ZnO-based TFT. However, as ZnO is mainly used as a n-channel material, this hole barrier (i.e., the VBO) is not that important.

Figure 6.12 shows the schematic diagram of the band alignment at the HfO_2/ZnO heterojunction. The VBOs obtained from the core-level measurements and CBOs obtained with the measured values of the respective band gaps of the films can be seen from the diagram.

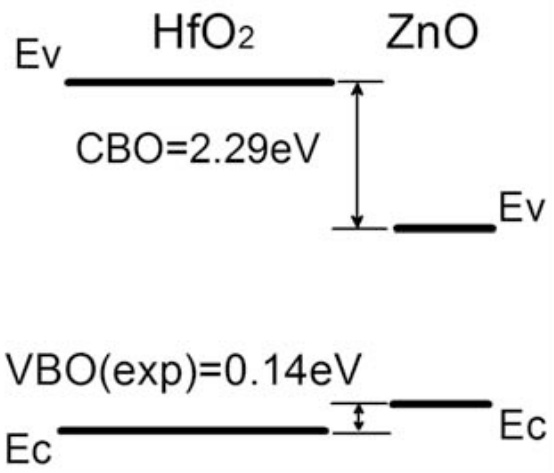

Figure 6.12 Schematic diagram showing the band alignment of the HfO_2/ZnO heterojunction. The VBOs can be obtained from the core-level measurements as can be seen from the diagram. The CBOs are obtained with the measured values of the respective band gaps of the films

6.3.1.3 **Concluding Remarks**

In conclusion, good quality HfO_2 have been deposited on ZnO (0001) substrates using DC sputtering. The energy band alignments for the HfO_2/ZnO heterojunction have been investigated using the x-ray photoemission method. The valence band offset of the HfO_2/ZnO heterojunction was obtained to be 0.14 eV ± 0.05 eV while the conduction band offset was obtained as 2.29 ± 0.05 eV. This shows that HfO_2 is a promising candidate as a high-*k* gate dielectric to integrate into full transparency ZnO–based electronics as there is a sufficient barrier height for electrons to minimize the gate leakage current.

6.3.2 Fabrication of TFT using ZnO Film as Channel Layer

Thin film transistors (TFTs) are important building blocks for applications in displays technology.[106,315] Hydrogenated amorphous silicon (a-Si:H) thin-film transistors (TFTs) with silicon nitride (Si_3N_4, dielectric constant k ~7) gate dielectric or organic semiconductors with silicon dioxide (SiO_2, k ~3.9) gate dielectric have been the main materials used in fabrication of TFTs in current displays.[316-319] Zinc oxide (ZnO) is a wide band gap (3.37 eV) n-type semiconductor that has various attributes such as non-toxicity, low cost and moderate Hall mobilities (>1 cm^2/Vs) at room temperature, which make it a good candidate as an alternative channel layer for TFTs.[179] The use of high-dielectric constant (high-k) oxides can increase the capacitive coupling between the gate electrode and the channel layer even at low gate voltages. Therefore, the integration of high-k dielectric into ZnO-based TFTs possibly allows for lower operation voltages that can be important for portable devices.[320] In addition, due to its wide band gap, the active channel layer is also not affected by photoexcitation from visible light that can adversely affect its performances.[320]

ZnO-based TFTs have thus far been favourably compared with amorphous silicon or even organic TFTs for electronics application. Most of the ZnO-based TFTs reported typically showed large threshold voltages such as +6 V or +10 V and high operating voltages of up to 40 V.[285,321,322] Many research groups have reported on the fabrication of ZnO-based TFTs using various high-k dielectrics such as Y_2O_3, HfO_2, Al_2O_3, $Zn_{0.7}Mg_{0.3}O$, TiO_x and superlattice structures of AlO_x and TiO_x.[2,133,138,286,302,312,323,324]Among these candidates, HfO_2, in particular, is considered to be one of the more promising materials due to its advantages mentioned in section 6.3.1. Therefore, in this work, the electrical characteristics of thin film

ZnO-based TFT with high-*k* HfO_2 as the gate dielectric were investigated to examine low operation voltage conditions. The effect of gate leakage current was clearly demonstrated and shown that it must be corrected to obtain accurate transistor transfer characteristics. A simple method to account for this leakage by examining an equivalent model is introduced. Using this model, one can obtain the true source-drain current without gate leakage influence and it is shown that this makes a substantial difference to measurements of threshold voltage and subthreshold voltage swing.

6.3.2.1 **Experimental Details**

HfO_2 films were prepared on p-type silicon (Si) substrates by reactive DC sputtering using a metallic hafnium (Hf) target (99.9% purity) at room temperature. Prior to deposition, the chamber was evacuated to a pressure < 10^{-6} Torr and the Hf target was pre-sputtered to remove any surface contamination or oxides on the target. The sputtering pressure was maintained at 5 mTorr with an oxygen partial pressure of 0.8 mTorr and an argon flow rate of 30 sccm. Prior to deposition, the substrates were ultrasonically cleaned for 5 minutes each in acetone, ethanol and deionized water, before being blown dry using compressed air. After depositing the high-*k* oxide, a ZnO active channel layer was fabricated using a ceramic ZnO target by pulsed laser deposition under an oxygen pressure of 5 mTor at room temperature with an oxygen flow rate of 10 sccm. Next, post-thermal annealing of the samples was carried out at 950 °C under an oxygen pressure of 5 mTorr for 30 min. The thickness of the HfO_2 and ZnO films were 85 nm and 25 nm respectively. For capacitance measurements, circular dots (diameter = 600 μm) were deposited using a shadow mask as top electrode to form capacitor test structures. For transistor characteristics measurement, rectangular source-drain contacts or top electrodes were deposited, giving a channel

length (L) of 200 μm and channel width (W) of 2000 μm (W/L = 10). The top electrode is a bilayer of Ti (5 nm) and Au (100 nm) while the bottom electrode is a 50 nm thick Au blanket layer; both electrodes were deposited by thermal evaporation. A bottom gate transistor as shown in Figure 6.13 was then fabricated for measuring the electrical properties of the TFT.

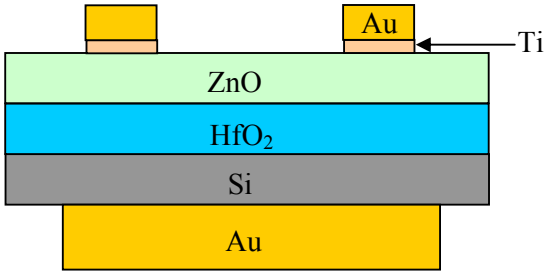

Figure 6.13 Schematic of the thin film transistor structure

6.3.2.2 **Results and Discussion**

Figure 6.14 shows a typical C-V plot of the HfO_2 gate dielectric deposited on p-type Si capacitor test structure measured at 100 kHz frequency. Using the relationship of a parallel-plate capacitor, the dielectric constant of HfO_2 is found to be 15 with an equivalent oxide thickness of 22 nm from the accumulation capacitance, similar to the typical values reported.[325,326] The flat band capacitance of Si is calculated using a hole concentration of 1.5×10^{16} cm^{-3}. This doping concentration is calculated from the resistivity value of the Si substrate and using the hole mobility of Si as 400 cm^2/Vs at room temperature. The total flat band capacitance of the structure can then be calculated and this gives an experimental flat band voltage of -0.88 V.[327] The extracted permittivity and flat band voltage values showed that deposited HfO_2 yielded reasonable electrical characteristics despite the high temperature annealing. The high temperature anneal typically enhances the permittivity of the

dielectric at the expense of a larger leakage current due to crystallization. Nam *et al.* has demonstrated that the advantages of annealing in 800 °C oxygen in terms of compensation of negative fixed charges and leakage current.[328] Similarly in this work, a good quality oxide was achieved by annealing in high oxygen partial pressure whereby during the process, defects were passivated.

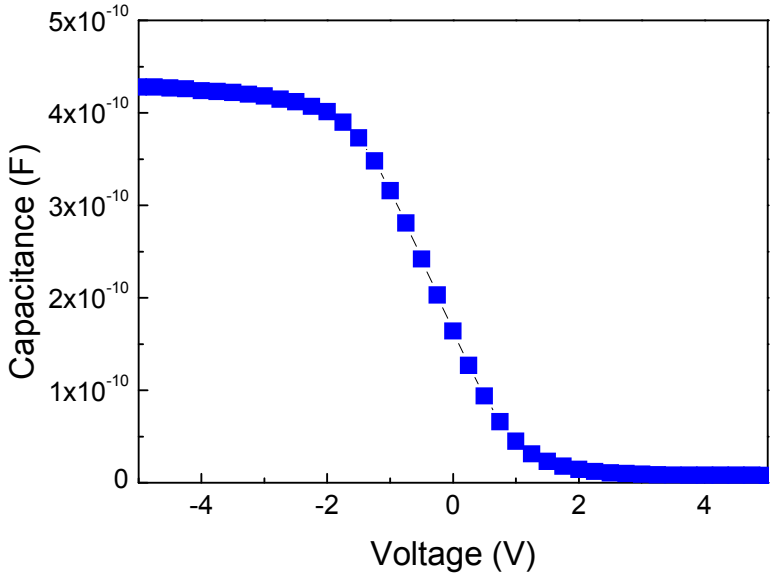

Figure 6.14 Capacitance-voltage plot of HfO_2 film on p-type silicon at 100 kHz frequency after anneal at 950 °C in oxygen pressure of 5 mTorr for 30 min. The measured capacitance in accumulation is 4.3×10^{-10} F

Figure 6.15 shows a typical output characteristic of an *n*-channel enhancement mode TFT whereby a non-zero gate voltage (V_G) is required to induce a conducting channel. However, it has to be noted that the increase in conductivity with a larger positive gate bias brings the ZnO semiconductor into higher surface accumulation unlike a typical n-channel Si transistor. An enhancement mode device is preferred as it has less power dissipation (normally off) and can reduce the complexity in circuit design.[183] The drain currents (I_D) show clear current saturation behaviour for larger drain voltages and the flatness of the I_D curves suggests that the channel length

modulation effect is negligible which is also observed in other ZnO TFT literature.[329]

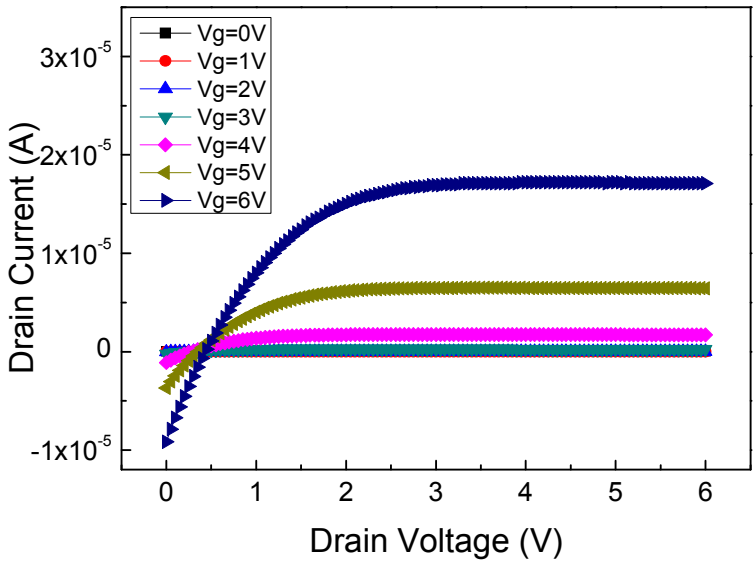

Figure 6.15 Output characteristics of HfO_2/ZnO TFT annealed at 950 °C in oxygen pressure of 5 mTorr for 30 min

Examining Figure 6.15 for drain voltages (V_D) of less than ~0.5 V, it is found that the measured drain current is actually negative and its magnitude is more pronounced at higher V_G. Many TFTs reported showed such phenomenon but its significance and importance is often not highlighted nor discussed.[329,330-332] Intuitively, the negative current is simply a result of the gate leakage current as described by Kwon *et al*. and is also likely for the annealed gate dielectric reported in this work.[333] This leakage current is also observed in other reported work with SiO_2 or even for unannealed samples.[334-335] While the drain-source current is expected to dominate the current flow of the whole device structure under saturation condition ($V_D > V_G - V_{TH}$), the presence of this gate leakage phenomenon affects greatly the determination of the subthreshold swing. Therefore, it is important that this gate

leakage current is accounted for in order not to be misled. Here, a simple and fast procedure was introduced to account for the gate leakage current using a simplified model of the TFT as shown in Figure 6.16. In this model, the measured currents (external) are represented by the source current (I_S), drain current (I_D) and gate current (I_G). Internally, if one assume independence in respective terminal currents (no significant cross-coupling and communication), one can divide I_G into a combination of the gate-source (i_{GS}) current and gate-drain (i_{GD}) current, as shown in equation (6.3). The actual drain-source current (or channel current) (i_{DS}) needed for the switching characteristics is shown in equation (6.4). Simple relationships between the external and internal currents are shown in the equations below:

$$I_G = i_{GS} + i_{GD} \tag{6.3}$$

$$i_{DS} = I_D + i_{GD} \tag{6.4}$$

In equation 6.4, for a fixed applied gate voltage, the gate leakage current consists of both the i_{GS} and i_{GD}. i_{GS} will be a constant regardless of the V_D variation. Therefore, i_{GS} can easily be found from I_G by setting V_G and V_D to be of equal potential (i_{GD} = 0; $I_G = i_{GS}$ from equation (6.3)). Once this is known, one can easily generate the variation of i_{GD} with V_D using the known constant i_{GS}. With the knowledge of i_{GD} variation with V_D, one can compute the true drain-source current i_{DS} without the influence from any gate leakage currents. Figure 6.17 shows a plot of the corrected I_D as a function of V_D. It can be observed that the 'negative current phenomenon' is clearly corrected for and this indicates good accuracy in the assumption mentioned previously and method for correction. While one expected the saturation current not to be affected significantly, the region of I_D increase is substantially different and this is of utmost importance in the linear and non-linear region (before saturation) whereby V_{TH} and subthreshold swing are computed.

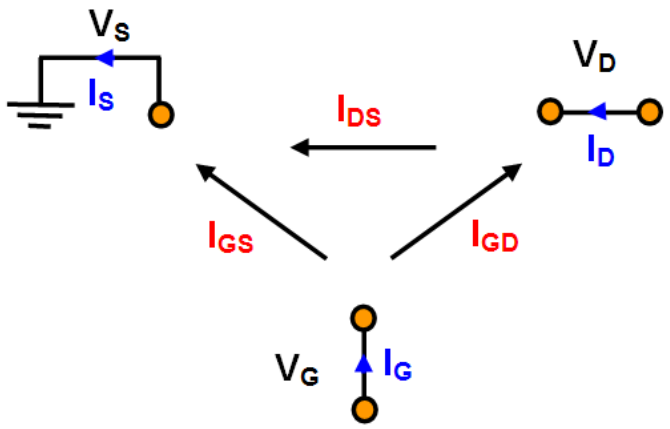

Figure 6.16 Simplified operation model of the TFT

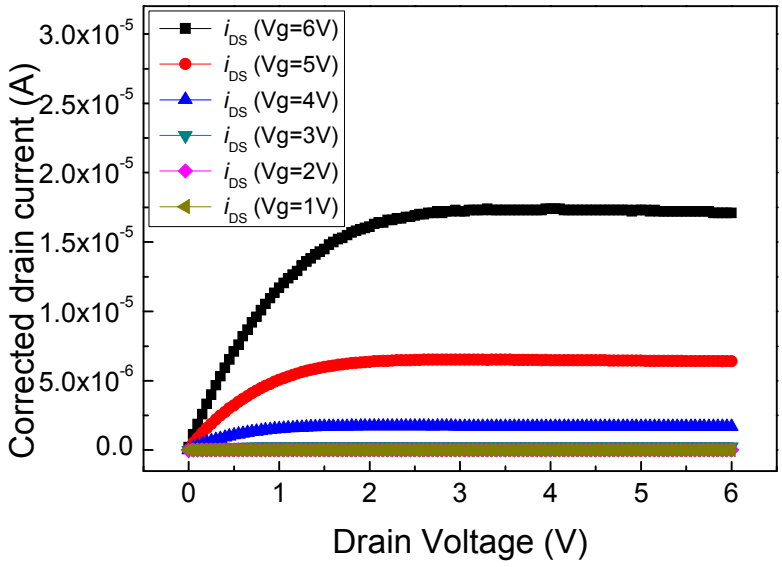

Figure 6.17 Plot of corrected drain current as a function of drain voltage

In the linear region, I_D is related to the gate voltage V_G by equation (6.5) as follows:

$$I_D = \left(\frac{W}{L}\mu_n C_{ox}\right)\left(V_G - V_{TH} - \frac{V_D}{2}\right) \text{ for } V_D << (V_G\text{-}V_{TH}) \quad (6.5)$$

where C_{ox} is the oxide capacitance per area, μ_n is the electron mobility and V_{TH} is the threshold voltage.[336] The extrapolation to the gate voltage axis in the I_D versus V_G plot gives the experimental value of (V_{TH} + 1/2V_D). Even without considering the difference in selecting the correct region, the uncorrected data yields a V_{TH} of +3.49 V while the corrected data gives a V_{TH} of +3.78 V at V_D = 1 V due to a result of a change in the slope. More importantly, the corrected reading of the V_{TH} should be taken at ~V_D = 0.5 V, something that is not possible for the uncorrected data due to the gate leakage shown in the plot at the 0 to 1 V region of V_D. Therefore, a true V_{TH} of +3.78 V was obtained with our corrected i_{DS}. The difference of ~0.3 V (~8 %) is substantial and demonstrates the importance of correction for the gate leakage current especially for the linear and non-linear regions of the I_D-V_D plot. Uncorrected I_D typically gives a lower estimate of the V_{TH} since gate leakage current contributes and forms a significant part of the measured I_D. This can give a false representation of actual device parameters in this region. The second significant influence is in the calculation of the subthreshold swing (S), where

$$S = (-[dV_{GS}/d(\log I_{DS})]) \quad (6.6)$$

From the uncorrected I_D, S of 350 mV/decade was measured while the corrected I_D gives S of 300 mV/decade instead. This again shows that the correction is important to obtain accurate transfer characteristics of the TFT. Finally, the saturation mobility (μ_{sat}) was reported by examining the equation in the saturation drain current equation (for $V_D > V_G$-V_{TH}). In the saturation region (V_D = 6 V), the μ_{sat} calculated was 3.55

cm^2/Vs for the uncorrected data while the corrected μ_{sat} is 4.54 cm^2/Vs. This value is in the range of the typical mobility value reported ranging from 0.2 to $7cm^2/Vs$.[337] While the saturation current is not greatly affected, it is noted that the equation relies on an accurate prediction of the V_{TH} that implicitly determines the amount of carrier concentration. The uncorrected measurements therefore give an inaccurate V_{TH} and hence a different derived μ_{sat} value. Overall, the on-to-off current ratio in the saturation region was measured to be about $\sim 10^6$ which is similar to the values reported in other literatures.[338,339] This demonstrates the viability of the device even for the thin semiconductor (ZnO ~25 nm) used in the TFT.

6.3.2.3 **Concluding Remarks**

In conclusion, a n-channel enhancement mode ZnO-based TFT device using HfO_2 as the gate dielectric was fabricated with reasonable transistor properties. The 'negative current phenomenon', often observed in many reports, was found to be related to the gate leakage current. A simple and accurate procedure was presented to account for this gate leakage that is critical for accurate electrical measurements in order to obtain accurate transistor transfer characteristics.

Chapter 7 Conclusion

7.1 Summary of Findings

The effect of oxygen pressure and substrate temperature on the structural, surface morphology, optical and electrical properties of GZO thin films, fabricated using pulsed laser deposition, were investigated. From the results, one observes that oxygen has significant influence on the vacancy and interstitial defects at the low and mid oxygen pressure regimes. At higher oxygen pressure, variations in the carrier concentration and mobility were observed and this was attributed to the in-plane orientation of the grains as observed in the XRD large area diffraction maps. Therefore, we conclude that to achieve GZO films with good electrical properties, there should be a balance between too much oxygen (causing oxygen interstitials) and too little oxygen (causing oxygen vacancies) during deposition at room temperature. The important role of grain boundary scattering is demonstrated by samples deposited at higher oxygen pressures and this is affirmed by samples deposited at higher temperatures. After examining the electrical characteristics and correlating these to the structural properties, optical properties of the GZO films were also examined and a transparency index that takes into account the different intensity of the practical AM 1.5 solar spectrum was introduced. This transparency index takes the absolute value of the total transmitted solar spectrum and normalized it with the film thickness, resulting in an accurate account of transmission of the film across the entire solar spectrum. This makes the normalized transparency index a versatile and useful standard for comparison especially for photovoltaics application. Using this normalized transparency index, the transparency at different wavelengths was examined and the influence by oxygen pressure, carrier concentration and band gap

changes were clearly demonstrated. Therefore, a clear understanding of factors that can affect the transmittance of the thin film resulted, which will be important for obtaining good quality transparent electrodes. In this work, room temperature deposited GZO films having low resistivity of ~3.9×10^{-4} Ω-cm with a transparency index of ~0.84 at an oxygen pressure of 1×10^{-4} Torr was obtained. In addition, the optimized GZO films have a root mean square roughness of less than 1 nm. This is crucial for GZO films to be a potential transparent electrode material candidate for use in plastic electronics.

Other than single layer GZO films, metal/semiconductor layered films were also investigated. Using pulsed laser deposition and e-beam evaporation, high quality transparent and conductive Ag/GZO, Ag/Ge/GZO, GZO/Ag/GZO and GZO/Ag/Ge/GZO thin film structures, grown on low cost borosilicate glass substrates, were obtained. In this work, the effect of variation in the metal (Ag) thickness on the surface morphology, electrical and optical properties were investigated. In addition, the effect of a Ge buffer layer prior to depositing the Ag layer was also investigated. With the addition of a Ge buffer layer, the surface morphology of Ag/GZO and Ag/Ge/GZO film structures were improved with lower rms roughness for all thicknesses of Ag. Additionally, the electrical resistivity was also improved (decreased) by one order for the Ag/Ge/GZO structure and half an order for the GZO/Ag/Ge/GZO structure. In terms of the optical property, an additional Ge buffer layer also improved the transparency of the investigated structures in the UV-Visible region and enhanced the reflection in the NIR range.

After examining GZO films, aluminum doped zinc oxide (AZO) was also investigated. AZO films on both borosilicate glass and flexible PET substrates were deposited at room temperature using pulsed laser deposition. In this work, the structural, electrical and optical properties were examined as a function of oxygen pressure and film thickness. An appropriate thickness of good quality films is important as it is directly related to the cost of material needed. The refractive index of AZO film on glass was also obtained, with a value of 1.9 at a wavelength of 600 nm which is similar to ITO. For the optimized AZO/PET structure, a low resistivity of ~6.6×10^{-4} Ω-cm with normalized transparency index of 0.78 (78 % of total solar spectrum transmitted) was achieved. With the results obtained, the optimized highly conducting and high transparency AZO thin film (film thickness of 110 ± 10 nm) can be an ideal candidate to replace ITO, making it a possible choice for low cost transparent conducting oxides for flexible solar cells and flat panel displays.

Next, AZO multilayer sandwich structures, obtained by varying the Ag thickness and various stacking combinations, were examined. All the multilayer structures resulted in a lower resistivity as compared to a single AZO thin film but at the expense of lower transparency in the visible region. However, the multilayer sandwich structure is still beneficial as it provides a control over the transparency of the film in the NIR region while having moderate transparency in the visible region, by controlling the number of sandwich stacks of semiconductor/metal/semiconductor layers and the thickness of the Ag layer. In this work, a low resistivity of ~2.2 x 10^{-4} Ω-cm, carrier mobility of ~3.1 cm^2/Vs and a carrier concentration of ~9.1 x 10^{21} cm^{-3} and transmittance of ~75 % at a wavelength of 550 nm were obtained for the case of a single sandwich structure with 10 nm thick Ag layer, which gives optimized electrical

properties with high transparency. Single sandwich structure has a transparency of up to ~75 % in the visible range and less than 20 % in the NIR range. Compared to a triple sandwich structure, the visible transparency is reduced to ~45 % but the NIR transparency is less than 5 %. Therefore, depending on the desired application of these films, the sandwich structure can provide control of transparency in the NIR region and also fulfil the aim of seeking a low-cost TCO on low-cost substrate.

Having obtained good quality GZO and AZO films on low cost glass and flexible plastic substrates, the next part of the work was to incorporate them into test structures to demonstrate potential applications in photovoltaics, sensing and electronics. For photovoltaic applications, investigation on potential p-n heterojunctions using p-type cuprous oxide (Cu_2O) and n-type (gallium)-doped ZnO in a Cu_2O/(G)ZnO heterostructure was performed. As the pure phase of Cu_2O was difficult to obtain, the experimental conditions for obtaining pure Cu_2O were optimized using DC sputtering by varying the oxygen partial pressure for room temperature deposition. Next, (G)ZnO was deposited onto the Cu_2O film on ITO-glass substrate by pulsed laser deposition to form the p-n heterojunction. In photovoltaics application, charge separation at the interface is critical as it affects the efficiency of the heterojunction, and therefore the band alignment of this heterojunction is studied. This heterojunction structure gives a Type II band structure with a valence band offset of ~2.82 to 2.85 eV. The invariant valence band offset shows that doping (non-degenerate) has no major influence on the band line up even for heterojunctions of narrow band gap materials. This band alignment study shows that the Cu_2O/(G)ZnO heterojunction is suitable for solar cell application based on energy levels consideration.

In order to investigate the effect of using transparent and non-transparent electrodes on a photo-sensing ZnO device, an experiment was carried out to investigate the photoconductivity of undoped ZnO film using different electrodes such as gold, AZO and ITO. A shadow mask was used in this experiment with an electrode area which covered ~32 % of the ZnO sample area. An increase of ~3.7 times in the photocurrents was observed due to the use of transparent AZO electrode as compared to gold electrode. In comparing the performance of ITO and AZO electrodes on photocurrent sensing, AZO is still slightly inferior, and hence more research is needed in this area.

For electronics application, thin film transistors are demonstrated. Good quality HfO_2 has been deposited on ZnO (0001) substrates using DC sputtering. The energy band alignment for the HfO_2/ZnO heterojunction was investigated using x-ray photoemission. The valence band offset at the HfO_2/ZnO heterojunction was obtained to be 0.14 eV ± 0.05 eV while the conduction band offset was obtained as 2.29 ± 0.05 eV. This shows that HfO_2 is a promising high-*k* gate dielectric to integrate into full transparency ZnO–based electronics as there is a sufficient barrier height for electrons. Besides the band alignment study, bottom-gate ZnO-based thin film transistors (TFTs) using high-*k* HfO_2 as a gate dielectric was fabricated. Overall, a corrected threshold voltage of +3.7 V, a subthreshold swing of ~300 mV/decade, on-off current ratio of 10^6 and a saturation mobility of 4.6 cm^2/V-s were obtained. All these findings serve as an initial study on the potential combinations for future integration in fully transparent electronics.

7.2 Future Works

7.2.1 Studying the Mechanical Properties of Group III-Doped ZnO Films

For flexible substrates, it is known that too thick a film will crack easily due to strain energy on the film surface. Currently, commercial ITO/PET has a sheet resistance of 30 Ω/□ for a nominal 100 nm thickness.[144] In order for Group III-doped ZnO to be a viable alternative to ITO on flexible substrates, the mechanical properties of GZO and AZO films on flexible polymeric substrates, such as the degree of bending, bending curvature and number of bending cycles and its reliability (bending), need to be investigated further for potential commercialization. Thus, more work need to be done to improve on the electrical and mechanical properties of Group III-doped ZnO film on flexible substrates.

7.2.2 P-type TCOs for Photovoltaic Devices

To realise photovoltaics devices, there need to be a p-type semiconductor which Cu_2O is one potential candidate. More investigations can be done to improve the electrical properties of Cu_2O so as to increase the electron transport in the photovoltaic devices. Other than pure Cu_2O, nitrogen doping in Cu_2O can also be investigated to shift the optical bandgap towards the UV region which might improve the transparency of Cu_2O. Cu_2O films have also been shown to demonstrate resistive switching effect.[340] Currently, the electrodes used in resistive switching structures are mainly metals. Group III-doped ZnO electrodes or other TCOs can perhaps also be applied in resistive switching devices where transparency of the electrodes is required. More researches are needed in this area.

7.2.3 Integrating GZO and AZO films as Transparent Electrodes

ZnO is known to have a large exciton energy of ~60 meV and is an ideal candidate for UV-blue LED.[341] Using full transparent electrodes can also enhance the optical power and decrease the forward voltage of GaN-based LED.[211] In the past, organic solar cells mostly make use of ITO as the electrode. Recently, some research work using AZO as an electrode for organic solar cells has been reported.[342,343] Therefore, Group III-doped ZnO films still have vast potential applications in various fields that are yet to be explored. In the near future, work can also be done to incorporate doped zinc oxide as electrode materials for future electronic devices.

7.2.4 Fabricating High Performance Transparent Thin Film Transistors

Transparent amorphous oxide semiconductors have gained lots of attraction for potential applications in high drive current devices and large area displays due to their superior electrical performance compared with conventional amorphous silicon and polycrystalline TFTs. Among these transparent oxide semiconductors, IGZO has gained popularity due to IGZO TFTs having field effect mobility exceeding that of amorphous silicon TFTs by a factor of 100, small sub-threshold swing, low off current, stability under electrical stress and low processing temperature.[344] Thus, additional research effort is needed to achieve high quality fully transparent IGZO-based transistors on low cost transparent glass and even on flexible plastic substrates.

7.2.5 Band Alignment of Transparent Amorphous Oxide

Since the transistor is a building block for many devices, having an amorphous IGZO channel layer is not enough. Investigation of stable amorphous dielectrics such as lanthanum aluminum oxide (LAO) and yttrium oxide (Y_2O_3) is also essential. Therefore, the effect of oxygen partial pressure, substrate temperature, film thickness and various post deposition annealing methods on these amorphous layers can be investigated. Incorporating high-k gate dielectrics into TFTs will also help to improve the device performance. In order to further understand the device performance, there is a need to understand the charge transport between the interfaces so as to minimise the leakage current. Therefore, the band alignment of the IGZO on dielectric layers such as LAO and Y_2O_3 can also be investigated. With these band alignment studies, there is a better understanding on the applications in transistors, photovoltaics, and even sensors. Thereby, a fully transparent transistor could be made possible using IGZO, LAO, GZO as electrode and as a transparent substrate. An additional research area to explore is to fabricate these devices on low cost transparent glass substrates and even on flexible plastic substrates.

References

[1] Granqvist, C. G. Transparent Conductors as Solar Energy Materials: Panoramic Review, Sol. Energy Mater. Sol. Cells, 91, pp. 1529-1598. 2007.

[2] Wager, J. F. Transparent Electronics, Science, 300, pp. 1245-1246. 2003.

[3] Nomura, K., H. Ohta, K. Ueda. T. Kamiya, M. Hirano and H. Hosono. Thin-Film Transistor Fabricated in Single-Crystalline Transparent Oxide Semiconductor, Science, 23, pp. 1269-1272. 2003.

[4] Granqvist, C.G. Transparent Conductive Electrodes for Electrochromic Devices: A Review, Appl. Phys. A, 57, pp. 19-24. 1993.

[5] Somani, P. R. and S. Radhakrishnan. Electrochromic Materials and Devices: Present and Future, Mater. Chem. Phys., 77, pp. 117-133, 2002.

[6] T. Minami. Transparent Conducting Oxide Semiconductors for Transparent Electrodes, Semicond. Sci. Technol., 20, pp. S35-S44. 2005.

[7] Granqvist , C.G. and A. Hultåker. Transparent and Conducting ITO films: New Developments and Applications, Thin Solid films, 411, pp. 1-5. 2002.

[8] Benjamin, P. and C. Weaver. Adhesion of Metal Films to Glass, Proc. Roy. Soc. London Ser. A, 254, 1277, pp. 177-183. 1960.

[9] http://www.abodewindowfilms.co.uk/acatalog/Silver_Reflecftive_Privacy_Window_Film.html last accessed 30th Apr 2012

[10] Busch, G. Early History of the Physics and Chemistry of Semiconductors – From Doubts to Fact in a Hundreds Years, Eur. J. Phys. 10, pp. 254-264. 1989.; Badeker, K. Ueber die elektrische Leitfähigkeit und die thermoelektrische Kraft einiger Schwermetall-Verbindungen (On the Electrical Conductivity and Thermoelectric Power of some Heavy Metal Compounds), Ann. Phys. (Leipzig) 22, pp.749-746. 1907.

[11] Miller, P. H. JR. The Electrical Conductivity of Zinc Oxide, Phys. Rev., 60, pp. 890-895. 1941.

[12] Busch, G. Early History of the Physics and Chemistry of Semiconductors – From Doubts to Fact in a Hundreds Years, Eur. J. Phys., 10, pp. 254-264. 1989.; Fritsch, O., Elektrisches and optisches Verhalten von Halbleitern. Electricches Messungen an Zinkoxid (Electrical and Optical Behavior of Semiconductors. Electricches measurements of zinc oxide), Ann. d. Physik, 414, 4, pp. 375-401. 1935.

[13] Chopra, K. L., S. Major and D. K. Pandya. Transparent Conductors – A Status Review, Thin Solid Films, 102, pp. 1-46. 1983.

[14] Özgür, Ü., Ya. I. Alivov, C. Liu, A. Teke, M. A. Reshchikov, S. Doğan, V. Avrutin, S.-J. Cho and H. Morkoç. A Comprehensive Review of ZnO Materials and Devices, J. Appl. Phys., 98, pp. 041301-1-041301-103. 2005.

[15] Janotti, A. and C. G Van de Walle. Fundamentals of Zinc Oxide as a Semiconductor, Rep. Prog. Phys., 72, pp. 126501-126529. 2009.

[16] Klaus, E., K. Andreas and R. Bernd (Eds.). Transparent Conductive Zinc Oxide. pp. 1-27. New York: Springer Science+Business Media, LLC. 2008.

[17] Pearton, S. J., D. P. Norton, K. Ip and Y. W. Heo and T. Steiner. Recent Advances in Processing of ZnO, J. Vac. Sci. Technol. B, 22, 3, pp. 932-948. 2004.

[18] Facchetti, A. and T. J. Marks. Transparent Electronics: From Synthesis to Applications. pp. xvi- xviii, John Wiley & Sons, Ltd. 2010.

[19] Moon, C. -H. The Effect of the ITO Electrode Structure on the Luminous Characteristics of a Plasma Display Panel, IEEE Trans. Plasma Sci., 38, 9, pp. 2445-2450. 2010.

[20] http://www.minormetals.com/ last accessed 30th Apr 2012

[21] Tolcin , Amy C. 2009 Minerals Yearbook- Indium [advance release], pp. 1-6, Jan. 2011.

[22] Kumar, A. and C. Zhou. The Race to Replace Tin-Doped Indium Oxide: Which Material Will Win?, ACS Nano, 4, 1, pp. 11-14. 2010.

[23] Wu, Z., Z. Chen, X. Du, J. M. Logan, J. Sippel, M. Nikolou, K. Kamaras, J. R. Reynolds, D. B. Tanner and A. F. Hebard. Transparent Conductive carbon nanotube films, Science, 305, pp. 1273-1276. 2004.

[24] Tung, V. C., L. Chen, M. J. Allen, J. K. Wassei, K. Nelson, R. B. Kaner, and Y. Yang. Low-Temperature Solution Processing of Graphene − Carbon Nanotube Materials for High-Performance Transport Conductors, Nano Lett., 9, pp. 1949-1955. 2009.

[25] Kang, M.-G. and L. J. Guo. Nanoimprinted Semitransparent Metal Electrodes and their Application in Organic Light-Emitting Diodes, Adv. Mater., 19, 10, pp. 1391-1396. 2007.

[26] Andersson, A., N. Johansson, P. Bröms, N. Yu, D. Lupo and W. R. Salaneck. Holographic Data Storage in Amorphous Polymers, Adv. Mater., 10, 11, pp. 855-859. 1998.

[27] Huang, Y. -C., Z. -Y. Li, H. -H. Chen, W. -Y. Uen, S. -M. Lan, S. -M. Liao, Y. -H. Huang, C. -T. Ku, M. -C. Chen, T. -N. Yang and C. -C. Chiang. Characterizations of Gallium-doped ZnO Films on Glass Substrate Prepared

by Atmospheric Pressure Metal-Organic Chemical Vapor Deposition, Thin Solid Films, 517, 18, pp. 5537-5542. 2009.

[28] Hamaguchi,T., K. Omae, T. Takebayashi, Y. Kikuchi, N. Yoshioka, Y. Nishiwaki, A. Tanaka, M. Hirata, O. Taguchi and T. Chonan, Exposure to Hardly Soluble Indium Compounds in ITO Production and Recycling Plants is a New Risk for Interstitial Lung Damage, Occup. Environ. Med., 65, pp. 51-55. 2008.

[29] Bhosle, V. and J. Narayan. Microstructure and Electrical Property Correlations in Ga:ZnO Transparent Conducting Thin Films, J. Appl. Phys., 100, pp. 093519-1- 093519-7. 2006.

[30] Minami, T. Substitution of Transparent Conducting Oxide Thin Films for Indium Tin Oxide Transparent Electrode Applications, Thin Solid Films, 516, pp. 1314-1321. 2008.

[31] Xiao ,Y. B., S. M. Kong, E. H. Kim and C. W. Chung, Characteristics of Indium Zinc Oxide Thin Films Prepared by Direct Current Magnetron Sputtering for Flexible Solar Cells, Sol. Energy Mater. Sol. Cells, 95, 1, pp. 264-269. 2011.

[32] Khrypunov, G., A. Romeo, F. Kurdesau, D. L. Bätzner, H. Zogg and A. N. Tiwari, Recent Developments in Evaporated CdTe Solar Cells, Sol. Energy Mater. Sol. Cells, 90, pp. 664-677, 2006.

[33] Hung, L. S. and C. H. Chen. Recent Progress of Molecular Organic Electroluminescent Materials and Devices, Mat. Sci. and Eng. R: Rep., 39, pp. 143 -222. 2002.

[34] Tak, Y. -H., K. -B. Kim, H. -G. Park, K. -H. Lee and J. -R. Lee. Criteria for ITO (indium–tin-oxide) Thin Film as the Bottom Electrode of an Organic Light Emitting Diode, Thin Solid Films, 411, pp. 12-16. 2002.

[35] Adurodija, F. O., L. Semple and R. Brüning. Crystallization Process and Electro-Optical Properties of In_2O_3 and ITO Thin Films, J. Mater. Sci., 41, pp. 7096-7102. 2006.

[36] Ma, H., J. -S. Cho and C. -H. Park. A Study of Indium Tin Oxide Thin Film Deposited at Low Temperature Using Facing Target Sputtering System, Surf. Coat. Technol., 153, pp. 131-137. 2002.

[37] Jonda, C., A. B. R. Mayer, U. Stolz, A. Elschner and A. Karbach. Surface Roughness Effects and Their Influence on the Degradation of Organic Light Emitting Devices, J. Mater. Sci., 35, pp. 5645-5651. 2000.

[38] Minami, T. Present Status of Transparent Conducting Oxide Thin-Film Development for Indium-Tin-Oxide (ITO) Substitutes, Thin Solid Films, 516, pp. 5822-5828. 2008.

[39] Jung, K., W. -K. Choi, S. -J. Yoon, H. J. Kim and J. -W. Choi. Electrical and Optical Properties of Ga doped Zinc Oxide Thin Films Deposited at Room Temperature by Continuous Composition Spread, Appl. Surf. Sci., 256, pp. 6219-6223. 2010.

[40] Gong, L., J. Lu and Z. Ye. Transparent and Conductive Ga-doped ZnO Films Grown by RF Magnetron Sputtering on Polycarbonate Substrates, Sol. Energy Mater. Sol. Cells, 94, pp. 937-941. 2010.

[41] Fortunato, E., L. Raniero, L. Silva, A. Gonc-alves, A. Pimentel, P. Barquinha, H. Aguas, L. Pereira, G. Gonc-alves, I. Ferreira, E. Elangovan and R. Martins. Highly Stable Transparent and Conducting Gallium-doped Zinc Oxide Thin Films for Photovoltaic Applications, Sol. Energy Mater. Sol. Cells, 92, pp.1605-1610. 2008.

[42] Park, H. -K., J. -A. Jeong, Y. -S. Park, S. -I. Na, D. -Y. Kim and H. -K. Kim, Room-Temperature Indium-Free Ga:ZnO/Ag/Ga:ZnO Multilayer Electrode for Organic Solar Cell Applications, Electrochem. Solid-State Lett., 12, pp. H309-H311. 2009.

[43] Thomas, G. Invisible Circuits, Nature, 389, pp. 907-908. 1997.

[44] Hanus, F., A. Jadin and L.D. Laude, Pulsed Laser Deposition of High Quality ITO Thin Films, Appl. Surf. Sci., 96-98, pp. 807-810. 1996.

[45] Kogure, T. and Y. Bando. Formation of ZnO Nanocrystallites on ZnS Surface by Electron Beam Radiation, J. Electron Microsc., 47, 2, pp. 135-141. 1998.

[46] Ashrafi, A. B. M. A., A. Ueta, A. Avramescu, H. Kumano, I. Suemune, Y.W Ok and T.Y. Seong. Growth and Characterization of Hypothetical Zinc-Blende ZnO Films on GaAs (001) Substrates With ZnS Buffer Layers, Appl. Phys. Lett., 76, pp. 550-552. 2000.

[47] Bates, C. H., W. B. White and R. Roy. New High-Pressure Polymorph of Zinc Oxide, Science, 137, pp. 993-994. 1962.

[48] Decremps, F., J. Z. Jiang and R. C. Liebermann. New Phase Boundary and High-Pressure Thermoelasticity of ZnO, Europhys. Lett., 51, pp. 268-274. 2000.

[49] Nause, J. E. Cermet Inc, USA –III-Vs Review, 12, 4, pp. 28-31, July-August 1999.

[50] Look, D. C., D. C. Reynolds, J. R. Sizelove, R. L. Jones, C. W. Litton, G. Cantwell and W. C. Harsch. Electrical Properties of Bulk ZnO, Solid-State Comm., 105, 6, pp. 399-401. 1998.

[51] Oshima, E., H. Ogino, I. Niikura, K. Maeda, M. Sato, M. Ito and T. Fukuda. Growth of the 2-in-size Bulk ZnO Single Crystals by the Hydrothermal Method, J. Cryst. Growth, 260, pp. 166–170. 2004.

[52] Maeda, K., M. Sato, I. Niikura and T. Fukuda. Growth of 2 inch ZnO Bulk Single Crystal by the Hydrothermal Method, Semicond. Sci. Technol., 20, pp. S49-S54. 2005.

[53] El-Shaer, A., A. Che Mofor, A. Bakin, M. Kreye and A. Waag. High-Quality ZnO Layers Grown by MBE on Sapphire, Superlattices Microstruct., 38, pp. 265–271. 2005.

[54] Kim, J. -H., S. K. Han, S. I. Hong, S. -K. Hong, J. W. Lee, J. Y. Lee, J. -H. Song, J. S. Park and T. Yao. Growth and Structural Properties of ZnO Films on (10−10) *m*-Plane Sapphire Substrates by Plasma-Assisted Molecular Beam Epitaxy, J. Vac. Sci. Technol. B, 27, 3, pp. 1625-1630. 2009.

[55] Vispute, R. D., V. Talyansky, S. Choopun, R. P. Sharma, T. Venkatesan, M. He, X. Tang, J. B. Halpern, M. G. Spencer, Y. X. Li, L. G. Salamanca-Riba, A. A. Iliadis and K. A. Jones. Heteroepitaxy of ZnO on GaN and its Implications for Fabrication of Hybrid Optoelectronic Devices, Appl. Phys. Lett., 73, pp. 348-350. 1998.

[56] Kim, K. S., H. W. Kim and N. H. Kim. Structural Characterization of ZnO Films Grown on SiO_2 by the RF Magnetron Sputtering, Phys. B, 334, 3-4, pp. 343-346. 2003.

[57] Triboulet, R. and J. Perrière. Epitaxial Growth of ZnO Films, Prog. Cryst. Growth Charact. Mater., 47, 2-3, pp. 65-138. 2003.

[58] Houng, B., C. S. Hsi, B. Y Hou and S. L. Fu, Fabrication and Properties Evaluation of Aluminum and Ruthenium Co-Doped Zinc Oxide Thin Films, J. Alloys Compd., 456, 1-2, pp. 64-71, 2008.

[59] Suchea, M., S. Christoulakis, N. Katsarakis, T. Kitsopoulos and G. Kiriakidis. Comparative Study of Zinc Oxide and Aluminum Doped Zinc Oxide Transparent Thin Films Grown by Direct Current Magnetron Sputtering, Thin Solid Films, 515, pp. 6562-6566. 2007.

[60] Lin, S. -S., J. -L. Huang and P. Sajgalik. Effects of Substrate Temperature on the Properties of Heavily Al-Doped ZnO Films by Simultaneous R.F. and D.C. Magnetron Sputtering, Surf. Coat. Technol., 190, pp. 39-47. 2005.

[61] Horwat, D. and A. Billard. Effects of Substrate Position and Oxygen Gas Flow Rate on the Properties of ZnO: Al Films Prepared by Reactive Co-Sputtering, Thin Solid Films, 515, pp. 5444-5448. 2007.

[62] Bai, S. N. and T. Y. Tseng. Effect of Alumina Doping on Structural, Electrical, and Optical Properties of Sputtered ZnO Thin Films, Thin Solid Films, 515, pp. 872-875. 2006.

[63] Park, Y. -S., K. -H. Choi and H. -K. Kim. Atmospheric Plasma Treatment of Flexible IZO Electrode Grown on PET Substrate for Flexible Organic Solar Cells, Electrochem. Solid-State Lett., 12, 12, pp. H426-H429. 2009.

[64] Park, S. -M., T. Ikegami and K. Ebihara. Effects of Substrate Temperature on the Properties of Ga-doped ZnO by Pulsed Laser Deposition, Thin Solid Films, 513, pp. 90-94. 2006.

[65] Gong, L., J. G. Lu and Z. Z. Ye. Room-temperature Growth and Optoelectronic Properties of GZO/ZnO Bilayer Films on Polycarbonate Substrates by Magnetron Sputtering, Sol. Energy Mater. Sol. Cells, 94, pp. 1282-1285. 2010.

[66] Kim, J. K., J. M. Lee, J. W. Lim, J. H. Kim and S. J. Yun. High-Performance Transparent Conducting Ga-Doped ZnO Films Deposited by RF Magnetron Sputter Deposition, Jpn. J. Appl. Phys., 49, pp. 04DP09-1-04DP09-4. 2010.

[67] Khranovskyy, V., U. Grossner, O. Nilsen, V. Lazorenko, G.V. Lashkarev, B. G. Svensson and R. Yakimova. Structural and Morphological Properties of ZnO:Ga Thin Films, Thin Solid Films, 515, pp. 472-476. 2006.

[68] Henleya, S. J., M. N. R. Ashfold and D. Cherns. The Growth of Transparent Conducting ZnO Films by Pulsed Laser Ablation. Surf. Coat. Technol., 177-178. pp. 271-276. 2004.

[69] Ahn, B. D., J. H. Kim, H. S. Kang, C. H. Lee, S. H. Oh, K. W. Kim, G. -e. Jang and S. Y. Lee. Thermally Stable, Highly Conductive, and Transparent Ga-doped ZnO Thin Films, Thin Solid Films, 516, pp. 1382-1385. 2008.

[70] Tseng, J. -Y., Y. -T. Chen, M. -Y. Yang, C. -Y. Wang, P. -C. Li, W. -C. Yu, Y. -F. Hsu and S. -F. Wang. Deposition of Low-resistivity Gallium-doped Zinc Oxide Films by Low-temperature Radio-Frequency Magnetron Sputtering, Thin Solid Films, 517, pp. 6310-6314. 2009.

[71] Ahn, B. D., Y. G. Ko, S. H. Oh, J. -H. Song and H. J. Kim. Effect of Oxygen Pressure of SiOx Buffer Layer on the Electrical Properties of GZO Film Deposited on PET Substrate, Thin Solid Films, 517, pp. 6414-6417. 2009.

[72] Fortunato, E., V. Assuncão, A. Goncalves, A. Marques, H. Águas, L. Pereira, I. Ferreira, P. Vilarinho and R. Martins. High Quality Conductive Gallium-doped Zinc Oxide Films Deposited at Room Temperature, Thin Solid Films, 451-452, pp. 443-447. 2004.

[73] Liang, S. and X. F. Bi. Structure, Conductivity, and Transparency of Ga-doped ZnO Thin Films Arising from Thickness Contributions, J. Appl. Phys., 104, pp.113533-1- 113533-5. 2008.

[74] Makino, H., N. Yamamoto, A. Miyake, T. Yamada, Y. Hirashima, H. Iwaoka, T. Itoh, H. Hokari, H. Aoki and T. Yamamoto. Influence of Thermal Annealing on Electrical and Optical Properties of Ga-doped ZnO Thin Films, Thin Solid Films, 518, pp. 1386-1389. 2009.

[75] Ma, Q. -B., Z. -Z. Ye, H. -P. He, S. -H. Hu, J. -R. Wang, L. -P. Zhu, Y. -Z.

Zhang and B. -H. Zhao. Structural, Electrical, and Optical Properties of Transparent Conductive ZnO:Ga Films Prepared by DC Reactive Magnetron Sputtering, J. Cryst. Growth, 304, pp. 64-68. 2007.

[76] Yamada, T., T. Morizane, T. Arimitsu, A. Miyake, H. Makino, N. Yamamoto and T. Yamamoto. Application of Low Resistivity Ga-doped ZnO films to Transparent Electromagnetic Interference Shielding Material, Thin Solid Films, 517, pp. 1027-1031. 2008.

[77] Lee, J. -H. Effects of Sputtering Pressure and Thickness on Properties of ZnO:Al Films Deposited on Polymer Substrates, J. Electroceram., 23, pp. 512-518. 2009.

[78] Yun, D. -J. and S. -W. Rhee. Deposition of Al-doped ZnO Thin-Films with Radio Frequency Magnetron Sputtering for a Source/drain Electrode for Pentacene Thin-Film Transistor, Thin Solid Films, 517, 16, pp. 4644-4649. 2009.

[79] Kim, J. -M., P. Thiyagarajan and S. -W. Rhee. Deposition of Al-doped ZnO Films on Polyethylene Naphthalate Substrate with Radio Frequency Magnetron Sputtering, Thin Solid Films, 518, pp. 5860-5865. 2010.

[80] Fortunato, E., P. Nunes, A. Marques, D. Costa, H. Águas, I. Ferreira, M. E. V. Costa, M. H. Godinho, P. L. Almeida, J. P. Borges and R. Martins. Transparent, Conductive ZnO:Al Thin Film Deposited on Polymer Substrates by RF Magnetron Sputtering, Surf. Coat. Technol., 151-152, pp. 247-251. 2002.

[81] Lee, J. -H. and J. -T. Song. Dependence of the Electrical and Optical Properties on the Bias Voltage for ZnO:Al Films Deposited by R.F. Magnetron Sputtering, Thin Solid Films, 516, pp. 1377-1381. 2008.

[82] Lee, J., D. Lee, D. Lim and K. Yang. Structural, Electrical and Optical Properties of ZnO:Al Films Deposited on Flexible Organic Substrates for Solar Cell Applications, Thin Solid Films, 515, pp. 6094-6098. 2007.

[83] Jung , Y. S., H. W. Choi, K. H. Kim, S. J. Park and H. H. Yoon. Properties of AZO Thin Films for Solar Cells Deposited on Polycarbonate Substrates, J. Korean Phys. Soc., 55, pp. 1945-1949. 2009.

[84] Lee, K. -I., E. K. Kim, H. -D. Kim, H. -I. Kang and J. -T. Song. Low Temperature Al Doped ZnO Films on a Flexible Substrate by DC Sputtering, Phys. Stat. Sol. (c), 5, pp. 3344-3347. 2008.

[85] Lee, J. -H. Effects of Sputtering Pressure and Thickness on Properties of ZnO: Al Films Deposited on Polymer Substrates, J.Electroceram., 20, pp. 225-229. 2008.

[86] Fernández, S. and F. B. Naranjo. Optimization of Aluminum-doped Zinc Oxide Films Deposited at Low Temperature by Radio Frequency Sputtering

on Flexible Substrates for Solar Cell Applications, Sol. Energy Mater. Sol. Cells, 94, pp. 157-163. 2010.

[87] Fernández, S., A. Martínez-Steele, J. J. Gandía and F. B. Naranjo. Radio Frequency Sputter deposition of High-quality Conductive and Transparent ZnO:Al Films on Polymer Substrates for Thin Film Solar Cells Applications, Thin Solid Films, 517, pp. 3152-3156. 2009.

[88] Hao, X. -T., J. Ma, D. -H. Zhang, Y. -G. Yang, H. -L. Ma, C. -F. Cheng and X. -D. Liu. Comparison of the Properties for ZnO:Al Films Deposited on Polyimide and Glass Substrates. Mater. Sci. Eng., B90, pp. 50-54. 2002.

[89] Bhuvana, K.P., J. Elanchezhiyan, N. Gopalakrishnan and T. Balasubramanian. Optimization of $Zn_{1-x}Al_xO$ Film for Antireflection Coating by RF sputtering. J Alloy Compd. 473, pp. 534-537. 2009.

[90] http://www.webelements.com/aluminium/atom_sizes.html last accessed 30th Apr 2012

[91] http://periodictable.com/Properties/A/CrustAbundance.v.log.html last accessed 30th Apr 2012

[92] Wyckoff, R. W. G., Crystal Structures, Vol. 1, 2nd Ed. pp. 111-113, New York: John Wiley. 1963.

[93] Jagadish, C. and S. Pearton. Zinc Oxide Bulk, Thin Films and Nanostructures: Processing, Properties and Applications. pp. 2-2, United States: Elsevier Inc. 2006.

[94] Desgreniers, S. High-Density Phases of ZnO: Structural and Compressive Parameters, Phys. Rev. B, 58, 21, pp. 14102-14105. 1998.

[95] Jagadish, C. and S. Pearton. Zinc Oxide Bulk, Thin Films and Nanostructures: Processing, Properties and Applications. pp. 4-7, United States: Elsevier Inc. 2006.

[96] Zhang, S. B., S.-H. Wei, and A. Zunger. Intrinsic *n*-type versus *p*-type Doping Asymmetry and the Defect Physics of ZnO, Phys. Rev. B, 63, pp. 075205-1-075205-7. 2001.

[97] Ohtomo,A., M. Kawasaki, T. Koida, K. Masubuchi, H. Koinuma, Y. Sakurai, Y. Yoshida, T. Yasuda and Y. Segawa. $Mg_xZn_{1-x}O$ as a II–VI Widegap Semiconductor Alloy, Appl. Phys. Lett., 72, pp. 2466-2468. 1998.

[98] Makino,T., Y. Segawa, M. Kawasaki, A. Ohtomo, R. Shiroki, K. Tamu, T. Yasuda and H. Koinuma. Band Gap Engineering Based on $Mg_xZn_{1-x}O$ and $Cd_yZn_{1-y}O$ Ternary Alloy Films, Appl. Phys. Lett. 78, pp. 1237-1239. 2001.

[99] Sze, S. M. Semiconductors Devices: Physics and Technology, 2nd ed. pp. 51-55, New York: John Wiley & Sons, Inc. 2002.

[100] Chen, M., Z. L. Pei, X. Wang, Y. H. Yu, X. H. Liu, C. Sun and L. S. Wen. Intrinsic limit of electrical properties of transparent conductive oxide films, J. Phys. D: Appl. Phys., 33, pp. 2538 -2548. 2000.

[101] Kasap, S.O. Principles of Electronics Materials and Devices, 2rd ed. pp. 99-132, McGraw Hill. 2000.

[102] Morin, F. J. Lattice-Scattering Mobility in Germanium, Phys. Rev. 93, 1, pp. 62-63, 1954.

[103] Lyo, S. K. Electron-Electron Scattering and Mobilities in Semiconductors and Quantum Wells, Phys. Rev. B, 34, 10, pp. 7129-7134. 1986.

[104] Appel, J. Electron-Electron Scattering and Transport Phenomena in Nonpolar Semiconductors, Phys. Rev., 122, 6, pp. 1760-1772. 1961.

[105] Noguchi, S. and H. Sakata. Electrical Properties of Sn-doped In_2O_3 Films Prepared by Reactive Evaporation, J. Phys. D: AppI. Phys., 14, pp. 1523-1529. 1981.

[106] Yang, X. C. and N. C. Giles. Hall Effect Analysis of Bulk ZnO Comparing Different Crystal Growth Techniques, J. Appl. Phys., 105, pp. 063709-1-063709-8. 2009.

[107] Kasap, S.O. Principles of Electronics Materials and Devices, 2nd ed. pp. 60-65, McGraw Hill. 2000.

[108] Hartnagel, H. L., A. L. Dawar, A. K. Jain and C. Jagadish. Semiconducting Transparent Thin Films. pp. 223-224, Institute of Physics Publishing. 1995.

[109] Simonis, F., M. V. D Leij and C. J. Hoogendoorn. Physics of Doped Tin Dioxide Films for Spectral-Selective Surfaces, Sol. Energy Mater., 1, pp. 221-231. 1979.

[110] Sze, S. M. and K. K. Ng. Physics of Semiconductors Devices, 3rd ed. pp. 651-652. New York: John Wiley & Sons, Inc. 2007.

[111] Sze, S. M. and K. K. Ng. Physics of Semiconductors Devices, 3rd ed. pp. 51. New York: John Wiley & Sons, Inc. 2007.

[112] Neamen, D. A. Semiconductor Physics and Devices : Basic Principles, 4th ed. pp. 650-651, McGraw Hill. 2012.

[113] Jeong, H. H., S. Y. Lee, J. -O. Song, K. K. Choi, S. -H. Lee, H. S. Choi, T. -H. Oh, Y. -H. Lee and T. -Y. Seong, Fabrication of High Performance GaN-Based Vertical Light-Emitting Diodes Using a Transparent Conducting Indium Tin Oxide Channel Layer, Electrochem. Solid-State Lett., 12, 9, pp. H322-H324. 2009.

[114] Kuo, C. H., C. L. Yeh, P. H. Chen, W. C. Lai, C. J. Tun, J. K. Sheu and G. C. Chia, Low Operation Voltage of Nitride-Based LEDs with Al-Doped ZnO Transparent Contact Layer, Electrochem. Solid-State Lett., 11, 9, pp. H269-H271. 2008.

[115] Hartnagel, H. L., A. L. Dawar, A. K. Jain and C. Jagadish. Semiconducting Transparent Thin Films. Pp. 225-230., Institute of Physics Publishing. 1995.

[116] Burstein, E. Anomalous Optical Absorption Limit in InSb. Phys. Rev. Lett., 93, pp. 632-632. 1954 ; Moss, T.S. Proc. Phys. Soc. London Ser. B, 67, pp. 775-775. 1954.

[117] Grundmann, M. The Physics of Semiconductors, pp. 235-236, New York: Springer Science+Business Media, LLC. 2006.

[118] Roth, A. P., J. B. Webb and D. F. Williams. Band-Gap Narrowing in Heavily Defect-Doped ZnO, Phy. Rev. B, 25, pp. 7836-7839. 1982.

[119] Hamberg, I., C. G. Granqvist, K. -F. Berggren, B. E. Sernelius and L. Engström. Band-Gap Widening in Heavily Sn-Doped In_2O_3, Phy. Rev. B, 30, 6, pp. 3240 -3249. 1984.

[120] Sze, S. M. and K. K. Ng. Physics of Semiconductors Devices, 3rd ed. pp. 603-608, New York: John Wiley & Sons, Inc. 2007.

[121] Wyckoff, R. W. G., Crystal Structures, Vol. 1, 2nd Ed. pp. pp. 331-332, New York: John Wiley. 1963.

[122] Liu, Y. L., Y. C. Liu, R. Mu, H. Yang, C. L. Shao, J. Y. Zhang, Y. M. Lu, D. Z. Shen and X. W. Fan. The Structural and Optical Properties of Cu_2O Films Electrodeposited on Different Substrates, Semicond. Sci. Technol., 20, pp. 44-49. 2005.

[123] Pollack, G. P. and D. Trivich. Photoelectric Properties of Cuprous Oxide, J. Appl. Phys., 46, pp. 163-172. 1975.

[124] Porat, O. and I. Riess. Defect Chemistry of $Cu_{2-y}O$ at Elevated Temperatures. Part II: Electrical Conductivity, Thermoelectric Power and Charged Point Defects, Solid State Ionics, 81, pp. 29-41. 1995.1

[125] Nolan, M. and S. D. Elliott. The p-type Conduction Mechanism in Cu_2O: a First Principles Study, Phys. Chem. Chem. Phys., 8, pp. 5350-5358. 2006.

[126] Rakhshani, A. E. Preparation, Characterization and Photovoltaic Properties of Cuprous Oxide: A Review, Solid-State Electron., 29, 1, pp. 7-17. 1986.

[127] Ishizuka,S., T. Maruyama and K. Akimoto. Thin-Film Deposition of Cu_2O by Reactive Radio-Frequency Magnetron Sputtering, Jpn. J. Appl. Phys., 39, pp. L786-L788. 2000.

[128] Chu, C. -L., H. -C. Lu, C. -Y. Lo, C. -Y. Lai and Y. -H. Wang. Physical Properties of Copper Oxide Thin Films Prepared by DC Reactive Magnetron Sputtering under Oxygen Partial Pressures, Phys. B, 404, 23-24, pp. 4831-4834. 2009.

[129] Ogwu, A. A., E. Bouquerel, O. Ademosu, S. Moh, E. Crossan and F. Placido. The Influence of RF Power and Oxygen Flow Rate During Deposition on the Optical Transmittance of Copper Oxide Thin Films Prepared by Reactive Magnetron Sputtering, J. Phys. D: Appl. Phys., 38, pp. 266-271. 2005.

[130] Ishizuka, S., S. Kato, T. Maruyama and K. Akimoto. Nitrogen Doping into Cu_2O Thin Films Deposited by Reactive Radio-Frequency Magnetron Sputtering , Jpn. J. Appl. Phys., 40, pp. 2765-2768. 2001.

[131] Nakano, Y., S. Saeki and T. Morikawa. Optical Bandgap Widening of p-Type Cu_2O Films by Nitrogen Doping, Appl. Phys. Lett., 94, pp. 022111-1-022111-3. 2009.

[132] Edwards, P. P., A. Porch, M. O. Jones, D. V. Morga and R. M. Perks. Basic Materials Physics of Transparent Conducting Oxides, Dalton Trans., 19, pp. 2995-3002. 2004.

[133] Nomura, K., H. Ohta, A. Takagi, T. Kamiya, M. Hirano and H. Hosono. Room-Temperature Fabrication of Transparent Flexible Thin-Film Transistors Using Amorphous Oxide Semiconductors, Nature, 432, pp. 488-492. 2004.

[134] Nomura, K., A. Takagi, T. Kamiya, H. Ota, M. Hirano and H. Hosono. Amorphous Oxide Semiconductors for High-Performance Flexible Thin-Film Transistors, Jpn. J. Appl. Phys., 45, pp. 4303-4308. 2006.

[135] Tahar, R. B. H., T. Ban, Y. Ohya and Y. Takahashi. Tin Doped Indium Oxide Thin Films: Electrical Properties, J. Appl. Phys., 83, pp. 2631-2645. 1998.

[136] Presley, R. E., C. L. Munsee, C. -H. Park, D. Hong, J. F. Wager and D. A. Keszler. Tin Oxide Transparent Thin-Film Transistors, J. Phys. D., 37, pp. 2810-2813. 2004.

[137] Cheong, W. S., S. M. Yoon, C. S. Hwang and H. Y. Chu. High-Mobility Transparent SnO_2 and ZnO-SnO_2 Thin-Film Transistors with SiO_2/Al_2O_3 Gate Insulators, Jpn. J. Appl. Phys., 48, 4, 2, pp. 04C090-1-04C090-4. 2009.

[138] Chiang, H. Q., J. F. Wager, R. L. Hoffman, J. Jeong and D. A. Keszler. High Mobility Transparent Thin-Film Transistors With Amorphous Zinc Tin Oxide Channel Layer, Appl. Phys. Lett., 86, pp. 013503-1-013503-3. 2005.

[139] Dehuff, N. L., E. S. Kettenring, D. Hong, H. Q. Chiang, J. F. Wager, R. L. Hoffman, C. -H. Park and D. A. Keszler. Transparent Thin-Film Transistors With Zinc Indium Oxide Channel Layer, J. Appl. Phys., 97, pp. 064505-1-064505-5. 2005.

[140] Barquinha, P., A. Pimentel, A. Marques, L. Pereira, R. Martins and E. Fortunato. Effect of UV and Visible Light Radiation on the Electrical Performances of Transparent TFTs Based on Amorphous Indium Zinc Oxide, J. Non-Cryst. Solids, 352, pp. 1756-1760. 2006.

[141] Moon, Y. -K., S. Lee, D. -H. Kim, D. -H. Lee, C. -O. Jeong and J. -W. Park. Application of DC Magnetron Sputtering to Deposition of InGaZnO Films for Thin Film Transistor Devices, Jpn. J. Appl. Phys., 48, pp. 031301-1-031301-4. 2009.

[142] Hong, D., H. Q. Chiang , R. E. Presley , N. L. Dehuff , J. P. Bender, C. -H. Park, J. F. Wager and D. A. Keszler. Transparent, Conductive ZnO:Al Thin Film Deposited on Polymer Substrates by RF Magnetron Sputtering, Thin Solid Films, 515, pp. 2717-2721. 2006.

[143] http://www.kintec.hk/ last accessed 30th Apr 2012

[144] Fonash, S. J. Solar cell device physics, 2nd ed. pp. 1-8, Academic Press, Elsevier. 2010.

[145] Hegedus, S. Thin Film Solar Modules: The Low Cost, High Throughput and Versatile Alternative to Si Wafers, Prog. Photovolt: Res. Appl., 14, pp. 393-411. 2006.

[146] C. del Cañizo, G. del Coso and W.C. Sinke. Crystalline Silicon Solar Module Technology: Towards the 1s Per Watt-Peak Goal, Prog. Photovolt: Res. Appl., 17, pp. 199 -209. 2009.

[147] M. A. Green. Consolidation of Thin-film Photovoltaic Technology: The Coming Decade of Opportunity, Prog. Photovolt: Res. Appl., 14, pp. 383-392. 2006.

[148] Kawazoe, H., H. Yanagi, K. Ueda and H. Hosono. Transparent *p*-Type Conducting Oxides: Design and Fabrication of *p*-*n* Heterojunctions, MRS BULLETIN, pp 28-36. 2000.

[149] S. Fay, U. Kroll, C. Bucher, E. Vallat-Sauvain and A. Shah. Low Pressure Chemical Vapour Deposition of ZnO Layers for Thin-Film Solar Cells: Temperature-Induced Morphological Changes. Sol. Energy Mater. Sol. Cells, 86, pp. 385-397. 2005.

[150] Rai, B. P. Cu_2O Solar Cells: A Review, Solar Cells, 25, pp. 265-272. 1988.

[151] Look, D. C. Electrical and Optical Properties of p-Type ZnO, Semicond. Sci. Technol., 20, pp. S55-S61. 2005.

[152] Deng, R., B. Yao, Y. F. Li, Y. M. Zhao, B. H. Li, C. X. Shan, Z. Z. Zhang, D. X. Zhao, J. Y. Zhang, D. Z. Shen and X. W. Fan. X-ray Photoelectron Spectroscopy Measurement of *n*-ZnO/*p*-NiO Heterostructure Valence-Band Offset, Appl. Phys. Lett., 94, pp. 022108-1-022108-3. 2009.

[153] Raebiger, H., S. Lany and A. Zunger. Origins of the *p*-Type Nature and Cation Deficiency in Cu_2O and Related Materials, Phys. Rev. B: Condens. Matter Mater. Phys., 76, pp. 045209-1- 045209-5. 2007.

[154] Jeong, S. H. and E. S. Aydil. Heteroepitaxial Growth of Cu_2O Thin Film on ZnO by Metalorganic Chemical Vapour Deposition, J. Cryst. Growth, 311, pp. 4188-4192. 2009.

[155] Jeong, S. S., A. Mittiga, E. Salza, A. Masci and S. Passerini. Electrodeposited ZnO/Cu_2O Heterojunction Solar Cells, Electrochimica Acta, 53, pp. 2226-2231. 2008.

[156] Izaki, M., T. Shinagawa, K -T Mizuno, Y. Ida, M. Inaba and A. Tasaka. Electrochemically constructed p-Cu_2O/n-ZnO Heterojunction Diode for Photovoltaic Device, J. Phys. D: Appl. Phys., 40, pp. 3326-3329. 2007.

[157] Mittiga, A., E Salza, F. Sarto, M. Tucci and R. Vasanthi. Heterojunction Solar Cell With 2% Efficiency Based on a Cu_2O Substrate, Appl. Phys. Lett., 88, pp. 163502-1-163502-3. 2006.

[158] Jagadish, C. and S. Pearton. Zinc Oxide Bulk, Thin Films and Nanostructures: Processing, Properties and Applications. pp 443-489, United States: Elsevier Inc. 2006.

[159] Miller, B. G., T. W. Traut and R. Wolfenden. A Role for Zinc in OMP Decarboxylase, an Unusually Proficient Enzyme, J. Am. Chem. Soc., 120, pp. 2666-2667. 1998.

[160] Das, S. N., J. P. Kar, J. -H. Choi, T. I. Lee, K. -J. Moon and J. -M. Myou. Fabrication and Characterization of ZnO Single Nanowire-Based Hydrogen, J. Phys. Chem. C, 114, pp. 1689-1693. 2010.

[161] Basu, S. and A. Dutta. Modified Heterojunction Based on Zinc Oxide Thin for Hydrogen Gas-Sensor Application, Sens. Actuators, B, 22, pp. 83-87. 1994.

[162] Hsueh, T. -J., Y. -W. Chen, S. -J. Chang, S. -F. Wang, C. -L. Hsu, Y. -R. Lin, T. -S. Lin and I. -C. Chen. ZnO Nanowire-Based CO Sensors Prepared at Various Temperatures, J. Electrochem. Soc., 154, 12, pp. J393-J396. 2007.

[163] Martins, R., E. Fortunato, P. Nunes, I. Ferreira, A. Marques, M. Bender, N. Katsarakis, V. Cimalla and G. Kiriakidis. Zinc Oxide as an Ozone Sensor, J. Appl. Phys., 96, 3, pp. 1398-1408. 2004.

[164] Chiu, Y. -S. and C. -T. Lee. pH Sensor Investigation of Various-Length Photoelectrochemical Passivated ZnO Nanorod Arrays, J. Electrochem. Soc., 158, 9, pp. J282-J285. 2011.

[165] Chen, Y. F., D. Bagnall and T. Yao. ZnO as a Novel Photonic Material for the UV Region, Mater. Sci. Eng. B, 75, pp. 190-198. 2000.

[166] Razeghi, M. and A. Rogalski. Semiconductor Ultraviolet Detectors, J. Appl. Phys., 79, 10, pp. 7433-7473. 1996.

[167] Basak,D., G. Aminb, B. Mallikb, G. K. Paulc and S. K. Sen. Photoconductive UV Detectors on Sol-Gel-Synthesize ZnO Films, J. Cryst. Growth, 256, pp. 73-77. 2003.

[168] Munoz, E., E. Monroy, J. L. Pau, F. Calle, F. Omnes and P. Gibart. III Nitrides and UV Detection. J. Phys.: Condens. Matter., 13, pp. 7115-7137. 2001.

[169] Khan, M. A., J. N. Kuznia, D. T. Olson, W. Schaff, J. Burm and M. S. Shur. Microwave Performance of a 0.25 μm Gate AlGaN/GaN Heterostructure Field Effect Transistor, Appl. Phys. Lett., 65, pp. 1121-1-1121-3. 1994.

[170] Look, D.C. Recent Advances in ZnO Materials and Devices. Mater. Sci. Eng. B, 80, pp. 383-387. 2001.

[171] Gruber, Th., C. Kirchner, R. Kling, F. Reuss and A. Waag. ZnMgO Epilayers and ZnO-ZnMgO, Quantum Wells for Optoelectronic Applications in the Blue and UV Spectral Region. Appl. Phys. Lett., 84, pp. 5359-5361. 2004.

[172] Liu, K. W., M. Sakurai and M. Aono. ZnO-Based Ultraviolet Photodetectors, Sensors, 10, pp. 8604-8634. 2010.

[173] Bai, S., W. W. Wu, Y. Qin, N. Y. Cui, D. J. Bayerl and X. D. Wang. High-Performance Integrated ZnO Nanowire UV Sensors on Rigid and Flexible Substrates, Adv. Funct. Mater., 21, 23, pp. 4464-4469. 2011.

[174] Liang, S., H. Sheng, Y. Liu, Z. Huo, Y. Lu and H. Shen. ZnO Schottky ultraviolet photodetectors , J. Cryst. Growth, 225, pp. 110-113. 2001.

[175] Gimenez, A. J., J. M. Yáñez-Limón and Jorge M. Seminario. ZnO-Paper Based Photoconductive UV Sensor, J. Phys. Chem. C, 115, pp. 282-287. 2011.

[176] Sun, Y. and J. A. Rogers. Inorganic Semiconductors for Flexible Electronics, Adv. Mater., 19, pp. 1897-1916. 2007.

[177] Yabuta, H., M. Sano, K. Abe, T. Aiba, T. Den, H. Kumomi, K. Nomura, T. Kamiya and H. Hosono. High-Mobility Thin-Film Transistor With Amorphous $InGaZnO_4$ Channel Fabricated by Room Temperature RF-Magnetron Sputtering, Appl. Phys. Lett., 89, pp. 112123-1- 112123-3. 2006.1

[178] Sasabayashi, T., N. Ito, E. Nishimura, M. Kon, P. K. Song, K. Utsumi, A. Kaijo and Y. Shigesato. Comparative Study on Structure and Internal Stress in Tin-Doped Indium Oxide and Indium-Zinc Oxide Films Deposited by R.F. Magnetron Sputtering, Thin Solid Films, 445, pp.219-223. 2003.\

[179] Carcia, P. F., R. S. McLean, M. H. Reilly and G. Nunes. Jr. Transparent ZnO Thin-Film Transistor Fabricated by RF Magnetron Sputtering, Appl. Phys. Lett., 82, pp. 1117-1119. 2003.

[180] Lavareda, G., C. Nunes de Carvalho, E. Fortunato, A.R. Ramos, E. Alves, O. Conde and A. Amaral. Transparent Thin Film Transistors Based on Indium Oxide Semiconductor, J. Non-Cryst. Solids, 352, pp. 2311-2316. 2006.

[181] Fortunato, E., P. M. C. Barquinha, A. C. M. B. G. Pimentel, A. M. F. Gonçalves, A. J. S. Marques, L. M. N. Pereira and R. Martins. Fully Transparent ZnO Thin-Film Transistor Produced at Room Temperature, Adv. Mater., 17, pp. 590-594 2005.

[182] Sasa, S., M. Ozaki, K. Koike, M. Yano and M. Inoue. High-Performance ZnO/ZnMgO Field-Effect Transistors Using a Hetero-Metal-Insulator-Semiconductor Structure, Appl. Phys. Lett., 89, pp. 053502-1- 053502-3. 2006.

[183] Hoffman, R. L., B. J. Norris and J. F. Wager. ZnO-Based Transparent Thin-Film Transistors, Appl. Phys. Lett., 82, 5, pp. 733-735. 2003.

[184] Dijkkamp, D. and T. Venkatesan. Preparation of Y‐Ba‐Cu Oxide Superconductor Thin Films Using Pulsed Laser Evaporation from high Tc Bulk Material, Appl. Phys. Lett., 51, 8, pp. 619-621. 1987.

[185] Chrisey, D. B. and G. K. Hubler. Pulsed Laser Deposition of Thin Films. pp. 85-174, New York: John Wiley & Sons, Inc. 1994.

[186] http://www.pvdproducts.com/products/pulsed-laser-deposition last accessed 19th Dec 2012

[187] Chrisey, D. B. and G. K. Hubler. Pulsed Laser Deposition of Thin Films. pp. 13-19, New York: John Wiley & Sons, Inc. 1994.

[188] Lieberman, M. A. and A. J. Lichtenberg. Principles of Plasma Discharges and Materials Processing 2nd ed. pp. 43-85, New York: John Wiley and Sons Inc. 2005.

[189] Mattox. D. M. The Foundations of Vacuum Coating Technology. pp.11-33, Norwich, New York: Noyes Publications/William Andrew Pub. 2003.

[190] Pauw, I. J. V. D. A Method of Measuring the Resistivity and Hall Coefficient on Lamellae of Arbitrary Shape, Philips Res. Repts, 20, 8, pp. 220-224. 1958.

[191] Neamen, D. A. Semiconductor Physics and Devices : Basic Principles, 4th ed. pp. 180-182, McGraw Hill. 2012.

[192] Koon, D. W. and C. J. Knickerbocker. What Do You Measure When You Measure Resistivity?, Rev. Sci. Instrum., 63, pp. 207-210. 1992.

[193] Koon, D. W. and C. J. Knickerbocker. What Do You Measure When You Measure the Hall Effect?, Rev. Sci. Instrum., 64, pp. 510-513. 1993.

[194] Koon, D. W. Effect of Contact Size and Placement, and of Resistive Inhomogeneities on Van der Pauw Measurements, Rev. Sci. Instrum., 60, pp. 271-274. 1989.

[195] Koon, D. W. and C. J. Knickerbocker. Effects of Macroscopic Inhomogeneities on Resistive and Hall Measurements on Crosses, Cloverleafs, and Bars, Rev. Sci. Instrum., 67, pp. 4282-4285. 1996.

[196] http://www.perkinelmer.com/Catalog/Product/ID/L750 last accessed 30th Apr 2012

[197] http://microspectra.com/component/content/article/34-products/129-microspectrophotometer last accessed 30th Apr 2012

[198] http://www.jawoollam.com/vase_home.html last accessed 30th Apr 2012

[199] http://www.bruker-axs.de/discover_with_gadds.html last accessed 30th Apr 2012

[200] Ko, H. J., Y. F. Chen, S. K. Hong, H. Wenisch, T. Yao and D. C. Look. Ga-doped ZnO Films Grown on GaN Templates by Plasma-Assisted Molecular-Beam Epitaxy, Appl. Phys. Lett., 77, pp. 3761-3763, 2000.

[201] Elmer, K. Resistivity of Polycrystalline Zinc Oxide Films: Current Status and Physical Limit, J. Phys. D: Appl. Phys., 34, pp. 3097-3108. 2001.

[202] Medvedeva, J. E. and C. L. Hettiarachchi. Tuning the Properties of Complex Transparent Conducting Oxides: Role of Crystal Symmetry Chemical Composition, Carrier Generation, Phys. Rev. B, 81, pp. 125116-1-125116-16. 2010.

[203] Minami, T. New n-Type Transparent Conducting Oxides, Mater. Res. Bull., 35, pp. 38-44. 2000.

[204] Yamamoto, N., H. Makino, T. Yamada, Y. Hirashima, H. Iwaoka, T. Ito, A. Ujihara, H. Hokari, H. Morita and T. Yamamoto. Heat Resistance of Ga-Doped ZnO Thin Films for Application as Transparent Electrodes in Liquid Crystal Displays, J. Electrochem. Soc., 157, pp. J13-J20. 2010.

[205] Sakai, N., Y. Umeda, F. Mitsugi and T. Ikegami. Characterization of zinc oxide thin films prepared by pulsed laser deposition at room temperature, Surf. Coat. Technol., 202, pp. 5467-5470. 2008.

[206] Oh, M. -S., D. -K. Hwang, D. -J. Seong, H. -S. Hwang, S. -J. Park and E. D. Kim. Improvement of Characteristics of Ga-Doped ZnO Grown by Pulsed Laser Deposition Using Plasma-Enhanced Oxygen Radicals, J. Electrochem. Soc., 155, pp. D599-D603. 2008.

[207] Park, S. -M., T. Ikegami, K. Ebihara and P. -K. Shin. Structure and Properties of Transparent Conductive Doped ZnO Films by Pulsed Laser Deposition, Appl. Surf. Sci., 253, pp.1522-1527. 2006.

[208] Chen, D. -Y. and C. -Y. Hsu. Growth of Ga-Doped ZnO Films With ZnO Buffer Layer by Sputtering at Room Temperature, Superlattices Microstruct., 44, pp. 742-753. 2008.

[209] Sang, B., K. Kushiya, D. Okumura and O. Yamase. Performance Improvement of CIGS-Based Modules by Depositing High-Quality Ga-Doped ZnO Windows With Magnetron Sputtering, Sol. Energy Mater. Sol. Cells, 67, pp. 237-245. 2001.

[210] Raniero, L., I. Ferreira, A. Pimentel, A. Gonçalves, P. Canhola, E. Fortunato and R. Martins. Role of Hydrogen Plasma on Electrical and Optical Properties of ZGO, ITO and IZO Transparent and Conductive Coatings, Thin Solid Films, 511-512, pp. 295-298. 2006.

[211] Park, T. -Y., Y. -S. Choi, J. -W. Kang, J. -H. Jeong, S. -J. Park, D. M. Jeon, J. W. Kim and Y. C. Kim. Enhanced Optical Power and Low Forward Voltage of GaN-Based Light-Emitting Diodes With Ga-Doped ZnO Transparent Conducting Layer, Appl. Phys. Lett., 96, pp. 051124-051126. 2010.

[212] Yen, W. T., Y. C. Lin, P. C. Yao, J. H. Ke and Y. L. Chen. Effect of Post-Annealing on the Optoelectronic Properties of ZnO:Ga Films Prepared by Pulsed Direct Current Magnetron Sputtering, Thin Solid Films, 518, pp. 3882-3885. 2010.

[213] McCluskey, M. D. and S. J. Jokela. Defects in ZnO, J. Appl. Phys., 106, pp. 071101-1-071101-13. 2009.

[214] Kim, J. H., B. D. Ahn, C. H. Lee, K. A. Jeon, H. S. Kang and S. Y. Lee. Effect of Rapid Thermal Annealing on Electrical and Optical Properties of Ga Doped ZnO Thin Films Prepared at Room Temperature, J. Appl. Phys., 100, pp. 113515-1- 113515-3. 2006.

[215] Wang, R., A. W. Sleight and D. Cleary. High Conductivity in Gallium-Doped Zinc Oxide Powders, Chem. Mater., 8, pp. 433-439. 1996.

[216] Lin, K. -M. and P. Tsai. Growth Mechanism and Characterization of ZnO: Al Multi-Layered Thin Films by Sol-Gel Technique, Thin Solid Films, 515, pp. 8601-8604. 2007.

[217] Sivaramakrishnan, K. and T. L. Alford. Metallic Conductivity and the Role of Copper in ZnO/Cu/ZnO Thin Films for Flexible Electronics, Appl. Phys. Lett., 94, pp. 052104-1-052104-3. 2009.

[218] Lee, C., R. P. Dwivedi, W. Lee, C. Hong, W. I. Lee and H. W. Kim. IZO/Al/GZO Multilayer Films to Replace ITO Films, J. Mater. Sci: Mater Electron, 19, pp. 981-985. 2008.

[219] Cheng, C. -H. and J. -M. Ting. Transparent Conducting GZO, Pt/GZO, and GZO/Pt/GZO Thin Films, Thin Solid Films, 516, pp. 203-207. 2007.

[220] Valkonen, E., B. Karlsson and C. -G. Ribbing, Solar Optical Properties of Thin Films of Cu, Ag, Au, Cr, Fe, Co, Ni and Al, .Sol. Energy. 32, 2, pp. 211-222. 1984.

[221] Logeeswaran, V. J., N. P. Kobayashi, M. Saif Islam, W. Wu, P. Chaturvedi, N. X. Fang, S. Y. Wang and R. S. Williams, Ultrasmooth Silver Thin Films Deposited with a Germanium Nucleation Layer, Nano Lett., 9, 1, pp. 178-182. 2009.

[222] Janotti, A. and C. G. Van de Walle. New Insights into the Role of Native Point Defects in ZnO, J. Cryst. Growth, 287, pp. 58-65. 2006.

[223] Oba, F., A. Togo and I. Tanaka. Defect Energetics in ZnO: A hybrid Hartree-Fock Density Functional Study, Phys. Rev. B, 77, pp. 245202-1-245202-6. 2008.

[224] Janotti, A. and C. G. Van de Walle. Oxygen Vacancies in ZnO, Appl. Phys. Lett., 87, pp. 122102-1-122102-3. 2005.

[225] Janotti, A. and C. G. Van de Walle. Native Point Defects in ZnO, Phys. Rev. B, 76, pp. 165202-1-165202-22. 2007.

[226] Lany, S. and A. Zunger. Anion Vacancies as a Source of Persistent Photoconductivity in II-VI and Chalcopyrite Semiconductors, Phys. Rev. B, 72, 035215-1-035215-13. 2005.

[227] Catlow, C. R. A., S. A. French, A. A. Sokol, A. A. Al-Sunaidi and S. M. Woodley. Zinc Oxide: A Case Study in Contemporary Computational Solid State Chemistry, J. Comput. Chem., 29, 13, pp. 2234-2249. 2008.

[228] Zhao, J. -L., W. Zhang, X. -M. Li, J. -W. Feng and X. Shi. Convergence of the Formation Energies of Intrinsic Point Defects in Wurtzite ZnO: First-Principles Study by Projector Augmented Wave Method, J. Phys.: Condens. Matter, 18, 5, pp.1495-1508. 2006.

[229] Kisi, E. H. and M. M. Elcombe. *u* Parameters for the Wurtzite Structure of ZnS and ZnO Using Powder Neutron Diffraction, Acta Crystallogr., Sect. C: Cryst. Struct. Commun., 45, pp. 1867-1870. 1989; McMurdie, H., M. Morris, E. Evans, B. Paretzkin, W. Wong-Ng, L. Ettlinger and C. Hubbard. Standard X-Ray Diffraction Powder Patterns from the JCPDS Research Associateship, Powder Diffr., 1, pp. 76. 1986. (ICDD ZnO pattern 00-036-1451).

[230] Cullity, B. D. and S. R. Stock. Elements of X-ray diffraction, 3rd ed. pp. 167-

171, Prentice Hall, New Jersey, 2001.

[231] Park, S. -M., T. Ikegami and K. Ebihara. Effects of Substrate Temperature on the Properties of Ga-doped ZnO by Pulsed Laser Deposition, Thin Solid Films, 513, pp. 90-94. 2006.

[232] Hirata, G.A., J. McKittrick, T. Cheeks, J.M. Siqueiros, J.A. Diaz, O. Contreras and O.A. Lopez. Synthesis and Optelectronic Characterization of Gallium Doped Zinc Oxide Transparent Electrodes, Thin Solid Films, 288, pp. 29-31, 1996.

[233] Zhang, Z. G., F. Zhou, X. Q. Wei, M. Liu, G. Sun, C. S. Chen, C. S. Xue, H. Z. Zhuang and B.Y. Man. Effects of Oxygen Pressures on Pulsed Laser Deposition of ZnO Films, Phys. E, 39, pp. 253-257. 2007.

[234] Zhu, B. L., X. Z. Zhao, S. Xu, F. H. Su, G. H. Li, X. G. Wu, J. Wu, R. Wu and J. Liu. Oxygen Pressure Dependences of Structure and Properties of ZnO Films Deposited on Amorphous Glass Substrates by Pulsed Laser Deposition, Jpn. J. Appl. Phys., 47, pp. 2225-2229. 2008.\

[235] Wang, L., D. W. Matson, E. Polikarpov, J. S. Swensen, C. C. Bonham, L. Cosimbescu, J. J. Berry, D. S. Ginley, D. J. Gaspar and A. B. Padmaperuma. Highly Efficient Blue Organic Light Emitting Device Using Indium-Free Transparent Anode Ga:ZnO With Scalability For Large Area Coating, J. Appl. Phys., 107, pp. 043103-1-043103-8. 2010.

[236] Park, H. -K, J. -W. Kang, S. -I. Na, D. -Y. Kim and H. -K. Kim. Characteristics of Indium-Free GZO/Ag/GZO and AZO/Ag/AZO Multilayer Electrode Grown by Dual Target DC Sputtering at Room Temperature for Low-Cost Organic Photovoltaics, Sol. Energy Mater. Sol. Cells, 93, pp. 1994-2002. 2009.

[237] Snure, M. and A. Tiwari. Structural, Electrical, and Optical Characterizations of Epitaxial $Zn_{1-x}Ga_xO$ Films Grown on Sapphire (0001) Substrate, J. Appl. Phys., 101, pp. 124912-1-124912-6. 2007.

[238] Wong, L. M., S. Y. Chiam, J. Q. Huang, S. J. Wang, J. S. Pan and W. K. Chim. Role of oxygen for highly conducting and transparent gallium-doped zinc oxide electrode deposited at room temperature, Appl. Phys. Lett., 98, pp. 022106-1-022106-3. 2011.

[239] http://rredc.nrel.gov/solar/spectra/am1.5/ last accessed 30th Apr 2012

[240] Vanheusden, K., W. L. Warren, C. H. Seager, D. R. Tallant, J. A. Voigt and B. E. Gnade. Mechanisms behind green photoluminescence in ZnO phosphor powders, J. Appl. Phys., 79, pp. 7983-7990.1996.

[241] Heo, Y. W., D. P. Norton and S. J. Pearton. Origin of Green Luminescence in ZnO Thin Film Grown by Molecular-Beam Epitaxy, J. Appl. Phys., 98, pp. 073502-1-073502 -6. 2005.

[242] Sans, J. A., J. F. Sánchez-Royo and A. Segura. Study of the Bandgap Renormalization in Ga-doped ZnO Films by Means of Optical Absorption Under High Pressure and Photoelectron Spectroscopy, Superlattices Microstruct., 43, pp. 362-367. 2008.

[243] Yu, P. Y. and M. Cardona. Fundamentals of Semiconductors: Physics and Materials Properties, 3rd ed. pp. 306-310, New York: Springer Science+Business Media, LLC. 2007.

[244] Gong, L., J. Lu and Z. Ye. Transparent Conductive Ga-doped ZnO/Cu Multilayers Prepared on Polymer Substrates at Room Temperature, Sol. Energy Mater. Sol. Cells, 95, pp.1826-1830, 2011.

[245] Meerheim, R., R. Nitsche and K. Leo. High-Efficiency Monochrome Organic Light Emitting Diodes Employing Enhanced Microcavities, Appl. Phys. Lett., 93, pp. 043310-1-043310-3. 2008.

[246] Armstrong, N. R., P. A.Veneman, E. Ratcliff, D. Placenci and M. Brumbach. Oxide Contacts in Organic Photovoltaics : Characterization and Control of Near-Surface Composition in Indium-Tin Oxide (ITO) Electrodes, Acc. Chem. Res., pp. 1748-1757. 2009.

[247] Liu, H., B. Wang, E. S. P. Leong, P. Yang, Y. Zong, G. Si, J. Teng and S. A. Maier. Enhanced Surface Plasmon Resonance on a Smooth Silver Film with a Seed Growth Layer, ACS nano, 4, 6, pp. 3139-3146. 2010.

[248] Uda, M., A. Nakamura, T. Yamamoto and Y. Fujimoto. Work function of polycrystalline Ag, Au and Al**,** J. Electron Spectrosc. Relat. Phenom., 88-91, pp. 643 -648. 1998.

[249] Haneman, D. Photoelectric Emission and Work Functions of InSb, GaAs, Bi_2Te_3 and Germanium, J. Phys. Chem. Solids, 11, pp. 205-214. 1959.

[250] Dong, L., J. Jiao, D. W. Tuggle, J. M. Petty, S. A. Elliff and M. Coulter. ZnO Nanowires Formed on Tungsten Substrates and their Electron Field Emission Properties, Appl. Phys. Lett., 82, pp. 1096-1098. 2003.

[251] Forsythe, E. W., Y. Gao, L. G. Provost and G. S. Tompa. Photoemission Spectroscopy Analysis of ZnO:Ga Films for Display Applications, J. Vac. Sci. Technol. A, 17, pp. 1761-1764. 1999.

[252] Fowles, G. R. Introduction to Modern Optics, 2nd ed. pp.160-163, New York : Dover Publications, Inc. 1989.

[253] Gong, L., J. G. Lu and Z. Z. Ye. Conductive Ga Doped ZnO/Cu/Ga Doped ZnO Thin Films Prepared by Magnetron Sputtering at Room Temperature for Flexible Electronics, Thin Solid Films, 519, pp. 3870-3874. 2011.

[254] Wang, L., J. S. Swensen, E. Polikarpov, D. W. Matson, C. C. Bonham, W. Bennett, D. J. Gaspar and A. B. Padmaperuma. Highly Efficient Blue Organic

Light–Emitting Devices with Indium–Free Transparent Anode on Flexible Substrates, Org. Electron., 11, pp. 1555–1560. 2010.

[255] Niklasson, G. A. and C. G. Granqvist. Electrochromics for Smart Windows: Thin Films of Tungsten Oxide and Nickel Oxide, and Devices based on these, J. Mater. Chem., 17, pp. 127–156. 2007.

[256] Jau, H. -C., K. -T. Cheng, T. -H. Lin, Y. -S. Lo, J. -Y. Chen, C. -W. Hsu and A. Y. -G. Fuh. Photo–Rewritable Flexible LCD using Indium Zinc Oxide/ Polycarbonate Substrates, Appl. Optics, 50, pp. 213-217. 2011.

[257] Yoo, B., K. Kim, S. H. Lee, W. M. Kim and N. -G. Park. ITO/ATO/TiO_2 Triple–Layered Transparent Conducting Substrates for Dye–Sensitized Solar Cells, Sol. Energy Mater. Sol. Cells, 92, pp. 873-877. 2008.

[258] Ginley, D. S. and C. Bright. Transparent Conducting Oxides, MRS Bulletin, 35, pp. 15-18. 2000.

[259] Lee,B. J., H. J. Kim, W. -I. Jeong and J. -J. Kim. A Transparent Conducting Oxide as an Efficient Middle Electrode for Flexible Organic Tandem Solar Cells, Sol. Energy Mater. Sol. Cells, 94, pp. 542-546. 2010.

[260] Bowen, A., J. Li, J. Lewis, K. Sivaramakrishnan, T. L. Alford and S. Iyer. The Properties of Radio Frequency Sputtered Transparent and Conducting ZnO: Films on Polythelene Naphthalate Substrate, Thin Solid Films, 519, pp. 1809-1816. 2011.

[261] Gadre, M. J. and T. L. Alford. Highest Transmittance and High-Mobility Amorphous Indium Gallium Zinc Oxide on Flexible Substrate by Room-Temperature Deposition and Post-Deposition Anneals, Appl. Phys. Lett., 99, pp. 051901-1-051901-3. 2011.

[262] Hao, X., J. Ma, D. Zhang, T. Yang, H. Ma, Y. Yang, C Cheng and J. Huang. Thickness Dependence of Structural, Optical and Electrical Properties of ZnO:Al Films Prepared on Flexible Substrates, Appl. Surf. Sci., 183, pp. 137-142. 2001.

[263] Wong, L. M., S. Y. Chiam , J. Q. Huang, S. J. Wang, W. K. Chim and J. S. Pan. Examining the transparency of gallium-doped zinc oxide for photovoltaic applications, Sol. Energy Mater. Sol. Cells, 95, 8, pp. 2400-2406. 2011.

[264] http://materion.com/ResourceCenter/ProductData/InorganicChemicals/Oxides/Brochures AndDataSheets/AZOTransparentConductiveCoating.aspx
last accessed 30th Apr 2012

[265] Liu, H., V. Avrutin, N. Izyumskaya, Ü. Özgür and H. Morkoç. Transparent Conducting Oxides for Electrode Applications in Light Emitting and Absorbing Devices, Superlattices Microstruct., 48, pp. 458-484. 2010.\

[266] Lorenz, M., E. M. Kaidashev, H. Wenckstern, V. Riede, C. Bundesmann, D. Spemann, G. Benndorf, H. Hochmuth, A. Rahm, H. -C. Semmelhack and M. Grundmann. Optical and Electrical Properties of Epitaxial $(Mg,Cd)_xZn_{1-x}O$, ZnO, and ZnO:(Ga,Al) Thin Films on c-Plane Sapphire Grown by Pulsed Laser Deposition, Solid-State Electron., 47, pp. 2205-2209. 2003.

[267] Dong, B. -Z., G. -J. Fang, J. -F. Wang, W. -J. Guan and X. -Z. Zhao. Effect of Thickness on Structural, Electrical, and Optical Properties of ZnO: Al Films Deposited by Pulsed Laser Deposition, J. Appl. Phys., 101, pp. 033713-1-033713-7. 2007.

[268] Haacke, G. New Figure of Merit for Transparent Conductors, J. Appl. Phys. 47, pp. 4086-4089. 1976.

[269] http://www.laserfocusworld.com/articles/2010/06/uv-detectors-zinc-oxide-materials-and-their-alloys-redefine-uv-sensing.html last accessed 30th Apr 2012

[270] Bae, H. S. and S. Im, ZnO-Based Thin-Film Transistors of Optimal Device Performance, J. Vac. Sci. Technol. B, 22, pp. 1191-1195. 2004.\

[271] Ng, K. L., N. Zhan, C. W. Kok, M. C. Poon and H. Wong. Electrical Characterization of the Hafnium Oxide Prepared by Direct Sputtering of Hf in Oxygen With Rapid Thermal Annealing, Microelectron. Relia., 43, pp. 1289-1293. 2003.

[272] Liu, J., D. B. Buchholz, J. W. Hennek, R. P. H. Chang, A. Facchetti and T. J. Marks. All-Amorphous-Oxide Transparent, Flexible Thin-Film Transistors. Efficacy of Bilayer Gate Dielectrics, J. Am. Chem. Soc., 132, pp. 11934-11942. 2010.

[273] Moon, T. -H., M. -H. Ham, M. -S. Kim, I. Yun and J. -M. Myoung. Growth and Characterization of MOMBE grown HfO_2, Appl. Surf. Sci., 240, pp. 105-111. 2005.

[274] Liu, H. X., J. Sun, Q. X. Tang and Q. Wan. Ultralow-Voltage Electric Double-Layer SnO_2 Nanowire Transistors Gated by Microporous SiO_2-Based Solid Electrolyte, J. Phys. Chem. C., 114, pp. 12316v12319. 2010.

[275] Kirchartz, T., J. Mattheis and U. Rau. Detailed Balance Theory of Excitonic and Bulk Heterojunction Solar Cells, Phys. Rev. B, 78, pp. 235320-1-235320-13. 2008.

[276] Shanid, N. A. M. and M. A. Khadar. Evolution of Nanostructure, Phase Transition and Band Gap Tailoring in Oxidized Cu Thin Films, Thin Solid Films, 516, pp. 6245-6252. 2008.

[277] Serin, N., T. Serin, S. Horzum and Y. Celik. Annealing Effects on the Properties of Copper Oxide Thin Films Prepared by Chemical Deposition, Semicond. Sci. Technol., 20, pp. 398-401. 2005.

[278] Akimoto, K., S. Ishizuka, M. Yanagita, Y. Nawa, G. K. Paul and T. Sakurai. Thin Film Deposition of Cu_2O and Application for Solar Cells, Sol. Energy, 80, pp. 715-722. 2006.

[279] Poulston, S., P. M. Parlett, P. Stone and M. Bowker. Surface Oxidation and Reduction of CuO and Cu_2O Studied Using XPS and XAES, Surf. Interface Anal., 24, 12, pp. 811-820. 1996.

[280] Zhu, H., J. Zhang, C. Li, F. Pan, T. Wang and B. Huang. Cu_2O Thin Films Deposited by Reactive Direct Current Magnetron Sputtering, Thin Solid Films, 517, pp. 5700-5704. 2009.

[281] Chandra, R., P. Taneja and P. Ayyub. Optical Properties of Transparent Nanocrystalline Cu_2O Thin Films Synthesized by High Pressure Gas Sputtering, Nanostruct. Mater., 11, 4, pp. 505-512. 1999.

[282] Reddy, A. S., H. -H. Park, V. S. Reddy, K. V. S. Reddy, N. S. Sarma, S. Kaleemulla, S. Uthanna and P. S. Reddy. Effect of Sputtering Power on the Physical Properties of DC Magnetron Sputtered Copper Oxide Thin Films, Mater. Chem. Phys., 110, pp. 397-401. 2008.

[283] Pierson, J. F., A. Thobor-Keck and A. Billard. Cuprite, Paramelaconite and Tenorite Films Deposited by Reactive Magnetron Sputtering, Appl. Surf. Sci., 210, pp. 359-367. 2003.

[284] Muthe, K. P., J. C. Vyas, S. N. Narang, D. K. Aswal, S. K. Gupta, D. Bhattacharya, R. Pinto, G. P. Kothiyal and S. C. Sabharwal. A Study of CuO Phase Formation During Thin Film Deposition by Molecular Beam Epitaxy, Thin Solid Films, 324, pp. 37-43. 1998.

[285] Larson, P. E. X-Ray Induced Photoelectron and Auger Spectra of Cu, CuO, Cu_2O, and Cu_2S Thin Films, J. Electron Spectrosc. Relat. Phenom., 4, pp. 213-218. 1974.

[286] Schön, G. ESCA Studies of Cu, Cu_2O and CuO, Surf. Sci., 35, pp. 96-108. 1973.

[287] Kraut, E., R. Grant, J. Waldrop and S. Kowalczyk. Precise Determination of the Valence-Band Edge in X-Ray Photoemission Spectra: Application to Measurement of Semiconductor Inter face Potentials, Phys. Rev. Lett., 44, pp. 1620-1623. 1980.

[288] Chiam, S. Y., W. K. Chim, C. Pi, A. C. H. Huan, S. J. Wang, J. S. Pan, S. Turner and J. Zhang. Band Alignment of Yttrium Oxide on Various Relaxed and Strained Semiconductor Substrates, J. Appl. Phys., 103, pp. 083702-1-083702-12. 2008.

[289] Veal, T. D., P. D. C. King, S. A. Hatfield, L. R. Bailey, C. F. McConville, B. Martel, J. C. Moreno, E. Frayssinet, F. Semond and J. Zuniga-Pérez. Valence

Band Offset of the ZnO/AlN Heterojunction Determined by X-ray Photoemission Spectroscopy, Appl. Phys. Lett., 93, pp. 202108-1-202108-3 2008.

[290] Hamadani, B. H., H. Ding, Y. Gao and D. Natelson. Doping-Dependent Charge Injection and Band Alignment in Organic Field-Effect Transistors, Phys. Rev. B, 72, pp. 235302-1-235302-5. 2005.

[291] Harima,Y., H. Okazaki, Y. Kunugi, K. Yamashita, H. Ishii and K. Seki. Formation of Schottky Barriers at Interfaces Between Metals and Molecular Semiconductors of p‐ and n‐Type Conductances, Appl. Phys. Lett., 69, pp. 1059-1061. 1996.

[292] Archer, R. J. and T. O. Yep. Dependence of Schottky Barrier Height on Donor Concentration, J. Appl. Phys., 41, pp. 303-311, 1970.

[293] Edge, L. F., D. G. Schlom, S. A. Chambers, E. Cicerrella, J. L. Freeouf, B. Hollander and J. Schubert. Measurement of the Band Offsets Between Amorphous $LaAlO_3$ and Silicon, Appl. Phys. Lett., 84, pp. 726-728. 2004.

[294] Ley, L., J. Ristein, J. Schafer and S. Miyazaki. Near‐Surface Dopant Passivation After Wet‐Chemical Preparation, J. Vac. Sci. Technol. B, 14, pp. 3008-3012, 1996.

[295] Thornton, J. M. C. and R. H. Williams. An S/XPS Study of Hydrogen Terminated, Ordered Silicon (100) and (111) Surfaces Prepared by Chemical Etching, Phys. Scr., 41, pp. 1047-1052. 1990.

[296] Tung, R. T. Formation of an Electric Dipole at Metal-Semiconductor Interfaces, Phys. Rev. B, 64, pp. 205310-1-205310-15. (2001).

[297] Monroy, E., F. Omnes and F. Calle. Wide-Bandgap Semiconductor Ultraviolet Photodetectors, Semicond. Sci. Technol., 18, pp. R33-R51. 2003.

[298] Luo, L., Y. F. Zhang, S. S. Mao and L.W. Lin. Fabrication and Characterization of ZnO Nanowires Based UV Photodiodes, Sens. Actuators A, 127, 2, pp. 201-206. 2006.

[299] Cheng, J. P., Y.J. Zhang and R.Y. Guo. ZnO Microtube Ultraviolet Detectors, J. Cryst. Growth, 310, pp. 57-61. 2008.

[300] Masuoka, F., K. Ooba, H. Sasaki, H. Endo, S. Chiba, K. Maeda, H. Yoneyama, I. Niikura and Y. Kashiwaba. Applicability of ZnO Single Crystals for Ultraviolet Sensors, Phys. Status Solidi (c), 3, pp. 1238-1241. 2006.

[301] Chai, G. Y., O. Lupanb, L. Chow and H. Heinrich. Crossed Zinc Oxide Nanorods for Ultraviolet Radiation Detection, Sens. Actuators, A, 150, 2, pp. 184-187. 2009.

[302] Chen, Q., M. A. Khan, C. J. Sun and J. W. Yang. Visible-Blind Ultraviolet Photodetectors Based on GaN p-n Junctions, Electron. Lett., 31, pp. 1781-1782. 1995.

[303] Gorla, C. R., N. W. Emanetoglu, S. Liang, W. E. Mayo, Y. Lu, M. Wraback and H. Shen. Structural, Optical, and Surface Acoustic Wave Properties of Epitaxial ZnO Films on (0112) Sapphire by Metalorganic Chemical Vapor Deposition, J. Appl. Phys., 85, pp. 2595-2602. 1999.

[304] Lv, J. G., W. B. Gong, K. Huang, J. B. Zhu, F. M. Meng, X. P. Song and Z. Q. Sun. Effect of Annealing Temperature on Photocatalytic Activity of ZnO Thin Films Prepared by Sol-Gel Method, Superlattices Microstruct., 50, pp. 98-106. 2011.

[305] Robertson, J. and B. Falabretti. Band Offsets of High K Gate Oxides on III-V Semiconductors, J. Appl. Phys., 100, pp. 014111-1-014111-8. 2006.

[306] Robertson, J. and B. Falabretti. Band Offsets of High K Gate Oxides on High Mobility Semiconductors, Mater. Sci. Eng. B, 135, pp. 267-271. 2006.

[307] Edge, L. F., D. G. Schloma, P. Sivasubramani, R. M. Wallace, B. Holländer and J. Schubert. Electrical Characterization of Amorphous Lanthanum Aluminate Thin Films Grown by Molecular-Beam Deposition on Silicon, Appl. Phys. Lett., 88, pp. 112907-1-112907-3. 2006.

[308] Reiner, J. W., A. Posadas, M. Wang, M. Sidorov, Z. Krivokapic, F. J. Walker, T. P. Ma and C. H. Ahn. Electrical Properties and Interfacial Structure of Epitaxial $LaAlO_3$ on Si (001), J. Appl. Phys., 105, pp. 124501-1-124501-5. 2009.

[309] Robertson, J. Band Offsets of Wide-Band-Gap Oxides and Implications for Future Electronic Devices, J. Vac. Sci. Technol. B, 18, pp. 1785-1791. 2000.

[310] Kingon, A. I., J. -P. Maria and S. K. Streiffer. Alternative Dielectrics to Silicon Dioxide for Memory and Logic Devices, Nature, 406, pp. 1032-1038. 2000.

[311] Schlom, D. G. and J. H. Haeni. A Thermodynamic Approach to Selecting Alternative Gate Dielectrics, MRS bull., 27, pp. 198-204 (2002).

[312] Park, J. -S., J. K. Jeong, Y. -G. Mo and S. Kim. Impact of high-k TiO_x Dielectric on Device Performance of Indium-Gallium-Zinc Oxide Transistors, Appl. Phys. Lett., 94, pp. 042105-1-042105-3. 2009.

[313] Aygun, G. and I. Yildiz. Interfacial and Structural Properties of Sputtered HfO_2 Layers, J. Appl. Phys., 106, pp. 014312-1-014312-7. 2009.

[314] Hu, H., C. Zhu, Y. F. Lu, Y. H. Wu, T. Liew, M. F. Li, B. J. Cho, W. K. Choi and N. Yakovlev. Physical and Electrical Characterization of HfO_2 Metal-

Insulator-Metal Capacitors for Si Analog Circuit Applications, J. Appl. Phys., 94, pp. 551-557. 2003.

[315] Park, J. -H., S. Lee, K. Jeon, S. Kim, S. Kim, J. Park, I. Song, C. J. Kim, Y. Park, D. M. Kim and D. H. Kim. Density of States-Based DC I-V Model of Amorphous Gallium-Indium-Zinc-Oxide Thin-Film Transistors, IEEE Electr. Dev. L., 30, pp. 1069-1071. 2009.

[316] Wong, W. S., S. E. Ready, J. -P. Lu and R. A. Street. Hydrogenated Amorphous Silicon Thin-Film Transistor Arrays Fabricated by Digital Lithography, IEEE Electr. Dev. L., 24, pp. 577-579. 2003.

[317] Wilk, G. D., R.M. Wallace and J.M. Anthony. High-k Gate Dielectrics: Current Status and Materials Properties Considerations, J. Appl. Phys., 89, pp. 5243–5275. 2001.

[318] Qi, Q., A. Yu, P. Jiang and C. Jiang. Enhancement of Carrier Mobility in Pentacene Thin-Film Transistor on SiO_2 by Controlling the Initial Film Growth Modes, Appl. Surf. Sci., 255, pp. 5096-5099. 2009.

[319] Templier, F., B. Aventurier, P. Demars, J. -L. Botrel and P. Martin. Fabrication of High Performance Low Temperature Poly-Silicon Backplanes on Metal Foil for Flexible Active-Matrix Organic Light Emission Diode Displays, Thin Solid Films, 515, pp. 7428-7432. 2007.

[320] Kim, J. -J., J. -Y. Bak, J. -H. Lee, H. S. Kim, N. -W. Jang, Y. Yun and W. -J. Lee. Characteristics of Laser-Annealed ZnO Thin Film Transistors, Thin Solid Films, 518, pp. 3022-3025. 2010.

[321] Bae, H. S. and S. Im, ZnO-Based Thin-Film Transistors of Optimal Device Performance, J. Vac. Sci. Technol. B, 22, pp. 1191-1195. 2004.

[322] Park, K., D. -K. Lee, B. -S. Kim, H. Jeon, N. -E. Lee, D. Whang, H. -J. Lee, Y. J. Kim and J. -H. Ahn. Stretchable, Transparent Zinc Oxide Thin Film Transistors, Adv. Funct. Mater., 20, pp. 3577-3582. 2010.

[323] Levy, D. H., D. Freeman, S. F. Nelson, P. J. Cowdery-Corvan and L. M. Irving. Stable ZnO Thin Film Transistors by Fast Open Air Atomic Layer Deposition, Appl. Phys. Lett., 92, pp. 192101-1-192101-3. 2008.

[324] Ng, K. L., N. Zhan, C. W. Kok, M. C. Poon and H. Wong. Electrical Characterization of the Hafnium Oxide Prepared by Direct Sputtering of Hf in Oxygen With Rapid Thermal Annealing, Microelectron. Relia., 43, pp. 1289-1293. 2003.

[325] Sze, S. M. and K. K. Ng. Physics of Semiconductors Devices, 3rd ed. pp. 197-212, New York: John Wiley & Sons, Inc. 2007.

[326] Kim, J. H., B. D. Ahn, C. H. Lee, K. A. Jeon, H. S. Kang and S. Y. Lee. Characteristics of Transparent ZnO Based Thin Film Transistors with

Amorphous HfO_2 Gate Insulators and Ga doped ZnO Electrodes, Thin Solid Films, 516, pp. 1529-1532, 2008.

[327] Sze, S. M. and K. K. Ng. Physics of Semiconductors Devices, 3rd ed. pp. 205,306, New York: John Wiley & Sons, Inc. 2007.

[328] Nam, S. -W., J. -H. Yoo, S. Nam, H. -J. Choi, D. Lee, D. -H. Ko, J. H. Moon, J. -H. Ku and S. Choi. Influence of Annealing Condition on the Properties of Sputtered Hafnium Oxide, J. Non-Cryst. Solids., 303, pp. 139-143. 2002.

[329] Masuda, S., K. Kitamura, Y. Okumura, S. Miyatake, H. Tabata and T. Kawai. Transparent Thin Film Transistors Using ZnO as an Active Channel Layer and their Electrical Properties, J. Appl. Phys., 93, pp. 1624-1630. 2003.

[330] Kim, D. H., N. G. Cho, H. -G. Kim and I. -D. Kim. Highly Transparent $InGaZnO_4$ Thin Film Transistors Using Indium-Doped ZnO Electrodes on Plastic Substrate, Electrochem. Solid-State Lett., 12, 6, pp. H198-H201. 2009.

[331] Lim, W., E. A. Douglas, D. P. Norton, S. J. Pearton, F. Ren, Y. -W. Heo, S. Y. Son and J. H. Yuh. Low-Voltage Indium Gallium Zinc Oxide Thin Film Transistors on Paper Substrates, Appl. Phys. Lett., 96, pp. 053510-1-053510-3. 2010.

[332] Kwon, S., J. Park and P. D. Rack. Device Characteristics of Amorphous Indium Gallium Zinc Oxide TFTs Sputter Deposited with Different Substrate Biases, Electrochem. Solid-State Lett., 12, pp. H278-H280. 2009.

[333] Kwon, Y., Y. Li, Y. W. Heo, M. Jones, P. H. Holloway, D. P. Norton Z. V. Park and S. Li. Enhancement-Mode Thin-Film Field-Effect Transistor Using Phosphorus-Doped (Zn,Mg)O Channel, Appl. Phys. Lett., 84, pp. 2685-2687. 2004.

[334] Son, D. -H, D. -H. Kim, S. -J. Sung, E. -A. Jung and J. -K. Kang. High Performance and the Low Voltage Operating InGaZnO Thin Film Transistor, Curr. Appl. Phys., 10, pp. e157-e160. 2010.

[335] Son, D. -H., D. -H. Kim, J. -H. Kim, S. -J. Sung, E. -A. Jung and J. -K. Kang. Low Voltage, High Performance Thin Film Transistor with HfInZnO Channel and HfO_2 Gate Dielectric, Electrochem. Solid-State Lett., 13, pp. H274-H277. 2010.

[336] Sze, S. M. Semiconductor Devices: Physics and Technology, 2nd ed., pp.297-316, New York: John Wiley & Sons, Inc. 2002.

[337] Fortunato, E., P. Barquinha, A. Pimentel, A. Gonçalves, A. Marques, L. Pereira and R. Martins. Recent advances in ZnO transparent thin film transistors, Thin Solid Films, 487, 205– 211. 2005.

[338] Chen, H. J. H. and B. B. L. Yeh. Optimization of the Fabrication Process for ZnO Thin-Film Transistors with HfO_2 Gate Dielectrics, Jpn. J. Appl. Phys., 48, 031103-1-031103-5. 2009.

[339] Kim, G. H., H. S. Shin, B. D. Ahn, K. H. Kim, W. J. Park and H. J. Kim. Formation Mechanism of Solution-Processed Nanocrystalline InGaZnO Thin Film as Active Channel Layer in Thin-Film Transistor, J. Electrochem. Soc., 156, H7. 2009.

[340] Chen, A., S. Haddad, Y. C. Wu, Z. Lan, T. N. Fang and S. Kaza. Switching Characteristics of Cu_2O Metal-Insulator-Metal Resistive Memory, Appl. Phys. Lett., 91, pp. 123517-1-123517-3. 2007.

[341] Lim, J. -H., C. -K. Kang, K. -K. Kim, I.-K. Park, D.-K. Hwang and S. -J. Park. UV Electroluminescence Emission from ZnO Light-Emitting Diodes Grown by High-Temperature Radio Frequency Sputtering, Adv. Mater., 18, pp. 2720-2724. 2006.

[342] Park, J. -H., K. -J. Ahn, K. -I. Park, S. -I. Na and H. -K. Kim. An Al-Doped ZnO Electrode Grown by Highly Efficient Cylindrical Rotating Magnetron Sputtering for Low Cost Organic Photovoltaics, J. Phys. D: Appl. Phys., 43, pp. 115101-1-115101-6. 2010.

[343] Meyer, J., P. Görrn, S. Hamwi, H.-H. Johannes, T. Riedl and W. Kowalsky. Indium-Free Transparent Organic Light Emitting Diodes with Al doped ZnO Electrodes Grown by Atomic Layer and Pulsed Laser Deposition**,** Appl. Phys. Lett. 93, pp. 073308-1-073308-3. 2008.

[344] Kim, W. -S., Y. -K. Moon, S. Lee, B. -W. Kang, T. -S. Kwon, K. -T. Kim and J. -W. Park. Copper Source/Drain Electrode Contact Resistance Effects in Amorphous Indium-Gallium-Zinc-Oxide Thin Film Transistors, Phys. Status Solidi (RRL), 3, 7-8, pp. 239-241. 2009.

List of Publications

Thesis-related Publications

1. **L. M. Wong**, S. Y. Chiam, S. J. Wang, J. S. Pan and W. K. Chim, Highly conducting and transparent aluminium-doped zinc oxide thin films deposited on polyethylene terephthalate substrates, Submitted to Thin Solid Films

2. **L. M. Wong**, S. Y. Chiam, J. Q. Huang, S. J. Wang, W. K. Chim and J. S. Pan, "Examining the transparency of gallium-doped zinc oxide for photovoltaic applications", *Solar Energy Materials and Solar Cells*, vol. 95, Issue 8, pp. 2400–2406, 2011.
   *Highlighted as Key Scientific Articles in Renewable Energy Global Innovations
   * Highlighted A*Star Research, Electronics: A perfect vision, *11 Apr 2012*
   * Highlighted in Science Daily : Electronics: Low-Temperature Method Could 'Grow' Transparent Zinc Oxide Films for Displays and Solar Cells *Apr. 12, 2012*

3. **L. M. Wong**, S. Y. Chiam, J. Q. Huang, S. J. Wang, J. S. Pan and W. K. Chim, "Role of oxygen for highly conducting and transparent gallium-doped zinc oxide electrode deposited at room temperature", *Applied Physics Letters*, vol. 98, Issue 2, pp. 022106–1 to 022106–3, 2011.

4. **L. M. Wong**, S. Y. Chiam, J. Q. Huang, S. J. Wang, J. S. Pan and W. K. Chim, "Growth of Cu_2O on Ga-doped ZnO and their interface energy alignment for thin films solar cells", *Journal of Applied Physics*, vol. 108, Issue 3, pp. 033702–1 to 033702–6, 2010.

5. **L. M. Wong**, S. J. Wang and W. K. Chim**, "**Comparative study of aluminum-doped zinc oxide and ruthenium aluminum co-doped zinc oxide by magnetron co-sputtering"**,** *Thin Solid Films*, vol. 518, number 24, pp. e93–e97, 2010.

Other Publications

1. S. Y. Chiam, M. Y. Leung, H. Liu, Z. E. Ooi, **L. M. Wong**, C. Y. Jiang, K. L. Chang, W. L. Koh, J. Y. Ng and J. Zhang, "Investigating the stability of defects in MoO_3 and its role in organic solar cells", *Solar Energy Materials & Solar Cell,* vol. 99, pp. 197-203, 2012.

2. S. Y. Chiam, Z. Q. Liu, J. S. Pan , K. K. Manippady, **L. M. Wong** and W. K. Chim, "Effects of electric field in band alignment measurements using photoelectron spectroscopy", *Surface and Interface Analysis,* (accepted)

3. D. Sentosa, B. Liu, **L. M. Wong**, Y. V. Lim, T. I. Wong, Y. L. Foo, H. D. Sun and S. J. Wang, "Activation of phosphorous doping in high quality ZnO thin film grown on YSZ(111) by thermal treatment", *Thin Solid Films*, vol. 520, Issue 3, pp. 997-998, 2011.

4. X. L. Xu, B. Peng, D. H. Li, J. Zhang, **L. M. Wong**, Q. Zhang, S. J. Wang and Q. H. Xiong, Flexible Vis-IR metamaterials and their applications in highly sensitive chemical and biological sensing, *Nano Letters*, vol. 11, Issue 8, pp. 3232–3238, 2011.
   *Highlighted in *Nature Publishing Group Asia Materials research highlight:* "Photonics: Metamaterials on a stretch," 5 Sept. 2011.
   *Highlighted in *Nanowerk*: "Metamaterials on a stretch provide dynamic properties", 5 Sept. 2011.
5. G. P. Li, R. Chen, D. L. Guo, **L. M. Wong**, S. J. Wang, H. D. Sun and T. Wu, "Nanoscale semiconductor–insulator–metal core/shell heterostructures: facile synthesis and light emission", *Nanoscale*, vol. 3, pp. 3170-3177, 2011.

6. M. I. B. Utama, Z. P. Peng, R. Chen, B. Peng, X. L. Xu, Y. J. Dong, **L. M. Wong**, S. J. Wang, H. D. Sun and Q. H. Xiong, "Vertically Aligned Cadmium Chalcogenide Nanowire Arrays on Muscovite Mica: A Demonstration of Epitaxial Growth Strategy", *Nano Letters*, vol. 11, Issue 8, pp. 3051–3057, 2011.
   *Highlighted as Nano Letters journal cover in August 2011 issue.

7. W. F. Yang, **L. M. Wong**, S. J. Wang, H. D. Sun, C. H. Ge, Alex Y. S. Lee and H. Gong, "Photoluminescence characteristics of ZnCdO/ZnO single quantum well grown by pulsed laser deposition", *Applied Physics Letters*, vol. 98, Issue 12, pp. 121903–1 to 121903–3, 2011.

8. W. F. Yang, R. Chen, B. Liu, **L. M. Wong**, S. J. Wang and H. D. Sun, "Temperature dependence of weak localization effects of excitons in ZnCdO/ZnO single quantum well", *Journal of Applied Physics,* vol. 109, Issue 11, pp. 113521–1 to 113521–4, 2011.

9. D. Sentosa, B. Liu, **L. M. Wong**, Y. V. Lim, T. I. Wong, Y. L. Foo, H. D. Sun and S. J. Wang, "Temperature Dependent Photoluminescence Studies of ZnO Thin Film Grown on (111) YSZ Substrate", *Journal of Crystal Growth*, vol. 319, Issue 1, pp. 8–12, 2011.

10. Z. Peng, H. Hu, M. I. B. Utama, **L. M. Wong**, K. Ghosh, R. Chen, S. J. Wang, Z. Shen and Q. H. Xiong, "Heteroepitaxial Decoration of Ag Nanoparticles on Si Nanowires: A Case Study on Raman Scattering and Mapping", *Nano Letters*, vol. 10, Issue 10, pp. 3940–3947, 2010.

11. W. F. Yang, B. Liu, R. Chen, **L. M. Wong**, S. J. Wang and H. D. Sun, "Pulsed laser deposition of high-quality ZnCdO epilayers and ZnCdO/ZnO single quantum well on sapphire substrate"*, Applied Physics Letter,*vol. 97, Issue 6, pp. 061911–1 to 061911–3, 2010.

12. W. F. Yang, R. Chen, B. Liu, G. G. Gurzadyan, **L. M. Wong**, S. J. Wang and H. D. Sun, "Surface-plasmon enhancement of band gap emission from ZnCdO thin films by gold particles", *Applied Physics Letters*, vol. 97, Issue 6, pp. 061104–1 to 061104–3, 2010.

13. Z. P. Wei, M. Arredondo, H. Y. Peng, Z. Zhang, D. L. Guo, G. Z. Xing, Y. F. Li, **L. M. Wong**, S. J. Wang, N. Valanoor and T. Wu, "A template and catalyst-free metal-etching-oxidation method to synthesize aligned nanowire arrays: NiO as an example", *ACS Nano*, vol. 4, Issue 8, pp. 4785–4791, 2010.

14. Z. Zhang, **L. M. Wong**, H. X. Wang, Z. P. Wei, W. Zhou, S. J. Wang and T. Wu, "Self-assembled in-plane growth of Mg_2SiO_4 nanowires on Si substrates catalyzed by Au nanoparticles", *Advanced Functional Materials*, vol. 20, Issue 15, pp. 2511–2518, 2010.

15. Z. Zhang, R. Ranjith, B. T. Xie, L. You, **L. M. Wong**, S. J. Wang, J. L. Wang, W. Prellier, Y. G. Zhao and T. Wu, "Enhanced low field magnetoresistance in nanocrystalline $La_{0.7}Sr_{0.3}MnO_3$ synthesized on MgO nanowires", *Applied Physics Letters*, Vol. 96, Issue 22, pp. 222501–1 to 222501–3, 2010.

16. M. Yang, W. S. Deng, Q. Chen, Y. P. Feng, **L. M. Wong**, J. W. Chai , J. S. Pan, S. J. Wang and C. M. Ng, "Band alignments at $SrZrO_3$/Ge(0 0 1) interface: Thermal annealing effects", *Applied Surface science*, vol. 256, Issue 15, pp. 4850–4853, 2010.

17. H. T. Wang, Z. Zhang, **L. M. Wong**, S. J Wang, Z. P. Wei, G. P. Li, G. Z. Xing, D. L. Guo, D. D Wang and T. Wu, "Shape-Controlled Fabrication of Micro/ Nanoscale Triangle, Square, Wire-like, and Hexagon Pits on Silicon Substrates Induced by Anisotropic Diffusion and Silicide Sublimation", *ACS Nano*, vol. 4, Issue 5, pp. 2901–2909, 2010.

18. Z. P. Wei, D. L. Guo, B. Liu, R. Chen, **L. M. Wong**, W. F. Yang, S. J. Wang, H. D. Sun and T. Wu, "Ultraviolet light emission and excitonic fine structures in ultrathin single-crystalline indium oxide nanowires", *Applied Physics Letters*, vol. 96, Issue 3, pp. 031902–1 to 031902–3, 2010.

19. S. J. Wang, T. I. Wong, Q. Chen, M. Yang, **L. M. Wong**, J. W. Chai, Z. Zhang, J. S. Pan and Y. P. Feng, "Atomic and electronic structures at ZnO and ZrO_2 interface for transparent thin-film transistors", *Physica status solidi (a),* vol. 207, Issue 7, pp. 1731–1734, 2010.

20. M. Yang, W. S. Deng, Q. Chen, Y. P. Feng, **L. M. Wong**, J. W. Chai, J. S. Pan, S. J. Wang and C.M. Ng , "Band offsets of HfO_2/ZnO interface: In situ x-ray photoelectron spectroscopy measurement and ab initio calculation", *Applied Physics Letters*, vol. 95, Issue 16, pp. 162104–1 to 162104–3, 2009.

21. J. Q. Huang, W. K. Chim, S. J. Wang, S. Y. Chiam and **L. M**. **Wong**, "Germanium nanostructures: Under control", Nature Publishing Group, Asia Materials research highlight, 15 April 2009.

22. J. Q. Huang, W. K. Chim, S. J. Wang, S. Y. Chiam and **L. M. Wong**, "From Germanium Nanowires to Germanium-Silicon Oxide Nanotubes:Influence of Germanium Tetraiodide Precursor", *Nano Letters*, vol. 9, Issue 2, pp. 583–589, 2009.

23. Z. Zhang, J. Gao, **L. M. Wong**, J. G. Tao, L. Liao, Z. Zheng, G. Z. Xing, H. Y. Peng, T. Yu, Z. X. Shen, C. H. A. Huan, S. J. Wang and T. Wu, "Morphology-controlled synthesis and a comparative study of the physical properties of SnO_2 nanostructures: from ultrathin nanowires to ultrawide nanobelts", *Nanotechnology*, vol. 20, number 13, pp. 135605–135615, 2009.

24. J. Q. Huang, S. Y. Chiam, W. K. Chim, **L. M. Wong** and S. J. Wang, "Heterostructures of germanium nanowires and germanium-silicon oxide nanotubes and growth mechanisms", *Nanotechnology*, vol. 20, number 42, pp. 425604–425611, 2009.

25. G. Z. Xing, J. B. Yi, J. G. Tao, T. Liu, **L. M. Wong**, Z. Zhang, G. P. Li, S. J. Wang, J. Ding, T. C. Sum, C. H. A. Huan and T. Wu, "Comparative Study of Room-Temperature Ferromagnetism in Cu-Doped ZnO Nanowires enhanced by Structural Inhomogeneity", *Advanced Materials*, vol. 20, Issue 18, pp. 3521–3527, 2008.

26. Z. Zhang, **L. M. Wong**, H. G. Ong, X. J. Wang, J. L. Wang, S. J. Wang, H. Y. Chen, and T. Wu**, "**Self-Assembled Shape- and Orientation-Controlled Synthesis of Nanoscale Cu_3Si Triangles, Squares, and Wires", *Nano Letter*, vol. 8, Issue 10, pp. 3205–3210, 2008.

27. Z. Zhang, J. B. Yi, J. Ding, **L. M. Wong**, H. L. Seng, S. J. Wang, J. G. Tao, G. P. Li, G. Z. Xing, T. C. Sum, C. H. A. Huan and T. Wu, "Cu-Doped ZnO Nanoneedles and Nanonails: Morphological Evolution and Physical Properties", *Journal of Physical Chemistry C*, vol. 112, number 26, pp. 9579–9585, 2008.